UNTANGLING THE DEPTHS AND CONDITIONS OF MAGMA BODIES THROUGH TIME

By

Lydia Jane Harmon

Dissertation

Submitted to the Faculty of the

Graduate School of Vanderbilt University

in partial fulfillment of the requirements

for the degree of

DOCTOR OF PHILOSOPHY

in

Earth and Environmental Sciences

March 31, 2022

Nashville, Tennessee

Approved:

Guilherme A. R. Gualda, Ph.D.

Darren M. Gravley, Ph.D.

Calvin F. Miller, Ph.D.

David J. Furbish, Ph.D.

Mark S. Ghiorso, Ph.D.

To Dad for always seeing the fun side of life, and to Mum for always being in my pocket.

ACKNOWLEDGMENTS

Although it is my name on the front of this dissertation, it would not be possible without the unwavering support of many people. While I won't be able to convey how much your help has meant to me, I will try my best.

First (and foremost), I must thank my advisor, Guil Gualda. Throughout the years, it has become abundantly clear that he thinks about the world a bit differently compared to the rest of us. I have immensely enjoyed seeing his perspective on petrology, bicycling, climbing, IPAs, and life in general.

Darren Gravley has been paramount to my development as a scientist, especially in the field. If there's one thing I've learned from Darren, it is that we should all take a step back and think about the big picture. And there's always time for a coffee. Thank you for letting me come on that first Brazil field expedition and for inviting me to New Zealand for the year (or maybe I demanded all of that?!).

I secretly refer to Calvin Miller as my favorite committee member. His constantly upbeat attitude, willingness to chat about any topic, and field mochas are inspirational. I will always try to find the middle ground thanks to Calvin, who can usually find the novelty in even the worst papers.

Like many prospective graduate students, I had several books piled on my lap at the end of my first meeting with David Furbish. I think there was also a clementine involved. There was a time early on, when I would avoid eye contact and run past David's office because I hadn't made enough progress on my Transport project. However, every time I forced myself to go ask a question, I was met with kindness and thought provoking questions. I will try my best to continually ask more questions.

Mark Ghiorso has explained some of the most difficult thermodynamics in some of the most challenging and inspiring lectures I've encountered. He has always put me at ease, and has always made time for me. I consider myself especially lucky that the world's top expert has time to please restart the MELTS server again.

Samantha Tramontano has been my research partner since the beginning. Her warmth, kindness, late night mac and cheese, and, laterly, weekly or twice-weekly Zooms have kept me on track. One day, we will write a grant together, and it will be immediately funded and amazing.

Sarah Smithies makes the most beautiful figures and makes data dance. I am so pleased that we get to think about TVZ and magmas every week.

MESSY and PUMMUS are two of my weekly highlights with all of my favorite magma people!

The grad students (and postdocs and choice undergrads) at Vanderbilt have made this an absolutely wonderful time in my life. The old grad students - Leland Cohen, Moyo Ajayi, Tyler Doane, Chris Tasich, Aaron Covey, Jen Bradham, Siobhan Fathel - were the best people to welcome me to Nashville. The new grad students are carrying on the fun! A special shout-out to Liam Kelly, Samuel Heagney, and Sophia Wang for their contributions to science and friendship.

Outside of work, my roommates through the years have been outstanding. Elli Ronay, Tara Saxena, Kelly Dennen, Samantha Tramontano, Sarah Smithies, Elisabeth Bertolett, Francis Main, and Joseph Ward have made all the houses homes.

Marina Gualda, Amanda Gualda, and Malu Jorge are three of my favorite Brazilians.

Brandt Gibson is a fantastic second, who always gets there first. Sometimes third?

Elizabeth Teeter and Sarah Williams are (thankfully) always keen for bagels. Sometimes work is involved, but rarely!

Thanks to Tom Garden and Mary DeRoy for making my time in New Zealand adventurous.

Obrigada aos Alpinistas pela segurança que eles nos deram durante as viagens aos cânions!!

Christian Larberg has been a source of encouragement, except during intense games of backgammon.

Linh-Vy Shrauner, Alec Leverette, and Ross Stamper have been hanging out with me for more than half of our lives, and it's been a lot of fun!

Hopefully Michael Gibbs and I can jam in the same band one day.

And, finally, thanks to Mum and Dad. Maggie Harmon and Jerry Harmon have been unwavering in their support, no matter what I've decided to do. Thank you for always encouraging me, which has given me the confidence to try almost anything.

TABLE OF CONTENTS

LIST OF TABLES

LIST OF FIGURES

CHAPTER 1

Introduction

1.1 Motivation

Volcanic landscapes are the surface expression of volcanic and magmatic systems, and volcanism implies that there are times during which large volumes of eruptible magma are stored within the Earth's crust. Complex subsurface magmatic processes are only evidenced by their erupted deposits or once erosion exposes the interiors of the system. We know that these magma systems generate, store, and ultimately erupt magma, and petrologic tools help decipher the conditions and depths of these magma systems.

Recently, our understanding of the pre-eruptive configuration of magma systems has been evolving. The concept of a large, long-lived, melt-dominated magma chamber has been largely replaced by a perspective in which magma systems are more complex regions of both liquid-dominated bodies and more crystal-rich mushy bodies that span the depth of the crust (Cashman et al., 2017; Sparks et al., 2019). In the so-called transcrustal magmatic system, there can exist multiple levels of magma generation, extraction, and storage prior to eruption.

Our focus is on the upper crust (< 20 km and often < 5 km depth), which is the region from which most of the high-silica rhyolites erupt. We focus primarily on eruptible magma bodies, which are the final amalgamation of magma prior to eruption. There can be different configurations of magma bodies. While the traditional view of an eruptible magma body is a single magma body that has a melt-dominated region and a mushy region from which the melt-rich magma is extracted (Bachmann & Bergantz, 2008, 2004; Hildreth, 2004) eruptions can be fed by multiple magma bodies (Bégué et al., 2014; Cooper et al., 2012; Gualda & Ghiorso, 2013). Now that we have the ability to decipher instances in which multiple magma bodies feed eruptions, we must determine the storage conditions of the magma body (or bodies) to reconstruct how the crust can accommodate large volumes of magma prior to eruption.

The primary questions drive our research are:

• How many eruptible magma bodies exist prior to large eruptions?

• What are the storage conditions of these eruptible magma bodies?

• How do the number and depths of these eruptible magma bodies change through the lifecycle of a large magma system?

• Over what timescales are the magma bodies and magma systems active?

This dissertation focuses predominantly on the first three questions, but the fourth question is an important

extension of my research. By zooming in on the depths and conditions of these relatively shallow, eruptible magma bodies, we can better understand how magma is created, stored, and erupted.

In this dissertation, I apply a combination of field, analytical, and modeling techniques to answer these research questions. The bulk of my research focuses on the Whakamaru group eruptions, which erupted at 344 ka ± 4 ka in Aotearoa New Zealand as a series of large eruptions. There are multiple ignimbrites preserved across the TVZ, as well as several coastal pyroclastic fall deposits that have been hypothesized to be correlated to the Whakamaru group eruptions. My goal is to integrate the ignimbrite record with the pyroclastic fall deposit record to understand the pre-eruptive conditions of the magma bodies through time.

To do this, I utilize pumice clasts, which are preserved parcels of quenched magma. Pumice clasts represent the best proxies to eruptible magma, and they thus provide a window into the magma body (Figure 1). They can reveal the processes occurring in magma bodies kilometers below the surface – including those that can erupt 100s to 1000s km3 of magma.

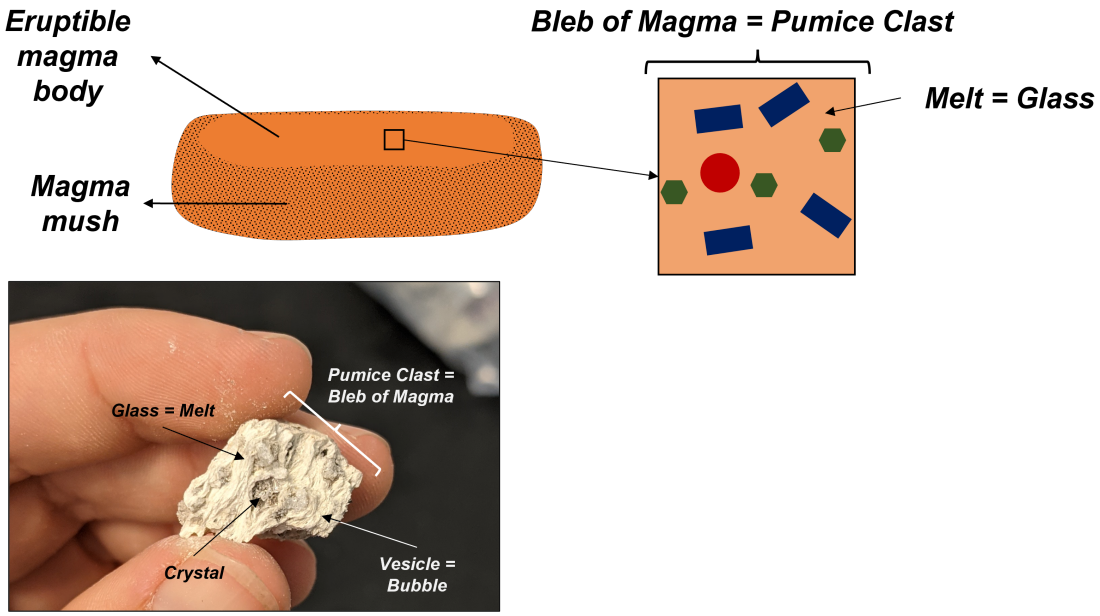

Figure 1.1: A conceptual model of a magma body. A pumice clast represents the eruptible magma. An individual pumice clast is a quenched bleb of magma with crystals, glass, and vesicles preserved. The glass represents the eruptible melt.

Chapters 2 and 3 focus on the Whakamaru group of deposits and associated tephras. Chapter 2 focuses on the pyroclastic fall deposits of the Whakamaru group eruptions – as well as tephras preceding and postdating the Whakamaru group. Chapter 3 focuses on the Whakamaru group ignimbrite deposits. We use a combination of different types of data in tephras and ignimbrites to better understand the pre-eruptive magma system that sourced the Whakamaru group eruptions.

Although the focus of this dissertation is the Whakamaru group eruptions, the loftier goal is to understand

magmatic storage conditions in general. In Chapter 5, we focus on ultra-shallow magma bodies, which extend our understanding of where magma can be stored in the crust. The three chapters are written as stand-alone manuscripts to be submitted to academic journals.

A personal motivation behind this work is that we do not know what we are going to discover when embarking on new research. There are hypotheses and ideas to test, but, ultimately, the pumice clasts will tell us their stories in little snippets and it is our privilege to discover how magma and volcanic systems exist and erupt. It is an exciting proposition that if we can elucidate different aspects of magma systems – from their origins in the mantle to the volcanic eruptions at the surface – we can further understand the what, when, where, and why of the magmatic systems.

1.2 References

Bachmann, O., & Bergantz, G. (2008). The magma reservoirs that feed supereruptions. Elements, 4(1), 17–21. https://doi.org/10.2113/GSELEMENTS.4.1.17

Bachmann, O., & Bergantz, G. W. (2004). On the origin of crystal-poor rhyolites: Extracted from batholithic crystal mushes. Journal of Petrology, 45(8), 1565–1582. https://doi.org/10.1093/petrology/egh019

Bégué, F., Deering, C. D., Gravley, D. M., Kennedy, B. M., Chambefort, I., Gualda, G. A. R., & Bachmann, O. (2014). Extraction, storage and eruption of multiple isolated magma batches in the paired Mamaku and Ohakuri eruption, Taupo Volcanic Zone, New Zealand. Journal of Petrology, 55(8), 1653–1684. https://doi.org/10.1093/petrology/egu038

Cashman, K. v., Stephen, R., Sparks, J., & Blundy, J. D. (2017). Vertically extensive and unstable magmatic systems: A unified view of igneous processes. Science, 355(6331). https://doi.org/10.1126/science.aag3055

Cooper, G. F., Wilson, C. J. N., Millet, M. A., Baker, J. A., & Smith, E. G. C. (2012). Systematic tapping of independent magma chambers during the 1Ma Kidnappers supereruption. Earth and Planetary Science Letters, 313–314(1), 23–33. https://doi.org/10.1016/j.epsl.2011.11.006

Gualda, G. A. R., & Ghiorso, M. S. (2013). The Bishop Tuff giant magma body: an alternative to the Standard Model. 2Contributions to Mineralogy and Petrology, 166, 755–775. https://doi.org/10.1007/s00410-013-0901-6

Hildreth, W. (2004). Volcanological perspectives on Long Valley, Mammoth Mountain, and Mono Craters: Several contiguous but discrete systems. Journal of Volcanology and Geothermal Research, 136(3–4), 169–198. https://doi.org/10.1016/j.jvolgeores.2004.05.019

Sparks, R. S. J., Annen, C., Blundy, J. D., Cashman, K. v., Rust, A. C., & Jackson, M. D. (2019). Formation and dynamics of magma reservoirs. Philosophical Transactions of the Royal Society A: Mathematical, Physical and Engineering Sciences, 377(2139). https://doi.org/10.1098/rsta.2018.0019

CHAPTER 2

The Conditions and Sequence of Magma Storage and Eruption Through the Whakamaru Group Eruptions

2.1 Introduction

Understanding the pre-eruptive distribution and storage conditions of eruptible magma bodies is critical in our quest to understand how the crust can accommodate and erupt large volumes of magma (Blundy & Cashman, 2008; Cashman & Giordano, 2014; Charlier *et al.*, 2007; K. M. Cooper & Kent, 2014; Gualda & Sutton, 2016; Wilson & Charlier, 2016). For some magma systems, multiple eruptible magma bodies can erupt together (Bégué, Deering, *et al.*, 2014; Cashman & Giordano, 2014; G. F. Cooper *et al.*, 2012; K. M. Cooper, 2017; Gravley *et al.*, 2007; Gualda & Ghiorso, 2013), or from a single, zoned magma body as originally proposed by Hildreth for the Bishop Tuff (Hildreth, 1979) and for magma bodies that generally follow the Mush Model (Bachmann & Bergantz, 2004, 2008; Chamberlain *et al.*, 2015; Deering *et al.*, 2011; Foley *et al.*, 2020; Hildreth & Wilson, 2007; Swallow *et al.*, 2018). There is a growing body of work suggesting that these eruptible magma bodies can be short-lived (G. F. Cooper *et al.*, 2017; K. M. Cooper & Kent, 2014; Gualda, Pamukcu, *et al.*, 2012; Gualda & Sutton, 2016; Pamukcu, Gualda, Bégué, *et al.*, 2015; Shamloo & Till, 2019; Stelten *et al.*, 2014), with the larger, longer-lived magma system from which the eruptible magma is sourced active over much longer timescales (Barboni *et al.*, 2015; Kaiser *et al.*, 2017; Reid & Vazquez, 2017; Simon & Reid, 2005).

We focus on the Whakamaru magma system, which produced a group of large, ignimbrite-forming eruptions in the central Taupō Volcanic Zone (TVZ), Aotearoa New Zealand (Briggs, 1976a, 1976b; S. J. A. Brown *et al.*, 1998; Ewart, 1965; Ewart & Healy, 1966; Houghton *et al.*, 1995; Martin, 1965; Wilson *et al.*, 1986, 2009). The Whakamaru group eruptions occurred after a $\sim$200 ka hiatus in caldera-forming volcanism (Deering *et al.*, 2010), and their eruptions mark the beginning of an ignimbrite flare-up episode that lasted from $\sim$350 to $\sim$280 ka, during which at least 7 additional large (50-150 km3), caldera-forming eruptions occurred (Gravley *et al.*, 2016; Houghton *et al.*, 1995; Wilson *et al.*, 2009). The Whakamaru group eruptions are unique within the flare-up, as they are the largest eruptions by an order of magnitude (>2000 km3) (Gravley *et al.*, 2016; Matthews, Smith, *et al.*, 2012; Wilson *et al.*, 2009) and contribute most of the erupted volume to the flare-up period (totaling >3000 km3), they are the only crystal-rich magmas erupted (up to $\sim$40 wt% crystals) (S. J. A. Brown *et al.*, 1998), and have distinct mineralogical and textural attributes.(S. J. A. Brown *et al.*, 1998; Deering *et al.*, 2010; Ewart, 1965; Gravley *et al.*, 2016). Thus, we focus on the development,

eruption, and death of a texturally and volumetrically unique magma system that kicked off an ignimbrite flare-up in one of the most active silicic systems in the world (Houghton *et al.*, 1995; Wilson *et al.*, 1995, 2009).

Deciphering how the eruptible magma bodies are organized in the crust and erupt through time is notoriously challenging for the Whakamaru magma system (S. J. A. Brown *et al.*, 1998; Downs *et al.*, 2014; Wilson *et al.*, 1984). The Whakamaru group ignimbrites are divided into 4 mappable units (Briggs, 1976a, 1976b; Ewart & Healy, 1966; Grindley, 1960; Healy *et al.*, 1964; Leonard *et al.*, 2010; Martin, 1961, 1965; Wilson *et al.*, 1984). However, it is not yet clear how the eruptions relate to the mapped units (Briggs, 1976a, 1976b; S. J. A. Brown *et al.*, 1998; Wilson *et al.*, 1986). With the exception of the later erupted Paeroa ignimbrites, the Whakamaru group ignimbrites' Ar-Ar ages are indistinguishable at 349 ka ± 4 ka (Downs *et al.*, 2014), and the ignimbrites do not overlap sufficiently in the field to definitively determine relative timing of the eruptions (S. J. A. Brown *et al.*, 1998; Wilson *et al.*, 1986). Tephra deposited as pyroclastic fall deposits (PFDs) offers a solution (Bonadonna & Phillips, 2003; R. J. Brown *et al.*, 2012; Costa *et al.*, 2012; Folch & Felpeto, 2005; Houghton & Carey, 2015). The tephras exhibit clear relative ages since they are deposited sequentially. By correlating the Whakamaru group ignimbrites to their fall deposits (Manning, 1996), we use evidence from physical volcanology, glass compositions, and rhyolite-MELTS geobarometry to decipher how the eruptible magma bodies were organized in the crust, and how they erupted and changed through time.

Our data are from two coastal tephra sequences ∼50 km from the northern end of the inferred Whakamaru caldera, on the coast of the Bay of Plenty, New Zealand (Figure 1a). We include tephra from eruptions that precede the Whakamaru group eruptions (the pre-Paerata Tablelands and Paerata tephras) through the Murupara and Bonisch tephras that postdate Whakamaru and predate the Matahina eruptions (Manning, 1995, 1996) (Figure 1b).

2.1.1 Nomenclature

A note on nomenclature: ***Magma*** is a geological material that includes (typically silicate in composition) melt, but which can also include crystals and bubbles. A ***magma body*** is a parcel of magma that is in contact with rocks or other magmas, with clear boundaries. We can define eruptible magma bodies and magma mush bodies. An ***eruptible magma body*** is composed of crystal-poor magma that is melt dominated and typically has a suspension of crystals and bubbles. It can be erupted imminently. A ***magma mush body*** is composed of crystal-rich magma that contains a framework of touching crystals, possibly with bubbles present. The magma mush resists shear and is unlikely to be readily erupted. A ***magma type*** is a compositionally and texturally homogeneous group of magmas where a given magma type may be characteristic of a magma body, or it may be present in multiple magma bodies. The collection of magma bodies that coexist in the

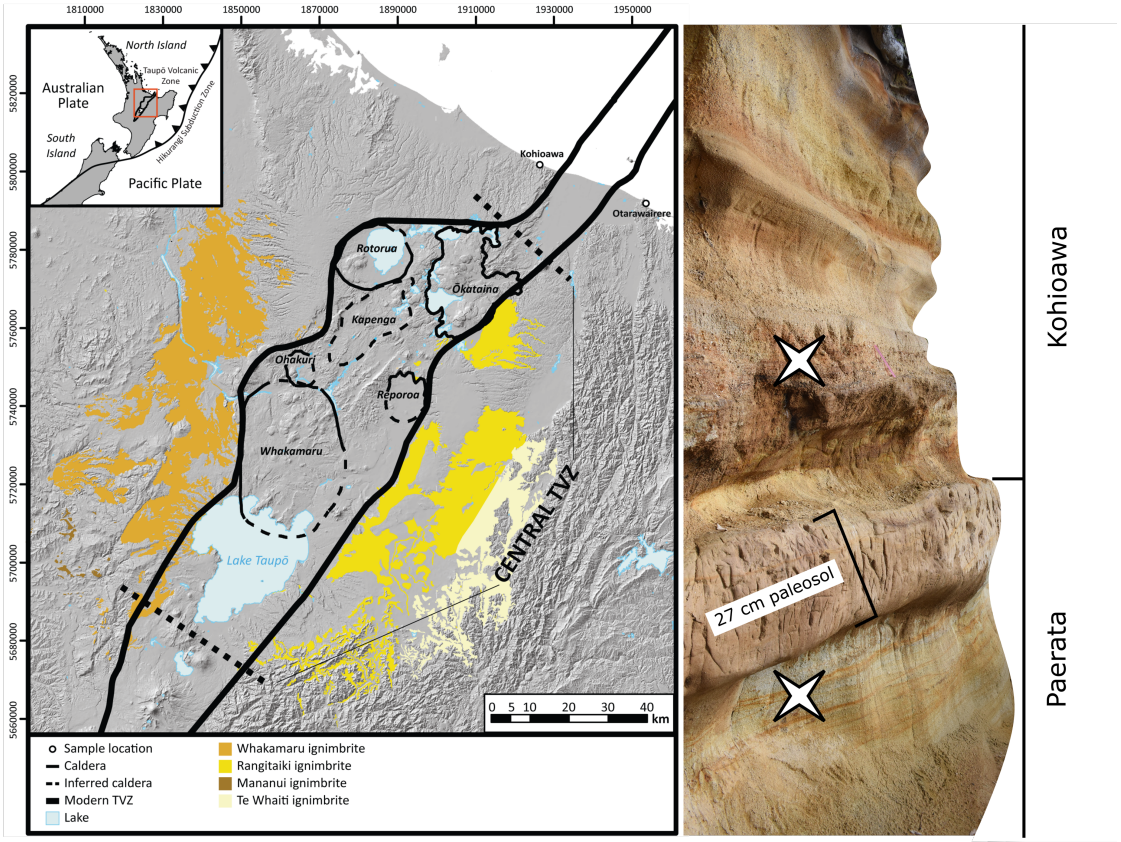

Figure 2.1: Map of the Taupō Volcanic Zone (TVZ), left, showing the outline of the TVZ and major calderas of the ignimbrite flare-up ($\sim$ 350-280 ka). The Whakamaru caldera is the southernmost and largest caldera. Locations of the two coastal tephra sequences, the Kohioawa Section and Ōtarawairere Section, are marked with circles at the coast, $\sim$ 50 km northeast of the caldera. The map inset shows the location of the TVZ within the North Island of New Zealand. Right, Field photo of the lower portion of the Ōtarawairere section with the Paerata, Kohioawa, and paleosol marked. Locations of two of the samples in this study are marked by stars (Unit B lower star and OK240404-IC upper star).

crust at any given point in time defines the ***magma reservoir***. The details of the compositions and distribution of magma bodies within the reservoir can be well or poorly defined. The ***magma system*** includes all magma bodies through time (G. A. R. Gualda, personal communication, January 4, 2022).

The erupted deposits are referred to as ignimbrites or pyroclastic fall deposits (PFDs), when the origin of emplacement is important (R. J. Brown & D. M. Andrews, 2015; Houghton & Carey, 2015). The two outcrops discussed here are composed primarily of volcanic material deposited as PFDs, so we refer to the erupted material as tephra. The larger tephra clasts studied are coarse-ash-sized to lapilli-sized pumice clasts.

2.1.2 Taupō Volcanic Zone (TVZ) and Flare-Up

The modern TVZ is situated in a northeast-southwest rifted arc in the North Island of New Zealand (Wilson *et al.*, 1995). The northern and southern ends of the TVZ produce predominantly andesitic eruptions, while the central TVZ is dominated by high-silica rhyolite eruptions with only minor amounts of dacite, andesite, and basalt (Wilson *et al.*, 1984). The modern TVZ is one of the most active silicic volcanic systems in the world (Houghton *et al.*, 1995; Wilson *et al.*, 1995), having produced at least 6000 km3 of silicic magma over the last ∼1.6 Ma (Wilson *et al.*, 2009), with silicic activity starting at ∼1.9 Ma (Eastwood *et al.*, 2013).

Over this time, there have been three ignimbrite flare-up periods in the TVZ, which are especially intense periods of ignimbrite-forming volcanism (Houghton *et al.*, 1995). The largest ignimbrite flare-up occurred from ∼350 to ∼280 ka (Gravley *et al.*, 2007, 2016; Houghton *et al.*, 1995; Wilson *et al.*, 2009), which erupted >3000 km3 of magma from 8 calderas from the 90 x 40 km area of the central TVZ (see Figure 1a; Gravley *et al.*, 2016, and references therein). The Whakamaru group eruptions are the first of this ignimbrite flare-up, occurring at 349 ± 4 ka (Downs *et al.*, 2014; Wilson *et al.*, 1986). They erupted >2,000 km3 of magma, and are the largest eruptions in the modern TVZ (Downs *et al.*, 2014; Houghton *et al.*, 1995; Matthews, Smith, *et al.*, 2012; Wilson *et al.*, 1986).

Although the Whakamaru group eruptions began the ignimbrite flare-up, they are distinct from the later eruptions of the period, as they have different textural and mineralogical signatures (Briggs, 1976a, 1976b; S. J. A. Brown *et al.*, 1998; Deering *et al.*, 2010; Ewart, 1965; Gravley *et al.*, 2016; Saunders *et al.*, 2010). They are relatively crystal rich (∼15-40 wt% crystals)(S. J. A. Brown *et al.*, 1998; Houghton *et al.*, 1995), sometimes contain sanidine (which is unusual in the TVZ) (S. J. A. Brown *et al.*, 1998; Downs *et al.*, 2014) and abundant hydrous phases (e.g. biotite and hornblende) (S. J. A. Brown *et al.*, 1998; Ewart, 1965, 1967b, 1967a), and are characterized by containing large quartz crystals (Briggs, 1976a, 1976b; S. J. A. Brown *et al.*, 1998; Matthews, Pyle, *et al.*, 2012; Saunders *et al.*, 2010). The Whakamaru group ignimbrites are described as part of the "cold, wet, oxidizing" R1 type magma of Deering *et al.* 2010 classification. In contrast, the later ignimbrite flare-up magmas erupted 50-150 km3 at a time, are crystal poor (<10 wt% and sometimes <5 wt% crystals)(Gravley *et al.*, 2016), do not contain sanidine, and are generally part of the "hot, dry, reducing" R2 type magma of Deering *et al.* 2010 classification. The Whakamaru group ignimbrites and the later-erupted flare-up ignimbrites thus represent the two geochemical types (R1 and R2, respectively) of silicic volcanism from the central TVZ (Deering *et al.*, 2010; Gravley *et al.*, 2016). The distinctions between the magmas imply potential differences in source and evolution of the magmas through time (Deering *et al.*, 2010; Gravley *et al.*, 2016; Gualda *et al.*, 2018).

2.1.3 Whakamaru Magma System and Eruptions

The Whakamaru magma system had a complex history of magma generation (Saunders *et al.*, 2010) and of erupting multiple, distinct magma types (S. J. A. Brown *et al.*, 1998) likely over multiple eruptions (Grindley, 1960; Houghton *et al.*, 1995; Martin, 1961; Wilson *et al.*, 1986). Prior to the Whakamaru group eruptions, there was a period of relative quiescence in the TVZ lasting $\sim$ 200 ka (Deering *et al.*, 2010), wherein there were no documented caldera-forming eruptions between the Utu and Whakamaru group eruptions. Zircon ages from the Whakamaru group eruptions show that the magma system was active $\sim$ 50-100 ka prior to eruption (Matthews, 2011), with older zircon ages implying that it was active up to $\sim$ 250 ka prior to eruption (S. J. A. Brown & Fletcher, 1999), indicating a long history of maturation. Evidence from plagioclase and quartz minerals show much shorter timescales (<300 a) for the final assembly, homogenization, and eruption (Matthews, Pyle, *et al.*, 2012; Saunders *et al.*, 2010), which imply relatively short timescales for the ephemeral eruptible magma bodies (Gualda, Pamukcu, *et al.*, 2012; Pamukcu, Gualda, Bégué, *et al.*, 2015).

Within the Whakamaru group eruptions, the ignimbrites are distinguished from one another by their differences in mineralogy, welding, and crystal content (Briggs, 1976a, 1976b; S. J. A. Brown *et al.*, 1998; S. J. A. Brown & Fletcher, 1999; Leonard *et al.*, 2010; Wilson *et al.*, 1986, 1995). Four mappable ignimbrite units are described – the Whakamaru, Manunui, Rangitaiki, and Te Whaiti ignimbrites (Briggs, 1976a, 1976b; Ewart, 1965; Ewart & Healy, 1966; Grindley, 1960; Healy *et al.*, 1964; Martin, 1965), with the Paeroa subgroup described as a younger ignimbrite (339 ± 5 ka) derived from the same magma system but likely erupted from a separate volcanic source (Downs *et al.*, 2014; Houghton *et al.*, 1995; Leonard *et al.*, 2010; Wilson *et al.*, 2009). The Whakamaru and Manunui ignimbrites outcrop to the west of the caldera, and the Rangitaiki and Te Whaiti ignimbrites outcrop to the east of the caldera. Wilson (1986) proposes that the Manunui and Te Whaiti ignimbrites could be correlative and erupted first, and that the Whakamaru and Rangitaiki ignimbrites could be correlative and erupted second. There is no documented significant time-break between the eruptions (S. J. A. Brown *et al.*, 1998; Downs *et al.*, 2014).

The ignimbrite units have not been definitively linked to the different magma types. Brown *et al.* (1998) determines four different rhyolite pumice types (Types A, B, C, D). The characteristics of the magma types are given in Table 1. Brown *et al.* (1998) interprets that the least evolved and hottest ignimbrites (Manunui and Te Whaiti) likely erupted first, with sanidine only present in the latter, more evolved eruptions. The presence of sanidine is corroborated by drillcore and field data (Briggs, 1976a; Ewart, 1965; Ewart & Healy, 1966; Martin, 1961, 1965). However, the lack of overlap and the presence of multiple pumice types in the ignimbrites begs the question of how the eruptible magma bodies were stored in the crust and erupted through time.

Table 2.1: Magma types and attributes, as characterized by Brown *et al.* (1998)

Pumice Type	Crystallinity	Mineralogy	General	Mafic Assemblage	SiO_2	Rb	Sr	Ba
A	crystal-rich (typically 30-40%); plag are large, euhedral to subhedral, and complexly zoned, commonly intergrown, and twinned; qtz are large (< 12 mm) resorbed and rounded; opx+/-hbl+/-bt	plag, qtz, opx, hbl, bt, magnetite/ilmenite	low silica rhyolite; high-Mg bt	opx +hbl +/- bt	70-74	80-140	140-200	750-1000
B	15-25% xtls; bt is predominant ferromag phase; san is Or68; qtz are smaller (< 3 mm), euhedral to subhedral, with less resorption than type A; plag smaller (< 3 mm), complexly zoned and twinned, commonly aggregates; bt less Mg-rich than Type A (Mg# 38.6-39.5)	plag, qtz, san, bt, mag +/- hbl microlites	low-Mg bt; types B and C distinguishable in Rb and Sr; not easily distinguished in hand sample or thin section	bt +/- hbl	>74	>120		1000-1400
C	15-25% xtls; bt is predominant ferromag phase; san is Or68; qtz are smaller (< 3 mm), euhedral to subhedral, with less resorption than type A; plag dominant over qtz, smaller (< 3 mm), complexly zoned and twinned, commonly aggregates; bt less Mg-rich than Type A (Mg# 39); no hbl	qtz, plag, san, bt, mag, ilm	low Ba; bt rich; low-Mg bt	bt	>75	>170		700-1000
D	30% xtls; plag-rich (21%), An25-35, large (< 4 mm), euhedral to subhedral, distinct melt inclusion at 0.1 - 0.3 mm from the xtl rim (resorption and regrowth), complexly zoned and twinned, forms in clusters; no plag-opx intergrowths (like in type A); qtz is subordinate (?) (5%), small (< 3 mm), strongly embayed to subhedral; no san; bt the main ferromag min; small amts of hbl and opx; bt similar Mg# to type A; elongate microlites of hbl and plag in matrix	plag, qtz, bt, hbl, opx	high Rb (>200 ppm); bt rich			~240	<155 (large range)	750-1000

The Rangitawa tephra (formerly the Mt. Curl tephra) has been linked to the Whakamaru group eruptions, and has been interpreted to be a later, crystal-rich phreato-plinian eruption, linked to the Paeroa eruptions (Matthews, Smith, *et al.*, 2012; Wilson *et al.*, 1986) based on glass shard major element compositions, ferromagnesian mineralogy, and similarity in paleomagnetic dates and zircon fission-track ages (Alloway *et al.*, 1993; Kohn *et al.*, 1992; Lowe *et al.*, 2001; Pillans *et al.*, 1996).

2.2 Field Relations and Previous Work

In order to understand the time-progressive evolution of the Whakamaru magma system, we focus on the tephras that outcrop $\sim$ 50 km northeast of the caldera in the Bay of Plenty (Manning, 1995, 1996). Tephra deposited as pyroclastic fall deposits can be transported much farther than material in pyroclastic density currents and can record important transitions in the eruption intensity (e.g. with changes in grain size, changes in ratios of ash, pumice, and lithics) (Bonadonna *et al.*, 2015; Houghton & Carey, 2015) and longer time-breaks between eruptions if soil horizons develop (Shoji *et al.*, 1994). The simple vertical organization of successive units makes their relative age easy to determine, in contrast with the Whakamaru group ignimbrites.

We study two locations that have preserved the tephras of interest: the Kohioawa Section and the Ōtarawairere Section (Figures 1 and 2). We refer to the different units of the tephras after the convention described by Manning (1995,1996), in which Manning (1995, 1996) correlates tephras, defines large paleosol boundaries and transitions in volcanism using traditional tephrastratigraphy methods, and determines transitions in texture and mineralogy of tephras in the Bay of Plenty.

We divide the tephras into four main units: Pre-Paerata, Paerata, Kohioawa, Murupara-Bonisch (Manning, 1995, 1996). We provide a brief overview below, and refer the reader to Manning (Manning, 1995, 1996) for additional details.

2.2.1 Pre-Paerata Tephras

The Pre-Paerata tephras are from the smaller eruptions from the Tablelands subgroup that erupted before the Paerata eruption. Their magmatic relationship with the Whakamaru magma system is not clear. The Pre-Paerata tephras are the result of much smaller volcanic events, and just precede or are similar in age to the Paerata tephras. In the Kohioawa Section, the Pre-Paerata tephras present are from the Tablelands C and Tablelands D eruptions ($\sim$375 and 370 ka respectively) (Manning, 1995). Together, their minimum volume is estimated to be 2.5 km^3. At the Ōtarawairere Section, the Pre-Paerata eruption sampled for this study was the Tablelands B tephra (also known as the Ōtarawairere tephra (Manning, 1995, 1996)), which sits atop weathered gravels. The Ōtarawairere Section is the type locality for this unit, which erupted a minimum estimate of 10 km3 at $\sim$380-390 ka. Results from the Pre-Paerata tephra are shown in yellow in all figures.

2.2.2 Paerata Tephras

The Paerata tephras are present in both locations, deposited from an eruption that precedes the Whakamaru group eruptions by ∼10-20 ka (Manning, 1995), with a minimum volume estimate of 15 km3. Its age is ∼360-370 ka, which is ∼0-15 ka after the Pre-Paerata eruptions (Manning, 1995). The correlation of Paerata magma to the Whakamaru magma system is not clear, although it is suggested that the Paerata could have been erupted from the Okataina caldera (Manning, 1995, 1996). Importantly, there is a well-developed paleosol at the top of the Paerata tephras at both Kohioawa Section and Ōtarawairere Section, indicating a substantial time break between eruptions. Results for the Paerata are also shown in yellow in all figures.

2.2.3 Kohioawa Tephras

The Kohioawa tephras are the thickest of all tephras in the Bay of Plenty, and they sit directly on top of the Paerata at both the Kohioawa Section and Ōtarawairere Section. The Kohioawa tephras are correlative with the Rangitawa tephra (Manning, 1995, 1996), found in drill cores off the coast of the Bay of Plenty. The Rangitawa tephra has previously been correlated to the Whakamaru group ignimbrites (Alloway *et al.*, 1993; Kohn *et al.*, 1992; Lowe *et al.*, 2001; Matthews, Smith, *et al.*, 2012; Pillans *et al.*, 1996). Matthews et al (2012) emphasizes that the distal Rangitawa tephra, which is interpreted to represent the Plinian eruption phase, is compositionally similar to Whakamaru ignimbrite Type A pumice, which is found in both the Whakamaru and Rangitaiki ignimbrites. Manning (1995) recognizes two distinct rhyolite compositions within the Kohioawa tephra, one which matches the Rangitawa tephra and a second, slightly different composition, both erupted from the same source (Manning, 1995). Therefore, the more proximal Kohioawa tephras are interpreted as correlative with both the distal Rangitawa tephra and the Whakamaru group ignimbrites (Froggatt *et al.*, 1986; Kohn *et al.*, 1992; Manning, 1996; Matthews, Smith, *et al.*, 2012). The presence of sanidine throughout the Kohioawa tephras and the matching of the O-isotope sea-level curve indicate that the Kohioawa tephras are correlative with the Whakamaru group ignimbrites. This correlation is discussed in greater detail below, where we compare our glass compositions with literature glass compositions from the Rangitawa tephra (Matthews, Smith, *et al.*, 2012) and Whakamaru group ignimbrites (Gualda *et al.*, 2018; Matthews, Smith, *et al.*, 2012). Results for the Kohioawa tephras are shown in red in Figure 2. Data from the Kohioawa tephra are shown in red, orange, and dark blue in the compositional and geobarometry figures.

The Whakamaru group ignimbrites have most recently been Ar-Ar dated to 349 ± 4 ka, with the smaller (with a volume estimate on the order of 110 km3) Paeroa subgroup ignimbrites having slightly younger ages of 339 ± 5 ka (Downs *et al.*, 2014). Manning (1995) estimates the age for the Kohioawa tephras to be ∼350 ka using the reconstructed paleo sea level curve from O-isotopes, suggesting that the tephras were deposited just before the glacial maximum (delta-O18 stage). The presence of glacial loess within the

Kohioawa tephras confirms that the Kohioawa tephras were erupted during colder conditions (Manning, 1995, 1996). However, in the O-isotope sea level reconstruction, several Ar-Ar ages from ignimbrites are used to constrain the O-isotope ages, including older Whakamaru ignimbrite age estimates (330-350 ka) (Houghton *et al.*, 1995). While the O-isotope sea level curve is helpful, we also focus on field evidence, mineralogy, and glass compositions to support the correlation of Kohioawa tephras to Whakamaru group ignimbrites. The correlation is further affirmed in the discussion.

To link the Kohioawa tephras to the Whakamaru group eruptions, the compositional glass data from this study are compared to glass compositional data from both Rangitawa distal tephra deposits (Matthews, Smith, *et al.*, 2012) and Whakamaru ignimbrite pumice (Gualda *et al.*, 2018) (Figures 5 and 6).

2.2.4 Murupara-Bonisch Tephras

The Murupara-Bonisch tephras post-date the Whakamaru group eruptions and precede the Matahina ignimbrite (Manning, 1995, 1996). The Murupara and Bonisch tephras erupted at ∼340-330 ka and have a combined volume of ∼50 km3 (Manning, 1995, 1996). Both the Murupara-Bonisch and the subsequent Matahina ignimbrite are interpreted to have erupted from the Okataina volcanic center (Manning, 1995, 1996). The Matahina ignimbrite is the next large eruption in the flare-up period, having erupted ∼150 km3 (Carr, 1994) of magma at 322 ± 7 ka (Leonard *et al.*, 2010). The Matahina ignimbrite has magmatic characteristics of both R1 type (typified by the Whakamaru group eruptions) and R2 type (typified by the later flare-up magmas) (Deering *et al.*, 2010). The Murupara-Bonisch tephras show the lead-up to the Matahina ignimbrite. Results for the Murupara-Bonisch tephras are shown in cyan on Figure 2. Data from the Murupara and Bonisch tephra are shown in cyan and magenta in the compositional and geobarometry figures.

2.3 Methods

Our goal is to understand the conditions of the eruptible magma bodies and the magma system that produced the Whakamaru group eruptions, including how the magma system changed through time. To accomplish this, tephra from two correlative locations are sampled and analyzed. We combine field observations with major and trace element glass compositional analyses. We focus on the mineralogy (when possible) and glass compositions recorded by coarse-ash to lapilli sized pumice clasts to determine the pre-eruptive conditions. We also utilize zircon saturation geothermometry and rhyolite-MELTS geobarometry based on the compositions of the clasts. The mineralogical characterization of the horizons was conducted by Chad Deering (personal communications). All other analytical data were collected at Vanderbilt University.

2.3.1 Field Observations and Sampling

The Kohioawa Section is ∼6 km north of Matata, along South Highway 2, just to the north of Kohioawa Beach turnoff, (37°52'27.25"S, 176°42'40.85"E). The Ōtarawairere Section is along the Kohi Point Scenic track at the north side of Ohope Beach, (37°57'11.80"S, 177° 1'26.20"E). The two locations are ∼30 km apart along the coast, and ∼50 km northeast of the caldera (Figure 1a). Each section was described and sampled during two field seasons in 2007 (samples labeled OK220707 and OK240707) and 2017 (samples labeled WHAK432), when we collected ∼1 kg of bulk tephra per horizon. Bulk tephra was sampled where distinct changes or differences in characteristics of the tephra material were observed, above and below paleosols, and where fresher tephra was available. We sampled 22 horizons at the Kohioawa Section and 8 horizons at the Ōtarawairere Section (see Figure 2). General descriptions of each unit are available in Table 2; detailed descriptions of the two sections are available in Table 4. Figure 2 shows the correlations, grain sizes, and paleosols within the outcrops.

2.3.2 Horizon Characterization

In addition to the sedimentological and mineralogical observations made in the field, a few key horizons were further characterized in the laboratory, in particular with respect to its mineralogy. Mineral componentry was conducted on several of the horizons from the Kohioawa Section – OK220707-1B (Pre-Paerata tephra), OK220707-1C (Paerata tephra), OK220707-1E, OK220707-1G, OK220707-1I, OK220707-1L, OK220707-1O (Kohioawa tephra), OK220707-1P, and OK220707-1Q (Murupara-Bonisch tephra). Particular attention to the felsic assemblage (including the presence of sanidine) was conducted on horizons OK220707-1G, OK220707-1I, OK220707-1L, OK220707-1O, OK220707-1Q.

Five to six pristine, generally larger coarse-ash to lapilli pumice clasts from each horizon were chosen for further study, particularly for determination of major and trace-element glass compositions. Most chosen clasts are 0.01-0.03 cm3 (∼0.15 cm diameter), although clast sizes vary between horizons. We focused on individual clasts because they represent individual parcels of magma that erupted but did not fully fragment. A total of 157 clasts were analyzed in this study. Each clast was mounted in epoxy for glass analysis.

Unfortunately, due to their small sizes, it is impractical to determine the mineralogy of each individual clast, as the total area exposed for each clast is unlikely to be representative of the mineralogy of the individual clast. Instead, we focus on the mineralogy of each horizon, which obscures potential differences in mineralogy between magma types present in the same horizon (particularly for horizons correlative with Whakamaru, for which some of the clasts are sanidine-bearing, while others are sanidine-free).

An additional 3-5 lapilli clasts were chosen per horizon to check for the presence of sanidine. Each clast was lightly crushed with a spoon to preserve the intact minerals and was placed on a glass slide with 1.544

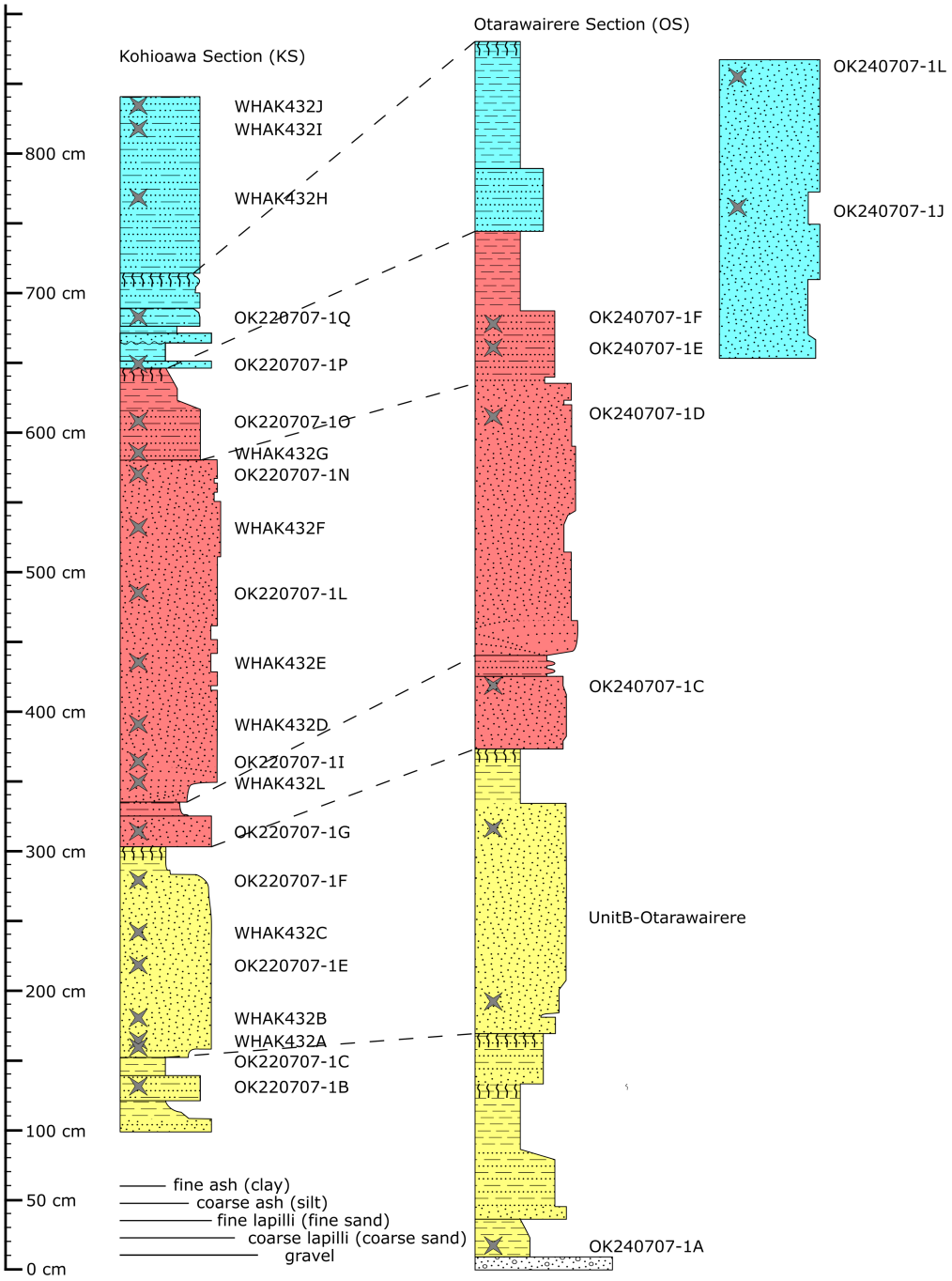

Figure 2.2: Schematic of the two tephra sequences, the Kohioawa Section and Ōtarawairere Section. The 22 samples from the Kohioawa Section and 8 samples from the Ōtarawairere Section are marked with X's and labeled with sample names. The width of the units corresponds to grain size. The patterns follow the Federal Geographic Data Committee Digital Cartographic Standard for Geologic Map Symbolization (FGDC-STD-013-2006). The paleosols are marked with vertical wiggly lines. Correlations between the two locations are marked with dashed lines. A general description of the units are found in Table 2; a detailed description of each horizon is found in Table 4.

refractive index oil. Sanidine was determined on the basis of negative optical relief and tabular habit. In contrast to sanidine, plagioclase and quartz exhibit positive optical relief in 1.544 refractive index oil.

2.3.3 Glass Geochemistry

Glass major-element compositions were obtained at Vanderbilt University using an Oxford X-max 50-mm2 Energy Dispersive Spectrometer (EDS) attached to a Tescan Vega 3 LM Variable Pressure Scanning Electron Microscope (SEM). Most glass analyses were obtained using 15 kV accelerating voltage (with several obtained with an accelerating voltage 18-20 kV to achieve a higher output count rate) and a specimen current of $\sim$2 nA at a working distance of 15 mm. The USGS-Rhyolite Glass Mountain (RGM-1) standard was measured at the beginning of each SEM session as a secondary standard. Data reduction for all SEM-EDS analyses was performed using the Aztec Oxford software, which uses internal standards for calibration. Results from the USGS RGM-1 standard are provided in the supplementary data.

Per clast, we analyzed $\sim$15 spots of the largest, most pristine sections of glass, far from crystals. Analyses were excluded if 1) a mineral (usually feldspar or a Fe-Ti oxide) was encountered; 2) the SiO_2 was > 82 wt% which likely indicates silicification of the glass; 3) the composition of individual elements was outside 1.5 times the interquartile range (IQR) for that individual clast which likely indicates glass alteration. This IQR test was performed once, and not iteratively, to identify and remove analyses that fall outside the natural variability of the glass.

Glass trace-element compositions were obtained via laser ablation inductively coupled plasma mass spectrometry (LA-ICP-MS) at Vanderbilt University. The system is a Photon Machines Excite 193 nm excimer laser attached to a Thermo iCAP Q quadrupole ICP-MS system. For each analysis, a 50 μm × 50 μm square laser spot size was ablated for 25 s at a pulse frequency of 10 Hz. NIST 610 was used as the primary standard and NIST 612 and RGM-1 were used as secondary standards. The isotope 28Si was used as an internal standard, using average SiO_2 contents determined for each sample by SEM-EDS analysis prior to trace element collection. Concentrations were processed through the data reduction program Glitter (Griffin *et al.*, 2008; van Achterbergh *et al.*, 2001).

We analyzed $\sim$15-20 spots per clast for trace-element compositions, where the spot locations were not the same as those analyzed for major-element compositions. Trace-element analyses were discarded if 1) a mineral (usually feldspar or a Fe-Ti oxide) was encountered; 2) or if an analysis had at least 5 elements below the detection limit; individual analytes were discarded if they failed the same IQR method as the major element data; if < 3 spots were adequate analyses, data from those clasts were not considered.

For both major and trace elements, values reported in Tables 5-15 are the mean values and standard deviations of each clast. In all figures, error bars represent one standard deviation of each clast.

2.3.4 Geothermometry

Zircon saturation temperatures are calculated using the mean glass compositions of the individual lapilli clasts using the formulations of Watson and Harrison (1983) and Boehnke *et al.* (2013). Both formulations are based on the major elements and zirconium concentration in the glass. If the melt is saturated in zircon, the temperature represents the temperature of zircon-melt equilibrium (likely a pre-eruptive storage temperature; see, for instance, Pitcher *et al.*, 2021); if the melt is undersaturated in zircon, the calculations return a minimum temperature.

2.3.5 Geobarometry

Thermodynamic modeling was conducted using rhyolite-MELTS (Gualda, Ghiorso, *et al.*, 2012; Gualda & Ghiorso, 2015). We used the rhyolite-MELTS geobarometer (Gualda, Ghiorso, *et al.*, 2012; Gualda & Ghiorso, 2014) to determine the pressure at which certain mineral phases are in equilibrium with the input major-element glass composition. The glass composition is a proxy for the melt composition, which is assumed to be in equilibrium with the observed crystallizing mineral assemblage. This method retrieves pre-eruptive storage conditions, and we focus on the pre-eruptive storage pressures to determine the depths of the magma bodies (Figure 3) (Bégué, Gualda, *et al.*, 2014; Gualda & Ghiorso, 2014; Harmon *et al.*, 2018; Pamukcu, Gualda, Ghiorso, *et al.*, 2015).

As discussed above, the lapilli clasts are too small for us to unequivocally determine their mineral assemblages by direct observation. While rhyolite-MELTS has previously been used with a known mineral assemblage, we can use the modeled presence of sanidine to determine whether sanidine is present in the individual lapilli clasts. We can leverage measured glass compositions to model not only the pre-eruptive storage pressures, but also the mineral assemblages of the individual lapilli clasts. We consider quartz, plagioclase, and sanidine in the geobarometry and mineral assemblage calculations, considering the two options: 1. quartz+plagioclase (qtz-1feld) 2. quartz+plagioclase+sanidine (qtz-2feld) For each rhyolite-MELTS calculation, if the melt was in equilibrium with the mineral assemblage, the saturation surfaces of each mineral will intersect at the pressure of equilibration (Figure 3). This pressure represents the conditions of magma storage prior to eruption. If the sanidine saturation curve intersects the quartz and plagioclase curves and calculates a pressure, we use the presence of a quartz+plagioclase+sanidine (qtz-2feld) pressure calculation as evidence for the presence of sanidine (Figure 4a). The absence of sanidine in the rhyolite-MELTS pressure calculation, in contrast, suggests that sanidine is not in equilibrium with the input glass composition. For example, if the quartz, plagioclase, and sanidine saturation curves intersect at 125 MPa, we interpret the storage pressure to be 125 MPa with a mineral assemblage of quartz+plagioclase+sanidine (qtz-2feld) in equilibrium with the input glass composition. If, however, only quartz+plagioclase is present at 125 MPa, we interpret

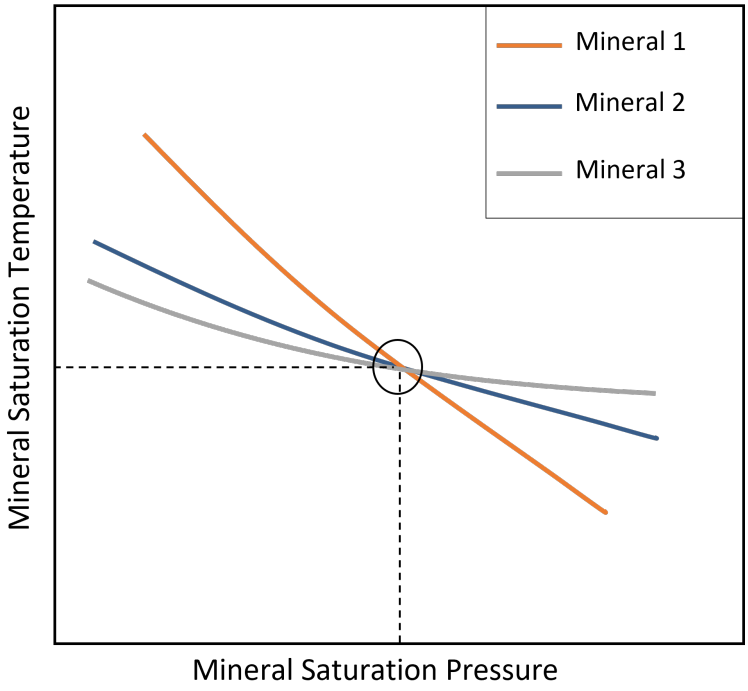

Figure 2.3: Schematic of Rhyolite-MELTS geobarometry calculations, after Harmon et al (2018). The saturation surface of a given mineral represents the conditions (temperature and pressure in this diagram) at which a mineral starts crystallizing when the equilibration is modeled down temperature (from super-liquidus, high temperature). Each mineral has a different saturation surface that is dependent on pressure. If the melt was in equilibrium with the mineral assemblage, the saturation surfaces will intersect at the temperature and pressure of equilibration, represented by the circle where all three saturation curves cross. In the case of pressures calculated using the glass composition, this represents the conditions of magma storage prior to eruption.

the storage pressure to be 125 MPa with a mineral assemblage of quartz+plagioclase (qtz-1feld) (Figure 4b).

Storage pressures are calculated if the saturation surfaces of the different mineral phases intersect within 5 °C (Figure 4). There are larger uncertainties for the qtz-1feld pressure calculations, since those pressures are only calculated using two mineral phases (Gualda & Ghiorso, 2014). The qtz-1feld calculations have ± 38 MPa uncertainty (Pitcher *et al.*, 2021). The uncertainty is smaller for the qtz-2feld pressures, since those pressure are calculated using the intersection of three saturation surfaces, which further constrain the storage pressure calculation. The qtz-2feld calculations have ± 24 MPa uncertainty (Pitcher *et al.*, 2021). We calculated pressures for mean glass compositions of all lapilli clasts (a total of 192 compositions after several lapilli clasts were discarded and some lapilli glass compositions were subdivided).

We model from the liquidus to 90 wt% crystals, 500-25 MPa in 25 MPa steps, and 1100-700 °C in 1 °C steps. We set all MnO and P2O5 values to 0. If MgO was reported to be 0 wt% from the SEM-EDS data, we interpret that the MgO value is below the detection limit from the EDS analysis. Rhyolite-MELTS calculations cannot be performed with MgO equal to zero, given that it would set the activity of MgO to zero

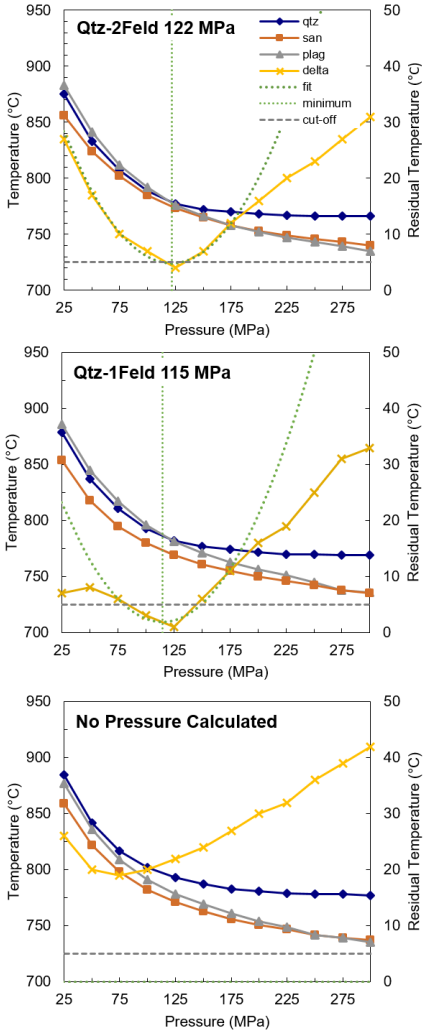

Figure 2.4: Representative Rhyolite-MELTS geobarometry calculations. The saturation surfaces of quartz, sanidine, and plagioclase are plotted in temperature vs pressure. The difference in temperature between the saturation surfaces of the mineral phases (residual temperature) are represented by the yellow "delta" line. In the top panel, all three mineral phases saturate within 5 C at 125 MPa (i.e. the residual temperature, represented by the delta line, is equal to or less than 5 C, represented by the gray "cutoff" line at 125 MPa), so a qtz-2feld pressure is calculated. The pressure is calculated by fitting a parabola to the minimum residual temperature and the two points above and below the minimum pressure (green dashed "fit" parabola). The minimum of the parabola represents the calculated storage pressure (green dashed vertical line), top panel. In the middle panel, the difference between the saturation surfaces of the three mineral phases is greater than 5 °C, but the difference between the quartz saturation surface and one of the feldspars is equal to or less than 5 C, so a qtz-1feld storage pressure is calculated. If the residual temperature of the saturation surfaces is greater than 5 C, then no pressure is calculated, bottom panel. Note that in the middle panel, the plagioclase and sanidine curves cross at $\sim$ 300 MPa. This is an invalid pressure, since the quartz saturation surface is at a higher temperature than the plagioclase-sanidine intersection. This indicates that the plagioclase-sanidine intersection would not be in equilibrium with the input glass composition. We perform this calculation on all average lapilli glass compositions to determine the storage pressures.

– rhyolite-MELTS is optimized for natural compositions, in which aMgO is never zero. To correct this, we input the detection limit of 0.05 wt% MgO in the cases where MgO was reported as 0 wt%. Because this only affects the stability of mafic minerals, it has no impact on the pressure calculations presented here. We assume H2O saturation (10 wt% H2O) and oxygen fugacity (f_{O_2}) equal to NNO. The calibration for rhyolite-MELTS is such that quartz, plagioclase, and sanidine saturation is not affected by f_{O_2}. For a full description of the geobarometer, see Gualda & Ghiorso (2014).

2.4 Results

This section is organized by the data sets of field observations, major element glass compositions, trace element glass compositions, zircon saturation geothermometry, and rhyolite-MELTS glass geobarometry. The main point in all cases is to note the variability (or similarities and differences) within and between units. While the patterns are different for each type of data, there are general patterns that arise and complement the different types of data.

2.4.1 Field Observations

We documented and sampled the Kohioawa Section in detail over 670 cm with an additional three samples and more limited observations collected from the upper section between 670 and 730 cm. The base of the Kohioawa Section is measured from the distinct, but not sharp, boundary with a sandy unit near the top of the Kohioawa cliffs, where the tephras outcrop above the sandy and vegetated slope. We sampled a total of 22 horizons at the Kohioawa Section. The Ōtarawairere Section was similarly documented over 1075 cm. The base is measured from the obvious basal gravels. The sampling of the Ōtarawairere Section was sparser, with 8 horizons sampled. The two sections are correlated using paleosols, grain size, and horizon thickness (Figure 2).

At both locations, the deposits are characterized by laterally continuous, mostly horizontal layers that can be traced for 10s of m. The outcrop is divided into horizons that range mostly from $\sim$1 cm to 10s of cm. The thickest three horizons at each location are > 1 m thick, while most of the horizons are 10-20 cm thick. The horizons are composed of mostly clast-supported, fine-grained volcanic material that ranges from orange-yellow to light-yellow to gray in color. Generally, the grain size within a specific horizon is consistent, although grain size varies from clay/ash-sized to very coarse sand-sized over the different horizons within the outcrops. The make-up of the material is predominantly juvenile volcanic pumice clasts, a variable amount of smaller volcanic lithics and loose crystals, and sometimes a sandy matrix that indicates post-depositional water interaction (Manning, 1995). There are occasional cross-beds observed. There are also 3 loess paleosols described at the Kohioawa Section and 4 loess paleosols described at the Ōtarawairere

Section. A general description of each unit is in Table 2; a detailed log of each horizon, including grain size, observed mineralogy, and paleosols is given in Table 3. We divide the outcrops into four major units, whose boundaries are defined by paleosols or distinct changes in physical volcanological characteristics.

The lowest horizons comprise the Pre-Paerata unit and Paerata unit. At the top of the Paerata unit is the thickest paleosol, which is $\sim$20 cm thick at the Kohioawa Section. The Kohioawa unit can be subdivided into three subunits. The lowest subunit is massive and grain supported, with a finer horizon on top, which indicates the transition from the first to second Kohioawa subunit. The middle subunit is the thickest of the outcrops and is massive and coarser grained than the rest of the outcrop. It is composed of predominantly coarser-grained juvenile lapilli clasts, crystals, and lava lithics. The top subunit, in contrast, has alternating $\sim$3 cm thick layers of coarse ash and grain-supported, very fine pumice clasts. This grades into a thick developed paleosol in the Kohioawa Section. The fourth unit, which contains the Murupara-Bonisch horizons, shows alternating layers between coarse and fine-grained material that becomes distinctly sandier than the rest of the outcrop. Due to the cliff-like outcrop, observations and sampling are more difficult, so this unit is not as well documented. The uppermost horizons are finer grained and comprise a thick (> 1 m) ash deposit at the top of the outcrops. The three described paleosols at the Kohioawa Section mark the boundaries between the Paerata and Kohioawa units, between the Kohioawa and Murupara-Bonisch units, and a boundary within the Murupara-Bonisch unit. An additional paleosol at the Ōtarawairere Section is between two Pre-Paerata horizons. However, there is not a discernible paleosol between Kohioawa and Murupara-Bonisch units at the Ōtarawairere Section. The thickest paleosol ($\sim$20 cm) marks the break between the Paerata and Kohioawa units.

Table 2.2: General descriptions of each unit of the Kohioawa Section and Ōtarawairere Section

Unit	Thickness (cm) KS; OS	KS Samples	OS Samples	General Field Characteristics	Magma Type	Mineralogy from field
Pre-Paerata	55; 170	OK220707-1B	OK240707-1A	"3̃ horizons at both KS and OS; at OS, Pre-Paerata sits atop a graywacke gravel base; layers vary from light cream/pink ash to orange-light brown ash and sand; mostly fine-grained, clay-sand, alternating layers with conspicuous biotite; the top of both sequences is finer grained, firm clay, with more sand at OS; the top of the sequence grades into a soil at OS and grades into soil at an adjacent outcrop at KS"	Pre-Paerata + Paerata	plag qtz amph bt
Paerata	150; 205	OK220707-1C WHAK432A WHAK432B OK220707-1E WHAK432C OK220707-1F	Ōtarawairere-B	"1 continuous horizon with subtle variations in grain size that define internal packages; the top and bottom of the package are fine-coarse clay-silt sized ash dominated; the main package of the unit is yellow-orange, massive with subtle variations in grain size (coarse sand to medium lapilli), grain supported with mostly fine pumice lapilli, lithics, and crystals; there is a conspicuous 20 cm thick black organic soil at the top of the unit that grades into the main package at KS; sharp contact that varies in thickness at OS"	Pre-Paerata + Paerata	plag qtz opx amph bt
Kohioawa	345; 370	OK220707-1G WHAK432L OK220707-1I WHAK432D WHAK432E OK220707-1L WHAK432F OK220707-1N WHAK432G OK220707-1O	OK240707-1C OK240707-1D OK240707-1E OK240707-1F	"4 horizons with the thickest 2̃20 cm thick; at OS, base is grain supported, yellow-rust colored alternating layers of ash to fine pumice lapilli; at KS, two basal units are massive, grain supported ash-sand and cream-light brown fine-coarse ash on top; subtle crossbeds mark the beginning of the thickest horizon; thickest horizon is yellow, massive, and has fluctuations in grain size that define internal, grain supported packages of varying sized sand-pumice lapilli; sharp contact with the upper horizons; top package is defined by thin alternating coarse and fine grain supported ash layers with a light brown clay; firm clay (paleosol at KS) at the top"	Kohioawa Types A, B, and C	plag qtz amph opx bt
Murupara-Bonisch	180; 350	OK220707-1P OK220707-1Q WHAK432H WHAK432I WHAK432J	OK240707-1J OK240707-1L	"at KS, 8̃ thinner horizons, predominantly grain supported, cream to yellow to light brown, fine pumice lapilli to silt-sized ashy alternating horizons, generally 5̃-10 cm thick; several horizons fine upward; at OS, fewer defined horizons with thicker, fine-grained clay-silt; wavy bedding and alternating layers between thicker, finer grained layers; a soild separates the upper horizons at both locations; at KS, accessed with a ladder to the left of the main outcrop; upper layers are ashy and less consolidated below a friable sandy deposit and below the Matahina ignimbrite"	Murupara-Bonisch Types A and B	qtz plag amph opx

2.4.2 Mineralogy

Plagioclase, quartz, hornblende, orthopyroxene, and Fe-Ti oxides are the main phases present in all horizons analyzed. The lowest samples, OK220707-1B, OK220707-1C, OK220707-1E likely contain cummingtonite. Biotite is observed in the middle section in samples OK220707-1I, OK220707-1L, OK220707-1O, OK220707-1P. Results are summarized in Table 3.

Additional felsic mineral componentry was conducted on a few key horizons at Kohioawa Section – OK220707-1G, OK220707-1I, OK220707-1L, OK220707-1O, OK220707-1Q. The first sample (OK220707-1G) is from the first subunit of the Kohioawa unit, OK220707-1I and OK220707-1L are from the middle, massive Kohioawa subunit, OK220707-1O is from the upper, interbedded Kohioawa subunit, and the last sample (OK220707-1Q) is interpreted to be within the Murupara-Bonisch unit. All of these horizons have both quartz and plagioclase; only OK220707-1G did not have sanidine. To corroborate the presence of sanidine, we optically determined its presence in all horizons. As discussed above, it was not possible to determine if sanidine is present in each of our studied clasts. It is thus possible that only a subset of our samples contains sanidine. In other words, both sanidine-bearing and sanidine-absent clasts may coexist within the Kohioawa unit. Sanidine is present in all Kohioawa horizons with the exception of the lowest subunit, OK220707-1G. No sanidine is observed in other units.

2.4.3 Glass Compositions

Of the 157 lapilli clasts analyzed, 5 were discarded after the major element analyses were excluded, see Methods. In most lapilli clasts, the major elements show a consistent composition; however, there are 14 clasts for which we subdivided the glass analyses into two populations. There is one additional clast that we subdivided the glass into three different populations. There were no subdivisions of glass data for the Pre-Paerata clasts, 2 subdivisions in the Paerata clasts (subdivisions for 5% of lapilli), 7 subdivisions in the Kohioawa clasts (subdivisions for 9% of lapilli clasts), and 6 subdivisions in the Murupara-Bonisch clasts (15% of the lapilli clasts). In all units, it is a minority of clasts that exhibit multiple glass compositions. Of the 15 clasts that were subdivided into multiple compositions, 7 of them appeared to be small accretions of $\sim$two lapilli and sediment. Those 7 lapilli were discarded from further analysis. Five of those lapilli were from Kohioawa samples, and 2 were Murupara-Bonisch lapilli; the percentages of lapilli with subdivisions decreases to 2% for Kohioawa clasts and 10% for Murupara-Bonisch clasts.

All compositional data are reported as the mean and standard deviation of individual lapilli, with subdivisions denoted by "-A" or of the "-B" for several of the clasts.

We define six groups using major and trace-element compositions. The major-element compositions show that glasses in all clasts are high-silica rhyolites with 76.0-78.5 wt% SiO_2. Na_2O and K_2O are neg-

atively correlated for all types, which could indicate Na-K exchange. The full data set of mean values and standard deviations of major and trace elements is in Tables 5-15. The different geochemical characteristics of the Kohioawa glass compositional groups are defined and detailed in Table 3 and in Figures 5-8. The six compositional types are defined below.

2.4.3.1 Pre-Paerata and Paerata Type

The first compositional type comprises the Pre-Paerata and Paerata clasts. This type is defined by fairly high CaO (average 1.0 wt%) and low K_2O (average 4.0 wt%) in major elements and low Rb (110-140 ppm) and Cs (4-5 ppm) in the trace elements. Pre-Paerata and Paerata lapilli clasts have the highest Ba. Pre-Paerata and Paerata type has the lowest LREE of all types.

2.4.3.2 Kohioawa Types

The Kohioawa lapilli clasts exhibit three compositional types, which appear throughout the Kohioawa tephra deposits. Together, the Kohioawa types are the lowest in CaO and highest in K_2O of all glass. Kohioawa types are higher in Rb, lower in Sr, and lower in Eu/Eu* when compared to the other types.

The Kohioawa tephras can be subdivided into Types A, B, and C, where Types B and C are more similar to each other. Type A (shown in dark blue) can be distinguished clearly from Types B and C by CaO and TiO_2, and by Mn, Sr, and Ba. It can be subtly distinguished by MgO and FeO, and by Cs, Zr, Eu, and Yb. There are no clear trends in SiO_2 and Al_2O_3. There are very subtle trends in many of the trace elements, but we highlight only those that have strong signatures. The REE values can also distinguish Type A from Types B and C.

Types B (shown in red) and C (shown in orange) are similar but can be clearly subdivided on the basis of Sr and Ba. They can be subdivided subtly in CaO and SiO_2, and by Eu, U, and Pb. Kohioawa Types B and C are similar to one another, but are compositionally distinct from all other compositions in this study, with little to no overlap with the other types in trace element compositions (e.g. Rb, Sr, Eu/Eu*, Ba). The quantitative trends to distinguish Kohioawa tephra types are provided in Table 3. Kohioawa Type A is the only type present in the lowest Kohioawa subunit. In the middle subunit, both Kohioawa Types A and B are present. In the upper Kohioawa subunit, Kohioawa Types A, B, and C are all present, although Kohioawa Type C is the dominant tephra type we analyzed (Figures 9 and 10).

There are 7 lapilli that do not clearly fall into the three Kohioawa groups. These are referred to as “undefined” and are not discussed further in this paper.

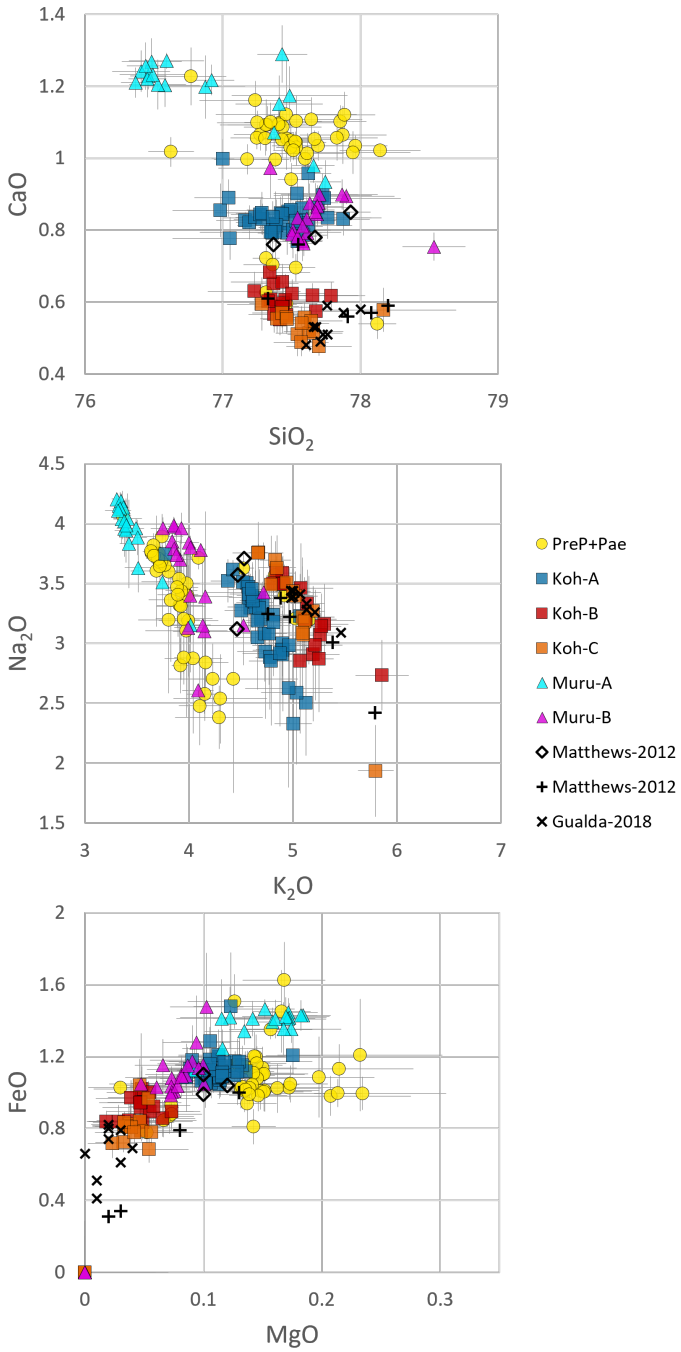

Figure 2.5: Major element glass composition of the tephra data and ignimbrite glass data from Gualda et al (2018), represented by black x's and data from Matthews et al (2012), ignimbrite data represented by crosses and ultra-distal tephra data represented by black open diamonds. The different symbols represent different units and the different colors represent the 6 different compositional groups from the tephra sequences. There is one group for the Pre-Paerata + Paerata unit represented by yellow circles, three groups for the Kohioawa unit represented by blue, red, and orange squares, and two groups for the Murupara-Bonisch unit cyan and magenta triangles. One sigma standard deviation of each clast from our data are represented by gray lines.

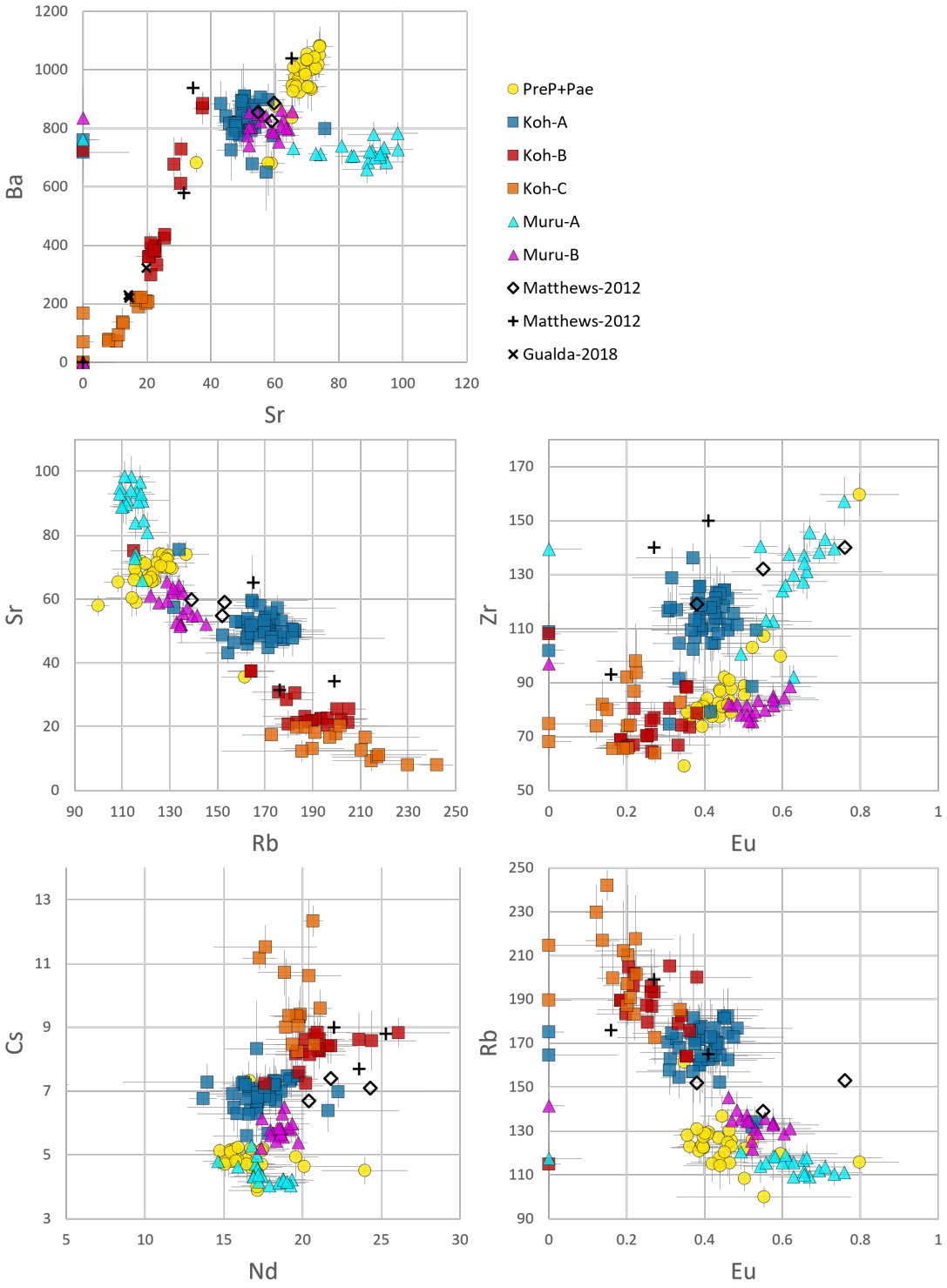

Figure 2.6: Trace element glass composition of the tephra data and ignimbrite glass data from Gualda et al (2018), represented by black x's and data from Matthews et al (2012), ignimbrite data represented by crosses and ultra-distal tephra data represented by black open diamonds.

Table 2.3: Distinguishing compositional signatures of the Kohioawa magma types

Distinguishing Element	Kohioawa-A	Kohioawa-B	Kohioawa-C
SiO_2	76.9-77.8	77.2-77.7	77.2-78.1
CaO	0.76-1.07	0.54-0.62	0.47-0.59
TiO_2	0.11-0.21	0.04-0.10	0.03-0.08
FeO	0.97-1.74	0.81-1.09	0.68-1.11
MgO	0.06-0.33	0.01-0.07	0.02-0.11
Sr	43.0-75.6	20.5-25.5	8.03-20.3
Ba	649-910	298-869	69-222
Mn	222-365	383-424	378-492
Eu	0.30-0.57	0.18-0.59	0.12-0.33
U	2.86-5.99	3.96-4.57	4.19-5.88
Pb	13.7-19.6	14.2-17.6	15.7-21.9
Cs	5.59-8.32	8.16-9.33	8.24-12.3
Zr	74.5-136	64.4-108	63.8-98.0
Yb	1.85-2.78	2.58-2.96	2.61-3.58
Y	15.1-23.6	19.0-26.0	21.7-30.3

2.4.3.3 Murupara-Bonisch Types

The Murupara-Bonisch clasts can be subdivided into two compositional types. The Murupara-Bonisch Type A (shown in cyan) has lower SiO_2 and higher CaO (average 1.2 wt%) and FeO (average 1.4 wt%) than all other types. The Murupara-Bonisch Type B (shown in magenta) overlaps with the Kohioawa Type A for CaO (average 0.8 wt%) and SiO_2 (average 77.7 wt%), but differs in other elements (Figure 6). Note that in some trace elements, the Pre-Paerata and Paerata type often overlaps the Murupara-Bonisch Type A (e.g. Cs and Nd), but that is not a ubiquitous characteristic, and the Pre-Paerata and Paerata type is distinguishable from both Murupara-Bonisch types, e.g. Ba. The Murupara-Bonisch Type A is not present in the first Murupara-Bonisch horizon, and it is the only type erupted in the final two Murupara-Bonisch horizons (Figures 9 and 10).

2.4.4 Geothermometry

We calculate the zircon saturation temperatures for all clasts using the calibrations of Watson and Harrison (1983) (Watson & Harrison, 1983) and Boehnke *et al.* (2013). The temperature for each clast is included in Table 6. The average zircon saturation temperatures for each type are (Figure 5): Pre-Paerata and Paerata 757 °C (717 °C Boehnke *et al.*, 2013), Kohioawa Type B 756 °C (718 °C), Kohioawa Type A 782 °C (746 °C), Murupara-Bonisch Type A 787 °C (748 °C), and Murupara-Bonisch Type B 757 °C (717 °C).

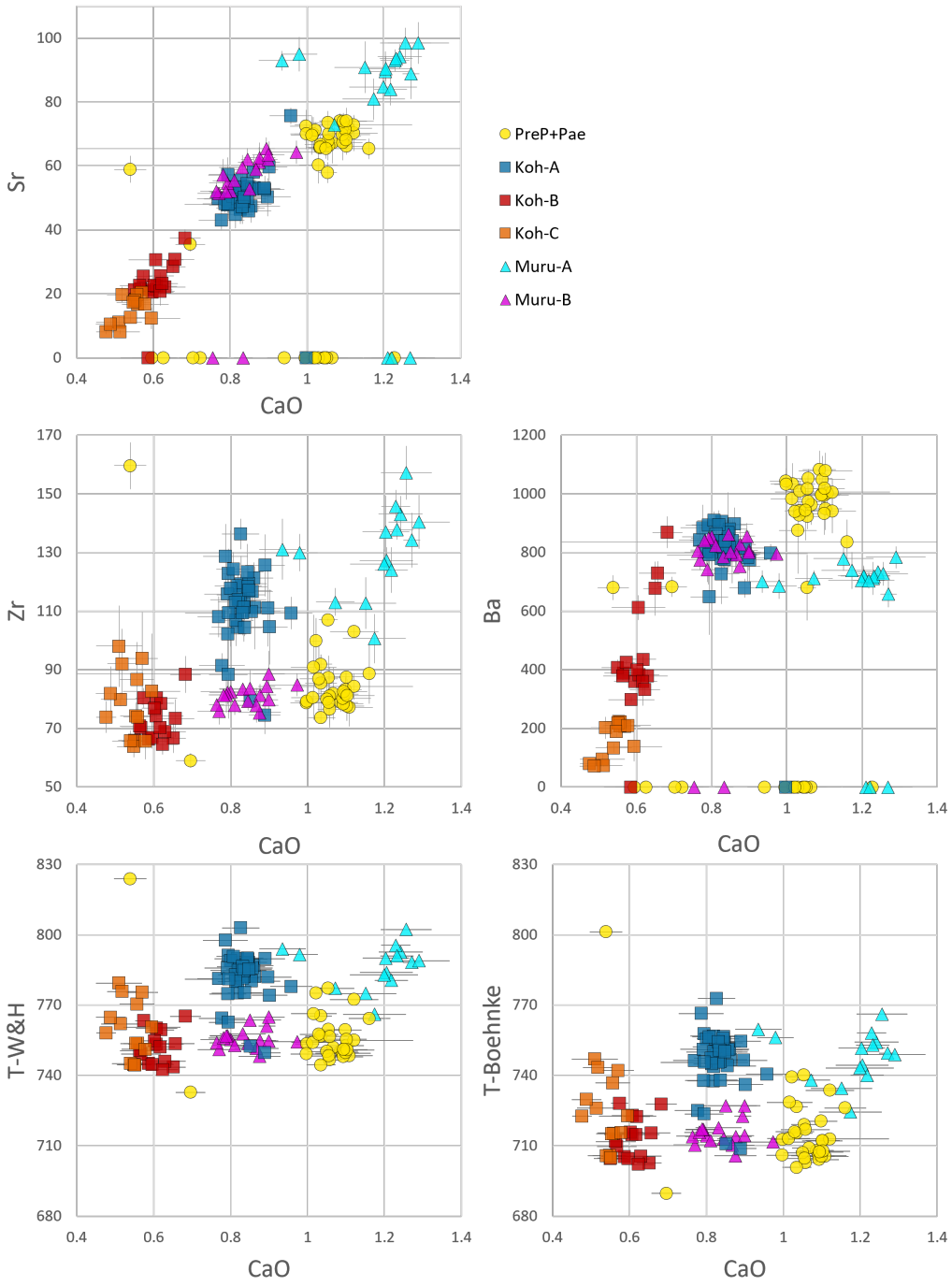

Figure 2.7: Select trace element glass vs CaO glass composition plots and zircon saturation temperatures using the Watson and Harrison calibration (1983) and the Boehnke et al calibration (2013); all magmas are assumed to be zircon saturated, so these temperature represent pre-eruptive magmatic temperatures. One sigma standard deviation of our data are represented by gray lines. T-W&H corresponds to zircon saturation temperature calculated using Watson and Harrison (1983) calibration and T-Boehnke corresponds to zircon saturation temperature using Boehnke et al (2013).

2.4.5 Geobarometry

We use rhyolite-MELTS geobarometry to determine the storage conditions of the pre-eruptive magmas (Figures 11 and 12). Of the 192 lapilli compositions, storage pressures are calculated for 153 compositions (80%), Table 6. See Figures 3 and 4 for a schematic of the geobarometer and representative model results, respectively. All storage pressures are shallow, upper crustal pressures of ∼40-315 MPa, with 90% of the data 50-240 MPa and with clasts of each compositional type exhibiting a narrower range of pressures. The Pre-Paerata and Paerata type shows a larger pressure range, with 75% of the pressures 75-175 MPa. The Kohioawa types all have shallow pressures, with 75% of the pressures 50-135 MPa, 80-120 MPa, and 45-130 MPa for Types A, B, and C, respectively. The Murupara-Bonisch Type B shows shallower pressures and Murupara-Bonisch Type A shows deeper pressures. For Type-B, 75% of the pressures are 50-140 MPa, contrasted with Type A, where 75% of the pressures are 105-245 MPa.

Most lapilli compositions that produced a storage pressure yield storage pressures with the mineral assemblage qtz-1feld (128/152 successful pressure calculations). With the exception of one Paerata clast, the Kohioawa types B and C are the only types to produce storage pressures with a qtz-2feld assemblage. The presence of a qtz-2feld assemblage indicates that these are the only compositional types that are saturated in sanidine. A total of 23/36 of the Kohioawa Types B and C clasts produced qtz-2feld pressures, while the other 13/36 Kohioawa types B and C clasts produced qtz-1feld pressures (Figure 8).

There are several pressure trends through time that become apparent. At the beginnings and ends of each major unit, there are shallow storage pressures. In the central Pre-Paerata and Paerata horizons and after the second horizon in the Murupara-Bonisch, there are deeper storage pressures. The youngest Murupara-Bonisch tephras show the highest pressures of 200-275 MPa. There are several horizons that show particularly low pressures, all within the Kohioawa horizons. These horizons have storage pressures < 100 MPa (Figures 11 and 12).

2.5 Discussion

2.5.1 Magma Types and Different Units

We interpret each clast as a small parcel of magma erupted but not fully fragmented during eruption. Glass compositions allow us to distinguish six compositional types in the lapilli clasts, which we interpret to represent six different types of magma that sourced the eruptions of the Pre-Paerata, Paerata, Kohioawa, and Murupara-Bonisch eruptions. The lowermost group includes a single type of magma that erupted to form the Pre-Paerata and Paerata tephras; the central unit – which overlies the thickest paleosol – includes three distinct magma types that make up the Kohioawa tephras; and, finally, the topmost unit includes two (possibly three) distinct magma types that make up the Murupara-Bonisch tephras.

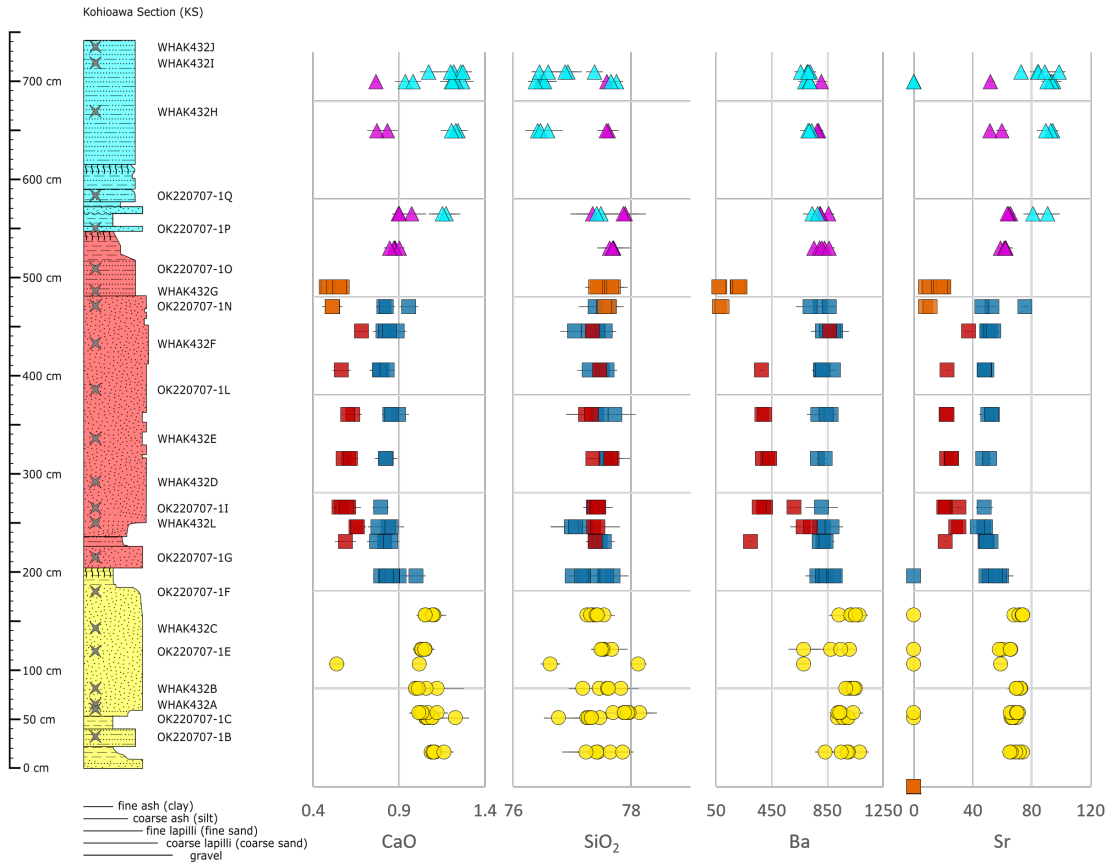

Figure 2.8: Major and trace element glass compositions with respect to height within outcrop for the Kohioawa section; the yellow basal unit is Pre-Paerata + Paerata, the red middle unit is Kohioawa unit, the top blue unit is the Murupara-Bonisch unit

The compositional differences between Pre-Paerata and Paerata, Kohioawa, and Murupara-Bonisch demonstrate that these magmas are likely derived from different magma systems, consistent with the interpretations of Manning (1995). Our sampling of multiple horizons allows us to constrain the compositional boundaries, even where paleosols are not present.

The distinct paleosols within the sequences indicate significant time breaks between eruptions (B. Houghton & Carey, 2015; Shoji *et al.*, 1994). It is difficult to constrain the duration of paleosol development but their thicknesses (e.g. 20 cm at the top of the Paerata unit at the Kohioawa Section and 15 cm at the top of the Kohioawa unit at the Kohioawa Section) suggests hundreds to thousands of years hiatus (Shoji *et al.*, 1994). After each paleosol, there is a change in glass composition that represents the onset of a new magma type.

The transitions in grain size within units (e.g. from 480-550 cm, the uppermost Kohioawa subunit at the Kohioawa Section) (Figures 1 and 2) indicate changes in eruption intensity for several of the eruptions (Houghton & Carey, 2015). There are two horizons at the Kohioawa Section (one from 50-180 cm within the

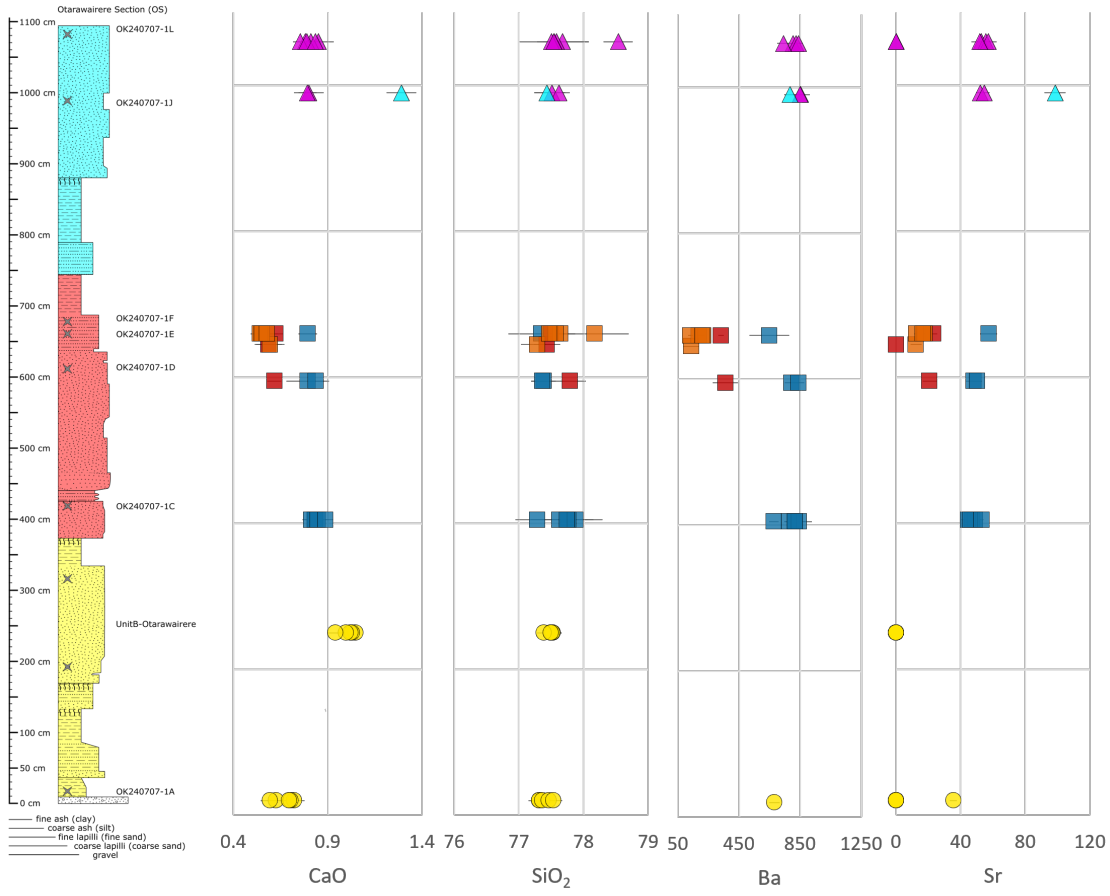

Figure 2.9: Major and trace element glass compositions with respect to outcrop stratigraphy for the Ōtarawairere section; the yellow basal unit is Pre-Paerata + Paerata, the red middle unit is Kohioawa unit, the top blue unit is the Murupara-Bonisch unit

Paerata unit, the other 240-480 cm in the Kohioawa unit) (Figures 1b and 2), that are much thicker and have larger pumice clasts than the other horizons, indicating more sustained and intense eruptions.

Three different chemical compositions recognized in the Kohioawa unit and two additional types recognized in the Murupara-Bonisch unit indicate that multiple eruptible magma bodies contributed to these eruptions, similar to some other large eruptions (Bégué, Deering, *et al.*, 2014; Cashman & Giordano, 2014; G. F. Cooper *et al.*, 2012; Gualda & Ghiorso, 2013; Pitcher *et al.*, 2021). The lack of evidence for mixing or mingling on the clast-scale suggests that the contemporaneous eruptible magma bodies were stored independently from one another and did not interact prior to eruption.

2.5.2 Magma Types in the Kohioawa Sequence

The thickest unit studied, the Kohioawa unit, shows important changes in the characteristics of the tephra through time. We identify three distinct subunits within the Kohioawa sequence. The lowest subunit ($\sim$30-50 cm -hick) is characterized by being massive, grain-supported ash- to sand-sized particles, and crystal-rich, which suggests formation during a sub-Plinian-style eruption based on grainsize characteristics (Houghton & Carey, 2015). Our samples from this package (OK220707-1G at Kohioawa Section and OK240707-1C at Ōtarawairere Section) exhibit exclusively Kohioawa Type A magma.

Above this subunit is the thickest subunit of the Kohioawa unit, which we interpret to be a Plinian-style PFD due to larger lapilli size and consistent grain size. Within this subunit, there are both Kohioawa Type A and Kohioawa Type B magma types in all horizons in this subunit, showing continued co-eruption of both magma types through most of the Kohioawa sequence (Figures 6 and 7).

At the top of the Kohioawa unit, the final subunit contains Kohioawa Types A, B, and C, with Kohioawa Type C exhibiting the most extreme compositions of the tephras (e.g. lowest CaO, Sr, and Ba) (Figure 6). This shift to include Kohioawa Type C is correlated with a change in grainsize and sorting morphology from massive in the lower two subunits to finely layered horizons in the uppermost Kohioawa subunit, which suggest that the tephras are deposited during pulsing eruptions, perhaps as co-ignimbrite PFDs (Bonadonna *et al.*, 2015; B. Houghton & Carey, 2015)(Bonadonna *et al.*, 2015; B. Houghton & Carey, 2015).

The topmost subunit exhibits exclusively Kohioawa Type C at the Kohioawa Section, while the topmost horizon we sampled at the Ōtarawairere Section exhibits all three Kohioawa magma types. This difference could be attributed to sampling bias. The shift in the uppermost subunit could be indicative of either: (1) the Kohioawa Type C magma being segregated from the Kohioawa Type B eruptible magma body as an independent eruptible magma body, and then further crystallized, giving the glass a more extreme, depleted signature; or (2) that the final dregs of the Kohioawa Type B eruptible magma body had a more fractionated geochemical signature of Kohioawa Type C, which would indicate that there are compositional changes within the eruptible magma body in space, time, or both.

The sharp transitions in magma composition before and after the Kohioawa unit indicate that the organization of magma in the upper crust must change between eruptive cycles. Within a given unit (e.g. Kohioawa unit), different, discrete compositions indicate that some eruptions are sourced from multiple, discrete magma bodies. Within a given unit, it is still unclear if magma of a given composition is sourced from an individual large eruptible magma body or if similar processes of magma generation create multiple smaller eruptible magma bodies throughout a prolonged eruption.

2.5.3 Kohioawa Magmas and the Whakamaru Group Eruptions

The Kohioawa unit is the thickest unit in this study, and it is stratigraphically located between the two thickest, best developed paleosols. This unit shows a coherent set of magma compositions, confirming evidence presented by Manning (1995). We interpret this sequence to be correlative with the Whakamaru group eruptions. In addition to two thick, massive layers, at the top of the Kohioawa unit is a series of interbedded layers that contain grains that alternate between coarse sand-sized and fine ash-sized.

The presence of sanidine in Whakamaru group ignimbrites distinguishes it from most other TVZ ignimbrite deposits (S. J. A. Brown *et al.*, 1998; Gravley *et al.*, 2016). From the mineralogy, with the exception of the one Murupara-Bonisch sample (OK220707-1Q), we found sanidine in the middle and upper Kohioawa subunits. This suggests that the Kohioawa tephras are likely the only ones in this sequence that are correlative with the Whakamaru group eruptions. Not only are the Kohioawa tephras the only ones that have sanidine observed in crushed lapilli clasts, but rhyolite-MELTS geobarometry also predicts a qtz-2feld mineral assemblage exclusively for the Kohioawa Types B and C (with the exception of one Paerata clast), suggesting that these magmas are saturated in sanidine.

We also compare the Kohioawa glass data to published Whakamaru ignimbrite glass data to determine if they are correlative. The similarity in glass composition between Kohioawa Types B and C data and Whakamaru ignimbrite pumice data from Gualda *et al.* (Gualda *et al.*, 2018) suggests that they are correlative (Figures 5 and 6). The Rangitawa tephra is a known correlative to the Whakamaru group ignimbrites. Glass data from Matthews et al (2012) (Matthews, Smith, *et al.*, 2012) is compositionally similar to the Kohioawa Type A glass data in both major and trace elements (Figures 5 and 6), reinforcing the idea of the Kohioawa tephras are correlative with the Whakamaru group eruptions.

Within the Kohioawa unit, the lack of paleosol indicates that the tephras were deposited without significant (100s to 1000s ka) time breaks, which is consistent with the overlapping ages from Whakamaru group ignimbrites, with the exception of the Paeroa subgroup (Downs *et al.*, 2014). As well, the Kohioawa unit is thickest and it includes the largest lapilli clasts, indicating they represent the largest, most extreme eruptions– this is to be expected for some of the largest eruptions in TVZ history, as it has been inferred to be the case for the >2000 km3 Whakamaru group eruptions (Briggs, 1976a; S. J. A. Brown *et al.*, 1998; Downs *et al.*, 2014; Matthews, Smith, *et al.*, 2012; Wilson *et al.*, 1986).

It is interesting that the Rangitawa tephra data and Whakamaru ignimbrite data overlap with the Kohioawa Type A and Kohioawa Types B and C, but that neither data set includes all types described in this study. Perhaps this indicates a sampling bias, or that the different types are preferentially concentrated in the distal tephra and the ignimbrites – the fact that both are present in the tephras described here could result from

the proximity of the tephras to the caldera, and include all magma types. Brown *et al.* (1998) describe four magma types in the Whakamaru ignimbrite, and other ignimbrites within the Whakamaru group ignimbrites also contain multiple types of pumice, based on whole rock analyses (see detailed discussion below). Future research by our group focuses on pumice from the different ignimbrites to understand the correlation between the ignimbrites and magma types.

The correlation of the Kohioawa tephras with the Whakamaru group ignimbrites allows us to interpret the composition of the Whakamaru magma system and its architecture through time. The three distinct subunits of the Kohioawa unit reveal three major eruptive phases of the Whakamaru group eruptions. Multiple eruptive pulses are consistent with previous work, which described the different ignimbrites as potentially different eruptions (Briggs, 1976a, 1976b; Grindley, 1960; Martin, 1961; Wilson *et al.*, 1986). The lack of paleosol within the Kohioawa unit is consistent with ages determining that the ignimbrites were erupted over a short period of time.(S. J. A. Brown, 1994; Downs *et al.*, 2014).

2.5.4 Chemistry and Storage Conditions of Kohioawa Magma Bodies

The tephra data show three distinct magma types that fed the Whakamaru group eruptions: Kohioawa Types A, B, and C. The large negative Eu anomaly, low Ba content (Figure 6), and low CaO (Figures 5 and 7), among other attributes, illustrate that the similar Kohioawa Types B and C magmas are the most distinct in this study. The presence of sanidine – as indicated by observed mineralogy and rhyolite-MELTS pressure results – suggests that Kohioawa Types B and C are the only magmas saturated in sanidine. In contrast, the Kohioawa Type A magma is mineralogically similar to pre-Kohioawa and post-Kohioawa magmas, although it is still compositionally distinct from the other magma types, as indicated by the glass compositions.

Kohioawa Type A is the exclusive magma type present in the lowest Kohioawa subunit; Kohioawa types A and B are present in approximately equal proportions in the middle subunit; and all three types are present in the uppermost subunit, where Kohioawa Type C dominates. Each clast has a distinct compositional signature, precluding any chemical mixing on the lapilli-scale prior to eruption. Kohioawa Type A magma appearing exclusively in the first Kohioawa subunit is consistent with the interpretation by Brown *et al.* (1998) that sanidine was only present in later stages of the Whakamaru group ignimbrites. However, the sanidine-bearing Kohioawa Type B is present from the second subunit through the top of the sequence, indicating that only the first phase of the eruptions lacked sanidine. The sequentially deposited tephras indicate that sanidine-bearing magmas erupted in all except the very first stage of the eruptions. The uppermost subunit introduces the Kohioawa Type C magmas, with lower Sr and Ba. This shift indicates that the final phase of the eruptions was compositionally more evolved than the Kohioawa Type B that erupted for the majority of the eruptions.

Brown *et al.* (1998) models the pre-eruptive Whakamaru reservoir as a single, stratified magma body,

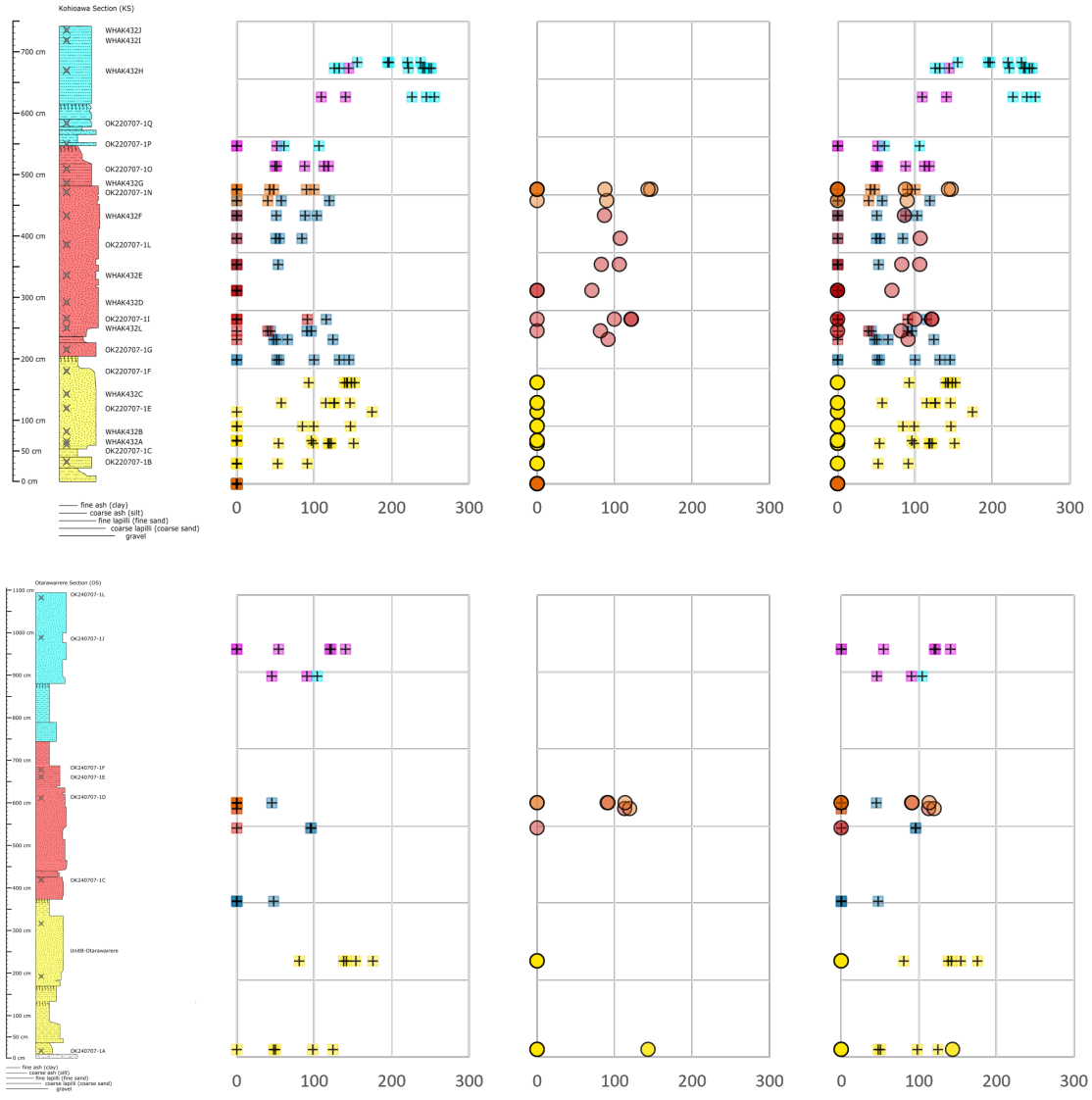

Figure 2.10: Rhyolite-MELTS storage pressure calculations as a function of height through the outcrop at Kohioawa Section (top) and Ōtarawairere section (bottom). Pressures are reported in MPa. Left panels show pre-eruptive storage pressures for clasts that returned a quartz+plagioclase (qtz+1feld) assemblage for the Kohioawa section (top) and Ōtarawairere section (bottom), represented by crosses. Middle panels show pre-eruptive storage pressures for clasts that returned a quartz+plagioclase+sanidine (qtz+2feld) assemblage for the Kohioawa Section and Ōtarawairere Section (in filled circles). Right panels show composite pre-eruptive storage pressures and calculated mineralogy for the Kohioawa Section and Ōtarawairere Section

with four main types of magma that are connected (Whakamaru Type A, B, C, and D, with a minor basalt magma), forming a zoned magma body with the most fractionated magma at the top of the magma body, with crystal fractionation playing a dominant role in differentiating magma types. Kohioawa Types A, B, and C correspond, respectively, to ignimbrite Types A, B, and C from Brown *et al.* (1998). We did not find any

glass compositions in the tephras that match compositions expected for Type D from Brown *et al.* (1998).

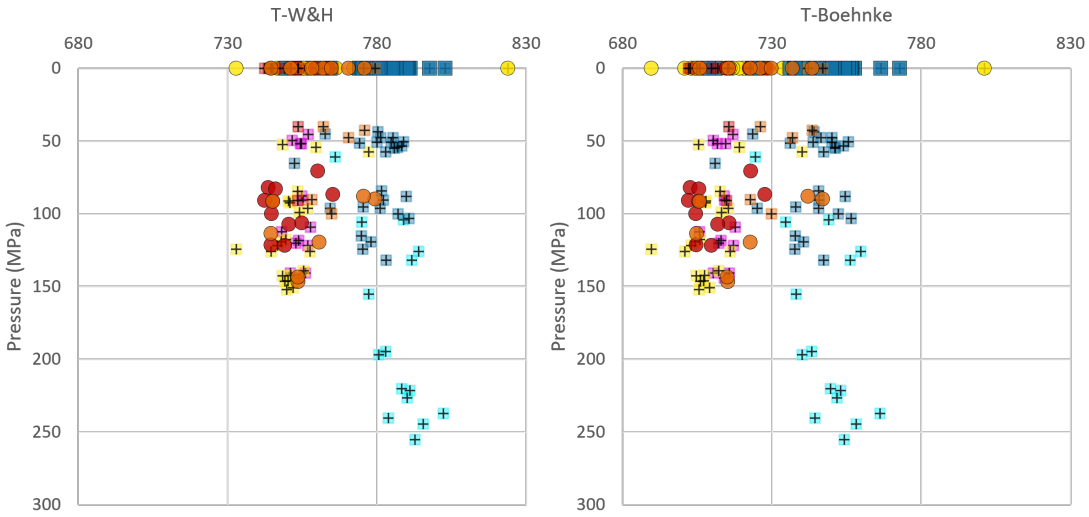

Figure 2.11: Rhyolite-MELTS storage pressure calculations vs zircon saturation pressures for the Watson and Harrison (1983) calibration (left) and the Boehnke et al (2013) calibration (right).

In contrast to Brown *et al.* (1998), we conclude that the different magma types comprise different eruptible magma bodies. One eruptible magma body consistently erupted Kohioawa Type A, while another eruptible magma body erupted Kohioawa Type B. The appearance of Kohioawa Type C in the later phases of the eruptions indicate a third eruptible magma body (possibly genetically linked to Type B), or eruption of a more evolved portion of the Type B eruptible magma body in the final stages of the Whakamaru group eruptions.

Further evidence for the presence of multiple eruptible magma bodies is provided by zircon saturation temperatures. The temperatures calculated for Kohioawa Type A are significantly hotter than those calculated for Kohioawa Types B and C. The cooler temperatures of Kohioawa Types B and C are very similar to both the Pre-Paerata and Paerata and the Murupara-Bonisch Type B temperatures. In contrast, Kohioawa Type A magmas are substantially hotter. While we have not documented zircon in the lapilli clasts, likely due to the small sizes of the clasts and likely sparse grains of zircon, there is compositional evidence for the presence of zircon. Since all Kohioawa magmas are high silica rhyolites, Zr is lowest in the most fractionated glasses, Zr/Hf is fairly low in Type A, very low in Type B, and extremely low in Type C, it is likely that they are saturated in zircon, indicating that the temperatures record the storage conditions of the magmas.

All three Kohioawa magma types are stored at the same shallow pre-eruptive storage pressures (75-150 MPa), indicating that the magmas coexist at the same pre-eruptive storage depth within the crust. There are certain horizons that show slightly shallower or slightly deeper storage pressures (Figure 11) but the storage pressures are predominantly 75-150 MPa. The smaller uncertainties of the qtz-2feld storage pressures (± 24

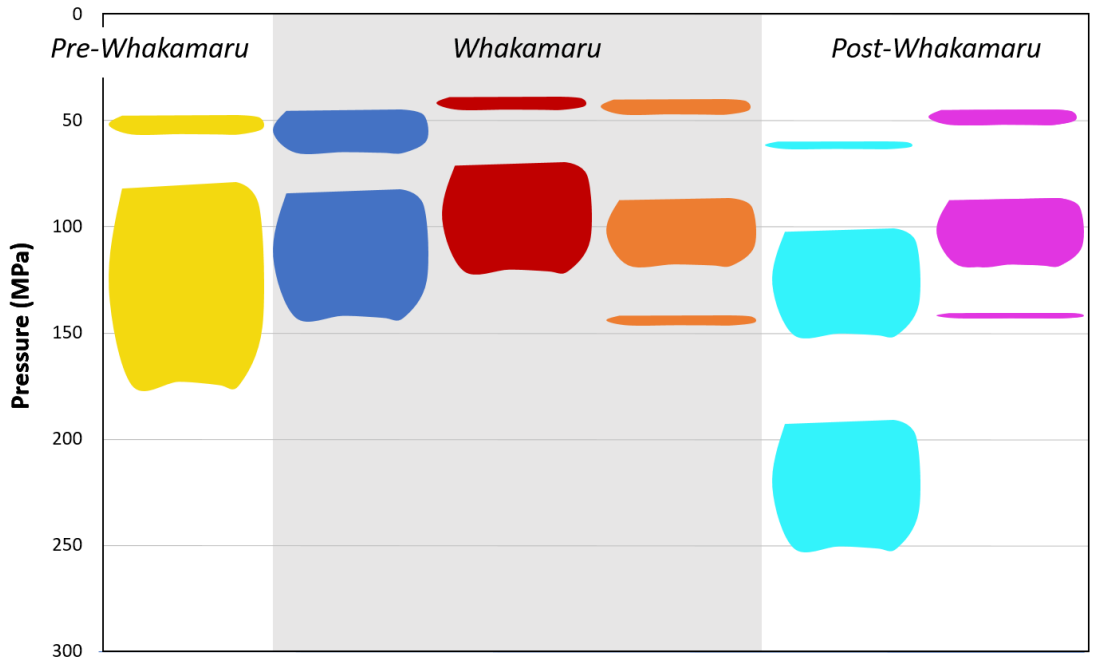

Figure 2.12: Pre-eruptive storage pressures and magma bodies for the Pre-Paerata through the Murupara-Bonisch tephras. Multiple magma bodies indicate multiple storage pressures for a given magma type.

MPa (Pitcher *et al.*, 2021)) indicate that the pressures are constrained to 75-125 MPa for the Kohioawa Types B and C magmas. rhyolite-MELTS storage pressures agree with the Al-in-Hornblende pressures, which suggest pressures in the 100-150 MPa range (S. J. A. Brown *et al.*, 1998). Kohioawa Type A compositions yield two distinct storage levels, one primary storage pressure that overlaps the Kohioawa Types B and C at 85-125 MPa and a shallower storage pressure of ∼50 MPa. There is a gap in the pressure data from 57 MPa to 85 MPa, indicating that there are likely two distinct storage levels for Kohioawa Type A. The significance of the shallow level pressures is unknown, but we note that such pressures have been obtained for glass from the TVZ before (Bégué, Deering, *et al.*, 2014).

Since both Kohioawa Types A and B had overlapping storage pressures and both erupted continuously throughout the eruption, it is unlikely for there to be a zoned single magma body. Instead, we conclude that the two eruptible magma bodies were laterally juxtaposed, existing at the same crustal level. The Kohioawa Type C magma only erupted in the final stages of the eruption, and it is likely geochemically linked to Kohioawa Type B, due to the compositional similarity. The overlap in storage pressures and temperatures indicates that there is a likely a segregated eruptible magma body that erupted Kohioawa Type C independently in the final stages of the eruptions.

It is still uncertain how the magma types and eruptible magma bodies correspond to the ignimbrites. The

Whakamaru ignimbrite contains Types A, B, C, and D, whereas the Rangitaiki ignimbrite shows only Type A, and Manunui ignimbrite shows Types A, C, and D (S. J. A. Brown *et al.*, 1998; Matthews, 2011). Pumice clasts from the Te Whaiti ignimbrite are not included in Brown *et al.* (1998). Using the tephras, we cannot pinpoint which eruptible magma bodies erupted to form each ignimbrite. However, the continuous deposition of both Kohioawa Types A and B in the middle and uppermost Kohioawa subunits indicates that they erupted continuously, together throughout the eruption. They likely erupted from two separate, laterally juxtaposed eruptible magma bodies. The Kohioawa Type C magma was also stored at the same crustal level, and only erupted in the final stages either as a third distinct eruptible magma body. While it is possible that Kohioawa Type C erupted as the dregs of the Kohioawa Type B magma body, it is more likely that the more fractionated Type C is a third, distinct eruptible magma body.

2.5.5 Whakamaru Group Eruptions in the Context of the TVZ Ignimbrite Flare-Up

Tephra compositions and calculated storage pressures show that each magma type displays a narrow compositional range, and they erupt from a narrow pressure range. Most units show storage pressures of 100-150 MPa, indicating a consistent and narrow storage zone within the shallow crust that is repeated through the eruptions. Given that this pressure interval prevails over most of the eruptions studied here, it seems likely that it reveals a structural or tectonic control on the storage level of these magmas. This is consistent with what can be inferred from the results from Bégué *et al.* (2014) or the central TVZ as a whole.

The Murupara-Bonisch unit is the only one that has a distinct pressure change through the eruptions, as the Murupara-Bonisch Type A magmas erupt from much deeper storage pressure of $\sim$200-275 MPa. This much deeper signature is consistent with the deeper storage pressures observed for the Matahina, Chimpanzee, and Pokai eruptions (Gualda *et al.*, 2018) – the caldera-forming eruptions that follow the Whakamaru group eruptions during the TVZ flare-up. The deeper storage pressures after the Whakamaru group eruptions show that there must have been a reorganization in the crust after the Whakamaru group eruptions excavated such a large volume of magma. The crust then recovered to the usual 100-150 MPa storage pressures (Bégué, Deering, *et al.*, 2014) by the end of the ignimbrite flare-up (Gualda *et al.*, 2018).

2.6 Implications, Conclusions, and Future Work

We see the compositional signatures and distribution of eruptible magma bodies in the crust changing through time using physical volcanology, geochemistry, geothermometry, and geobarometry in tephra from tephras that include deposits from the Whakamaru group eruptions, as well as preceding and subsequent eruptions. We reconstruct the eruptible magma bodies and the larger magma system through time. We find that a single magma type feeds the eruptions that precede the Whakamaru group eruptions. Two magma types erupt

continuously through most of the Whakamaru sequence, suggesting the presence of at least two independent magma bodies (one sanidine-bearing, and one sanidine-absent) for most of the duration for the Whakamaru group eruptions. The final stages of the Whakamaru group eruptions are include a third magma type, indicating a shift in the final stages of the eruptions to include a third magma body. The succeeding Murupara-Bonisch tephras show a significant change in composition from R1 (cold, wet, oxidizing) to R1+R2 (cold, wet, oxidizing and hot, dry, reducing) magmas (Deering *et al.*, 2010), and they also show eruption of different magma types sourced from different storage levels. The dramatic shift in composition between Whakamaru-related magmas and Murupara-Bonisch magmas shows that the central TVZ magmatic systems went through a thorough reorganization following the Whakamaru event (Gravley *et al.*, 2016; Gualda *et al.*, 2018).

The combination of different types of data together informs how we conceptualize the pre-eruptive crustal conditions, and we use the tephras to reconstruct how large eruptions influence the structure of the crust. Future work will focus on the Whakamaru group ignimbrites to see if we can use the tephra information to reconstruct the ignimbrites through time and have a more comprehensive understanding of the Whakamaru magma system.

Table 2.4: Detailed descriptions of the Kohioawa Section and Otarawairere Section

Kohioawa							
Start (cm)	Thickness (cm)	Notes	Samples	Sample Height (cm)	Sanidine	Minerals	Unit
-1	10	Unit grades into sand below, contact is distinct but not sharp					Pre-Paerata
9	13	pink to cream colored mottling/layers, very fine ash that grades into fine to coarse ash that is light gray; SOIL at adjacent outcrop at the top of this layer					Pre-Paerata
22	18	light gray alternations between fine grain supported layers (medium to coarse sand size) and fine to coarse ash layers, conspicuous biotite	OK220707_1B	35		plag, qtz, cum?, hbl, opx, ox	Pre-Paerata
40	13	creamy white very fine ash; SOIL at adjacent outcrop					Pre-Paerata
53	6	base is 6cm with fine to coarse ash layers alternating with grain supported sand-sized layers; fine ash is light gray in color, biotite bearing.					Paerata
59	125	yellowish to orange colored, massive with subtle variations in grain sizes that define internal packages. The top and bottom of the unit contain find and coarse ash but the main body is grain supported with a range of pumice lapilli sizes (mostly fine), lithics, and crystals. there is conspicuous biotites towards the base of the unit	OK220707_1C WHAK432A WHAK432D+ OK220707_1D OK220707_1E WHAK432C OK220707_1F	70 75 100 (45 cm above base) 125 (65 cm above base) 140 175 (top of coarse-gr. hor.)		OK220707_1C: plag, qtz, cum?, hbl, opx, ox OK220707_1E: plag, qtz, cum?, hbl, opx, ox	Paerata
184	20	black organic top grading into medium then lighter brown very firm clay (paleosol). This grades into the top of the unit below. Conspicuous woody fragments					Paerata
204	22	massive, grain supported fine pumice lapilli, lithic, crystal unit. Yellow to rust colored	OK220707_1G	215	no	plag, qtz, opx, hbl, ox	Kohioawa
226	10	cream to light brown fine to coarse ash with scattered crystals and some obsidian lithic ; normally graded with a very thin pink strip near the base					Kohioawa

236	25	cross-bedded with lensoid shaped layers of better sorted grains (reworked base) Pervasive rust colored iron oxide staining	OK220707_1H				Kohioawa
261	220	sharp upper contact but no sign of erosion or reworking (little to no time break). Massive yellowish unit with vertical fluctuations in pumice lapilli size and concentration that define a subtle bedding. Grain supported, generally crystal rich with >1% lava lithics. From OK220707_1I through OK220707_1O, crystal rich matrix for the entire unit. There are crystal-poor and crystal-rich pumice clasts.	OK220707_1I WHAK432D OK220707_1J WHAK432E OK220707_1K OK220707_1L OK20707_1M+ WHAK432F OK220707_1N	265 287 305 333 355 380 422 465	yes yes	OK220707_1I: plag, qtz, opx, hbl, ox, ±bt OK220707_1L: plag, qtz, opx, bt, hbl, ox	Kohioawa
481	66	light brown, very firm clay with developed but thick soil that grades down (by color) into yellowish, not as firm to fine to coarse ash with conspicuous biotite. Lower 48 cm is alternating fine to coarse ash layers and grain supported very fine pumice lapilli lithics and crystals. Log does not represent the fine scale detail of those alternations. Biotite is consistent throughout.	WHAK432G OK220707_1O	490 512	 yes	OK220707_1O: plag, qtz, bt, hbl, opx, ox	Kohioawa
547	5	yellowish, grain supported massive fine pumice lapilli, lithics, crystals (although less crystals and <1% lithics compared with units above)	OK220707_1P	550		plag, qtz, hbl, opx, ox, ±bt	Murupara-Bonisch
552	13	variable thickness because of wavy top, white to cream fine ash. Has same soft-sediment deformation as fine ash layers seen elsewhere, i.e. Rangitawa tephra in Awatarariki Stream					Murupara-Bonisch
565	7	yellow color, variably graded, grain supported fine pumice lapilli, lithics, crystals. Undulating basal contact with micro valley fill-like structures.					Murupara-Bonisch
572	5	cream to light brown fine ash with scattered fine pumice lapilli, lithics, and crystals					Murupara-Bonisch
577	13	cream to light brown silty ash with some fine pumice lapilli on top of variably graded clast supported pumice lapilli and lithic, crystal, massive, yellowish color >5% lithis into obsidian, pumice up to 10mm	OK220707_1Q	585	yes	plag, qtz, hbl, opx, ox	Murupara-Bonisch

590	25	light brown fine silt (weak soil maybe) on top of mostly clast-supported fine pumice lapilli, crystals, and ash, normal to reverse graded, >5% lava lithics, qtz, and amphibole. Unit is yellowish in color and massive, well sorted	OK220707_1R		Murupara-Bonisch
615	110	alternating fine (up to 3 cm) layers of coarse ash to fine lapilli layers and finer ash layers that are different shades of white. WHAK432H is at 670 cm in a fine lapilli layer. WHAK432I is fine lapilli layer at 720 cm and just below contact with grayish white fine ash. WHAK432J is base of grayish white fine ash that is >1 m thick. Looking along strike where it is exposed in cliff. This is below a friable sand deposit (beach?) below the Matahina ign.	WHAK432H WHAK432I WHAK432J	670 720 730	Murupara-Bonisch
725					

Otarawairere							
Start (cm)	Thickness (cm)	Notes	Samples	Sample Height (cm)	Sanidine	Minerals	Unit
-10	10	graywacke gravel base					Basement
0	27	medium brown clay with scattered graywacke pebbles	OK240707-1A	5		plag, qtz, bt, hbl, ox	Pre-Paerata
27	50	alternating coarse sand-sized and fine-ash layers, gray color except for the bottom 10 cm. Log does not accurately depict layers. Conspicuous qtz and biotite throughout this unit					Pre-Paerata
77	47	light orangeish brown very firm clay with crystals including biotite. Grades into biotite bearing material below. This looks like a loessic soil					Pre-Paerata
124	9	orange, not as firm, more sand than clay, closer to grain supported than material below and above, ferro-mag crystal poor (tephra?) gradational contacts					Pre-Paerata
133	27	light brown to orange clay to fine sand, not as much clay as 47 cm thick unit below, biotite bearing (loessic soil?)					Pre-Paerata
160	165	normally graded lower 10 cm that is rust stained at base and grades up into a light gray color, crystal-rich qtz, bt, and amph. Sharp change in grain size at this point (10 cm above base of unit), no biotite, possible cummingtonite. 165 cm thick massive, yellow colored, poorly sorted with very little variation in pumice concentrations (i.e. no real obvious or subtle bedding), grain supported, predominantly pumice ranging from sane size up to ~10 mm. lithic poor, crystal rich with large qtz, feldpsar, opx, amph	Unit-B Otarawairere	190 and 310 mixed		plag, qtz, cum?, hbl, opx, ox	Paerata
325	39	light brown to orange clay dominant with scattered crystals, firm (loessic soil), grades into the unit below and has a sharp irregular contact on top. Thickness varies laterally (up to 60 cm thick in plaves)					Paerata

364	52	Orange to yellow massive, reverse to normal graded grain supported irregular but sharp upper contact which means the thickness varies considerably (< 30 cm in places), crystal rich with plag qtz opx, amph	OK240707-1C	415		Kohioawa
416	15	light brown, thin alternating layers of ash matrix, fine pumice lapilli, obsidian lithics, and crystals of grai supported crystal rich latyers; qtz, plag and large opx crystals				Kohioawa
431	25	low angle crossbeds, reworked base of plinian-style fall, yellow to rust colored				Kohioawa
456	170	yellow to rusty orange, massive to subtle pumice cementation bedded with noticeable subpackages of finer and coarser grainsizes. Grain supported, plinian style. Crystal rich with conspicuous quartz and biotite. Did not record mineralogy at different levels here like at Kohioawa section; (higher up notes) This marks the approximate height where Darren noted the top of this unit at the Kohioawa cliff section; It was a more obvious contact there where it went from a massive plinian style deposit to a well bedded and layered sequence. Here, it is a more gradational relationship. From this point to the base is 170 cm. (see sharp color contrast, orange to light gray, to mark this height in photos 53-57).	OK240707_1D	610		Kohioawa
626	52	plane-parallel bedded coarser grained supported beds and fine to coarse ash beds. Most of these layers contain biotite. Log is not an accurate depiction.	OK240707_1E OK240707_1F	660 675	OK240707_1E: plag, qtz, bt»hbl, opx?, ox	Kohioawa
678	57	light gray very fine ash with conspicuous crystal rich and coarse pumice sand layers. Biotite throughout				Kohioawa

735	45	sequence of plan parallel to wavy bedded coarses and fine-grained layers. The wavy bedding looks more like contorted deformation due to loading above as opposed to primary low angle cross-bedding. Most layers have obvious biotite and amphibole.			Murupara-Bonisch
780	91	light gray ash with a ~2 cm thick weakly developed soil on top (not sure this is a soil). The ash is very fine grained but does not contain soil-like clay, crystal poor with some biotite and amphibole. The weakly developed soil on top is purplish brown and firm due to clay content. Can still see glass in the body of this unit underneath a hand lens.			Murupara-Bonisch
871	214	(~15 cm) scattered angular pumice up to 5-7 cm fragments and relatively crystal rich with conspicuous amphibole and biotite. Very poorly sorted with ash matrix (can see glass shards under hand lens). (115 cm) scattered angular pumice lapilli (up to 10 mm) and lithics with moderate crystal content (not as rich as base). Largest lithics are similar size to largest pumice. (145 cm) very little pumice, similar crystal content. (top) light gray, massive, very poorly sorted ash with variable amounts of pumice, lithics, and crystals.. Top 60-70 cm is very crystal rich with obvious amphibole and biotite. Sorting characteristics, glass shards, similar max pumice and lithic sizes suggests this is an ignimbrite. Chad has a firm buff paleosol-loess on top of this unit which may be the lateral equivalent of soil between biotite-bearing and non-biotite-bearing ash and crystal layers at Kohioawa fully in cliffs west of Matata. Also Chad has recorded an obsidian lithic bearing unit above this which also correlates with beds above same soil at Kohioawa	OK240707_1J OK240707-1L	980 1080	Murupara-Bonisch
1085					

Table 2.5: Lapilli sample catalog for the Kohioawa Section (KS) and Ōtarawairere Section (OS)

Location	Unit	Magma	Horizon-Number	Height	Horizon	Lapilli	Lapilli-subgroup
KS	PrePaerata	PreP+Pae	1	35	OK220707-1B	OK220707-1B-1	OK220707-1B-1
KS	PrePaerata	PreP+Pae	1	35	OK220707-1B	OK220707-1B-2	OK220707-1B-2
KS	PrePaerata	PreP+Pae	1	35	OK220707-1B	OK220707-1B-3	OK220707-1B-3
KS	PrePaerata	PreP+Pae	1	35	OK220707-1B	OK220707-1B-4	OK220707-1B-4
KS	PrePaerata	PreP+Pae	1	35	OK220707-1B	OK220707-1B-5	OK220707-1B-5
KS	Paerata	PreP+Pae	2	70	OK220707-1C	OK220707-1C-1	OK220707-1C-1
KS	Paerata	PreP+Pae	2	70	OK220707-1C	OK220707-1C-1	OK220707-1C-1-A
KS	Paerata	PreP+Pae	2	70	OK220707-1C	OK220707-1C-2	OK220707-1C-2
KS	Paerata	PreP+Pae	2	70	OK220707-1C	OK220707-1C-3	OK220707-1C-3
KS	Paerata	PreP+Pae	2	70	OK220707-1C	OK220707-1C-4	OK220707-1C-4
KS	Paerata	PreP+Pae	2	70	OK220707-1C	OK220707-1C-5	OK220707-1C-5
KS	Paerata	PreP+Pae	3	75	WHAK432A	WHAK432A-1	WHAK432A-1
KS	Paerata	PreP+Pae	3	75	WHAK432A	WHAK432A-2	WHAK432A-2
KS	Paerata	PreP+Pae	3	75	WHAK432A	WHAK432A-3	WHAK432A-3
KS	Paerata	PreP+Pae	3	75	WHAK432A	WHAK432A-4	WHAK432A-4
KS	Paerata	PreP+Pae	3	75	WHAK432A	WHAK432A-5	WHAK432A-5
KS	Paerata	PreP+Pae	3	75	WHAK432A	WHAK432A-6	WHAK432A-6
KS	Paerata	PreP+Pae	4	100	WHAK432B	WHAK432B-1	WHAK432B-1
KS	Paerata	PreP+Pae	4	100	WHAK432B	WHAK432B-2	WHAK432B-2
KS	Paerata	PreP+Pae	4	100	WHAK432B	WHAK432B-3	WHAK432B-3
KS	Paerata	PreP+Pae	4	100	WHAK432B	WHAK432B-4	WHAK432B-4

KS	Paerata	PreP+Pae	4	100	WHAK432B	WHAK432B-5	WHAK432B-5
KS	Paerata	PreP+Pae	5	125	OK220707-1E	OK220707-1E-1	OK220707-1E-1
KS	Paerata	PreP+Pae	5	125	OK220707-1E	OK220707-1E-1	OK220707-1E-1-A
KS	Paerata	PreP+Pae	6	140	WHAK432C	WHAK432C-1	WHAK432C-1
KS	Paerata	PreP+Pae	6	140	WHAK432C	WHAK432C-2	WHAK432C-2
KS	Paerata	PreP+Pae	6	140	WHAK432C	WHAK432C-3	WHAK432C-3
KS	Paerata	PreP+Pae	6	140	WHAK432C	WHAK432C-4	WHAK432C-4
KS	Paerata	PreP+Pae	6	140	WHAK432C	WHAK432C-5	WHAK432C-5
KS	Paerata	PreP+Pae	7	175	OK220707-1F	OK220707-1F-1	OK220707-1F-1
KS	Paerata	PreP+Pae	7	175	OK220707-1F	OK220707-1F-2	OK220707-1F-2
KS	Paerata	PreP+Pae	7	175	OK220707-1F	OK220707-1F-3	OK220707-1F-3
KS	Paerata	PreP+Pae	7	175	OK220707-1F	OK220707-1F-4	OK220707-1F-4
KS	Paerata	PreP+Pae	7	175	OK220707-1F	OK220707-1F-5	OK220707-1F-5
KS	Paerata	PreP+Pae	7	175	OK220707-1F	OK220707-1F-6	OK220707-1F-6
KS	Kohioawa	Koh-A	8	215	OK220707-1G	OK220707-1G-1	OK220707-1G-1
KS	Kohioawa	Koh-A	8	215	OK220707-1G	OK220707-1G-2	OK220707-1G-2
KS	Kohioawa	Koh-A	8	215	OK220707-1G	OK220707-1G-3	OK220707-1G-3
KS	Kohioawa	Koh-A	8	215	OK220707-1G	OK220707-1G-4	OK220707-1G-4
KS	Kohioawa	Koh-A	8	215	OK220707-1G	OK220707-1G-4	OK220707-1G-4-A
KS	Kohioawa	Koh-A	8	215	OK220707-1G	OK220707-1G-5	OK220707-1G-5
KS	Kohioawa	Koh-A	8	215	OK220707-1G	OK220707-1G-6	OK220707-1G-6
KS	Kohioawa	Koh-A	9	250	WHAK432L	WHAK432L-1	WHAK432L-1
KS	Kohioawa	Koh-B	9	250	WHAK432L	WHAK432L-2	WHAK432L-2

KS	Kohioawa	Koh-A	9	250	WHAK432L	WHAK432L-3	WHAK432L-3
KS	Kohioawa	Koh-A	9	250	WHAK432L	WHAK432L-4	WHAK432L-4
KS	Kohioawa	Koh-A	9	250	WHAK432L	WHAK432L-5	WHAK432L-5
KS	Kohioawa	Koh-A	10	265	OK220707-1I	OK220707-1I-1	OK220707-1I-1
KS	Kohioawa	Koh-A	10	265	OK220707-1I	OK220707-1I-2	OK220707-1I-2
KS	Kohioawa	Koh-A	10	265	OK220707-1I	OK220707-1I-3	OK220707-1I-3
KS	Kohioawa	Koh-B	10	265	OK220707-1I	OK220707-1I-4	OK220707-1I-4
KS	Kohioawa	Koh-B	10	265	OK220707-1I	OK220707-1I-5	OK220707-1I-5
KS	Kohioawa	Koh-B	11	285	WHAK432D	WHAK432D-1	WHAK432D-1
KS	Kohioawa	Koh-B	11	285	WHAK432D	WHAK432D-2	WHAK432D-2
KS	Kohioawa	Koh-A	11	285	WHAK432D	WHAK432D-3	WHAK432D-3
KS	Kohioawa	Koh-B	11	285	WHAK432D	WHAK432D-4	WHAK432D-4
KS	Kohioawa	Koh-B	11	285	WHAK432D	WHAK432D-5	WHAK432D-5
KS	Kohioawa	Koh-A	12	335	WHAK432E	WHAK432E-1	WHAK432E-1
KS	Kohioawa	Koh-B	12	335	WHAK432E	WHAK432E-2	WHAK432E-2
KS	Kohioawa	Koh-B	12	335	WHAK432E	WHAK432E-3	WHAK432E-3
KS	Kohioawa	Koh-A	12	335	WHAK432E	WHAK432E-4	WHAK432E-4
KS	Kohioawa	Koh-B	12	335	WHAK432E	WHAK432E-5	WHAK432E-5
KS	Kohioawa	Koh-A	13	380	OK220707-1L	OK220707-1L-1	OK220707-1L-1
KS	Kohioawa	Koh-A	13	380	OK220707-1L	OK220707-1L-2	OK220707-1L-2
KS	Kohioawa	Koh-A	13	380	OK220707-1L	OK220707-1L-3	OK220707-1L-3
KS	Kohioawa	Koh-B	13	380	OK220707-1L	OK220707-1L-4	OK220707-1L-4
KS	Kohioawa	Koh-B	13	380	OK220707-1L	OK220707-1L-5	OK220707-1L-5

KS	Kohioawa	Koh-A	14	425	WHAK432F	WHAK432F-1	WHAK432F-1
KS	Kohioawa	Koh-A	14	425	WHAK432F	WHAK432F-2	WHAK432F-2
KS	Kohioawa	Koh-B	14	425	WHAK432F	WHAK432F-3	WHAK432F-3
KS	Kohioawa	Koh-A	14	425	WHAK432F	WHAK432F-4	WHAK432F-4
KS	Kohioawa	Koh-A	14	425	WHAK432F	WHAK432F-5	WHAK432F-5
KS	Kohioawa	Koh-A	15	465	OK220707-1N	OK220707-1N-1	OK220707-1N-1
KS	Kohioawa	Koh-B	15	465	OK220707-1N	OK220707-1N-2	OK220707-1N-2
KS	Kohioawa	Koh-A	15	465	OK220707-1N	OK220707-1N-3	OK220707-1N-3
KS	Kohioawa	Koh-A	15	465	OK220707-1N	OK220707-1N-4	OK220707-1N-4
KS	Kohioawa	Koh-A	15	465	OK220707-1N	OK220707-1N-5	OK220707-1N-5
KS	Kohioawa	Koh-A	15	465	OK220707-1N	OK220707-1N-6	OK220707-1N-6
KS	Kohioawa	Koh-C	16	490	WHAK432G	WHAK432G-1	WHAK432G-1
KS	Kohioawa	Koh-A	16	490	WHAK432G	WHAK432G-2	WHAK432G-2
KS	Kohioawa	Koh-C	16	490	WHAK432G	WHAK432G-3	WHAK432G-3
KS	Kohioawa	Koh-A	16	490	WHAK432G	WHAK432G-4	WHAK432G-4
KS	Kohioawa	Koh-A	16	490	WHAK432G	WHAK432G-5	WHAK432G-5
KS	Kohioawa	Koh-C	17	510	OK220707-1O	OK220707-1O-1	OK220707-1O-1
KS	Kohioawa	Koh-C	17	510	OK220707-1O	OK220707-1O-2	OK220707-1O-2
KS	Kohioawa	Koh-C	17	510	OK220707-1O	OK220707-1O-3	OK220707-1O-3
KS	Kohioawa	Koh-C	17	510	OK220707-1O	OK220707-1O-4	OK220707-1O-4
KS	Kohioawa	Koh-C	17	510	OK220707-1O	OK220707-1O-5	OK220707-1O-5
KS	Kohioawa	Koh-C	17	510	OK220707-1O	OK220707-1O-6	OK220707-1O-6
KS	Kohioawa	Koh-C	17	510	OK220707-1O	OK220707-1O-7	OK220707-1O-7

KS	Murupara	Muru-B	18	550	OK220707-1P	OK220707-1P-1	OK220707-1P-1
KS	Murupara	Muru-B	18	550	OK220707-1P	OK220707-1P-2	OK220707-1P-2
KS	Murupara	Muru-B	18	550	OK220707-1P	OK220707-1P-3	OK220707-1P-3
KS	Murupara	Muru-B	18	550	OK220707-1P	OK220707-1P-5	OK220707-1P-5
KS	Murupara	Muru-B	18	550	OK220707-1P	OK220707-1P-6	OK220707-1P-6
KS	Murupara	Muru-A	19	585	OK220707-1Q	OK220707-1Q-1	OK220707-1Q-1
KS	Murupara	Muru-B	19	585	OK220707-1Q	OK220707-1Q-2	OK220707-1Q-2
KS	Murupara	Muru-A	19	585	OK220707-1Q	OK220707-1Q-3	OK220707-1Q-3
KS	Murupara	Muru-B	19	585	OK220707-1Q	OK220707-1Q-4	OK220707-1Q-4
KS	Murupara	Muru-B	19	585	OK220707-1Q	OK220707-1Q-5	OK220707-1Q-5
KS	Murupara	Muru-A	20	670	WHAK432H	WHAK432H-1	WHAK432H-1
KS	Murupara	Muru-A	20	670	WHAK432H	WHAK432H-2	WHAK432H-2
KS	Murupara	Muru-A	20	670	WHAK432H	WHAK432H-3	WHAK432H-3
KS	Murupara	Muru-B	20	670	WHAK432H	WHAK432H-4	WHAK432H-4
KS	Murupara	Muru-B	20	670	WHAK432H	WHAK432H-5	WHAK432H-5
KS	Murupara	Muru-A	21	720	WHAK432I	WHAK432I-1	WHAK432I-1
KS	Murupara	Muru-A	21	720	WHAK432I	WHAK432I-1	WHAK432I-1-A
KS	Murupara	Muru-A	21	720	WHAK432I	WHAK432I-2	WHAK432I-2
KS	Murupara	Muru-A	21	720	WHAK432I	WHAK432I-2	WHAK432I-2-A
KS	Murupara	Muru-A	21	720	WHAK432I	WHAK432I-3	WHAK432I-3
KS	Murupara	Muru-A	21	720	WHAK432I	WHAK432I-4	WHAK432I-4
KS	Murupara	Muru-B	21	720	WHAK432I	WHAK432I-5	WHAK432I-5
KS	Murupara	Muru-A	21	720	WHAK432I	WHAK432I-5	WHAK432I-5-A

KS	Murupara	Muru-A	22	730	WHAK432J	WHAK432J-1	WHAK432J-1
KS	Murupara	Muru-A	22	730	WHAK432J	WHAK432J-2	WHAK432J-2
KS	Murupara	Muru-A	22	730	WHAK432J	WHAK432J-3	WHAK432J-3
KS	Murupara	Muru-A	22	730	WHAK432J	WHAK432J-4	WHAK432J-4
KS	Murupara	Muru-A	22	730	WHAK432J	WHAK432J-5	WHAK432J-5
OS	Paerata	PreP+Pae	25	1020	OK240707-1A	OK240707-1A-1	OK240707-1A-1
OS	Paerata	PreP+Pae	25	1020	OK240707-1A	OK240707-1A-2	OK240707-1A-2
OS	Paerata	PreP+Pae	25	1020	OK240707-1A	OK240707-1A-3	OK240707-1A-3
OS	Paerata	PreP+Pae	25	1020	OK240707-1A	OK240707-1A-4	OK240707-1A-4
OS	Paerata	PreP+Pae	25	1020	OK240707-1A	OK240707-1A-5	OK240707-1A-5
OS	Paerata	PreP+Pae	26	1250	Ōtarawairere	Ōtarawairere-1	Ōtarawairere-1
OS	Paerata	PreP+Pae	26	1250	Ōtarawairere	Ōtarawairere-2	Ōtarawairere-2
OS	Paerata	PreP+Pae	26	1250	Ōtarawairere	Ōtarawairere-3	Ōtarawairere-3
OS	Paerata	PreP+Pae	26	1250	Ōtarawairere	Ōtarawairere-4	Ōtarawairere-4
OS	Paerata	PreP+Pae	26	1250	Ōtarawairere	Ōtarawairere-5	Ōtarawairere-5
OS	Kohioawa	Koh-A	27	1405	OK240707-1C	OK240707-1C-1	OK240707-1C-1
OS	Kohioawa	Koh-A	27	1405	OK240707-1C	OK240707-1C-2	OK240707-1C-2
OS	Kohioawa	Koh-A	27	1405	OK240707-1C	OK240707-1C-3	OK240707-1C-3
OS	Kohioawa	Koh-A	27	1405	OK240707-1C	OK240707-1C-4	OK240707-1C-4
OS	Kohioawa	Koh-A	27	1405	OK240707-1C	OK240707-1C-5	OK240707-1C-5
OS	Kohioawa	Koh-A	28	1595	OK240707-1D	OK240707-1D-1	OK240707-1D-1
OS	Kohioawa	Koh-B	28	1595	OK240707-1D	OK240707-1D-2	OK240707-1D-2
OS	Kohioawa	Koh-A	28	1595	OK240707-1D	OK240707-1D-3	OK240707-1D-3

OS	Kohioawa	Koh-C	29	1645	OK240707-1E	OK240707-1E-2	OK240707-1E-2
OS	Kohioawa	Koh-B	29	1645	OK240707-1E	OK240707-1E-5	OK240707-1E-5-B
OS	Kohioawa	Koh-C	30	1660	OK240707-1F	OK240707-1F-1	OK240707-1F-1
OS	Kohioawa	Koh-C	30	1660	OK240707-1F	OK240707-1F-2	OK240707-1F-2
OS	Kohioawa	Koh-C	30	1660	OK240707-1F	OK240707-1F-3	OK240707-1F-3
OS	Kohioawa	Koh-A	30	1660	OK240707-1F	OK240707-1F-4	OK240707-1F-4
OS	Kohioawa	Koh-C	30	1660	OK240707-1F	OK240707-1F-5	OK240707-1F-5
OS	Kohioawa	Koh-B	30	1660	OK240707-1F	OK240707-1F-6	OK240707-1F-6
OS	Murupara	Muru-A	31	1990	OK240707-1J	OK240707-1J-1	OK240707-1J-1
OS	Murupara	Muru-B	31	1990	OK240707-1J	OK240707-1J-2	OK240707-1J-2
OS	Murupara	Muru-B	31	1990	OK240707-1J	OK240707-1J-4	OK240707-1J-4
OS	Murupara	Muru-B	32	2060	OK240707-1L	OK240707-1L-1	OK240707-1L-1
OS	Murupara	Muru-B	32	2060	OK240707-1L	OK240707-1L-2	OK240707-1L-2
OS	Murupara	Muru-B	32	2060	OK240707-1L	OK240707-1L-3	OK240707-1L-3
OS	Murupara	Muru-B	32	2060	OK240707-1L	OK240707-1L-3	OK240707-1L-3-A
OS	Murupara	Muru-B	32	2060	OK240707-1L	OK240707-1L-4	OK240707-1L-4
OS	Murupara	Muru-B	32	2060	OK240707-1L	OK240707-1L-5	OK240707-1L-5

Table 2.6: Lapilli glass major element mean compositions

Lapilli-subgroup	SiO_2	Al_2O_3	TiO_2	MgO	FeO	MnO	CaO	Na_2O	K_2O	Zircon Sat Temp (°C) T-W&H	Zircon Sat Temp (°C) T-Boehnke	Storage Pressure (MPa)	Pressure calculated
OK220707-1B-1	77.4	12.7	0.15	0.14	1.20	0.07	1.09	3.19	4.00	750	708	91	qtz-1feld
OK220707-1B-2	77.6	12.6	0.18	0.15	1.14	0.05	1.11	3.10	3.97	748	705	53	qtz-1feld
OK220707-1B-3	77.4	13.0	0.19	0.16	1.35	0.05	1.10	2.58	4.15	759	721	-	-
OK220707-1B-4	77.9	12.9	0.14	0.15	1.10	0.05	1.10	2.81	3.92	753	712	-	-
OK220707-1B-5	77.2	13.1	0.18	0.17	1.45	0.09	1.16	2.48	4.11	764	726	-	-
OK220707-1C-1	77.5	12.8	0.16	0.14	1.11	0.06	1.05	3.32	3.91	760	719	54	qtz-1feld
OK220707-1C-1-A	76.8	13.1	0.19	0.17	1.63	0.04	1.23	2.54	4.30	-	-	99	qtz-1feld
OK220707-1C-2	77.2	12.7	0.16	0.14	1.13	0.06	1.06	3.50	3.98	747	703	122	qtz-1feld
OK220707-1C-3	77.3	12.6	0.19	0.14	1.20	0.06	1.09	3.44	3.93	749	706	118	qtz-1feld
OK220707-1C-4	77.3	12.7	0.18	0.13	1.15	0.06	1.07	3.60	3.80	752	709	151	qtz-1feld
OK220707-1C-5	77.3	12.7	0.17	0.13	1.15	0.07	1.09	3.40	3.99	748	704	119	qtz-1feld
WHAK432A-1	78.1	12.8	0.16	0.14	0.94	0.01	1.02	2.88	3.95	775	739	-	-
WHAK432A-2	77.9	12.8	0.22	0.21	1.13	0.01	1.07	2.38	4.29	-	-	-	-
WHAK432A-3	77.7	12.7	0.13	0.15	1.01	0.03	1.03	3.60	3.69	757	715	96	qtz-1feld
WHAK432A-4	78.0	12.6	0.13	0.17	1.03	0.03	1.03	3.20	3.81	765	727	-	-
WHAK432A-5	77.9	12.7	0.17	0.17	1.05	0.07	1.02	2.87	4.04	766	729	-	-
WHAK432A-6	77.9	12.5	0.15	0.20	1.09	0.03	1.12	2.84	4.16	772	734	-	-
WHAK432B-1	77.5	12.5	0.23	0.23	1.21	0.09	1.12	2.70	4.43	755	713	-	-
WHAK432B-2	77.8	12.8	0.16	0.21	1.00	0.01	1.06	2.70	4.23	757	717	-	-

WHAK432B-3	77.6	12.8	0.15	0.21	0.98	0.04	1.00	3.31	3.92	754	713	84	qtz-1feld
WHAK432B-4	77.2	12.8	0.17	0.16	1.02	0.07	1.00	3.89	3.74	749	706	147	qtz-1feld
WHAK432B-5	77.6	12.7	0.18	0.23	0.99	0.04	1.01	3.36	3.83	754	713	99	qtz-1feld
OK220707-1E-1	78.1	12.3	0.11	0.03	1.03	0.04	0.54	3.71	4.09	824	801	-	-
OK220707-1E-1-A	76.6	13.0	0.21	0.13	1.51	0.06	1.02	3.54	3.91	-	-	174	qtz-1feld
WHAK432C-1	77.5	12.7	0.20	0.15	1.01	0.03	1.04	3.47	3.89	-	-	115	qtz-1feld
WHAK432C-2	77.5	12.7	0.15	0.13	1.02	0.04	1.03	3.65	3.77	758	716	126	qtz-1feld
WHAK432C-3	77.7	12.7	0.14	0.13	1.03	0.09	1.05	3.21	3.95	777	740	58	qtz-1feld
WHAK432C-4	77.5	12.7	0.16	0.13	1.01	0.02	1.03	3.68	3.71	745	701	126	qtz-1feld
WHAK432C-5	77.5	12.7	0.16	0.15	1.00	0.05	1.05	3.72	3.68	750	707	146	qtz-1feld
OK220707-1F-1	77.3	12.6	0.19	0.14	1.14	0.07	1.10	3.71	3.70	755	712	139	qtz-1feld
OK220707-1F-2	77.3	12.6	0.17	0.15	1.16	0.09	1.10	3.74	3.70	750	706	152	qtz-1feld
OK220707-1F-3	77.3	12.7	0.16	0.15	1.10	0.07	1.05	3.75	3.71	748	705	143	qtz-1feld
OK220707-1F-4	77.5	12.7	0.16	0.14	1.04	0.05	1.10	3.41	3.89	751	708	93	qtz-1feld
OK220707-1F-5	77.4	12.7	0.16	0.15	1.08	0.04	1.09	3.69	3.74	751	707	142	qtz-1feld
OK220707-1F-6	77.4	12.7	0.13	0.14	1.11	0.05	1.05	3.75	3.64	-	-	148	qtz-1feld
OK220707-1G-1	77.5	12.3	0.17	0.13	1.15	0.04	0.90	3.27	4.50	774	736	52	qtz-1feld
OK220707-1G-2	77.4	12.4	0.16	0.12	1.12	0.02	0.79	3.34	4.64	791	758	-	-
OK220707-1G-3	77.7	12.3	0.18	0.13	1.17	0.04	0.86	2.93	4.73	782	747	-	-
OK220707-1G-4	77.2	12.5	0.20	0.11	1.11	0.01	0.82	3.50	4.56	783	747	132	qtz-1feld
OK220707-1G-4-A	77.0	12.5	0.16	0.18	1.21	0.03	1.00	3.30	4.59	-	-	145	qtz-1feld
OK220707-1G-5	77.6	12.3	0.15	0.13	1.09	0.03	0.86	3.52	4.38	787	751	54	qtz-1feld
OK220707-1G-6	77.2	12.5	0.19	0.14	1.12	0.04	0.83	3.38	4.68	787	752	100	qtz-1feld

WHAK432L-1	77.4	12.4	0.18	0.11	1.09	0.04	0.82	3.36	4.61	780	744	51	qtz-1feld
WHAK432L-2	77.4	12.6	0.07	0.03	0.84	0.05	0.59	3.16	5.30	745	705	91	qtz-2feld
WHAK432L-3	77.4	12.4	0.16	0.11	1.05	0.06	0.82	3.62	4.42	775	738	124	qtz-1feld
WHAK432L-4	77.5	12.4	0.15	0.11	1.05	0.05	0.85	3.30	4.64	752	711	65	qtz-1feld
WHAK432L-5	77.5	12.3	0.18	0.09	1.13	0.05	0.77	3.21	4.69	781	746	48	qtz-1feld
OK220707-1I-1	77.0	12.4	0.21	0.12	1.48	0.06	0.85	3.00	4.90	780	744	44	qtz-1feld
OK220707-1I-2	77.2	12.3	0.19	0.11	1.20	0.07	0.84	3.32	4.71	782	746	90	qtz-1feld
OK220707-1I-3	77.1	12.3	0.20	0.09	1.18	0.07	0.78	3.23	5.07	764	725	96	qtz-1feld
OK220707-1I-4	77.4	12.4	0.13	0.05	0.97	0.08	0.65	3.07	5.26	744	703	82	qtz-2feld
OK220707-1I-5	77.4	12.6	0.09	0.05	1.02	0.04	0.66	2.91	5.19	754	716	40	qtz-1feld
WHAK432D-1	77.5	12.5	0.08	0.05	0.92	0.05	0.61	3.50	4.81	753	715	91	qtz-1feld
WHAK432D-2	77.4	12.5	0.07	0.07	0.86	0.06	0.55	3.61	4.84	744	705	122	qtz-2feld
WHAK432D-3	77.4	12.5	0.17	0.11	1.07	0.01	0.79	3.51	4.52	775	738	115	qtz-1feld
WHAK432D-4	77.4	12.5	0.09	0.05	0.83	0.08	0.57	3.59	4.90	749	710	122	qtz-2feld
WHAK432D-5	77.4	12.5	0.09	0.02	0.84	0.04	0.60	3.33	5.14	745	704	100	qtz-2feld
WHAK432E-1	77.6	12.4	0.16	0.10	1.12	0.00	0.83	3.08	4.73	786	752	-	-
WHAK432E-2	77.3	12.5	0.06	0.05	0.89	0.07	0.61	3.14	5.28	760	723	71	qtz-2feld
WHAK432E-3	77.7	12.5	0.08	0.07	0.89	0.07	0.57	2.87	5.25	763	728	-	-
WHAK432E-4	77.6	12.5	0.14	0.10	1.13	0.06	0.82	3.05	4.66	790	757	-	-
WHAK432E-5	77.7	12.5	0.10	0.04	0.82	0.07	0.62	2.99	5.21	759	723	-	-
OK220707-1L-1	77.7	12.2	0.21	0.13	1.17	0.01	0.90	2.50	5.12	782	746	-	-
OK220707-1L-2	77.4	12.4	0.19	0.11	1.18	0.04	0.85	2.95	4.90	788	754	53	qtz-1feld
OK220707-1L-3	77.5	12.3	0.21	0.12	1.12	0.03	0.86	2.95	4.90	786	751	-	-

OK220707-1L-4	77.2	12.4	0.11	0.04	0.97	0.05	0.63	2.73	5.86	746	706	83	qtz-2feld
OK220707-1L-5	77.3	12.4	0.08	0.06	0.92	0.05	0.60	3.46	5.07	755	716	106	qtz-2feld
WHAK432F-1	77.5	12.5	0.16	0.11	1.08	0.03	0.80	3.08	4.77	789	756	50	qtz-1feld
WHAK432F-2	77.5	12.4	0.21	0.10	1.08	0.04	0.79	3.38	4.58	786	751	55	qtz-1feld
WHAK432F-3	77.5	12.6	0.05	0.05	0.84	0.06	0.56	3.49	4.92	751	712	107	qtz-2feld
WHAK432F-4	77.6	12.4	0.16	0.10	1.10	0.07	0.79	2.90	4.90	798	766	-	-
WHAK432F-5	77.3	12.4	0.18	0.11	1.15	0.04	0.83	3.29	4.68	782	746	84	qtz-1feld
OK220707-1N-1	77.4	12.4	0.18	0.11	1.09	0.04	0.81	3.47	4.57	791	756	103	qtz-1feld
OK220707-1N-2	77.3	12.4	0.14	0.05	1.00	0.04	0.68	3.20	5.13	765	728	87	qtz-2feld
OK220707-1N-3	77.6	12.4	0.19	0.10	1.05	0.03	0.82	3.19	4.66	785	750	51	qtz-1feld
OK220707-1N-4	77.4	12.5	0.21	0.12	1.14	0.07	0.84	2.88	4.78	790	757	-	-
OK220707-1N-5	77.0	12.5	0.20	0.11	1.21	0.04	0.89	3.24	4.81	790	755	88	qtz-1feld
OK220707-1N-6	77.3	12.4	0.20	0.10	1.12	0.07	0.84	3.17	4.82	790	756	-	-
WHAK432G-1	77.6	12.5	0.04	0.04	0.81	0.07	0.51	3.39	5.02	762	726	40	qtz-1feld
WHAK432G-2	77.6	12.6	0.13	0.10	1.06	0.04	0.96	3.75	3.77	778	741	119	qtz-1feld
WHAK432G-3	77.5	12.5	0.07	0.04	0.82	0.06	0.51	3.27	5.19	779	747	90	qtz-2feld
WHAK432G-4	77.4	12.4	0.16	0.12	1.09	0.02	0.81	3.40	4.61	783	747	58	qtz-1feld
WHAK432G-5	77.5	12.5	0.19	0.12	1.17	0.03	0.83	2.85	4.79	803	773	-	-
OK220707-1O-1	77.7	12.7	0.06	0.05	0.68	0.06	0.48	3.49	4.79	758	723	90	qtz-1feld
OK220707-1O-2	77.6	12.7	0.05	0.02	0.72	0.06	0.49	3.75	4.66	765	730	100	qtz-1feld
OK220707-1O-3	77.6	12.7	0.09	0.04	0.81	0.05	0.56	3.07	5.10	770	737	48	qtz-1feld
OK220707-1O-4	77.7	12.7	0.05	0.03	0.72	0.06	0.52	3.18	5.11	776	743	42	qtz-1feld
OK220707-1O-5	77.5	12.6	0.06	0.05	0.79	0.06	0.56	3.76	4.67	754	715	147	qtz-2feld

OK220707-1O-6	77.4	12.7	0.08	0.05	0.84	0.04	0.57	3.22	5.09	775	742	88	qtz-2feld
OK220707-1O-7	77.4	12.6	0.06	0.03	0.81	0.05	0.55	3.70	4.83	754	715	144	qtz-2feld
OK220707-1P-1	77.7	12.4	0.13	0.08	1.10	0.06	0.88	3.70	3.91	755	714	88	qtz-1feld
OK220707-1P-2	77.6	12.5	0.13	0.10	1.05	0.06	0.87	3.85	3.84	748	706	112	qtz-1feld
OK220707-1P-3	77.7	12.5	0.13	0.09	1.09	0.05	0.87	3.74	3.88	752	710	49	qtz-1feld
OK220707-1P-5	77.7	12.5	0.13	0.09	1.17	0.06	0.90	3.40	4.01	755	714	52	qtz-1feld
OK220707-1P-6	77.7	12.5	0.12	0.07	1.08	0.05	0.85	3.79	3.86	754	713	118	qtz-1feld
OK220707-1Q-1	77.5	12.4	0.15	0.12	1.41	0.07	1.17	3.15	4.01	766	724	61	qtz-1feld
OK220707-1Q-2	77.9	12.5	0.12	0.10	1.15	0.05	0.89	3.10	4.15	761	723	-	-
OK220707-1Q-3	77.4	12.4	0.19	0.12	1.42	0.04	1.15	3.51	3.75	775	735	106	qtz-1feld
OK220707-1Q-4	77.3	12.2	0.18	0.10	1.48	0.09	0.97	3.15	4.52	754	712	52	qtz-1feld
OK220707-1Q-5	77.9	12.6	0.11	0.10	1.14	0.05	0.90	3.15	4.13	765	727	-	-
WHAK432H-1	76.4	13.0	0.13	0.15	1.46	0.06	1.24	4.20	3.30	793	754	255	qtz-1feld
WHAK432H-2	76.5	13.0	0.16	0.17	1.45	0.04	1.23	4.04	3.41	796	758	245	qtz-1feld
WHAK432H-3	76.6	12.9	0.20	0.14	1.41	0.05	1.20	4.15	3.32	790	752	226	qtz-1feld
WHAK432H-4	77.6	12.6	0.12	0.07	1.03	0.06	0.83	3.96	3.75	758	718	109	qtz-1feld
WHAK432H-5	77.6	12.5	0.16	0.08	1.01	0.05	0.77	3.98	3.86	751	710	141	qtz-1feld
WHAK432I-1	77.7	12.5	0.12	0.09	1.12	0.05	0.93	3.96	3.49	794	760	126	qtz-1feld
WHAK432I-1-A	76.5	13.1	0.20	0.17	1.42	0.06	1.27	3.96	3.38	-	-	242	qtz-1feld
WHAK432I-2	77.7	12.5	0.12	0.09	1.13	0.07	0.98	4.11	3.32	792	756	132	qtz-1feld
WHAK432I-2-A	76.5	13.0	0.18	0.18	1.43	0.03	1.22	4.13	3.37	-	-	248	qtz-1feld
WHAK432I-3	76.5	13.1	0.18	0.16	1.41	0.07	1.23	4.04	3.35	791	753	222	qtz-1feld
WHAK432I-4	76.5	13.0	0.19	0.17	1.41	0.05	1.20	4.13	3.34	784	744	240	qtz-1feld

WHAK432I-5	77.6	12.6	0.11	0.07	1.00	0.04	0.76	3.99	3.85	754	714	144	qtz-1feld
WHAK432I-5-A	76.4	13.0	0.18	0.16	1.39	0.11	1.21	4.19	3.35	-	-	251	qtz-1feld
WHAK432J-1	76.9	12.7	0.18	0.17	1.35	0.07	1.22	3.98	3.40	781	740	197	qtz-1feld
WHAK432J-2	76.4	13.1	0.23	0.17	1.42	0.09	1.26	3.94	3.39	802	766	237	qtz-1feld
WHAK432J-3	76.9	12.8	0.23	0.13	1.34	0.05	1.20	4.02	3.38	783	743	195	qtz-1feld
WHAK432J-4	76.6	13.0	0.20	0.18	1.43	0.09	1.27	3.83	3.42	788	750	220	qtz-1feld
WHAK432J-5	77.4	12.6	0.19	0.12	1.25	0.05	1.07	3.88	3.51	777	738	155	qtz-1feld
OK240707-1A-1	77.3	12.6	0.10	0.07	0.93	0.05	0.63	3.19	5.15	-	-	48	qtz-1feld
OK240707-1A-2	77.3	12.5	0.11	0.07	0.87	0.05	0.72	3.40	4.92	-	-	98	qtz-1feld
OK240707-1A-3	77.4	12.6	0.12	0.07	0.88	0.05	0.70	3.21	5.03	-	-	50	qtz-1feld
OK240707-1A-4	77.5	12.5	0.10	0.05	0.78	0.07	0.60	3.57	4.83	-	-	144	qtz-2feld
OK240707-1A-5	77.5	12.6	0.08	0.07	0.85	0.07	0.70	3.63	4.52	733	690	124	qtz-1feld
Ōtarawairere-1	77.5	12.7	0.15	0.14	1.01	0.05	1.05	3.73	3.67	-	-	138	qtz-1feld
Ōtarawairere-2	77.5	12.7	0.15	0.14	1.02	0.06	1.03	3.77	3.64	-	-	142	qtz-1feld
Ōtarawairere-3	77.5	12.8	0.14	0.14	0.99	0.05	1.02	3.64	3.72	-	-	80	qtz-1feld
Ōtarawairere-4	77.4	12.8	0.13	0.15	0.98	0.06	1.00	3.82	3.66	-	-	154	qtz-1feld
Ōtarawairere-5	77.5	13.0	0.15	0.14	0.81	0.04	0.94	4.07	3.36	-	-	176	qtz-1feld
OK240707-1C-1	77.9	12.5	0.20	0.12	1.11	0.06	0.83	2.33	5.00	786	754	-	-
OK240707-1C-2	77.8	12.3	0.18	0.11	1.16	0.02	0.83	2.59	5.04	785	751	-	-
OK240707-1C-3	77.6	12.3	0.18	0.11	1.12	0.04	0.81	2.92	4.87	780	745	-	-
OK240707-1C-4	77.3	12.3	0.19	0.11	1.28	0.04	0.85	2.98	4.96	785	750	48	qtz-1feld
OK240707-1C-5	77.7	12.4	0.13	0.13	1.12	0.03	0.89	2.63	4.96	750	709	-	-
OK240707-1D-1	77.4	12.5	0.16	0.09	1.08	0.03	0.79	3.41	4.58	781	746	96	qtz-1feld

OK240707-1D-2	77.8	12.5	0.08	0.05	0.95	0.06	0.62	2.85	5.07	752	715	-	-
OK240707-1D-3	77.4	12.4	0.20	0.12	1.09	0.05	0.84	3.36	4.62	775	738	95	qtz-1feld
OK240707-1E-2	77.3	12.4	0.08	0.05	1.04	0.07	0.59	3.63	4.85	761	723	120	qtz-2feld
OK240707-1E-5-B	77.4	12.5	0.06	0.05	0.94	0.06	0.59	3.50	4.90	-	-	113	qtz-2feld
OK240707-1F-1	77.6	12.5	0.06	0.05	0.97	0.04	0.55	3.09	5.09	745	706	-	-
OK240707-1F-2	77.6	12.5	0.05	0.04	0.78	0.06	0.54	3.43	5.00	745	706	92	qtz-2feld
OK240707-1F-3	77.5	12.6	0.04	0.03	0.83	0.08	0.55	3.51	4.94	744	705	114	qtz-2feld
OK240707-1F-4	77.3	12.5	0.17	0.10	1.05	0.01	0.79	3.45	4.61	763	724	45	qtz-1feld
OK240707-1F-5	78.2	12.6	0.06	0.06	0.78	0.07	0.58	1.94	5.80	751	716	-	-
OK240707-1F-6	77.5	12.6	0.05	0.04	0.84	0.05	0.62	3.20	5.11	742	702	91	qtz-2feld
OK240707-1J-1	77.4	12.3	0.23	0.17	1.35	0.06	1.29	3.63	3.51	789	749	104	qtz-1feld
OK240707-1J-2	77.5	12.3	0.13	0.05	1.05	0.06	0.80	3.43	4.72	755	714	90	qtz-1feld
OK240707-1J-4	77.6	12.5	0.13	0.07	0.99	0.04	0.79	3.78	4.11	757	717	45	qtz-1feld
OK240707-1L-1	77.7	12.8	0.11	0.09	1.28	0.03	0.85	3.13	3.99	764	727	-	-
OK240707-1L-2	77.6	12.6	0.08	0.06	1.03	0.05	0.81	3.80	4.01	753	712	120	qtz-1feld
OK240707-1L-3	77.5	12.5	0.09	0.08	1.09	0.06	0.78	3.96	3.93	756	716	141	qtz-1feld
OK240707-1L-3-A	78.5	12.7	0.11	0.09	1.15	0.02	0.75	2.61	4.09	-	-	-	-
OK240707-1L-4	77.5	12.6	0.13	0.08	1.04	0.05	0.79	3.84	4.00	757	717	122	qtz-1feld
OK240707-1L-5	77.5	12.7	0.14	0.07	1.15	0.06	0.83	3.39	4.16	-	-	54	qtz-1feld

Table 2.7: Lapilli glass major element standard deviation of the mean compositions

Lapilli-subgroup	SiO_2	Al_2O_3	TiO_2	MgO	FeO	MnO	CaO	Na_2O	K_2O
OK220707-1B-1	0.28	0.17	0.04	0.02	0.12	0.04	0.04	0.47	0.29
OK220707-1B-2	0.37	0.17	0.04	0.03	0.12	0.04	0.06	0.72	0.39
OK220707-1B-3	0.46	0.28	0.07	0.04	0.05	0.05	0.04	0.22	0.17
OK220707-1B-4	0.19	0.21	0.04	0.04	0.11	0.05	0.04	0.23	0.08
OK220707-1B-5	0.41	0.48	0.03	0.02	0.23	0.07	0.05	0.33	0.21
OK220707-1C-1	0.17	0.13	0.05	0.03	0.10	0.05	0.03	0.43	0.22
OK220707-1C-1-A	0.26	0.72	0.08	0.03	0.21	0.05	0.08	0.37	0.45
OK220707-1C-2	0.19	0.15	0.05	0.03	0.10	0.05	0.03	0.26	0.12
OK220707-1C-3	0.28	0.19	0.04	0.03	0.14	0.04	0.07	0.27	0.15
OK220707-1C-4	0.19	0.16	0.02	0.03	0.03	0.06	0.04	0.06	0.09
OK220707-1C-5	0.34	0.16	0.05	0.03	0.14	0.06	0.05	0.35	0.13
WHAK432A-1	0.29	0.21	0.04	0.02	0.13	0.01	0.01	0.14	0.09
WHAK432A-2	0.32	0.31	0.03	0.06	0.14	0.02	0.08	0.26	0.42
WHAK432A-3	0.19	0.06	0.07	0.05	0.12	0.04	0.04	0.46	0.25
WHAK432A-4	0.23	0.08	0.08	0.06	0.06	0.03	0.03	0.61	0.30
WHAK432A-5	0.42	0.05	0.08	0.03	0.10	0.07	0.06	0.62	0.28
WHAK432A-6	0.22	0.13	0.09	0.05	0.22	0.02	0.06	0.36	0.22
WHAK432B-1	0.51	0.33	0.08	0.07	0.31	0.10	0.15	0.95	0.62
WHAK432B-2	0.30	0.11	0.03	0.02	0.08	0.01	0.06	0.30	0.18
WHAK432B-3	0.09	0.14	0.08	0.07	0.11	0.03	0.03	0.61	0.24
WHAK432B-4	0.24	0.05	0.06	0.04	0.14	0.08	0.04	0.19	0.20

WHAK432B-5	0.27	0.19	0.06	0.07	0.09	0.03	0.06	0.52	0.22
OK220707-1E-1	0.14	0.14	0.03	0.03	0.04	0.02	0.04	0.09	0.02
OK220707-1E-1-A	0.17	0.11	0.05	0.04	0.15	0.06	0.04	0.15	0.10
WHAK432C-1	0.22	0.09	0.06	0.04	0.10	0.04	0.06	0.34	0.20
WHAK432C-2	0.15	0.13	0.05	0.03	0.11	0.03	0.05	0.09	0.09
WHAK432C-3	0.27	0.05	0.03	0.04	0.12	0.08	0.02	0.55	0.27
WHAK432C-4	0.16	0.10	0.05	0.01	0.12	0.03	0.04	0.08	0.07
WHAK432C-5	0.17	0.05	0.04	0.03	0.11	0.05	0.05	0.13	0.08
OK220707-1F-1	0.08	0.03	0.04	0.02	0.09	0.06	0.05	0.10	0.12
OK220707-1F-2	0.09	0.09	0.07	0.02	0.10	0.07	0.03	0.10	0.06
OK220707-1F-3	0.11	0.11	0.03	0.04	0.03	0.03	0.05	0.10	0.04
OK220707-1F-4	0.19	0.11	0.04	0.04	0.09	0.05	0.07	0.35	0.20
OK220707-1F-5	0.11	0.12	0.03	0.03	0.08	0.03	0.06	0.12	0.10
OK220707-1F-6	0.12	0.07	0.03	0.01	0.10	0.06	0.05	0.03	0.03
OK220707-1G-1	0.17	0.07	0.04	0.03	0.11	0.04	0.05	0.18	0.16
OK220707-1G-2	0.22	0.07	0.06	0.03	0.09	0.03	0.01	0.35	0.18
OK220707-1G-3	0.27	0.06	0.05	0.03	0.06	0.03	0.04	0.56	0.27
OK220707-1G-4	0.10	0.07	0.02	0.01	0.04	0.01	0.05	0.04	0.05
OK220707-1G-4-A	0.08	0.04	0.04	0.02	0.11	0.03	0.06	0.28	0.15
OK220707-1G-5	0.18	0.10	0.06	0.03	0.08	0.03	0.05	0.18	0.17
OK220707-1G-6	0.21	0.08	0.05	0.02	0.06	0.04	0.02	0.24	0.16
WHAK432L-1	0.20	0.16	0.06	0.04	0.11	0.05	0.04	0.18	0.10
WHAK432L-2	0.16	0.14	0.06	0.03	0.09	0.04	0.06	0.34	0.23

WHAK432L-3	0.10	0.09	0.03	0.02	0.08	0.04	0.07	0.08	0.04
WHAK432L-4	0.09	0.12	0.08	0.04	0.08	0.04	0.05	0.31	0.27
WHAK432L-5	0.18	0.15	0.05	0.03	0.08	0.04	0.06	0.29	0.11
OK220707-1I-1	0.35	0.20	0.04	0.03	0.30	0.05	0.07	0.27	0.18
OK220707-1I-2	0.14	0.10	0.05	0.03	0.07	0.07	0.03	0.20	0.17
OK220707-1I-3	0.42	0.13	0.09	0.04	0.19	0.06	0.06	0.35	0.20
OK220707-1I-4	0.18	0.17	0.03	0.03	0.10	0.06	0.03	0.19	0.13
OK220707-1I-5	0.38	0.12	0.04	0.04	0.13	0.04	0.05	0.56	0.25
WHAK432D-1	0.19	0.12	0.05	0.03	0.13	0.05	0.07	0.15	0.14
WHAK432D-2	0.12	0.12	0.06	0.03	0.10	0.05	0.04	0.12	0.07
WHAK432D-3	0.10	0.07	0.08	0.04	0.09	0.02	0.05	0.17	0.14
WHAK432D-4	0.19	0.07	0.04	0.03	0.09	0.06	0.05	0.13	0.12
WHAK432D-5	0.25	0.12	0.06	0.02	0.06	0.04	0.06	0.28	0.16
WHAK432E-1	0.26	0.10	0.06	0.03	0.09	0.02	0.06	0.40	0.22
WHAK432E-2	0.12	0.11	0.05	0.04	0.11	0.05	0.05	0.27	0.19
WHAK432E-3	0.18	0.03	0.06	0.02	0.10	0.06	0.02	0.45	0.14
WHAK432E-4	0.08	0.14	0.04	0.05	0.06	0.06	0.06	0.43	0.22
WHAK432E-5	0.33	0.06	0.05	0.03	0.11	0.07	0.03	0.46	0.26
OK220707-1L-1	0.36	0.25	0.09	0.06	0.13	0.02	0.06	0.44	0.31
OK220707-1L-2	0.33	0.13	0.03	0.02	0.18	0.04	0.05	0.51	0.29
OK220707-1L-3	0.32	0.11	0.08	0.03	0.04	0.04	0.05	0.26	0.25
OK220707-1L-4	0.34	0.20	0.06	0.02	0.10	0.03	0.05	0.29	0.26
OK220707-1L-5	0.42	0.05	0.06	0.02	0.08	0.06	0.03	0.37	0.31

WHAK432F-1	0.20	0.16	0.07	0.05	0.08	0.05	0.03	0.43	0.14
WHAK432F-2	0.08	0.12	0.08	0.05	0.11	0.05	0.06	0.24	0.19
WHAK432F-3	0.11	0.10	0.04	0.04	0.08	0.05	0.05	0.16	0.17
WHAK432F-4	0.17	0.13	0.06	0.02	0.06	0.05	0.06	0.24	0.13
WHAK432F-5	0.21	0.10	0.05	0.04	0.10	0.03	0.04	0.24	0.14
OK220707-1N-1	0.10	0.11	0.06	0.03	0.09	0.04	0.04	0.09	0.09
OK220707-1N-2	0.29	0.11	0.06	0.04	0.05	0.04	0.04	0.32	0.29
OK220707-1N-3	0.16	0.09	0.02	0.04	0.07	0.03	0.07	0.28	0.12
OK220707-1N-4	0.31	0.15	0.05	0.03	0.06	0.06	0.05	0.44	0.14
OK220707-1N-5	0.25	0.12	0.05	0.03	0.14	0.03	0.05	0.27	0.28
OK220707-1N-6	0.21	0.09	0.04	0.02	0.12	0.07	0.04	0.45	0.27
WHAK432G-1	0.24	0.09	0.04	0.03	0.13	0.07	0.05	0.21	0.21
WHAK432G-2	0.17	0.07	0.05	0.03	0.03	0.04	0.05	0.16	0.09
WHAK432G-3	0.07	0.07	0.05	0.03	0.10	0.05	0.06	0.21	0.11
WHAK432G-4	0.29	0.09	0.08	0.03	0.06	0.03	0.05	0.27	0.15
WHAK432G-5	0.28	0.11	0.05	0.04	0.07	0.04	0.05	0.54	0.21
OK220707-1O-1	0.24	0.13	0.05	0.03	0.08	0.05	0.03	0.41	0.24
OK220707-1O-2	0.20	0.10	0.05	0.02	0.08	0.03	0.04	0.26	0.24
OK220707-1O-3	0.11	0.07	0.02	0.02	0.06	0.04	0.04	0.27	0.14
OK220707-1O-4	0.22	0.09	0.05	0.02	0.06	0.05	0.04	0.34	0.13
OK220707-1O-5	0.11	0.07	0.05	0.03	0.06	0.05	0.04	0.07	0.09
OK220707-1O-6	0.22	0.13	0.05	0.03	0.09	0.04	0.04	0.42	0.31
OK220707-1O-7	0.12	0.06	0.02	0.02	0.05	0.04	0.04	0.16	0.15

OK220707-1P-1	0.14	0.07	0.04	0.03	0.08	0.05	0.04	0.16	0.14
OK220707-1P-2	0.11	0.08	0.06	0.03	0.08	0.05	0.05	0.08	0.07
OK220707-1P-3	0.19	0.10	0.06	0.01	0.07	0.03	0.06	0.26	0.12
OK220707-1P-5	0.28	0.17	0.03	0.02	0.15	0.05	0.02	0.39	0.15
OK220707-1P-6	0.15	0.10	0.05	0.03	0.06	0.04	0.02	0.07	0.06
OK220707-1Q-1	0.42	0.21	0.05	0.04	0.22	0.05	0.08	0.40	0.19
OK220707-1Q-2	0.35	0.11	0.04	0.02	0.11	0.05	0.02	0.69	0.31
OK220707-1Q-3	0.32	0.14	0.05	0.04	0.17	0.05	0.08	0.30	0.20
OK220707-1Q-4	0.38	0.20	0.03	0.03	0.30	0.09	0.08	0.33	0.46
OK220707-1Q-5	0.26	0.16	0.04	0.03	0.05	0.04	0.04	0.56	0.30
WHAK432H-1	0.21	0.08	0.07	0.03	0.05	0.04	0.06	0.06	0.05
WHAK432H-2	0.13	0.09	0.02	0.02	0.08	0.05	0.04	0.21	0.14
WHAK432H-3	0.25	0.11	0.07	0.03	0.10	0.04	0.06	0.06	0.06
WHAK432H-4	0.18	0.07	0.05	0.04	0.10	0.07	0.06	0.09	0.12
WHAK432H-5	0.15	0.10	0.04	0.03	0.09	0.05	0.06	0.07	0.06
WHAK432I-1	0.12	0.12	0.06	0.02	0.08	0.04	0.06	0.08	0.08
WHAK432I-1-A	0.22	0.08	0.04	0.03	0.08	0.06	0.06	0.23	0.07
WHAK432I-2	0.15	0.07	0.07	0.03	0.12	0.05	0.05	0.09	0.13
WHAK432I-2-A	0.14	0.13	0.07	0.01	0.04	0.03	0.05	0.04	0.05
WHAK432I-3	0.24	0.11	0.05	0.04	0.11	0.07	0.04	0.21	0.08
WHAK432I-4	0.21	0.14	0.07	0.02	0.06	0.05	0.07	0.13	0.08
WHAK432I-5	0.10	0.10	0.06	0.05	0.03	0.04	0.02	0.07	0.03
WHAK432I-5-A	0.11	0.06	0.08	0.02	0.08	0.08	0.04	0.07	0.06

WHAK432J-1	0.16	0.02	0.04	0.04	0.08	0.06	0.04	0.10	0.07
WHAK432J-2	0.14	0.10	0.06	0.04	0.11	0.08	0.07	0.27	0.11
WHAK432J-3	0.29	0.11	0.06	0.03	0.08	0.05	0.09	0.08	0.07
WHAK432J-4	0.27	0.12	0.05	0.03	0.08	0.06	0.02	0.37	0.09
WHAK432J-5	0.14	0.06	0.03	0.03	0.11	0.04	0.05	0.15	0.09
OK240707-1A-1	0.13	0.10	0.04	0.02	0.10	0.05	0.04	0.37	0.44
OK240707-1A-2	0.10	0.06	0.07	0.02	0.10	0.04	0.06	0.16	0.27
OK240707-1A-3	0.21	0.14	0.05	0.03	0.08	0.04	0.03	0.39	0.30
OK240707-1A-4	0.12	0.04	0.06	0.04	0.06	0.06	0.05	0.12	0.08
OK240707-1A-5	0.14	0.08	0.05	0.03	0.09	0.05	0.04	0.11	0.10
Ōtarawairere-1	0.13	0.09	0.03	0.01	0.06	0.04	0.03	0.10	0.07
Ōtarawairere-2	0.10	0.08	0.05	0.02	0.06	0.05	0.04	0.10	0.08
Ōtarawairere-3	0.15	0.08	0.05	0.03	0.06	0.04	0.03	0.17	0.06
Ōtarawairere-4	0.10	0.08	0.03	0.02	0.09	0.05	0.02	0.10	0.05
Ōtarawairere-5	0.10	0.12	0.06	0.02	0.10	0.03	0.05	0.20	0.08
OK240707-1C-1	0.19	0.10	0.05	0.02	0.06	0.06	0.05	0.31	0.18
OK240707-1C-2	0.39	0.16	0.04	0.04	0.11	0.02	0.06	0.60	0.34
OK240707-1C-3	0.32	0.14	0.06	0.04	0.11	0.04	0.05	0.61	0.36
OK240707-1C-4	0.34	0.21	0.05	0.02	0.17	0.05	0.06	0.65	0.35
OK240707-1C-5	0.55	0.13	0.07	0.03	0.18	0.03	0.04	0.83	0.42
OK240707-1D-1	0.19	0.13	0.07	0.05	0.19	0.04	0.11	0.31	0.19
OK240707-1D-2	0.25	0.30	0.04	0.03	0.17	0.05	0.04	0.60	0.15
OK240707-1D-3	0.17	0.08	0.07	0.03	0.02	0.04	0.04	0.20	0.13

OK240707-1E-2	0.25	0.12	0.05	0.02	0.15	0.05	0.07	0.27	0.18
OK240707-1E-5-B	0.20	0.06	0.05	0.03	0.10	0.05	0.07	0.23	0.18
OK240707-1F-1	0.22	0.13	0.04	0.04	0.10	0.03	0.04	0.63	0.38
OK240707-1F-2	0.20	0.07	0.03	0.03	0.07	0.05	0.05	0.19	0.17
OK240707-1F-3	0.03	0.07	0.04	0.03	0.06	0.05	0.04	0.14	0.18
OK240707-1F-4	0.51	0.10	0.06	0.06	0.14	0.01	0.05	0.23	0.23
OK240707-1F-5	0.53	0.16	0.05	0.03	0.08	0.06	0.06	0.38	0.17
OK240707-1F-6	0.24	0.08	0.04	0.03	0.10	0.04	0.04	0.35	0.10
OK240707-1J-1	0.18	0.16	0.05	0.03	0.15	0.05	0.08	0.20	0.13
OK240707-1J-2	0.27	0.35	0.06	0.03	0.28	0.06	0.08	0.41	0.55
OK240707-1J-4	0.10	0.06	0.03	0.02	0.05	0.04	0.05	0.05	0.05
OK240707-1L-1	0.40	0.22	0.03	0.03	0.26	0.03	0.08	0.67	0.14
OK240707-1L-2	0.15	0.09	0.05	0.03	0.08	0.05	0.06	0.10	0.06
OK240707-1L-3	0.14	0.11	0.06	0.03	0.11	0.06	0.04	0.13	0.10
OK240707-1L-3-A	0.23	0.12	0.03	0.01	0.10	0.03	0.04	0.05	0.15
OK240707-1L-4	0.13	0.10	0.05	0.03	0.07	0.04	0.04	0.12	0.10
OK240707-1L-5	0.54	0.12	0.08	0.02	0.14	0.05	0.02	0.71	0.26

Table 2.8: Lapilli glass trace element mean compositions (Li7-Fe58)

Lapilli-subgroup	Li7	B11	Na23	Mg24	Al27	Si28	P31	K39	Ca43	Sc45	Ti47	Ti49	V51	Cr53	Mn55	Fe58
OK220707-1B-1	54	27	24050	922	68877	361190	145	30544	7208	13	689	655	2.5	0.9	340	76
OK220707-1B-2	46	26	22785	890	64728	362686	182	29291	7208	14	689	675	5.4	1.6	336	78
OK220707-1B-3	41	26	19510	1158	75566	361611	353	30442	7354	14	755	770	3.9	2.7	332	100
OK220707-1B-4	37	28	18621	978	66775	364042	318	30607	7009	12	656	663	3.7	1.1	311	71
OK220707-1B-5	33	28	15944	1388	72813	360443	575	28594	6892	15	870	854	5.4	3.5	281	122
OK220707-1C-1	35	31	16304	1404	78926	360957	554	29408	7009	15	851	852	10	3.4	340	119
OK220707-1C-1-A	-	-	-	-	-	-	-	-	-	-	-	-	-	-	-	-
OK220707-1C-2	48	24	23749	926	66562	361938	161	32920	6785	14	640	653	3.2	0.8	349	77
OK220707-1C-3	50	24	23644	913	68810	359975	156	32076	7441	14	646	627	3.4	1.2	350	74
OK220707-1C-4	46	23	21759	1043	70335	361471	266	31036	6979	14	695	705	6.3	2.0	352	87
OK220707-1C-5	51	24	25007	910	68708	361237	155	32627	6958	12	648	685	3.9	1.0	351	79
WHAK432A-1	42	27	21100	5947	85781	-	420	33342	6901	11	821	824	8.3	3.6	406	99
WHAK432A-2	-	-	-	-	-	-	-	-	-	-	-	-	-	-	-	-
WHAK432A-3	40	27	20543	4821	73235	-	224	32600	6743	9.5	671	651	7.8	3.0	364	75
WHAK432A-4	39	29	21442	4582	78648	-	325	32614	6569	10	736	722	7.5	2.7	361	82
WHAK432A-5	54	24	26009	1392	68283	-	98	33182	7066	8.6	664	695	3.1	1.5	381	69
WHAK432A-6	45	38	26016	10167	88961	-	498	35510	7418	12	1071	898	18	4.6	653	117
WHAK432B-1	50	28	29646	8122	72361	-	359	35735	7468	11	692	683	3.4	1.2	422	74
WHAK432B-2	53	26	25595	4198	69778	-	212	33962	7307	11	692	701	2.8	0.8	396	69
WHAK432B-3	52	24	31013	4196	67184	-	173	32719	7203	9.5	648	640	2.1	0.3	362	66
WHAK432B-4	56	25	29259	3375	69190	-	170	33693	7527	9.5	663	653	2.1	0.3	375	67

WHAK432B-5	49	28	28475	5050	68925	-	185	35485	7137	9.7	640	641	2.4	0.9	403	72
OK220707-1E-1	43	16	23641	802	66248	359975	73	32381	6283	13	843	802	1.7	1.0	350	81
OK220707-1E-1-A	-	-	-	-	-	-	-	-	-	-	-	-	-	-	-	-
WHAK432C-1	-	-	-	-	-	-	-	-	-	-	-	-	-	-	-	-
WHAK432C-2	41	29	25876	2791	57829	-	264	22133	6061	12	755	809	3.8	6.1	331	106
WHAK432C-3	29	39	27749	10574	77011	-	533	27983	3623	17	933	1049	8.0	7.0	313	176
WHAK432C-4	52	27	25192	876	46645	-	91	21216	6398	8.8	599	612	2.0	1.4	344	64
WHAK432C-5	43	28	23766	2416	51240	-	204	22498	6581	11	648	658	2.6	3.1	345	83
OK220707-1F-1	47	22	22194	1262	85173	362873	133	31215	7527	16	750	745	8.0	1.8	343	193
OK220707-1F-2	45	28	21020	1169	81086	361424	167	30930	7243	15	709	803	8.0	5.5	323	148
OK220707-1F-3	50	26	22357	972	68805	362032	97	31549	7269	15	696	682	4.6	0.6	348	105
OK220707-1F-4	49	27	22321	878	69273	363715	109	35242	7579	14	654	679	3.1	1.5	362	80
OK220707-1F-5	51	25	23319	877	67298	363107	108	32846	7366	12	663	655	3.6	0.6	359	76
OK220707-1F-6	-	-	-	-	-	-	-	-	-	-	-	-	-	-	-	-
OK220707-1G-1	46	28	17751	802	63088	363013	111	41037	5845	12	891	935	5.9	3.4	248	78
OK220707-1G-2	50	29	19476	1029	74240	362079	100	39216	5255	16	1048	1113	17	4.7	260	148
OK220707-1G-3	44	26	17629	800	70839	363481	101	42683	5953	12	971	987	5.3	2.8	248	86
OK220707-1G-4	50	30	21990	781	71165	360723	100	38755	5539	13	924	937	9.3	2.5	261	109
OK220707-1G-4-A	-	-	-	-	-	-	-	-	-	-	-	-	-	-	-	-
OK220707-1G-5	55	29	24299	843	69096	363107	83	38793	6402	13	1045	1065	6.3	1.8	274	91
OK220707-1G-6	51	30	19961	837	72026	361237	105	41499	5954	15	991	975	7.2	1.6	295	101
WHAK432L-1	49	29	23633	676	47079	-	66	28850	5761	12	822	780	3.7	6.2	246	73
WHAK432L-2	42	35	22677	366	48622	-	108	32608	3621	9.6	363	358	1.0	1.9	425	62

WHAK432L-3	56	30	24359	618	44629	-	81	26240	5396	9.8	742	725	2.5	1.7	258	64
WHAK432L-4	46	31	23887	619	42934	-	81	27207	5078	7.8	626	605	2.4	3.4	273	63
WHAK432L-5	57	30	23568	633	48099	-	77	28001	5021	8.8	784	793	2.7	4.0	256	74
OK220707-1I-1	56	28	21244	732	68248	359040	68	39652	5442	13	867	895	6.7	1.2	263	90
OK220707-1I-2	51	27	18562	718	63356	360302	88	35743	5496	14	947	933	13	1.4	324	113
OK220707-1I-3	52	28	21145	513	61733	361564	56	36722	4736	11	633	693	2.1	1.0	277	61
OK220707-1I-4	49	34	18540	349	63922	361377	56	42262	4038	11	503	414	1.5	1.7	358	71
OK220707-1I-5	55	31	19360	343	64633	362266	69	42595	4382	12	445	438	2.6	0.6	365	71
WHAK432D-1	52	33	20416	904	61583	-	66	45182	4452	11	430	432	0.6	2.7	402	57
WHAK432D-2	50	32	17718	521	63255	-	85	46297	3918	11	363	370	1.3	3.6	405	57
WHAK432D-3	49	26	18671	774	62469	-	94	43238	5419	12	772	765	3.6	0.9	250	65
WHAK432D-4	63	33	22573	638	64634	-	65	44567	3687	12	376	383	1.1	3.6	401	57
WHAK432D-5	45	37	16504	796	63293	-	63	48764	3746	10	377	368	0.7	4.0	410	55
WHAK432E-1	47	32	16441	833	72724	-	95	41691	5116	11	881	936	4.0	1.7	238	82
WHAK432E-2	52	39	18409	453	68259	-	67	48370	3736	9.5	495	467	2.2	1.9	409	60
WHAK432E-3	62	34	18394	708	76414	-	85	46432	3998	11	549	628	3.8	2.2	415	112
WHAK432E-4	56	32	21522	826	67919	-	70	41565	5703	10	876	892	3.7	0.8	262	81
WHAK432E-5	54	39	18435	937	75230	-	131	49385	4207	10	496	528	2.8	1.0	406	80
OK220707-1L-1	45	31	17248	672	64759	361471	81	39492	5231	11	766	936	4.2	2.8	223	72
OK220707-1L-2	52	29	19935	707	67638	361237	71	44291	5771	11	819	834	3.3	1.0	254	74
OK220707-1L-3	48	31	16726	738	70673	361284	111	41517	5527	11	870	884	4.0	2.4	275	94
OK220707-1L-4	32	32	15056	353	60309	362172	60	46092	3637	8.6	373	371	0.7	1.7	389	52
OK220707-1L-5	75	36	24477	331	66574	362219	43	42367	4080	9.3	379	408	0.5	0.3	419	53

WHAK432F-1	46	30	16560	733	66541	-	108	43377	5014	16	1009	985	5.8	4.7	248	101
WHAK432F-2	50	29	20411	778	69326	-	89	42817	5776	15	876	856	2.9	8.4	246	77
WHAK432F-3	54	37	18331	419	66070	-	106	46870	4033	13	393	378	1.0	3.4	383	64
WHAK432F-4	51	40	15485	857	81835	-	234	45150	5698	15	1046	1029	5.6	8.8	236	117
WHAK432F-5	48	29	16458	780	65138	-	151	43566	4854	14	813	784	3.8	5.2	251	72
OK220707-1N-1	57	32	24260	708	72525	362920	66	42274	5962	11	845	895	3.1	0.8	285	73
OK220707-1N-2	49	31	18350	519	80073	362733	78	42362	4305	11	533	549	3.6	1.4	341	105
OK220707-1N-3	52	30	19261	717	72547	362593	79	40483	5655	11	796	798	3.3	1.2	258	79
OK220707-1N-4	59	31	23167	817	69430	361938	92	44764	6119	11	793	839	4.1	1.7	290	89
OK220707-1N-5	54	31	19765	893	85163	360396	105	38858	5616	12	924	949	5.4	2.4	241	140
OK220707-1N-6	55	30	24193	757	71701	362452	72	39497	5948	11	890	865	3.3	2.0	246	83
WHAK432G-1	71	45	23784	338	71826	-	43	45854	3588	8.8	400	424	2.4	0.8	493	71
WHAK432G-2	48	24	24003	743	76789	-	66	33530	6388	8.9	729	738	3.1	1.0	304	108
WHAK432G-3	57	41	17546	693	94048	-	76	43330	3544	10.0	841	850	9.1	1.9	392	119
WHAK432G-4	55	29	23967	759	73646	-	67	41402	5458	8.0	780	845	3.8	1.0	266	87
WHAK432G-5	45	29	15792	1136	100819	-	113	38791	5130	11	1286	1298	10	3.0	227	191
OK220707-1O-1	65	45	21128	346	72949	363247	51	40007	3340	9.9	431	448	4.9	0.9	448	64
OK220707-1O-2	78	45	24086	531	85246	363481	70	39934	3609	11	616	627	8.3	2.7	467	87
OK220707-1O-3	48	36	16786	676	88042	363060	111	41133	3978	11	798	853	12	3.1	399	117
OK220707-1O-4	56	40	15924	634	93420	362920	111	38982	3879	11	827	797	13	2.8	387	107
OK220707-1O-5	73	37	23676	294	69955	362452	42	41409	3892	9.1	359	365	2.0	0.6	421	56
OK220707-1O-6	52	43	18424	589	86312	362453	123	41943	4306	11	937	784	9.0	2.3	418	99
OK220707-1O-7	68	38	24364	368	71643	362172	56	41794	4145	9.6	430	440	2.0	0.7	457	68

OK220707-1P-1	42	24	23837	551	63819	363387	58	32634	5469	12	554	554	0.8	0.6	291	65
OK220707-1P-2	46	23	24064	527	64287	362639	54	30145	5435	12	526	516	0.9	0.3	298	58
OK220707-1P-3	44	23	24448	553	62282	363668	53	32629	5589	12	526	551	0.7	0.8	291	62
OK220707-1P-5	40	25	21519	629	67670	362967	82	33590	5850	12	542	547	1.5	0.7	317	73
OK220707-1P-6	47	24	25283	543	65201	363574	55	33600	5952	12	529	553	0.9	0.2	303	63
OK220707-1Q-1	39	20	21390	928	65764	362873	139	31507	6848	9.9	674	681	2.0	0.8	338	72
OK220707-1Q-2	50	26	26322	573	63240	363621	58	33421	6097	12	561	571	0.7	0.5	322	65
OK220707-1Q-3	42	19	24792	1039	71381	360910	129	31393	7684	11	755	759	3.7	0.9	344	89
OK220707-1Q-4	43	25	22789	689	66578	361938	99	34157	5707	13	579	575	1.3	1.0	305	71
OK220707-1Q-5	44	26	23561	649	68523	363948	92	33141	5845	14	592	563	1.0	0.6	322	70
WHAK432H-1	46	14	30064	964	70551	-	75	28808	8579	8.4	970	963	2.1	0.5	414	111
WHAK432H-2	43	15	27390	978	71107	-	91	28263	8746	8.4	959	946	2.9	0.8	431	112
WHAK432H-3	45	15	27296	938	69984	-	89	29177	8265	8.5	915	942	2.4	1.0	427	110
WHAK432H-4	53	23	27784	485	65775	-	51	32060	5372	9.7	527	522	0.3	0.5	325	80
WHAK432H-5	53	24	27139	449	65969	-	47	32790	5023	9.5	489	505	0.3	0.7	314	79
WHAK432I-1	37	19	23348	993	63786	-	173	30734	8184	13	888	895	4.3	2.6	392	90
WHAK432I-1-A	-	-	-	-	-	-	-	-	-	-	-	-	-	-	-	-
WHAK432I-2	40	18	27745	983	64777	-	119	28576	8047	14	893	918	4.3	2.8	423	94
WHAK432I-2-A	-	-	-	-	-	-	-	-	-	-	-	-	-	-	-	-
WHAK432I-3	40	17	26571	990	63419	-	88	29627	8787	12	876	886	2.9	2.9	403	89
WHAK432I-4	38	16	24581	948	64455	-	108	30560	8136	12	815	863	3.1	7.9	373	89
WHAK432I-5	51	24	26445	463	67280	-	51	33427	5017	10	523	502	0.3	0.6	323	79
WHAK432I-5-A	-	-	-	-	-	-	-	-	-	-	-	-	-	-	-	-

WHAK432J-1	43	15	25844	880	67229	-	94	29914	7636	8.0	886	900	3.3	0.9	381	103
WHAK432J-2	37	14	22432	1095	74453	-	148	30056	8743	8.9	999	1002	6.4	1.4	444	121
WHAK432J-3	37	15	23421	946	70818	-	145	30338	7732	8.3	905	926	3.6	1.5	375	105
WHAK432J-4	39	14	25796	1007	67689	-	123	28691	8224	8.1	917	932	3.5	0.8	404	110
WHAK432J-5	48	16	25611	728	66750	-	63	29920	6774	7.6	766	764	1.3	0.5	360	93
OK240707-1A-1	-	-	-	-	-	-	-	-	-	-	-	-	-	-	-	-
OK240707-1A-2	-	-	-	-	-	-	-	-	-	-	-	-	-	-	-	-
OK240707-1A-3	-	-	-	-	-	-	-	-	-	-	-	-	-	-	-	-
OK240707-1A-4	-	-	-	-	-	-	-	-	-	-	-	-	-	-	-	-
OK240707-1A-5	59	31	26740	387	67629	363948	51	36020	4635	12	424	426	0.9	0.2	373	58
Ōtarawairere-1	-	-	-	-	-	-	-	-	-	-	-	-	-	-	-	-
Ōtarawairere-2	-	-	-	-	-	-	-	-	-	-	-	-	-	-	-	-
Ōtarawairere-3	-	-	-	-	-	-	-	-	-	-	-	-	-	-	-	-
Ōtarawairere-4	-	-	-	-	-	-	-	-	-	-	-	-	-	-	-	-
Ōtarawairere-5	-	-	-	-	-	-	-	-	-	-	-	-	-	-	-	-
OK240707-1C-1	33	37	19220	913	64146	363855	79	43560	5219	12	914	868	6.0	3.9	256	92
OK240707-1C-2	46	31	20440	796	67344	363200	69	41086	5301	12	803	816	3.1	1.7	268	72
OK240707-1C-3	42	31	20886	658	60589	362312	68	38554	5211	12	821	810	2.8	2.2	247	74
OK240707-1C-4	46	31	23592	829	59951	359274	84	36955	5267	13	1409	1280	19	3.0	275	96
OK240707-1C-5	43	32	18978	576	61359	362219	53	38810	5214	8.9	533	532	1.1	0.5	366	62
OK240707-1D-1	39	27	24770	609	61914	362079	57	39560	5725	10	760	785	3.9	1.2	241	60
OK240707-1D-2	50	32	19282	264	62442	359134	41	44521	3957	10	352	392	2.4	1.4	393	52
OK240707-1D-3	43	26	18488	662	62087	359601	52	40560	5175	11	768	801	4.9	2.0	250	66

OK240707-1E-2	60	40	22229	1119	72017	362312	92	40399	3787	12	670	684	13	2.8	428	129
OK240707-1E-5-B	-	-	-	-	-	-	-	-	-	-	-	-	-	-	-	-
OK240707-1F-1	52	30	20696	791	62710	363154	134	33898	3401	10	443	453	33	3.0	395	102
OK240707-1F-2	35	39	16102	375	67412	363013	42	43551	3479	8.6	314	322	0.9	1.7	405	49
OK240707-1F-3	32	36	17281	331	62100	362453	49	44854	3538	9.0	340	362	1.7	1.5	410	56
OK240707-1F-4	38	27	17597	774	65610	363341	139	30201	5007	13	709	766	6.7	4.6	267	72
OK240707-1F-5	18	40	14221	402	63217	363247	68	45384	3209	9.7	428	417	4.7	2.3	379	63
OK240707-1F-6	43	37	16865	347	65188	362172	49	44349	3840	8.8	368	430	2.5	1.8	394	56
OK240707-1J-1	41	19	22962	1215	69968	361377	134	29940	8562	10	1019	1093	6.4	1.6	317	81
OK240707-1J-2	46	26	22198	509	66847	361611	69	36174	4998	10	512	510	1.0	1.1	321	57
OK240707-1J-4	57	27	24831	487	68675	360863	56	32346	5073	11	516	483	0.4	1.1	300	53
OK240707-1L-1	37	28	19580	772	67513	363528	125	32994	4945	12	558	642	14	1.4	299	118
OK240707-1L-2	42	27	24748	504	62845	362780	67	34912	5576	11	536	529	4.5	0.6	298	81
OK240707-1L-3	48	25	24204	562	64919	364743	73	33492	5118	12	501	495	11	0.7	290	95
OK240707-1L-3-A	-	-	-	-	-	-	-	-	-	-	-	-	-	-	-	-
OK240707-1L-4	38	28	21221	828	65134	362593	120	31880	4944	13	596	584	25	1.5	287	154
OK240707-1L-5	-	-	-	-	-	-	-	-	-	-	-	-	-	-	-	-

Table 2.9: Lapilli glass trace element mean compositions (Co59-La139)

Lapilli-subgroup	Co59	Ni60	Cu63	Zn64	Ga69	Ge74	Se77	Rb85	Sr88	Y89	Zr90	Nb93	Cs133	Ba137	Ba138	La139
OK220707-1B-1	0.6	0.4	2.2	20	25	1.8	1.0	126	74	19	79	4.8	4.8	1083	1046	23
OK220707-1B-2	0.6	0.4	2.5	22	25	1.9	0.9	118	72	19	77	5.0	4.8	1002	1008	21
OK220707-1B-3	0.7	0.9	4.0	14	24	2.1	1.1	115	69	20	83	5.0	5.2	994	911	23
OK220707-1B-4	0.6	0.4	3.8	19	24	2.0	1.5	115	66	19	78	4.6	4.7	950	930	22
OK220707-1B-5	0.7	1.6	3.5	20	25	1.8	0.7	108	65	22	89	4.6	3.9	836	881	23
OK220707-1C-1	0.9	1.1	7.0	17	26	1.8	0.7	116	68	18	87	4.5	4.6	923	933	22
OK220707-1C-1-A	-	-	-	-	-	-	-	-	-	-	-	-	-	-	-	-
OK220707-1C-2	0.6	0.3	2.5	23	77	1.8	0.6	123	66	16	77	4.7	4.9	974	1004	21
OK220707-1C-3	0.6	0.2	2.4	20	78	1.7	0.6	123	70	17	80	4.9	4.7	995	987	21
OK220707-1C-4	0.6	0.3	2.8	23	74	2.0	1.2	122	67	17	82	4.9	4.8	963	970	22
OK220707-1C-5	0.6	0.2	1.9	23	75	1.9	0.6	121	67	17	78	4.8	4.9	999	1020	21
WHAK432A-1	1.6	2.1	13	32	29	2.1	2.3	120	71	25	100	5.2	4.6	939	930	25
WHAK432A-2	-	-	-	-	-	-	-	-	-	-	-	-	-	-	-	-
WHAK432A-3	1.1	0.7	5.0	27	26	2.1	4.1	122	67	21	85	4.9	4.4	942	940	22
WHAK432A-4	1.2	1.9	6.3	27	27	2.3	0.8	120	66	22	92	4.8	4.8	927	903	22
WHAK432A-5	0.8	0.1	7.2	31	26	2.1	1.6	130	70	19	91	4.9	5.2	1034	998	25
WHAK432A-6	2.2	2.9	12	30	28	2.4	4.5	126	70	25	103	5.6	4.9	942	941	26
WHAK432B-1	1.2	0.3	5.2	36	28	2.1	1.7	128	73	20	84	4.9	5.2	1006	1004	22
WHAK432B-2	0.8	0.2	4.5	30	25	1.8	0.8	127	70	18	81	5.0	5.1	1053	1052	23
WHAK432B-3	0.8	0.3	3.1	32	26	1.7	0.2	128	70	18	79	5.0	5.1	1033	1026	21
WHAK432B-4	0.7	0.2	5.3	32	26	1.9	1.2	129	72	18	79	5.1	5.2	1043	1065	22

WHAK432B-5	0.8	0.3	3.4	35	26	1.8	1.7	131	70	18	80	5.0	5.1	984	1001	21
OK220707-1E-1	0.6	0.3	3.3	25	26	1.9	0.5	116	59	29	160	7.7	4.5	680	692	24
OK220707-1E-1-A	-	-	-	-	-	-	-	-	-	-	-	-	-	-	-	-
WHAK432C-1	-	-	-	-	-	-	-	-	-	-	-	-	-	-	-	-
WHAK432C-2	0.9	1.5	4.4	21	27	2.1	7.8	114	60	19	87	4.8	4.7	876	857	23
WHAK432C-3	1.3	3.4	11	24	35	2.5	19	100	58	24	107	4.4	4.0	680	676	21
WHAK432C-4	0.6	0.4	1.6	30	21	1.3	1.5	124	66	17	74	4.7	5.1	1009	1010	21
WHAK432C-5	0.6	1.4	4.0	22	23	1.9	5.5	123	65	19	80	4.9	5.1	945	939	22
OK220707-1F-1	0.5	1.3	3.7	29	76	2.2	0.2	123	68	20	88	5.2	4.7	1019	1053	23
OK220707-1F-2	0.8	2.7	3.3	28	31	2.2	1.8	125	71	19	82	4.7	4.7	933	988	25
OK220707-1F-3	0.7	0.8	4.4	25	27	2.1	0.7	129	74	19	79	4.8	4.8	1018	1048	24
OK220707-1F-4	0.9	0.6	2.7	18	27	2.1	3.4	137	74	19	81	5.0	5.1	1080	1105	24
OK220707-1F-5	0.5	0.5	2.0	24	27	1.8	2.0	127	74	19	83	4.8	4.8	1051	1051	23
OK220707-1F-6	-	-	-	-	-	-	-	-	-	-	-	-	-	-	-	-
OK220707-1G-1	1.0	0.5	9.2	13	25	2.0	3.3	164	60	17	105	5.9	6.5	775	779	21
OK220707-1G-2	1.0	2.0	7.1	31	27	2.1	1.7	165	49	21	123	6.2	6.7	822	814	28
OK220707-1G-3	1.1	0.9	4.0	19	26	2.0	2.8	177	53	19	111	6.0	6.7	816	855	25
OK220707-1G-4	1.0	1.4	8.2	23	26	1.7	1.0	170	51	20	114	6.4	7.1	842	862	26
OK220707-1G-4-A	-	-	-	-	-	-	-	-	-	-	-	-	-	-	-	-
OK220707-1G-5	0.9	0.5	7.8	27	26	1.6	1.5	168	58	22	121	6.9	7.3	897	885	27
OK220707-1G-6	2.2	3.4	7.3	35	26	2.1	1.3	172	56	20	119	6.5	6.9	906	879	29
WHAK432L-1	0.6	3.0	5.9	17	22	2.0	9.1	175	49	18	109	6.7	6.8	820	828	23
WHAK432L-2	0.5	2.0	5.6	17	17	2.3	6.2	205	21	22	66	7.1	9.3	298	304	29

WHAK432L-3	0.5	0.9	3.6	27	20	1.3	3.2	168	49	18	104	6.2	7.3	820	826	25
WHAK432L-4	0.4	1.2	3.7	20	20	1.4	3.6	166	53	15	79	5.6	7.2	792	778	22
WHAK432L-5	1.0	1.2	2.7	16	22	1.5	4.9	170	50	18	108	6.4	7.2	842	853	25
OK220707-1I-1	0.8	1.0	5.3	24	27	1.5	3.7	162	47	20	110	6.8	7.2	794	818	28
OK220707-1I-2	1.1	1.2	5.7	26	24	1.6	0.3	152	49	20	114	6.6	6.4	822	874	31
OK220707-1I-3	0.6	0.2	2.6	18	25	1.5	0.9	154	43	17	91	6.4	6.8	885	880	25
OK220707-1I-4	0.4	8.4	93	16	20	1.9	0.7	179	28	22	67	6.6	8.6	677	631	32
OK220707-1I-5	0.2	1.5	2.8	21	23	1.8	1.1	176	31	19	73	6.4	7.6	729	747	29
WHAK432D-1	0.3	5.3	2.5	19	19	1.7	5.1	183	31	21	74	6.6	8.1	611	619	30
WHAK432D-2	0.3	2.9	2.7	17	17	1.8	10	183	21	21	66	7.1	8.8	408	393	30
WHAK432D-3	0.7	4.6	0.5	16	20	1.8	9.7	181	48	19	102	6.7	7.3	808	787	26
WHAK432D-4	0.4	3.0	2.0	20	16	1.8	5.9	187	21	22	70	7.2	8.3	390	393	31
WHAK432D-5	0.2	7.3	2.0	17	17	1.7	10	196	21	22	67	7.1	8.6	360	358	31
WHAK432E-1	0.7	1.2	5.0	26	28	2.1	1.6	173	47	20	116	6.8	7.0	780	790	33
WHAK432E-2	0.3	0.1	3.0	18	20	1.7	2.7	202	22	24	80	7.9	8.6	382	394	36
WHAK432E-3	0.5	1.2	7.5	37	22	2.4	2.9	205	25	26	80	8.4	8.6	425	430	41
WHAK432E-4	0.8	1.0	6.7	28	26	2.0	0.7	164	52	19	119	6.7	7.1	836	830	28
WHAK432E-5	0.4	0.7	6.5	24	21	2.0	2.3	200	26	26	79	8.0	8.8	436	429	44
OK220707-1L-1	0.7	1.4	6.0	11	23	1.7	1.1	163	50	18	111	6.0	6.4	782	800	25
OK220707-1L-2	0.7	0.5	4.4	19	24	1.8	1.3	174	53	20	119	6.6	7.0	879	875	27
OK220707-1L-3	1.3	2.7	6.5	22	25	2.1	2.7	171	53	18	117	6.3	6.6	842	841	25
OK220707-1L-4	0.5	0.4	3.3	11	17	1.9	1.7	190	22	22	69	7.0	8.3	379	383	29
OK220707-1L-5	0.4	0.3	2.3	23	18	2.1	1.5	193	23	24	77	8.1	8.4	399	395	33

WHAK432F-1	0.6	6.3	5.4	16	21	1.5	7.4	173	48	20	118	7.3	6.8	801	795	26
WHAK432F-2	1.2	4.2	3.8	20	22	1.4	18	177	50	19	116	6.5	7.2	893	872	25
WHAK432F-3	0.3	3.3	3.9	18	17	1.6	2.6	196	23	22	71	7.3	8.8	378	368	29
WHAK432F-4	0.9	19	5.4	26	23	2.3	15	175	48	19	129	7.1	6.9	802	785	25
WHAK432F-5	0.9	14	1.2	17	20	2.8	14	177	48	20	111	6.6	6.9	817	830	26
OK220707-1N-1	0.7	0.2	4.5	26	25	1.9	1.3	181	51	21	124	7.6	7.5	910	882	29
OK220707-1N-2	0.4	1.7	6.1	24	26	2.3	2.9	164	37	19	88	6.9	7.2	869	892	30
OK220707-1N-3	0.8	1.5	5.6	17	24	2.0	2.2	172	50	19	114	6.8	6.9	895	883	25
OK220707-1N-4	0.6	1.1	7.8	20	24	2.3	0.8	182	50	21	118	6.6	7.5	868	862	28
OK220707-1N-5	0.6	2.2	6.2	30	26	2.6	1.1	160	53	20	126	6.6	6.5	816	773	26
OK220707-1N-6	0.9	0.6	6.4	23	25	1.8	2.0	170	54	21	123	6.8	7.4	845	855	28
WHAK432G-1	0.3	0.4	3.1	27	17	2.3	1.4	242	8.0	30	80	10	12	73	76	26
WHAK432G-2	0.7	0.7	3.6	35	25	1.9	1.3	134	76	20	109	6.5	5.7	798	801	24
WHAK432G-3	1.0	1.8	5.6	37	22	3.2	1.7	218	11	27	98	10	11	94	92	24
WHAK432G-4	0.8	0.4	6.1	29	25	1.8	1.1	170	53	18	113	6.8	7.2	864	863	25
WHAK432G-5	1.4	2.1	7.3	43	31	2.8	1.5	157	46	18	136	8.5	6.3	727	762	23
OK220707-1O-1	0.4	1.2	3.3	22	16	2.4	1.5	230	8.1	28	74	10	11	79	77	21
OK220707-1O-2	1.2	3.0	4.1	36	20	3.0	1.7	217	10	27	82	11	12	72	73	21
OK220707-1O-3	1.2	3.7	6.3	31	22	3.4	1.6	183	20	22	87	11	8.2	209	216	28
OK220707-1O-4	1.1	5.0	7.5	46	22	3.7	1.9	187	20	22	92	11	8.5	202	213	27
OK220707-1O-5	0.4	0.6	2.3	25	17	2.1	0.6	197	17	25	74	8.1	9.4	222	209	28
OK220707-1O-6	0.8	2.9	6.7	35	20	3.1	1.8	201	20	23	94	10	9.0	207	204	30
OK220707-1O-7	0.5	0.8	3.0	25	17	2.2	0.8	191	18	25	74	8.4	9.6	223	229	31

OK220707-1P-1	0.5	0.1	2.3	35	23	1.6	0.9	133	63	20	81	6.4	5.8	828	807	23
OK220707-1P-2	0.4	0.1	1.7	40	23	1.4	1.2	122	61	19	75	5.8	5.2	753	760	22
OK220707-1P-3	0.5	0.2	3.4	38	23	1.7	0.7	125	59	20	78	6.2	5.6	792	777	22
OK220707-1P-5	0.5	0.5	3.6	29	24	1.6	0.9	136	62	21	80	6.3	5.8	807	800	24
OK220707-1P-6	0.4	0.2	2.8	65	22	1.6	0.6	131	62	20	79	6.1	5.8	862	799	23
OK220707-1Q-1	0.6	0.3	2.5	19	21	1.5	1.2	121	81	17	101	5.7	4.6	739	700	21
OK220707-1Q-2	0.5	0.1	2.0	31	23	1.6	1.2	129	65	22	84	6.1	5.9	857	853	25
OK220707-1Q-3	0.7	0.7	4.5	18	22	1.4	1.0	119	91	18	113	6.0	4.7	780	726	23
OK220707-1Q-4	0.4	0.2	3.0	20	26	1.7	1.5	134	64	22	85	6.1	5.6	796	786	24
OK220707-1Q-5	0.7	0.5	3.0	22	26	1.8	0.8	131	64	22	88	6.4	5.6	800	810	25
WHAK432H-1	0.8	0.2	2.0	45	69	1.6	0.7	114	94	21	143	7.9	4.2	734	737	24
WHAK432H-2	1.0	0.2	7.6	40	69	1.4	0.9	109	93	22	146	7.8	4.0	711	720	25
WHAK432H-3	0.9	0.2	6.1	38	66	1.5	0.8	112	90	21	137	7.5	4.2	720	715	24
WHAK432H-4	0.4	0.1	2.7	35	72	1.6	0.5	129	60	21	83	6.8	5.7	786	773	23
WHAK432H-5	0.3	0.2	3.8	34	71	1.7	0.4	134	51	21	76	6.8	5.8	775	776	23
WHAK432I-1	1.4	4.8	6.2	28	20	1.8	3.7	118	93	20	131	6.8	4.3	701	693	24
WHAK432I-1-A	-	-	-	-	-	-	-	-	-	-	-	-	-	-	-	-
WHAK432I-2	1.6	5.7	5.4	36	21	1.3	11	109	95	20	130	6.9	4.2	686	689	24
WHAK432I-2-A	-	-	-	-	-	-	-	-	-	-	-	-	-	-	-	-
WHAK432I-3	1.0	3.2	4.0	30	20	1.4	5.8	116	94	21	138	7.0	4.1	720	712	24
WHAK432I-4	0.9	4.1	4.3	25	22	1.3	7.6	117	90	20	127	6.4	4.6	722	725	24
WHAK432I-5	0.4	0.3	4.4	35	73	1.8	0.7	134	52	21	78	7.1	5.8	804	802	24
WHAK432I-5-A	-	-	-	-	-	-	-	-	-	-	-	-	-	-	-	-

WHAK432J-1	0.7	0.2	5.1	35	65	1.5	0.6	116	84	19	124	7.4	4.3	705	710	23
WHAK432J-2	1.5	0.2	23	40	72	1.5	0.5	111	99	23	157	8.0	4.1	728	728	25
WHAK432J-3	0.8	0.2	4.7	32	65	1.6	0.3	119	85	20	126	7.5	4.3	706	694	23
WHAK432J-4	0.9	0.2	8.1	37	61	1.5	0.8	110	89	20	134	7.6	4.2	659	671	22
WHAK432J-5	0.5	0.2	2.6	39	63	1.5	0.4	115	73	20	113	7.2	4.4	712	702	23
OK240707-1A-1	-	-	-	-	-	-	-	-	-	-	-	-	-	-	-	-
OK240707-1A-2	-	-	-	-	-	-	-	-	-	-	-	-	-	-	-	-
OK240707-1A-3	-	-	-	-	-	-	-	-	-	-	-	-	-	-	-	-
OK240707-1A-4	-	-	-	-	-	-	-	-	-	-	-	-	-	-	-	-
OK240707-1A-5	0.3	0.2	2.4	25	50	1.7	1.0	161	36	18	59	7.4	7.3	683	722	25
Ōtarawairere-1	-	-	-	-	-	-	-	-	-	-	-	-	-	-	-	-
Ōtarawairere-2	-	-	-	-	-	-	-	-	-	-	-	-	-	-	-	-
Ōtarawairere-3	-	-	-	-	-	-	-	-	-	-	-	-	-	-	-	-
Ōtarawairere-4	-	-	-	-	-	-	-	-	-	-	-	-	-	-	-	-
Ōtarawairere-5	-	-	-	-	-	-	-	-	-	-	-	-	-	-	-	-
OK240707-1C-1	1.3	0.5	7.9	15	24	1.7	3.3	178	47	19	109	6.5	8.3	818	815	24
OK240707-1C-2	1.1	0.1	5.6	16	25	1.5	1.6	175	49	19	111	6.6	7.0	776	742	25
OK240707-1C-3	0.9	0.1	8.0	19	23	1.5	0.1	171	45	18	107	6.0	7.0	842	810	24
OK240707-1C-4	1.3	0.3	9.7	27	23	1.7	0.2	163	46	19	117	7.3	7.0	816	826	24
OK240707-1C-5	0.5	0.2	2.4	18	20	1.6	1.2	158	53	15	75	5.5	6.8	678	655	22
OK240707-1D-1	0.9	0.2	3.0	19	25	1.8	1.4	162	48	19	109	6.4	7.1	792	897	26
OK240707-1D-2	0.5	0.4	1.8	21	17	1.9	2.1	180	21	22	70	6.7	8.2	361	362	29
OK240707-1D-3	0.8	0.5	3.6	21	25	1.8	2.1	171	50	20	104	6.1	7.3	840	780	25

OK240707-1E-2	7.8	8.1	3.8	30	19	2.6	1.1	185	12	25	83	8.2	9.0	138	135	26
OK240707-1E-5-B	-	-	-	-	-	-	-	-	-	-	-	-	-	-	-	-
OK240707-1F-1	0.7	1.7	6.9	20	15	1.8	5.4	173	17	25	64	7.4	8.5	189	186	29
OK240707-1F-2	0.6	2.0	2.4	11	17	2.4	3.0	210	13	26	66	8.3	11	134	145	27
OK240707-1F-3	0.6	2.2	2.6	15	17	1.9	1.2	200	18	24	66	7.3	9.4	217	216	29
OK240707-1F-4	1.1	1.8	7.9	27	23	1.5	1.3	132	57	20	88	6.1	5.6	649	682	24
OK240707-1F-5	0.6	1.7	3.2	14	17	2.0	3.0	212	17	23	66	7.8	9.4	210	206	28
OK240707-1F-6	0.5	1.5	3.3	17	17	1.7	0.9	187	23	21	64	7.2	8.2	332	334	26
OK240707-1J-1	1.2	1.1	3.4	23	24	1.6	1.3	114	98	15	140	5.8	4.8	784	721	22
OK240707-1J-2	0.7	0.4	2.1	19	24	1.6	2.2	145	52	22	82	6.1	6.5	854	836	25
OK240707-1J-4	0.5	0.3	2.5	28	24	1.6	1.0	139	55	21	82	6.2	6.3	848	853	26
OK240707-1L-1	0.9	0.7	8.0	25	24	1.4	2.6	133	53	20	84	6.4	6.1	802	805	24
OK240707-1L-2	0.6	0.2	2.9	28	22	1.7	3.1	136	55	20	78	6.0	6.0	823	802	25
OK240707-1L-3	0.9	0.7	3.0	30	23	1.7	1.8	137	57	22	81	6.2	5.4	841	816	25
OK240707-1L-3-A	-	-	-	-	-	-	-	-	-	-	-	-	-	-	-	-
OK240707-1L-4	1.4	1.3	4.6	40	23	1.7	1.4	135	52	20	81	6.0	5.4	741	733	24
OK240707-1L-5	-	-	-	-	-	-	-	-	-	-	-	-	-	-	-	-

Table 2.10: Lapilli glass trace element mean compositions (Ce140-Ta181)

Lapilli-subgroup	Ce140	Pr141	Nd143	Sm147	Eu151	Gd157	Tb159	Gd160	Dy163	Ho165	Er166	Tm169	Yb173	Lu175	Hf179	Ta181
OK220707-1B-1	40	4.2	16	3.2	0.5	2.8	0.5	2.7	3.0	0.6	1.9	0.3	2.3	0.4	2.9	0.4
OK220707-1B-2	40	4.0	15	3.2	0.4	2.8	0.4	2.9	2.8	0.6	2.0	0.3	2.2	0.4	2.8	0.4
OK220707-1B-3	35	4.3	17	3.5	0.5	3.1	0.6	3.1	3.2	0.7	2.0	0.3	2.6	0.4	3.0	0.5
OK220707-1B-4	35	3.9	15	3.2	0.4	2.7	0.5	2.8	2.8	0.6	2.0	0.3	2.4	0.4	2.7	0.4
OK220707-1B-5	32	4.2	17	3.0	0.5	3.3	0.5	3.0	3.0	0.7	2.0	0.3	2.7	0.4	3.0	0.5
OK220707-1C-1	37	4.1	17	3.5	0.4	3.0	0.5	2.5	3.1	0.6	1.8	0.3	2.2	0.4	2.9	0.5
OK220707-1C-1-A	-	-	-	-	-	-	-	-	-	-	-	-	-	-	-	-
OK220707-1C-2	37	3.9	15	2.9	0.4	3.2	0.4	2.3	2.6	0.6	1.7	0.3	2.0	0.3	2.4	0.4
OK220707-1C-3	37	4.0	15	3.0	0.4	3.1	0.5	2.5	2.8	0.6	1.8	0.3	2.3	0.3	2.7	0.4
OK220707-1C-4	37	4.0	15	3.1	0.4	3.0	0.4	2.4	2.7	0.6	1.8	0.3	2.2	0.3	2.5	0.4
OK220707-1C-5	39	4.1	15	2.9	0.4	2.9	0.4	2.6	2.9	0.6	1.8	0.3	2.2	0.3	2.6	0.4
WHAK432A-1	41	4.6	20	3.7	0.6	4.0	0.6	3.8	3.7	0.9	2.4	0.4	2.9	0.5	3.2	0.6
WHAK432A-2	-	-	-	-	-	-	-	-	-	-	-	-	-	-	-	-
WHAK432A-3	37	4.3	17	3.1	0.5	3.1	0.5	3.4	3.1	0.7	2.2	0.3	2.4	0.4	3.3	0.5
WHAK432A-4	37	4.1	16	3.2	0.5	3.1	0.5	2.8	3.4	0.7	2.0	0.3	2.6	0.4	3.2	0.5
WHAK432A-5	42	5.6	16	3.4	0.5	2.7	0.5	2.6	3.2	0.7	1.9	0.3	2.6	0.4	3.0	0.5
WHAK432A-6	43	5.6	20	3.6	0.5	3.8	0.6	3.7	3.9	0.9	2.6	0.5	2.9	0.5	3.4	0.6
WHAK432B-1	39	4.3	17	3.4	0.4	3.0	0.5	2.8	3.3	0.7	2.0	0.3	2.4	0.4	2.8	0.5
WHAK432B-2	41	4.3	16	3.1	0.4	2.5	0.4	2.7	3.0	0.6	1.8	0.3	2.3	0.4	2.7	0.5
WHAK432B-3	40	4.1	15	3.1	0.4	2.7	0.5	2.5	2.7	0.6	1.9	0.3	2.3	0.4	2.5	0.4
WHAK432B-4	41	4.3	16	3.1	0.4	2.7	0.5	2.6	3.0	0.6	1.9	0.3	2.3	0.3	2.8	0.4

WHAK432B-5	39	4.2	15	3.0	0.4	2.7	0.4	2.7	3.0	0.6	1.8	0.3	2.2	0.3	2.7	0.4
OK220707-1E-1	48	5.4	24	4.4	0.8	3.9	0.7	4.4	4.4	1.0	2.7	0.5	3.2	0.5	4.4	0.6
OK220707-1E-1-A	-	-	-	-	-	-	-	-	-	-	-	-	-	-	-	-
WHAK432C-1	-	-	-	-	-	-	-	-	-	-	-	-	-	-	-	-
WHAK432C-2	38	4.6	16	3.2	0.4	3.6	0.5	3.1	3.1	0.7	2.1	0.3	2.7	0.4	3.2	0.6
WHAK432C-3	33	4.7	17	3.6	0.6	3.1	0.6	3.4	4.1	0.8	2.5	0.4	3.0	0.5	3.8	0.8
WHAK432C-4	39	4.0	15	2.8	0.4	2.7	0.4	2.2	2.7	0.6	1.8	0.3	2.2	0.3	2.6	0.4
WHAK432C-5	38	4.1	15	2.9	0.4	2.6	0.5	2.8	3.4	0.6	1.7	0.3	2.2	0.4	2.8	0.5
OK220707-1F-1	38	4.7	17	3.1	0.5	3.3	0.5	2.7	3.0	0.7	1.9	0.3	2.6	0.4	3.0	0.5
OK220707-1F-2	42	4.3	17	3.2	0.5	2.8	0.5	3.1	3.2	0.7	1.9	0.3	2.3	0.4	2.7	0.5
OK220707-1F-3	42	4.4	16	3.2	0.4	2.9	0.5	2.9	3.0	0.7	1.8	0.3	2.3	0.3	2.6	0.4
OK220707-1F-4	43	4.5	17	3.4	0.4	2.9	0.5	2.9	3.1	0.7	1.9	0.3	2.5	0.3	2.6	0.4
OK220707-1F-5	43	4.5	16	3.1	0.4	2.6	0.5	2.9	3.1	0.7	2.0	0.3	2.5	0.4	2.9	0.4
OK220707-1F-6	-	-	-	-	-	-	-	-	-	-	-	-	-	-	-	-
OK220707-1G-1	59	3.8	16	2.8	0.4	2.6	0.4	2.4	2.8	0.5	1.7	0.3	1.9	0.3	3.2	0.5
OK220707-1G-2	49	4.8	18	3.3	0.4	3.0	0.5	3.1	3.2	0.7	2.1	0.3	2.4	0.4	3.7	0.6
OK220707-1G-3	58	4.3	18	3.2	0.4	3.0	0.5	2.7	2.9	0.6	1.7	0.3	2.0	0.3	3.0	0.5
OK220707-1G-4	50	4.7	17	3.3	0.4	2.9	0.5	3.0	3.0	0.7	1.8	0.3	2.3	0.4	3.4	0.6
OK220707-1G-4-A	-	-	-	-	-	-	-	-	-	-	-	-	-	-	-	-
OK220707-1G-5	53	5.1	18	3.9	0.4	3.1	0.6	3.3	3.3	0.8	2.1	0.4	2.8	0.4	3.7	0.6
OK220707-1G-6	57	5.2	18	3.5	0.4	3.2	0.6	3.2	3.3	0.7	2.2	0.3	2.4	0.3	3.6	0.6
WHAK432L-1	44	4.3	16	3.6	0.4	2.9	0.5	2.5	3.0	0.6	1.7	0.2	2.0	0.3	3.3	0.6
WHAK432L-2	56	5.8	20	3.7	0.2	2.9	0.5	3.2	3.4	0.7	2.1	0.3	2.6	0.4	2.4	0.7

WHAK432L-3	45	4.5	16	3.4	0.3	2.8	0.5	2.5	2.9	0.6	2.0	0.3	2.2	0.3	3.3	0.6
WHAK432L-4	43	4.3	16	2.5	0.4	2.4	0.4	2.2	2.4	0.5	1.4	0.2	2.0	0.3	2.6	0.5
WHAK432L-5	45	4.8	18	2.7	0.4	3.8	0.5	2.8	2.9	0.7	1.9	0.3	2.2	0.4	3.3	0.6
OK220707-1I-1	49	5.1	18	3.9	0.4	3.1	0.5	2.8	3.3	0.6	2.0	0.3	2.4	0.3	2.9	0.6
OK220707-1I-2	58	5.9	22	4.4	0.4	3.3	0.6	3.3	3.4	0.7	2.1	0.3	2.4	0.3	3.3	0.6
OK220707-1I-3	46	4.9	17	3.2	0.3	2.7	0.5	2.8	3.0	0.6	1.7	0.3	2.3	0.3	3.1	0.5
OK220707-1I-4	58	6.4	20	4.2	0.3	3.1	0.5	3.0	3.6	0.7	2.2	0.4	2.4	0.4	2.0	0.7
OK220707-1I-5	51	5.2	20	3.4	0.4	3.1	0.5	2.8	3.3	0.7	1.9	0.3	2.2	0.3	2.7	0.6
WHAK432D-1	54	5.4	20	3.8	0.3	2.9	0.5	2.9	3.3	0.7	1.9	0.3	2.6	0.4	2.8	0.7
WHAK432D-2	54	5.5	21	3.7	0.2	3.0	0.5	3.1	3.8	0.8	2.4	0.3	3.0	0.4	2.9	0.7
WHAK432D-3	48	5.0	14	3.9	0.4	3.2	0.5	2.8	2.8	0.7	1.9	0.3	2.0	0.3	3.0	0.5
WHAK432D-4	57	5.7	21	3.7	0.3	3.1	0.6	3.2	3.6	0.8	2.2	0.4	2.6	0.4	2.8	0.7
WHAK432D-5	56	5.9	21	4.2	0.2	3.2	0.7	3.1	3.5	0.7	1.9	0.3	2.7	0.4	2.5	0.7
WHAK432E-1	57	5.9	22	3.9	0.5	3.4	0.5	3.1	3.3	0.7	1.9	0.3	2.3	0.4	3.4	0.6
WHAK432E-2	60	6.3	24	4.3	0.2	3.5	0.7	3.3	4.3	0.9	2.2	0.4	2.8	0.4	2.8	0.8
WHAK432E-3	69	6.9	24	4.9	0.3	3.7	0.7	4.0	4.1	0.9	2.5	0.4	2.9	0.4	2.8	0.8
WHAK432E-4	46	4.8	18	3.3	0.4	2.8	0.5	3.0	3.2	0.7	2.0	0.3	2.3	0.3	3.6	0.6
WHAK432E-5	64	7.8	26	4.7	0.4	3.8	0.7	4.2	4.0	0.8	2.4	0.4	2.8	0.4	2.6	0.7
OK220707-1L-1	46	4.2	17	3.7	0.4	2.9	0.5	2.7	3.1	0.7	1.8	0.3	2.2	0.3	3.3	0.5
OK220707-1L-2	47	4.8	17	3.3	0.4	2.9	0.5	2.7	3.1	0.7	2.1	0.3	2.3	0.4	3.5	0.6
OK220707-1L-3	44	4.6	17	3.0	0.3	2.5	0.5	2.4	3.0	0.6	1.8	0.3	1.9	0.3	3.7	0.6
OK220707-1L-4	54	5.4	21	3.5	0.2	2.7	0.6	2.9	3.2	0.8	2.2	0.3	2.8	0.4	2.6	0.7
OK220707-1L-5	60	6.0	22	4.1	0.3	3.3	0.6	3.4	3.9	0.8	2.3	0.4	2.8	0.4	2.9	0.8

WHAK432F-1	48	5.1	17	3.1	0.4	2.9	0.5	2.8	3.2	0.7	2.1	0.3	2.3	0.3	3.4	0.6
WHAK432F-2	46	4.9	18	3.3	0.4	2.8	0.4	2.9	2.8	0.6	1.8	0.4	2.6	0.4	3.2	0.6
WHAK432F-3	55	5.6	21	3.3	0.3	3.3	0.6	3.1	3.4	0.7	2.3	0.3	2.6	0.4	2.9	0.7
WHAK432F-4	44	4.8	16	3.0	0.3	2.9	0.5	2.7	3.0	0.7	1.8	0.3	2.2	0.4	4.4	0.7
WHAK432F-5	46	4.4	17	3.3	0.5	2.6	0.4	2.8	3.0	0.7	1.9	0.3	2.4	0.4	3.6	0.6
OK220707-1N-1	54	5.4	20	4.0	0.5	3.1	0.6	3.3	3.5	0.7	2.3	0.3	2.6	0.4	3.8	0.6
OK220707-1N-2	53	5.0	18	3.5	0.4	2.8	0.5	3.1	3.1	0.7	2.2	0.3	2.4	0.4	3.0	0.7
OK220707-1N-3	47	4.6	18	3.2	0.4	2.9	0.5	2.9	3.0	0.6	2.0	0.3	2.0	0.3	3.4	0.6
OK220707-1N-4	52	5.3	19	3.8	0.4	3.1	0.5	3.2	3.3	0.7	2.2	0.4	2.6	0.3	3.5	0.7
OK220707-1N-5	46	4.5	17	3.4	0.4	2.8	0.5	2.7	3.1	0.7	2.0	0.3	2.2	0.3	3.6	0.5
OK220707-1N-6	51	5.1	19	3.4	0.4	2.9	0.5	3.0	3.4	0.7	2.1	0.3	2.3	0.4	3.7	0.6
WHAK432G-1	49	5.4	21	4.7	0.2	4.3	0.8	4.2	4.8	1.0	3.0	0.5	3.6	0.6	3.3	1.1
WHAK432G-2	44	4.7	18	3.5	0.5	3.0	0.5	3.0	3.1	0.7	2.1	0.3	2.4	0.4	3.6	0.6
WHAK432G-3	44	5.2	19	4.2	0.2	3.6	0.7	3.7	4.2	0.9	2.7	0.4	3.3	0.5	3.8	1.1
WHAK432G-4	45	4.6	16	3.2	0.4	2.7	0.5	2.6	3.0	0.6	1.8	0.3	2.3	0.3	3.4	0.7
WHAK432G-5	41	4.3	16	2.9	0.4	2.4	0.5	2.6	2.7	0.6	1.9	0.3	2.0	0.3	4.1	0.7
OK220707-1O-1	43	4.9	17	4.1	0.1	3.7	0.7	3.8	4.5	0.9	2.8	0.4	3.4	0.5	3.2	1.0
OK220707-1O-2	43	4.7	18	3.9	0.1	3.5	0.7	3.5	4.0	0.9	2.8	0.5	3.2	0.5	3.4	1.1
OK220707-1O-3	50	5.2	20	3.8	0.2	3.1	0.6	3.1	3.4	0.7	2.2	0.4	2.7	0.4	3.8	1.2
OK220707-1O-4	54	5.2	19	3.8	0.2	3.1	0.6	3.2	3.6	0.7	2.4	0.4	2.7	0.4	3.9	1.2
OK220707-1O-5	57	5.6	19	3.9	0.2	3.4	0.6	3.5	3.8	0.8	2.4	0.4	3.0	0.5	3.0	0.8
OK220707-1O-6	56	5.8	20	4.0	0.2	3.0	0.6	3.2	3.7	0.8	2.3	0.4	3.0	0.5	3.9	1.1
OK220707-1O-7	59	6.0	21	4.1	0.2	3.6	0.6	3.5	3.8	0.9	2.5	0.4	3.2	0.5	2.9	0.9

OK220707-1P-1	44	4.8	18	3.6	0.6	3.0	0.5	3.3	3.5	0.7	2.2	0.3	2.3	0.4	3.0	0.5
OK220707-1P-2	45	4.5	17	3.5	0.5	3.1	0.5	2.9	3.1	0.7	1.9	0.3	2.2	0.3	2.7	0.5
OK220707-1P-3	45	4.9	18	3.6	0.5	3.2	0.5	3.1	3.2	0.7	2.0	0.3	2.3	0.4	2.9	0.5
OK220707-1P-5	45	4.7	19	3.9	0.6	3.5	0.6	3.2	3.4	0.7	2.2	0.3	2.5	0.4	3.0	0.5
OK220707-1P-6	47	4.8	18	3.6	0.5	3.3	0.5	3.1	3.4	0.7	2.2	0.3	2.5	0.4	2.9	0.5
OK220707-1Q-1	41	4.0	16	3.0	0.5	2.6	0.4	2.3	2.7	0.6	1.7	0.3	2.0	0.3	3.1	0.5
OK220707-1Q-2	48	5.2	19	3.9	0.6	3.5	0.6	3.3	3.6	0.8	2.3	0.4	2.7	0.4	3.1	0.5
OK220707-1Q-3	43	4.7	17	3.2	0.6	2.7	0.4	2.8	2.9	0.6	1.9	0.3	2.3	0.4	3.6	0.5
OK220707-1Q-4	47	4.8	19	3.7	0.6	3.3	0.5	3.4	3.6	0.8	2.1	0.3	2.5	0.4	2.8	0.5
OK220707-1Q-5	48	4.8	19	3.7	0.6	3.3	0.6	3.3	3.7	0.8	2.3	0.4	2.7	0.4	3.0	0.5
WHAK432H-1	46	4.9	19	3.8	0.7	5.7	0.5	3.2	3.4	0.7	2.1	0.3	2.6	0.4	4.0	0.6
WHAK432H-2	45	4.9	19	3.7	0.7	5.5	0.5	3.2	3.5	0.8	2.3	0.3	2.5	0.4	4.0	0.5
WHAK432H-3	45	4.7	19	3.7	0.7	5.7	0.5	3.0	3.3	0.8	2.2	0.3	2.6	0.4	3.9	0.6
WHAK432H-4	45	4.8	19	3.5	0.5	5.8	0.6	3.3	3.5	0.8	2.2	0.3	2.5	0.4	2.8	0.5
WHAK432H-5	46	4.8	19	3.7	0.5	5.8	0.5	3.3	3.5	0.7	2.2	0.3	2.5	0.4	2.8	0.6
WHAK432I-1	46	4.8	17	3.6	0.7	2.8	0.5	2.8	3.2	0.7	2.1	0.3	2.2	0.4	3.6	0.5
WHAK432I-1-A	-	-	-	-	-	-	-	-	-	-	-	-	-	-	-	-
WHAK432I-2	45	4.8	19	3.5	0.6	2.8	0.5	3.1	3.0	0.7	2.0	0.3	2.5	0.4	3.3	0.5
WHAK432I-2-A	-	-	-	-	-	-	-	-	-	-	-	-	-	-	-	-
WHAK432I-3	47	5.1	19	3.5	0.6	3.2	0.5	3.0	3.5	0.8	2.0	0.3	2.4	0.4	3.9	0.5
WHAK432I-4	46	4.9	17	3.8	0.7	3.1	0.5	2.8	3.1	0.7	2.0	0.3	2.3	0.4	3.8	0.5
WHAK432I-5	47	4.8	19	3.7	0.5	6.0	0.6	3.3	3.7	0.7	2.2	0.3	2.5	0.4	2.8	0.6
WHAK432I-5-A	-	-	-	-	-	-	-	-	-	-	-	-	-	-	-	-

WHAK432J-1	43	4.5	17	3.3	0.6	5.1	0.5	2.8	3.2	0.7	2.0	0.3	2.5	0.3	3.6	0.5
WHAK432J-2	45	5.0	19	3.8	0.8	6.4	0.6	3.4	3.6	0.7	2.3	0.4	2.8	0.4	4.2	0.5
WHAK432J-3	43	4.5	17	3.5	0.6	5.3	0.5	2.9	3.2	0.7	2.0	0.3	2.4	0.3	3.6	0.6
WHAK432J-4	42	4.4	17	3.3	0.7	5.5	0.5	3.0	3.3	0.7	2.0	0.3	2.4	0.4	3.8	0.5
WHAK432J-5	44	4.6	17	3.3	0.6	5.3	0.5	2.9	3.3	0.7	2.0	0.3	2.4	0.4	3.3	0.6
OK240707-1A-1	-	-	-	-	-	-	-	-	-	-	-	-	-	-	-	-
OK240707-1A-2	-	-	-	-	-	-	-	-	-	-	-	-	-	-	-	-
OK240707-1A-3	-	-	-	-	-	-	-	-	-	-	-	-	-	-	-	-
OK240707-1A-4	-	-	-	-	-	-	-	-	-	-	-	-	-	-	-	-
OK240707-1A-5	47	4.6	17	3.0	0.3	3.0	0.4	2.6	2.9	0.6	2.0	0.3	2.3	0.3	2.6	0.6
Ōtarawairere-1	-	-	-	-	-	-	-	-	-	-	-	-	-	-	-	-
Ōtarawairere-2	-	-	-	-	-	-	-	-	-	-	-	-	-	-	-	-
Ōtarawairere-3	-	-	-	-	-	-	-	-	-	-	-	-	-	-	-	-
Ōtarawairere-4	-	-	-	-	-	-	-	-	-	-	-	-	-	-	-	-
Ōtarawairere-5	-	-	-	-	-	-	-	-	-	-	-	-	-	-	-	-
OK240707-1C-1	51	4.7	17	2.8	0.4	3.0	0.5	2.8	2.9	0.7	1.8	0.3	2.0	0.3	3.2	0.5
OK240707-1C-2	46	4.9	17	3.6	0.5	2.6	0.5	2.7	3.2	0.6	1.9	0.3	2.1	0.4	3.1	0.5
OK240707-1C-3	43	4.9	17	3.6	0.4	2.6	0.5	2.6	3.1	0.6	1.6	0.3	2.2	0.3	3.2	0.6
OK240707-1C-4	47	5.2	19	3.3	0.4	3.1	0.5	3.2	3.2	0.7	2.2	0.3	2.5	0.3	3.3	0.5
OK240707-1C-5	40	4.1	14	2.5	0.3	2.1	0.3	2.0	2.2	0.5	1.5	0.2	1.9	0.3	2.5	0.5
OK240707-1D-1	48	4.5	17	3.6	0.5	2.9	0.5	2.8	3.2	0.6	1.9	0.3	2.0	0.4	2.8	0.5
OK240707-1D-2	54	5.4	20	3.8	0.3	3.3	0.5	3.1	3.6	0.8	2.2	0.3	2.6	0.4	2.6	0.7
OK240707-1D-3	49	5.1	18	3.1	0.4	3.1	0.5	2.8	2.9	0.6	1.9	0.3	2.2	0.3	3.1	0.6

OK240707-1E-2	51	5.6	19	4.3	0.3	3.9	0.6	3.6	4.1	0.9	2.6	0.4	3.1	0.5	3.2	0.9
OK240707-1E-5-B	-	-	-	-	-	-	-	-	-	-	-	-	-	-	-	-
OK240707-1F-1	55	5.9	21	3.8	0.3	3.5	0.7	3.4	3.7	0.8	2.4	0.4	2.7	0.4	2.9	0.7
OK240707-1F-2	52	5.5	20	4.4	0.2	3.8	0.7	3.7	4.1	0.9	2.7	0.4	2.6	0.4	3.0	0.8
OK240707-1F-3	56	5.5	20	3.8	0.2	3.3	0.6	3.4	3.5	0.8	2.3	0.4	2.7	0.4	2.6	0.7
OK240707-1F-4	49	4.7	16	3.3	0.5	3.3	0.5	3.2	3.2	0.7	2.1	0.3	2.5	0.4	2.7	0.5
OK240707-1F-5	54	5.2	20	3.6	0.2	3.4	0.5	3.1	3.2	0.7	2.3	0.3	2.6	0.4	2.6	0.7
OK240707-1F-6	54	5.6	20	3.5	0.3	2.9	0.5	3.0	3.4	0.7	2.2	0.3	2.7	0.4	2.8	0.7
OK240707-1J-1	41	4.0	15	2.8	0.5	2.3	0.4	2.2	2.3	0.5	1.5	0.2	2.0	0.3	3.6	0.5
OK240707-1J-2	47	5.3	19	4.0	0.5	3.6	0.5	3.4	3.4	0.8	2.2	0.3	2.3	0.4	3.3	0.5
OK240707-1J-4	50	5.1	19	3.8	0.5	3.3	0.6	3.3	3.5	0.7	2.1	0.3	2.5	0.4	2.8	0.5
OK240707-1L-1	47	5.0	17	3.8	0.6	3.3	0.6	3.0	3.3	0.8	2.0	0.3	2.8	0.3	3.0	0.6
OK240707-1L-2	49	5.1	19	3.5	0.5	2.9	0.6	3.1	3.6	0.7	2.0	0.3	2.4	0.4	2.9	0.6
OK240707-1L-3	48	5.0	20	3.7	0.5	3.4	0.6	3.3	3.5	0.8	2.3	0.3	2.5	0.4	2.8	0.5
OK240707-1L-3-A	-	-	-	-	-	-	-	-	-	-	-	-	-	-	-	-
OK240707-1L-4	47	4.7	18	3.6	0.5	3.2	0.5	3.1	3.3	0.7	2.2	0.3	2.3	0.3	2.7	0.5
OK240707-1L-5	-	-	-	-	-	-	-	-	-	-	-	-	-	-	-	-

Table 2.11: Lapilli glass trace element mean compositions (Tl203-U238)

Lapilli-subgroup	Tl203	Tl205	Pb206	Pb207	Th232	U235	U238
OK220707-1B-1	0.5	0.5	13	11	11	6.9	2.5
OK220707-1B-2	0.5	0.5	12	11	11	8.7	2.5
OK220707-1B-3	0.5	0.5	12	11	10	6.1	2.5
OK220707-1B-4	0.5	0.5	13	12	10	7.7	2.5
OK220707-1B-5	0.4	0.4	11	9.9	8.9	7.1	2.3
OK220707-1C-1	0.5	0.5	13	12	9.7	5.7	2.6
OK220707-1C-1-A	-	-	-	-	-	-	-
OK220707-1C-2	0.5	0.5	13	12	10	7.1	2.5
OK220707-1C-3	0.5	0.5	13	10	10	8.8	2.5
OK220707-1C-4	0.5	0.4	12	10	9.8	7.0	2.5
OK220707-1C-5	0.5	0.5	13	12	11	7.1	2.4
WHAK432A-1	0.5	0.5	13	12	11	7.0	2.7
WHAK432A-2	-	-	-	-	-	-	-
WHAK432A-3	0.5	0.4	12	11	11	5.6	2.4
WHAK432A-4	0.5	0.6	14	12	10	5.0	2.4
WHAK432A-5	0.6	0.6	14	13	12	9.3	2.7
WHAK432A-6	0.7	0.6	14	13	13	12	2.8
WHAK432B-1	0.5	0.6	15	14	11	8.2	2.7
WHAK432B-2	0.5	0.5	14	13	12	5.9	2.7
WHAK432B-3	0.5	0.5	14	13	11	8.0	2.5
WHAK432B-4	0.5	0.6	14	13	11	8.1	2.6

WHAK432B-5	0.6	0.6	14	14	11	6.9	2.7
OK220707-1E-1	0.7	0.7	15	13	9.6	7.2	2.5
OK220707-1E-1-A	-	-	-	-	-	-	-
WHAK432C-1	-	-	-	-	-	-	-
WHAK432C-2	0.4	0.5	13	11	10	10	2.6
WHAK432C-3	0.5	0.5	10	9.5	9.4	-	2.5
WHAK432C-4	0.4	0.6	13	12	11	8.6	2.6
WHAK432C-5	0.6	0.5	14	12	10	7.3	2.7
OK220707-1F-1	0.4	0.5	12	11	12	9.8	2.3
OK220707-1F-2	0.5	0.5	12	11	11	6.6	2.6
OK220707-1F-3	0.5	0.5	13	11	11	5.3	2.7
OK220707-1F-4	0.5	0.5	13	12	11	7.1	2.6
OK220707-1F-5	0.5	0.5	13	12	11	5.7	2.6
OK220707-1F-6	-	-	-	-	-	-	-
OK220707-1G-1	0.7	0.7	15	14	12	9.6	3.0
OK220707-1G-2	0.7	0.8	17	15	14	10	3.5
OK220707-1G-3	0.7	0.8	17	14	12	9.4	3.2
OK220707-1G-4	0.7	0.7	18	15	14	7.9	3.6
OK220707-1G-4-A	-	-	-	-	-	-	-
OK220707-1G-5	0.7	0.7	17	15	15	12	3.5
OK220707-1G-6	0.8	0.8	17	15	15	14	3.5
WHAK432L-1	0.8	0.9	19	15	14	4.3	3.7
WHAK432L-2	0.7	0.8	20	17	17	8.6	4.6

WHAK432L-3	0.7	0.7	18	16	15	6.4	3.7
WHAK432L-4	0.7	0.8	18	16	13	8.2	3.4
WHAK432L-5	0.7	0.7	17	17	15	11	3.9
OK220707-1I-1	0.7	0.6	15	14	14	9.9	3.4
OK220707-1I-2	0.7	0.7	16	14	15	14	3.5
OK220707-1I-3	0.6	0.7	15	15	14	11	3.4
OK220707-1I-4	1.0	1.4	27	17	15	26	5.8
OK220707-1I-5	0.8	0.8	18	15	15	7.3	3.6
WHAK432D-1	0.9	0.8	19	18	17	11	3.9
WHAK432D-2	0.9	0.8	17	17	17	6.8	4.1
WHAK432D-3	0.7	0.8	16	16	14	3.5	3.1
WHAK432D-4	0.8	0.9	18	16	18	12	4.1
WHAK432D-5	0.8	0.8	20	17	17	8.3	4.2
WHAK432E-1	0.8	0.7	18	16	15	9.6	3.3
WHAK432E-2	0.8	0.8	19	17	18	8.1	4.5
WHAK432E-3	0.7	0.8	19	17	19	13	4.2
WHAK432E-4	0.8	0.8	19	16	15	10.0	3.5
WHAK432E-5	0.8	0.8	18	16	19	16	4.0
OK220707-1L-1	0.7	0.7	17	15	13	11	3.2
OK220707-1L-2	0.6	0.7	18	16	15	10	3.8
OK220707-1L-3	0.6	0.7	18	15	14	9.9	3.2
OK220707-1L-4	0.8	0.7	18	17	17	15	4.0
OK220707-1L-5	0.8	0.8	18	17	19	12	4.4

WHAK432F-1	0.5	0.8	18	20	17	11	3.6
WHAK432F-2	0.8	0.8	19	16	15	20	3.7
WHAK432F-3	0.6	0.7	18	17	17	8.9	4.1
WHAK432F-4	0.8	0.7	18	17	16	6.1	3.5
WHAK432F-5	0.8	0.7	18	15	15	5.5	3.7
OK220707-1N-1	0.8	0.7	18	17	17	10	4.1
OK220707-1N-2	0.7	0.7	17	16	16	14	3.7
OK220707-1N-3	0.7	0.6	17	16	14	9.6	3.5
OK220707-1N-4	0.7	0.7	18	15	16	9.2	3.8
OK220707-1N-5	0.6	0.7	16	15	14	9.7	3.5
OK220707-1N-6	0.7	0.7	18	16	16	11	3.5
WHAK432G-1	1.0	1.0	20	19	24	16	5.9
WHAK432G-2	0.6	0.6	17	16	12	7.6	2.9
WHAK432G-3	0.8	0.9	22	19	24	15	5.5
WHAK432G-4	0.7	0.7	19	17	16	11	3.6
WHAK432G-5	0.6	0.6	20	18	17	8.8	3.2
OK220707-1O-1	0.9	0.9	19	16	22	17	5.5
OK220707-1O-2	0.8	0.9	21	18	24	14	5.4
OK220707-1O-3	0.7	0.7	22	20	22	12	4.2
OK220707-1O-4	0.7	0.7	24	22	24	13	4.2
OK220707-1O-5	0.8	0.8	18	16	21	13	4.9
OK220707-1O-6	0.7	0.8	21	19	23	15	4.5
OK220707-1O-7	0.8	0.8	20	19	20	14	4.8

OK220707-1P-1	0.6	0.6	15	14	11	9.1	2.8
OK220707-1P-2	0.6	0.5	14	13	11	8.0	2.7
OK220707-1P-3	0.6	0.6	16	14	11	8.9	2.7
OK220707-1P-5	0.6	0.6	15	13	11	5.9	2.7
OK220707-1P-6	0.6	0.6	16	14	11	8.2	2.9
OK220707-1Q-1	0.5	0.5	15	13	9.8	9.1	2.6
OK220707-1Q-2	0.6	0.6	16	15	12	9.3	2.8
OK220707-1Q-3	0.4	0.5	14	12	11	11	2.8
OK220707-1Q-4	0.6	0.6	16	14	11	6.9	2.8
OK220707-1Q-5	0.6	0.6	16	14	11	8.8	2.8
WHAK432H-1	0.5	0.5	15	13	11	6.9	2.6
WHAK432H-2	0.6	0.5	15	14	11	7.1	2.5
WHAK432H-3	0.5	0.5	15	14	10	8.1	2.5
WHAK432H-4	0.6	0.6	17	15	11	6.7	2.7
WHAK432H-5	0.6	0.6	17	15	11	8.3	2.8
WHAK432I-1	0.6	0.5	15	13	9.6	5.3	2.5
WHAK432I-1-A	-	-	-	-	-	-	-
WHAK432I-2	0.6	0.5	15	14	9.9	5.1	2.5
WHAK432I-2-A	-	-	-	-	-	-	-
WHAK432I-3	0.5	0.6	15	13	9.9	6.7	2.5
WHAK432I-4	0.7	0.6	16	14	10	8.0	2.6
WHAK432I-5	0.6	0.6	17	16	12	9.1	2.9
WHAK432I-5-A	-	-	-	-	-	-	-

WHAK432J-1	0.5	0.5	15	13	10	6.9	2.6
WHAK432J-2	0.5	0.5	15	14	11	6.9	2.4
WHAK432J-3	0.5	0.6	14	13	10	7.8	2.4
WHAK432J-4	0.5	0.5	14	13	9.6	7.2	2.4
WHAK432J-5	0.5	0.5	15	13	10	7.4	2.6
OK240707-1A-1	-	-	-	-	-	-	-
OK240707-1A-2	-	-	-	-	-	-	-
OK240707-1A-3	-	-	-	-	-	-	-
OK240707-1A-4	-	-	-	-	-	-	-
OK240707-1A-5	0.7	0.7	17	15	16	9.3	3.5
Ōtarawairere-1	-	-	-	-	-	-	-
Ōtarawairere-2	-	-	-	-	-	-	-
Ōtarawairere-3	-	-	-	-	-	-	-
Ōtarawairere-4	-	-	-	-	-	-	-
Ōtarawairere-5	-	-	-	-	-	-	-
OK240707-1C-1	0.9	1.0	19	16	14	9.8	3.7
OK240707-1C-2	0.6	0.9	18	17	14	8.0	3.1
OK240707-1C-3	0.7	0.7	16	17	14	11	3.2
OK240707-1C-4	0.6	0.8	17	17	16	14	4.2
OK240707-1C-5	0.7	0.8	17	15	14	9.7	3.3
OK240707-1D-1	0.7	0.7	17	15	14	10	3.4
OK240707-1D-2	0.8	0.8	18	16	18	15	4.3
OK240707-1D-3	0.7	0.8	17	17	14	10	3.7

OK240707-1E-2	0.8	0.8	18	16	20	15	4.6
OK240707-1E-5-B	-	-	-	-	-	-	-
OK240707-1F-1	0.7	0.7	18	16	18	20	5.0
OK240707-1F-2	1.0	0.8	18	17	20	14	4.8
OK240707-1F-3	0.9	0.8	19	18	18	16	4.4
OK240707-1F-4	0.6	0.6	17	14	11	21	6.0
OK240707-1F-5	0.8	0.8	18	17	17	11	4.4
OK240707-1F-6	0.9	0.8	18	17	17	11	4.1
OK240707-1J-1	0.6	0.5	15	13	11	8.6	2.7
OK240707-1J-2	0.5	0.5	16	15	13	7.4	3.1
OK240707-1J-4	0.6	0.6	16	15	13	12	3.2
OK240707-1L-1	0.6	0.6	17	15	12	9.8	2.8
OK240707-1L-2	0.6	0.6	15	14	12	8.1	2.9
OK240707-1L-3	0.6	0.6	15	13	12	8.9	3.0
OK240707-1L-3-A	-	-	-	-	-	-	-
OK240707-1L-4	0.6	0.6	15	14	12	9.6	2.9
OK240707-1L-5	-	-	-	-	-	-	-

Table 2.12: Lapilli glass trace element standard deviations of the mean compositions (Li7-Fe58)

Lapilli-subgroup	Li7	B11	Na23	Mg24	Al27	Si28	P31	K39	Ca43	Sc45	Ti47	Ti49	V51	Cr53	Mn55	Fe58
OK220707-1B-1	4.3	3.0	2134	104	2305	0.0	41	1770	228	1.4	45	50	0.6	0.7	20	12
OK220707-1B-2	6.5	3.1	3100	41	2929	-	101	978	266	0.6	87	80	2.8	1.2	24	16
OK220707-1B-3	7.1	1.4	2094	114	5752	0.0	72	924	353	1.5	49	40	0.9	0.9	7.1	18
OK220707-1B-4	6.0	4.4	1433	143	3347	-	89	2020	422	0.9	38	58	0.8	0.7	23	3.2
OK220707-1B-5	4.2	4.4	1459	353	5512	-	213	1500	493	2.1	126	144	1.5	1.4	14	24
OK220707-1C-1	6.6	6.0	2552	354	8744	0.0	241	2583	795	2.9	179	166	5.2	2.7	88	35
OK220707-1C-1-A	-	-	-	-	-	-	-	-	-	-	-	-	-	-	-	-
OK220707-1C-2	5.0	2.8	1633	151	3204	0.0	77	596	359	1.0	60	47	1.3	0.2	11	11
OK220707-1C-3	5.3	2.7	2299	55	4711	0.0	34	2849	496	0.9	17	20	0.9	1.1	13	1.8
OK220707-1C-4	9.6	3.1	3683	197	4695	0.1	161	1671	740	1.2	65	84	3.2	1.8	13	9.8
OK220707-1C-5	3.2	3.6	1659	115	1633	0.0	76	1017	436	0.9	41	46	1.8	0.7	18	10
WHAK432A-1	3.1	3.1	1136	532	8641	-	61	931	329	1.4	55	77	2.4	2.4	14	16
WHAK432A-2	-	-	-	-	-	-	-	-	-	-	-	-	-	-	-	-
WHAK432A-3	4.7	3.3	3224	1454	7152	-	93	1366	366	0.9	30	46	3.9	2.0	15	4.0
WHAK432A-4	4.3	3.8	3557	815	2820	-	40	566	151	0.9	58	32	3.2	0.5	19	9.7
WHAK432A-5	6.1	1.1	2392	470	2297	-	28	1952	390	0.4	65	24	1.2	1.6	11	5.4
WHAK432A-6	3.7	3.2	2353	953	7505	-	139	382	492	1.1	290	89	8.6	2.4	66	27
WHAK432B-1	5.9	3.5	4085	2681	3889	-	20	865	123	0.3	25	26	1.0	0.6	25	6.7
WHAK432B-2	9.4	1.7	4180	2936	6808	-	117	2512	190	0.9	33	6.7	0.7	0.8	58	10.0
WHAK432B-3	2.0	1.3	5204	2025	744	-	69	1147	660	0.3	43	16	0.6	0.2	20	5.6
WHAK432B-4	1.9	2.7	2907	2153	2081	-	82	1706	241	0.4	19	16	0.1	0.4	18	3.9

WHAK432B-5	2.7	2.2	2348	2278	3062	-	42	1692	516	0.4	17	23	0.4	0.9	43	4.4
OK220707-1E-1	10.0	1.6	2039	114	5376	0.0	8.0	3457	340	0.8	82	48	0.1	0.6	27	5.5
OK220707-1E-1-A	-	-	-	-	-	-	-	-	-	-	-	-	-	-	-	-
WHAK432C-1	-	-	-	-	-	-	-	-	-	-	-	-	-	-	-	-
WHAK432C-2	10	11	1909	1340	9815	-	125	1213	780	1.2	131	216	1.7	4.8	25	39
WHAK432C-3	1.3	3.0	396	672	3879	-	96	1488	878	1.7	55	39	2.5	3.4	19	39
WHAK432C-4	1.4	3.4	541	78	602	-	41	272	457	0.3	24	12	0.3	0.5	4.1	4.6
WHAK432C-5	10	7.8	2350	1555	5764	-	107	1405	562	1.6	37	49	0.8	2.1	13	20
OK220707-1F-1	3.8	2.6	376	393	4024	-	55	2427	31	2.2	74	69	4.9	1.4	31	91
OK220707-1F-2	6.6	2.7	3580	387	15408	0.0	80	4110	331	2.3	95	199	6.4	1.2	30	81
OK220707-1F-3	1.8	1.7	3410	232	3389	0.1	27	1879	330	2.8	80	72	3.5	0.3	16	50
OK220707-1F-4	2.8	3.7	2590	46	4583	0.0	17	3233	713	2.2	72	43	0.8	0.6	21	18
OK220707-1F-5	2.5	3.9	1694	64	2538	-	17	1079	312	0.9	57	37	1.4	0.3	16	15
OK220707-1F-6	-	-	-	-	-	-	-	-	-	-	-	-	-	-	-	-
OK220707-1G-1	9.3	2.5	1913	124	4600	0.0	24	6000	800	0.9	106	165	2.8	2.4	28	16
OK220707-1G-2	3.3	4.2	3091	266	6777	0.0	46	3115	261	4.0	220	265	12	2.9	13	73
OK220707-1G-3	6.8	3.4	4595	43	6082	-	19	4139	554	1.3	58	73	1.1	1.8	8.6	13
OK220707-1G-4	1.6	5.5	1739	51	3004	0.0	34	1758	449	1.4	79	123	5.6	2.1	10.0	33
OK220707-1G-4-A	-	-	-	-	-	-	-	-	-	-	-	-	-	-	-	-
OK220707-1G-5	4.0	3.1	1892	47	1928	0.0	18	2397	580	0.9	83	100	2.1	1.4	7.5	20
OK220707-1G-6	5.5	4.7	3821	80	5793	0.0	39	2555	160	2.0	69	127	2.9	0.9	29	16
WHAK432L-1	5.4	10	1906	20	6988	-	39	406	359	1.5	86	19	1.1	2.9	3.1	11
WHAK432L-2	13	13	470	40	1817	-	24	1254	323	1.5	46	44	0.5	1.0	28	9.3

WHAK432L-3	3.0	1.4	931	7.5	455	-	23	622	441	1.0	12	20	0.5	1.2	1.7	1.4
WHAK432L-4	6.8	7.2	2458	19	1297	-	22	1648	407	0.4	40	7.1	0.4	1.0	7.5	7.4
WHAK432L-5	3.4	8.1	1719	19	4579	-	50	1024	1029	1.8	56	69	0.5	2.2	6.2	21
OK220707-1I-1	2.3	3.7	1442	96	3804	0.0	6.2	7498	493	0.9	78	73	4.6	0.5	17	28
OK220707-1I-2	2.7	1.3	4487	65	1467	-	26	2756	491	0.4	219	245	12	1.3	82	47
OK220707-1I-3	3.9	4.5	1951	51	3360	0.0	14	3633	635	0.3	19	82	0.5	0.6	33	5.1
OK220707-1I-4	10	3.6	2249	41	2142	-	16	2234	194	0.0	188	16	0.5	2.0	9.4	15
OK220707-1I-5	4.3	2.4	1490	35	1832	-	11	1846	186	1.3	38	67	1.7	0.7	28	17
WHAK432D-1	4.4	6.5	1327	371	1516	-	41	3436	494	1.0	30	29	1.1	3.0	30	8.1
WHAK432D-2	13	8.3	2492	139	1864	-	35	2419	529	1.7	15	14	0.8	2.6	3.5	6.9
WHAK432D-3	12	4.8	4309	70	1448	-	24	2686	898	0.7	66	91	0.2	1.4	48	4.6
WHAK432D-4	6.9	3.2	2231	259	2041	-	12	2359	288	1.0	27	34	0.6	2.7	7.0	5.9
WHAK432D-5	3.7	3.2	1282	233	2161	-	32	2239	881	2.3	15	15	0.7	3.6	16	6.1
WHAK432E-1	10	5.3	2239	191	9945	-	25	2721	466	0.5	126	127	1.6	0.8	9.5	16
WHAK432E-2	6.5	3.4	1976	19	2348	-	24	887	62	0.7	100	93	0.9	1.3	11	1.3
WHAK432E-3	3.2	2.7	680	201	706	-	16	1373	206	0.7	112	184	2.3	0.7	14	34
WHAK432E-4	1.4	4.0	1417	136	4092	-	15	1525	164	0.8	46	70	0.8	0.6	8.5	16
WHAK432E-5	4.1	5.6	1386	487	8927	-	59	2203	261	0.6	111	124	2.1	0.7	18	23
OK220707-1L-1	5.6	6.3	2301	63	3537	-	9.1	3725	508	0.6	40	227	1.4	0.5	11	9.8
OK220707-1L-2	2.2	2.3	1294	23	2043	0.0	8.8	2013	187	0.3	40	42	0.3	0.5	6.6	8.4
OK220707-1L-3	5.9	7.8	777	81	10723	0.0	48	1903	221	1.4	125	75	1.2	1.5	36	36
OK220707-1L-4	4.4	4.8	1694	39	4525	0.0	14	4556	468	0.5	16	34	0.2	0.7	28	6.2
OK220707-1L-5	4.3	3.1	2535	23	4614	-	8.2	4515	220	0.9	24	24	0.1	0.2	29	3.8

WHAK432F-1	3.4	10	2553	84	9232	-	78	3887	1030	3.3	319	349	2.6	2.9	21	50
WHAK432F-2	7.5	16	3687	115	2308	-	28	2938	709	2.6	68	59	0.5	6.4	15	8.4
WHAK432F-3	6.0	4.1	3121	32	3328	-	95	1387	1010	1.6	50	34	0.8	1.0	23	13
WHAK432F-4	4.4	5.7	2044	119	12019	-	100	4203	1323	1.4	137	139	0.3	6.6	22	31
WHAK432F-5	5.9	5.8	1473	162	3687	-	71	2194	737	2.2	141	95	1.9	6.3	9.1	21
OK220707-1N-1	5.8	3.0	1743	26	1473	-	9.7	1888	226	0.8	43	50	0.4	0.3	10	3.3
OK220707-1N-2	2.7	4.2	748	94	4605	0.0	28	747	425	1.8	100	93	1.2	0.9	9.6	21
OK220707-1N-3	6.8	2.5	2090	83	4547	0.0	23	5837	348	1.4	58	64	0.8	0.7	17	20
OK220707-1N-4	4.4	4.1	717	47	4013	0.0	25	4751	783	0.4	43	70	0.7	1.3	21	12
OK220707-1N-5	3.2	4.6	3314	131	15860	0.0	24	6986	657	1.4	84	104	2.0	1.3	34	56
OK220707-1N-6	5.4	3.7	2947	58	4693	0.0	8.1	2570	609	1.2	89	70	0.4	1.1	25	15
WHAK432G-1	8.2	2.6	1263	66	2687	-	6.5	1838	164	0.3	38	78	1.4	0.5	22	13
WHAK432G-2	3.6	2.3	1691	101	9346	-	10	1534	405	0.8	90	88	1.6	0.7	14	33
WHAK432G-3	9.0	3.7	2411	234	13321	-	28	4245	227	1.0	299	311	4.9	0.7	51	28
WHAK432G-4	1.9	2.0	1878	128	7634	-	13	2274	249	0.5	73	125	1.8	0.6	9.2	23
WHAK432G-5	6.9	3.5	1988	277	19231	-	28	6513	671	1.0	261	282	4.6	1.0	37	79
OK220707-1O-1	9.4	5.4	1938	18	4313	0.0	20	3515	541	0.7	57	96	3.2	0.6	9.8	7.0
OK220707-1O-2	3.9	7.4	2121	188	5551	0.0	27	6774	342	1.2	153	180	4.2	1.2	58	12
OK220707-1O-3	10	5.6	4119	257	14792	0.0	44	2823	291	1.6	257	305	8.1	1.6	22	47
OK220707-1O-4	5.8	7.1	3112	217	16849	0.0	23	6404	380	1.2	288	299	7.9	1.7	68	35
OK220707-1O-5	8.3	2.1	1243	32	3718	0.0	13	2441	297	0.3	36	39	1.4	0.5	14	7.1
OK220707-1O-6	4.0	5.2	2110	159	9661	-	44	3390	306	0.8	394	248	4.5	1.3	44	22
OK220707-1O-7	6.1	2.8	2422	82	4183	0.0	17	2429	364	0.5	74	77	1.2	0.3	39	15

OK220707-1P-1	5.1	2.2	2659	27	2813	0.0	15	2879	248	0.4	35	21	0.2	0.4	12	3.5
OK220707-1P-2	3.6	1.4	1381	37	4309	0.0	5.2	2073	331	0.8	33	25	0.3	0.2	15	3.9
OK220707-1P-3	3.9	1.6	1701	66	3333	0.0	11	1659	346	1.3	51	33	0.2	0.6	19	5.3
OK220707-1P-5	6.6	4.3	3470	71	4175	0.0	29	1991	432	0.6	22	44	0.8	0.5	12	9.3
OK220707-1P-6	3.4	2.4	1662	51	3897	0.0	8.0	1601	330	0.4	18	22	0.4	0.2	3.0	3.4
OK220707-1Q-1	3.4	2.7	1744	115	4493	0.0	18	2418	556	0.9	51	39	0.4	0.5	16	5.3
OK220707-1Q-2	2.3	1.4	1054	34	1191	0.0	5.6	458	357	0.4	28	30	0.1	0.4	15	3.7
OK220707-1Q-3	2.4	1.6	4403	283	4815	-	47	790	689	1.4	55	76	2.2	0.5	23	19
OK220707-1Q-4	4.4	3.2	2463	91	1508	0.0	28	1227	434	0.8	37	64	0.5	0.4	19	6.9
OK220707-1Q-5	3.8	2.5	3002	76	4786	0.0	22	873	371	1.2	30	52	0.3	0.4	25	4.7
WHAK432H-1	2.6	1.0	442	44	2780	-	4.1	1054	427	0.5	32	43	0.2	0.2	9.0	1.3
WHAK432H-2	2.9	1.2	1282	71	1600	-	20	727	485	0.3	48	30	0.8	0.7	30	6.7
WHAK432H-3	1.5	1.2	1205	80	2719	-	18	1004	498	0.4	56	40	0.4	0.5	41	6.4
WHAK432H-4	4.4	2.3	1357	6.5	2133	-	8.6	1786	216	0.2	20	15	0.1	0.5	11	2.3
WHAK432H-5	2.3	2.0	894	18	2331	-	8.0	1125	137	0.5	14	27	0.1	0.3	14	3.1
WHAK432I-1	6.3	4.0	3142	62	3830	-	29	1057	276	1.4	77	47	2.4	1.4	40	10.0
WHAK432I-1-A	-	-	-	-	-	-	-	-	-	-	-	-	-	-	-	-
WHAK432I-2	2.4	2.7	1943	36	1914	-	73	253	496	1.4	57	53	2.4	3.5	23	7.1
WHAK432I-2-A	-	-	-	-	-	-	-	-	-	-	-	-	-	-	-	-
WHAK432I-3	2.0	4.2	1234	60	882	-	39	853	658	1.6	29	47	1.0	3.0	12	5.5
WHAK432I-4	3.7	7.2	3081	52	2046	-	9.3	861	442	2.1	28	39	2.0	4.0	8.6	4.1
WHAK432I-5	2.6	1.5	560	15	2343	-	9.4	1309	325	0.3	15	21	0.1	0.4	19	3.5
WHAK432I-5-A	-	-	-	-	-	-	-	-	-	-	-	-	-	-	-	-

WHAK432J-1	3.6	0.8	1390	30	2335	-	15	1026	340	0.4	22	33	1.0	0.6	6.2	4.3
WHAK432J-2	4.5	0.9	1240	34	3324	-	41	745	432	0.7	47	56	1.4	0.2	21	6.3
WHAK432J-3	5.0	1.1	2477	41	3132	-	45	1319	365	0.2	63	44	1.0	0.7	12	3.9
WHAK432J-4	3.4	1.3	761	78	3857	-	35	1058	766	0.4	38	41	1.2	0.6	18	5.4
WHAK432J-5	2.0	1.2	2125	14	1316	-	8.8	960	221	0.3	30	32	0.2	0.2	9.5	2.0
OK240707-1A-1	-	-	-	-	-	-	-	-	-	-	-	-	-	-	-	-
OK240707-1A-2	-	-	-	-	-	-	-	-	-	-	-	-	-	-	-	-
OK240707-1A-3	-	-	-	-	-	-	-	-	-	-	-	-	-	-	-	-
OK240707-1A-4	-	-	-	-	-	-	-	-	-	-	-	-	-	-	-	-
OK240707-1A-5	3.3	3.3	1680	22	7030	0.0	9.7	1672	275	1.4	35	24	0.2	0.1	10	4.6
Ōtarawairere-1	-	-	-	-	-	-	-	-	-	-	-	-	-	-	-	-
Ōtarawairere-2	-	-	-	-	-	-	-	-	-	-	-	-	-	-	-	-
Ōtarawairere-3	-	-	-	-	-	-	-	-	-	-	-	-	-	-	-	-
Ōtarawairere-4	-	-	-	-	-	-	-	-	-	-	-	-	-	-	-	-
Ōtarawairere-5	-	-	-	-	-	-	-	-	-	-	-	-	-	-	-	-
OK240707-1C-1	12	14	4240	256	5514	-	29	3739	379	1.0	115	124	3.4	0.2	9.0	28
OK240707-1C-2	8.7	0.1	1343	81	2018	-	9.4	5322	304	0.8	64	55	0.1	0.6	32	11
OK240707-1C-3	8.1	3.9	3775	86	5179	-	12	4071	622	1.4	98	70	0.3	0.5	23	16
OK240707-1C-4	0.6	2.5	511	186	535	0.1	20	3961	116	0.3	486	400	11	1.8	23	20
OK240707-1C-5	9.2	3.9	2214	66	4099	-	9.0	4027	447	0.5	26	29	0.2	0.4	16	4.1
OK240707-1D-1	20	1.1	4934	145	3940	0.0	1.9	3023	194	0.6	62	114	0.7	1.2	16	13
OK240707-1D-2	6.3	5.6	762	15	2867	-	10	2928	512	0.6	28	38	0.5	0.6	19	4.1
OK240707-1D-3	5.4	5.8	1852	30	2872	0.1	14	2513	534	0.9	59	45	3.0	1.3	10	4.8

OK240707-1E-2	16	5.2	1832	965	7670	-	70	2157	592	1.6	427	468	15	2.5	31	104
OK240707-1E-5-B	-	-	-	-	-	-	-	-	-	-	-	-	-	-	-	-
OK240707-1F-1	19	9.2	4867	535	2527	-	122	7701	675	4.3	241	257	39	3.3	42	65
OK240707-1F-2	8.0	2.9	1155	151	10699	0.0	20	7814	419	1.1	42	40	0.5	0.7	55	8.9
OK240707-1F-3	6.3	2.8	1058	77	3386	-	3.2	5296	373	1.1	48	55	1.6	1.4	13	12
OK240707-1F-4	4.9	5.7	2778	374	9327	0.0	105	1370	559	4.2	338	370	7.5	4.0	20	23
OK240707-1F-5	5.9	3.5	2059	87	4286	0.0	12	6371	392	0.8	107	67	3.8	0.8	18	13
OK240707-1F-6	9.4	2.1	2308	55	7663	0.0	21	4849	344	0.9	42	127	1.8	1.1	50	9.1
OK240707-1J-1	1.7	3.0	1723	101	2800	0.0	35	1518	394	0.4	32	60	0.9	1.2	17	7.9
OK240707-1J-2	7.7	6.2	3134	93	5723	0.0	15	1210	493	0.7	58	18	0.6	0.7	23	9.5
OK240707-1J-4	3.8	3.5	1922	28	3761	0.0	17	1946	317	0.3	23	27	0.1	0.6	19	5.9
OK240707-1L-1	4.4	2.7	3150	113	4812	0.0	27	1343	473	0.9	44	243	11	1.0	6.9	41
OK240707-1L-2	3.0	3.1	3737	142	2717	0.0	27	1644	192	0.7	22	38	5.0	0.4	25	23
OK240707-1L-3	3.4	3.6	2358	101	873	0.0	21	1975	248	0.8	51	54	7.6	0.4	23	24
OK240707-1L-3-A	-	-	-	-	-	-	-	-	-	-	-	-	-	-	-	-
OK240707-1L-4	9.4	4.4	2324	167	1774	-	56	771	65	1.1	88	123	17	0.6	4.5	77
OK240707-1L-5	-	-	-	-	-	-	-	-	-	-	-	-	-	-	-	-

Table 2.13: Lapilli glass trace element standard deviations of the mean compositions (Co59-La139)

Lapilli-subgroup	Co59	Ni60	Cu63	Zn64	Ga69	Ge74	Se77	Rb85	Sr88	Y89	Zr90	Nb93	Cs133	Ba137	Ba138	La139
OK220707-1B-1	0.1	0.4	0.3	3.7	1.2	0.1	0.5	5.8	2.4	0.8	3.1	0.1	0.2	65	66	0.6
OK220707-1B-2	0.2	0.2	1.2	6.9	1.1	0.3	0.6	7.6	1.8	1.0	6.5	0.1	0.2	54	49	1.2
OK220707-1B-3	0.2	0.5	1.7	1.8	0.6	0.6	0.2	9.6	3.2	0.8	6.1	0.5	0.2	41	29	1.5
OK220707-1B-4	0.2	0.1	2.8	4.2	2.0	0.2	1.0	8.3	2.6	2.0	5.1	0.3	0.4	73	77	2.1
OK220707-1B-5	0.1	0.5	0.9	2.7	0.8	0.5	0.7	6.1	3.2	2.8	10	0.3	0.1	76	39	1.3
OK220707-1C-1	1.1	0.7	4.8	1.9	1.8	0.3	1.2	6.3	6.0	1.1	7.4	0.3	0.5	44	33	1.3
OK220707-1C-1-A	-	-	-	-	-	-	-	-	-	-	-	-	-	-	-	-
OK220707-1C-2	0.1	0.2	0.6	4.0	5.2	0.2	0.3	3.8	2.2	0.7	6.3	0.2	0.2	47	48	0.9
OK220707-1C-3	0.1	0.2	0.6	3.0	4.3	0.3	0.6	7.7	3.6	0.7	3.9	0.3	0.3	51	70	0.8
OK220707-1C-4	0.1	0.1	1.0	8.8	4.8	0.1	1.0	12	6.4	1.9	8.9	0.3	0.5	69	75	0.9
OK220707-1C-5	0.1	0.1	0.6	4.2	3.6	0.2	0.3	5.5	5.5	1.0	2.8	0.3	0.3	13	53	1.6
WHAK432A-1	0.3	1.0	8.4	7.3	1.8	0.2	1.5	3.1	2.5	2.8	7.8	0.3	0.3	24	57	1.0
WHAK432A-2	-	-	-	-	-	-	-	-	-	-	-	-	-	-	-	-
WHAK432A-3	0.3	0.2	4.0	5.5	0.3	0.3	2.1	6.5	2.7	0.9	9.8	0.4	0.2	29	47	1.5
WHAK432A-4	0.5	1.0	1.8	0.9	1.2	0.3	0.2	3.3	1.9	2.2	3.2	0.1	0.1	5.0	21	0.5
WHAK432A-5	0.3	0.1	9.1	2.9	1.2	0.1	1.1	7.3	5.3	1.3	18	0.3	0.2	70	96	4.6
WHAK432A-6	0.5	1.3	8.2	5.4	1.1	0.5	3.7	5.7	5.6	1.3	1.9	0.4	0.6	75	90	2.3
WHAK432B-1	0.3	0.2	1.4	5.9	0.7	0.2	0.9	5.5	2.8	0.8	4.4	0.3	0.3	46	38	1.5
WHAK432B-2	0.2	0.2	3.0	4.9	1.5	0.2	0.5	2.9	1.1	1.5	10.0	0.4	0.1	31	46	0.5
WHAK432B-3	0.2	0.1	1.4	4.0	0.4	0.2	0.1	3.7	4.7	0.4	1.9	0.2	0.2	37	16	0.6
WHAK432B-4	0.1	0.1	4.2	3.0	1.0	0.2	0.4	3.4	5.1	1.1	1.0	0.2	0.1	46	46	1.3

WHAK432B-5	0.2	0.1	1.2	5.4	0.9	0.1	0.9	3.1	6.0	1.5	2.3	0.1	0.3	29	50	0.9
OK220707-1E-1	0.0	0.1	0.2	4.1	1.0	0.3	0.1	4.1	4.2	4.0	8.0	0.2	0.4	42	25	0.9
OK220707-1E-1-A	-	-	-	-	-	-	-	-	-	-	-	-	-	-	-	-
WHAK432C-1	-	-	-	-	-	-	-	-	-	-	-	-	-	-	-	-
WHAK432C-2	0.4	1.0	3.3	3.1	4.4	0.9	4.9	11	5.8	1.3	11	0.3	0.5	147	139	2.4
WHAK432C-3	0.4	2.5	1.8	7.0	4.6	0.4	3.1	4.8	3.3	3.0	0.4	0.4	0.2	112	114	2.0
WHAK432C-4	0.3	0.2	0.5	2.4	1.2	0.4	0.1	1.0	1.6	0.5	1.8	0.4	0.3	32	8.5	0.3
WHAK432C-5	0.2	1.6	2.5	6.3	2.5	0.6	2.0	4.0	3.1	1.7	6.1	0.3	0.2	104	97	0.7
OK220707-1F-1	0.0	0.9	0.1	5.9	2.5	0.1	0.1	9.9	1.9	1.1	1.5	0.2	0.0	19	16	1.2
OK220707-1F-2	0.2	2.5	1.4	5.6	5.0	0.3	1.3	15	1.9	0.8	5.8	0.3	0.5	73	58	2.6
OK220707-1F-3	0.2	0.6	2.7	2.1	1.5	0.5	0.3	7.3	3.6	1.1	4.7	0.3	0.1	44	51	0.6
OK220707-1F-4	0.5	0.3	1.1	5.9	1.6	0.3	3.2	9.5	4.1	1.3	5.6	0.3	0.4	61	64	1.9
OK220707-1F-5	0.2	0.3	0.6	4.0	2.0	0.2	1.3	2.1	2.5	0.7	2.8	0.2	0.2	78	45	0.4
OK220707-1F-6	-	-	-	-	-	-	-	-	-	-	-	-	-	-	-	-
OK220707-1G-1	0.5	0.3	4.6	1.9	2.5	0.4	0.8	23	8.1	2.5	13	0.7	0.8	85	115	0.8
OK220707-1G-2	0.4	1.5	2.6	10	2.0	0.4	1.0	13	3.3	2.5	8.5	0.6	0.5	89	104	2.3
OK220707-1G-3	0.3	0.4	0.6	4.2	2.4	0.7	2.1	11	4.6	1.7	14	0.2	0.5	79	110	1.3
OK220707-1G-4	0.4	1.0	2.7	5.4	2.5	0.4	0.5	7.2	3.4	1.3	6.8	0.2	0.2	22	52	0.7
OK220707-1G-4-A	-	-	-	-	-	-	-	-	-	-	-	-	-	-	-	-
OK220707-1G-5	0.2	0.3	2.9	6.6	1.5	0.4	0.6	11	5.4	2.1	5.3	0.3	0.5	56	28	1.8
OK220707-1G-6	1.3	2.5	3.1	3.2	2.4	0.1	0.8	8.1	3.5	1.2	9.6	0.4	0.3	17	9.4	3.2
WHAK432L-1	0.4	3.8	2.6	3.0	1.3	0.4	6.6	2.1	0.6	1.3	3.9	0.2	0.4	7.6	23	0.7
WHAK432L-2	0.3	1.3	2.3	4.9	0.6	0.5	5.0	5.0	0.7	1.0	3.0	0.6	0.5	8.6	9.6	0.9

WHAK432L-3	0.2	0.2	1.1	6.0	0.7	0.7	2.8	3.6	1.2	0.4	1.8	0.1	0.3	11	9.2	0.9
WHAK432L-4	0.2	0.9	0.3	2.4	0.6	0.5	2.6	6.3	1.4	0.4	0.8	0.2	0.4	12	14	0.8
WHAK432L-5	0.8	1.3	2.4	6.5	3.1	0.7	-	5.0	2.6	1.0	6.9	0.6	0.6	56	46	0.9
OK220707-1I-1	0.1	1.2	1.8	8.9	0.9	0.2	0.3	15	5.2	2.0	3.2	0.4	0.5	98	70	0.9
OK220707-1I-2	0.5	1.0	2.0	3.0	0.6	0.2	0.1	6.0	0.2	2.5	2.9	0.5	0.7	54	54	5.8
OK220707-1I-3	0.1	0.1	0.3	3.5	1.4	0.2	0.0	9.5	3.2	0.9	4.2	0.4	0.7	78	72	2.3
OK220707-1I-4	0.0	11	127	1.7	3.1	0.4	0.0	11	2.0	2.7	5.0	0.2	0.7	93	77	4.9
OK220707-1I-5	0.1	1.8	1.0	2.5	2.0	0.2	0.6	11	0.4	1.0	6.5	0.4	0.3	41	60	1.1
WHAK432D-1	0.2	6.2	1.7	3.3	1.3	0.9	6.7	8.2	2.0	0.6	3.0	0.4	0.1	42	46	1.7
WHAK432D-2	0.1	3.6	2.6	8.8	0.9	1.2	4.9	5.7	0.9	0.6	4.0	0.6	0.5	27	24	1.8
WHAK432D-3	0.6	5.0	0.8	2.2	0.8	0.5	0.6	39	5.8	0.6	12	0.7	0.6	117	112	0.5
WHAK432D-4	0.3	2.2	0.6	5.1	1.2	0.9	3.7	2.3	1.0	0.8	1.8	0.4	0.2	15	7.2	0.9
WHAK432D-5	0.7	5.8	2.1	6.4	1.4	0.9	8.5	11	2.1	3.7	0.7	0.5	0.5	14	17	1.3
WHAK432E-1	0.1	0.7	0.7	8.8	1.5	0.5	1.7	12	1.6	2.1	7.2	0.6	0.5	15	25	8.5
WHAK432E-2	0.1	0.1	0.1	1.4	0.4	0.6	1.2	10	1.5	0.7	3.9	0.7	0.9	3.4	3.7	2.5
WHAK432E-3	0.2	0.3	4.6	9.2	1.8	0.6	0.6	6.9	1.7	0.8	3.4	0.3	0.9	6.9	7.2	5.3
WHAK432E-4	0.2	0.9	2.3	4.1	1.0	0.2	0.7	5.3	2.1	0.7	7.0	0.4	0.3	14	21	4.3
WHAK432E-5	0.2	0.6	5.0	5.7	2.2	0.3	2.6	3.8	1.2	2.1	3.1	0.6	0.4	19	12	8.7
OK220707-1L-1	0.3	1.3	2.9	3.9	2.6	0.5	0.7	13	5.9	0.6	13	0.5	0.4	80	61	2.2
OK220707-1L-2	0.3	0.3	1.7	3.6	0.7	0.2	1.0	12	3.1	0.9	3.6	0.2	0.5	37	31	2.2
OK220707-1L-3	0.4	2.0	0.9	12	3.2	0.3	1.2	11	1.2	1.5	8.7	0.2	0.8	72	80	1.6
OK220707-1L-4	0.1	0.1	0.9	2.9	0.6	0.2	1.1	8.6	1.1	0.7	3.8	0.6	0.5	22	26	1.4
OK220707-1L-5	0.2	0.2	0.7	5.2	1.1	0.3	0.8	20	0.7	1.5	5.5	0.6	0.5	12	17	2.4

WHAK432F-1	0.4	3.8	0.7	11	2.5	0.7	6.8	17	3.5	2.4	20	0.9	0.7	62	69	1.7
WHAK432F-2	0.9	3.8	0.2	8.1	0.6	1.1	20	5.9	3.3	1.0	8.1	0.6	0.6	29	28	1.0
WHAK432F-3	0.4	3.7	0.6	6.8	0.6	0.2	2.3	10	1.2	1.3	4.1	0.4	0.4	14	25	1.9
WHAK432F-4	0.3	11	2.6	10	2.9	0.6	12	15	2.8	1.3	11	0.6	0.6	41	25	2.0
WHAK432F-5	0.6	7.6	2.5	5.1	1.6	0.6	15	9.6	2.5	1.6	3.3	0.6	0.6	59	66	1.7
OK220707-1N-1	0.1	0.2	1.1	5.8	1.2	0.3	0.2	5.6	3.3	0.3	5.8	0.3	0.2	30	33	1.0
OK220707-1N-2	0.3	0.5	1.7	7.3	2.9	0.1	1.9	9.8	2.8	0.3	6.3	0.3	0.6	54	69	4.4
OK220707-1N-3	0.1	1.7	1.8	8.0	1.5	0.9	1.3	14	3.1	0.9	4.9	0.3	0.1	49	60	2.5
OK220707-1N-4	0.3	0.4	1.8	7.2	1.9	0.4	0.3	12	3.5	2.5	7.3	0.5	0.6	137	119	1.6
OK220707-1N-5	0.3	1.5	2.6	13	1.8	0.7	0.7	17	4.2	2.0	11	0.5	1.1	62	85	2.8
OK220707-1N-6	0.2	0.6	2.5	5.9	2.2	0.4	0.8	12	4.2	2.0	9.5	0.6	0.6	36	72	2.7
WHAK432G-1	0.1	0.3	1.9	2.9	1.5	0.3	0.9	7.0	0.7	2.0	2.3	0.3	0.5	2.4	7.5	1.9
WHAK432G-2	0.2	0.5	0.9	5.8	1.6	0.4	0.4	5.9	2.5	0.5	5.5	0.4	0.2	30	29	0.8
WHAK432G-3	0.4	0.8	1.8	9.4	2.8	0.6	0.8	20	1.9	3.2	14	1.1	0.7	19	18	2.9
WHAK432G-4	0.1	0.4	2.4	9.7	2.2	0.3	0.7	9.2	2.9	1.3	6.2	0.5	0.3	51	39	1.9
WHAK432G-5	0.2	0.4	1.5	22	2.0	0.6	1.1	24	4.5	2.7	5.2	0.5	0.8	103	55	3.5
OK220707-1O-1	0.3	0.7	1.2	4.8	1.5	0.3	0.7	13	0.7	4.4	5.4	0.7	0.4	5.2	5.3	1.1
OK220707-1O-2	0.3	2.1	1.3	17	3.5	0.8	1.4	19	2.3	5.4	9.3	0.8	0.7	4.7	5.2	3.6
OK220707-1O-3	0.6	2.1	2.5	6.2	3.2	0.9	1.3	12	2.4	3.1	13	2.4	0.9	14	22	2.4
OK220707-1O-4	0.6	3.3	1.0	23	4.5	1.4	0.0	17	2.5	3.5	12	1.7	0.8	37	21	3.8
OK220707-1O-5	0.2	0.6	0.6	3.4	1.1	0.3	0.4	4.6	1.5	1.4	5.2	0.5	0.6	15	13	1.1
OK220707-1O-6	0.4	1.0	2.7	9.1	2.8	0.8	1.3	20	2.1	1.6	16	1.8	0.4	17	10.0	1.7
OK220707-1O-7	0.4	0.7	1.3	3.0	1.3	0.3	0.2	8.1	1.6	1.7	4.5	0.7	0.6	15	18	1.6

OK220707-1P-1	0.2	0.1	0.8	2.5	0.9	0.1	0.8	4.5	4.7	1.0	3.7	0.5	0.4	73	39	1.1
OK220707-1P-2	0.1	0.1	0.3	7.4	1.4	0.3	0.6	9.5	4.8	1.8	3.1	0.2	0.3	17	48	2.0
OK220707-1P-3	0.1	0.1	1.8	7.0	1.4	0.2	0.4	8.8	2.1	1.5	5.9	0.5	0.3	36	65	1.3
OK220707-1P-5	0.2	0.5	1.6	6.7	1.9	0.3	1.0	3.4	4.0	1.1	4.6	0.2	0.4	68	72	1.9
OK220707-1P-6	0.1	0.1	1.3	29	1.1	0.3	0.6	10	3.5	1.3	3.3	0.3	0.4	26	45	0.5
OK220707-1Q-1	0.1	0.3	0.7	3.6	2.1	0.2	1.0	8.2	6.5	1.4	8.4	0.4	0.3	63	61	1.7
OK220707-1Q-2	0.1	0.1	0.7	3.8	1.3	0.1	0.7	7.5	3.5	1.3	5.2	0.2	0.2	44	45	1.6
OK220707-1Q-3	0.3	0.4	1.6	3.5	1.9	0.3	0.4	11	8.1	1.2	8.8	0.6	0.4	43	87	1.7
OK220707-1Q-4	0.1	0.1	0.5	2.2	1.8	0.2	1.0	6.5	3.6	0.9	3.9	0.4	0.3	18	37	1.3
OK220707-1Q-5	0.4	0.4	0.8	5.7	0.8	0.1	0.5	5.1	2.3	1.3	8.0	0.7	0.5	43	46	1.1
WHAK432H-1	0.1	0.1	0.4	1.2	2.7	0.1	0.4	3.8	3.9	1.1	6.2	0.4	0.2	16	24	0.7
WHAK432H-2	0.3	0.1	4.3	4.5	5.8	0.2	0.6	5.1	3.4	1.0	5.6	0.4	0.3	56	36	1.5
WHAK432H-3	0.2	0.1	1.8	4.7	2.7	0.2	0.6	5.3	6.2	1.8	12	0.3	0.2	34	32	1.9
WHAK432H-4	0.1	0.1	0.7	2.3	1.3	0.3	0.2	5.3	3.9	1.0	1.7	0.6	0.3	33	40	1.5
WHAK432H-5	0.1	0.1	1.8	3.3	2.2	0.2	0.3	2.8	1.8	0.9	4.5	0.3	0.3	34	30	0.9
WHAK432I-1	0.5	1.4	3.5	5.8	1.5	0.6	3.2	5.9	3.1	1.0	10	0.6	0.1	39	38	0.9
WHAK432I-1-A	-	-	-	-	-	-	-	-	-	-	-	-	-	-	-	-
WHAK432I-2	1.1	1.6	4.3	16	1.4	0.5	9.0	0.8	5.4	0.8	6.4	0.5	0.1	43	37	0.8
WHAK432I-2-A	-	-	-	-	-	-	-	-	-	-	-	-	-	-	-	-
WHAK432I-3	0.4	2.0	1.9	6.1	1.4	0.5	6.8	6.0	1.7	0.3	3.4	0.5	0.3	14	15	1.0
WHAK432I-4	0.4	5.2	1.5	2.5	1.2	0.7	5.2	4.5	3.9	0.7	4.5	0.6	0.3	28	24	1.7
WHAK432I-5	0.1	0.2	2.2	2.2	4.4	0.2	0.6	5.2	2.9	0.9	2.1	0.4	0.2	42	48	1.5
WHAK432I-5-A	-	-	-	-	-	-	-	-	-	-	-	-	-	-	-	-

WHAK432J-1	0.1	0.1	1.3	4.2	3.2	0.1	0.3	2.5	5.1	1.5	7.8	0.4	0.2	27	33	1.7
WHAK432J-2	0.5	0.1	15	6.5	5.0	0.2	0.3	2.9	4.7	2.4	9.1	0.4	0.2	40	47	2.3
WHAK432J-3	0.1	0.1	1.4	3.8	3.9	0.3	0.3	6.0	3.6	1.1	5.0	0.3	0.2	17	36	1.6
WHAK432J-4	0.1	0.0	3.3	4.2	2.3	0.2	0.6	3.7	7.8	1.2	9.3	0.4	0.1	45	29	1.7
WHAK432J-5	0.1	0.1	0.7	2.5	2.1	0.2	0.3	1.9	2.4	0.9	4.7	0.3	0.1	27	25	1.1
OK240707-1A-1	-	-	-	-	-	-	-	-	-	-	-	-	-	-	-	-
OK240707-1A-2	-	-	-	-	-	-	-	-	-	-	-	-	-	-	-	-
OK240707-1A-3	-	-	-	-	-	-	-	-	-	-	-	-	-	-	-	-
OK240707-1A-4	-	-	-	-	-	-	-	-	-	-	-	-	-	-	-	-
OK240707-1A-5	0.1	0.1	0.1	2.5	2.8	0.3	0.2	9.7	2.2	1.2	2.5	0.2	0.0	34	42	2.1
Ōtarawairere-1	-	-	-	-	-	-	-	-	-	-	-	-	-	-	-	-
Ōtarawairere-2	-	-	-	-	-	-	-	-	-	-	-	-	-	-	-	-
Ōtarawairere-3	-	-	-	-	-	-	-	-	-	-	-	-	-	-	-	-
Ōtarawairere-4	-	-	-	-	-	-	-	-	-	-	-	-	-	-	-	-
Ōtarawairere-5	-	-	-	-	-	-	-	-	-	-	-	-	-	-	-	-
OK240707-1C-1	0.4	0.5	4.7	3.1	0.9	0.1	0.6	11	5.3	1.3	7.6	0.6	1.5	66	81	1.6
OK240707-1C-2	0.1	0.1	2.1	5.7	2.4	0.2	1.4	21	1.3	0.8	12	1.0	0.6	31	26	0.3
OK240707-1C-3	0.3	0.1	7.0	4.5	2.4	0.3	0.1	9.0	4.2	1.2	8.8	0.4	0.9	84	74	2.5
OK240707-1C-4	0.6	0.2	5.8	1.4	0.8	0.0	0.1	6.5	1.9	1.4	2.9	0.6	0.5	66	47	2.3
OK240707-1C-5	0.2	0.1	0.7	1.8	0.5	0.3	0.3	11	1.3	0.9	6.5	0.5	0.2	32	55	2.7
OK240707-1D-1	0.3	0.2	1.0	2.8	0.9	0.1	0.9	2.7	4.6	0.3	8.8	0.9	0.1	43	42	0.4
OK240707-1D-2	0.2	0.4	0.2	3.2	2.2	0.1	1.5	5.5	4.4	0.8	2.4	0.2	0.3	84	83	1.4
OK240707-1D-3	0.1	0.3	1.8	4.4	0.8	0.3	1.6	10	3.0	0.8	2.9	0.5	0.7	38	27	1.4

OK240707-1E-2	8.6	8.7	1.9	15	4.6	0.6	0.0	34	3.4	2.2	20	0.6	2.1	50	44	3.2
OK240707-1E-5-B	-	-	-	-	-	-	-	-	-	-	-	-	-	-	-	-
OK240707-1F-1	0.7	1.5	1.6	6.3	2.0	0.2	2.3	12	1.9	2.7	3.7	1.0	1.1	19	15	2.4
OK240707-1F-2	0.5	1.5	0.9	4.0	4.0	0.5	0.4	32	1.5	2.9	3.6	1.1	2.4	16	26	1.5
OK240707-1F-3	0.3	1.7	1.1	0.9	1.1	0.2	1.0	16	1.4	1.2	1.3	0.4	0.9	8.8	12	0.5
OK240707-1F-4	0.8	1.8	4.6	3.9	1.8	0.4	0.4	4.0	5.3	0.5	15	0.8	0.7	130	106	1.9
OK240707-1F-5	0.3	1.3	1.1	3.4	1.8	0.4	2.3	23	1.2	1.6	6.1	0.9	0.3	9.3	17	1.3
OK240707-1F-6	0.3	1.3	1.7	3.2	1.2	0.4	0.7	18	2.2	0.9	3.4	0.7	0.8	18	21	1.3
OK240707-1J-1	0.5	0.7	1.4	2.0	0.8	0.2	0.5	7.6	6.5	0.6	9.2	0.5	0.3	38	48	1.0
OK240707-1J-2	0.1	0.3	0.5	2.3	1.2	0.1	0.9	3.8	2.5	1.0	6.9	0.3	0.5	60	35	0.4
OK240707-1J-4	0.1	0.3	1.6	4.1	1.6	0.3	1.0	8.8	3.2	1.1	4.1	0.4	0.6	33	53	1.4
OK240707-1L-1	0.4	0.3	2.5	4.6	0.7	0.2	2.0	5.0	2.4	1.0	6.5	0.8	0.4	36	73	2.7
OK240707-1L-2	0.3	0.2	0.8	6.2	0.6	0.2	-	4.1	3.5	1.1	3.3	0.3	0.3	36	51	1.0
OK240707-1L-3	0.2	0.2	1.0	4.5	1.3	0.2	1.3	4.6	4.9	0.8	2.1	0.2	0.5	26	41	0.8
OK240707-1L-3-A	-	-	-	-	-	-	-	-	-	-	-	-	-	-	-	-
OK240707-1L-4	0.7	1.0	1.1	13	0.8	0.4	0.7	4.3	5.4	1.2	6.1	0.4	0.2	42	32	1.1
OK240707-1L-5	-	-	-	-	-	-	-	-	-	-	-	-	-	-	-	-

Table 2.14: Lapilli glass trace element standard deviations of the mean compositions (Ce140-Ta181)

Lapilli-subgroup	Ce140	Pr141	Nd143	Sm147	Eu151	Gd157	Tb159	Gd160	Dy163	Ho165	Er166	Tm169	Yb173	Lu175	Hf179	Ta181
OK220707-1B-1	1.8	0.2	0.8	0.3	0.0	0.3	0.0	0.2	0.1	0.0	0.1	0.0	0.2	0.0	0.3	0.0
OK220707-1B-2	1.2	0.1	0.5	0.5	0.0	0.2	0.0	0.1	0.2	0.0	0.2	0.0	0.3	0.0	0.3	0.0
OK220707-1B-3	1.1	0.3	1.7	0.5	0.0	0.2	0.1	0.4	0.1	0.1	0.2	0.1	0.4	0.1	0.1	0.1
OK220707-1B-4	2.5	0.3	1.0	0.4	0.1	0.2	0.0	0.4	0.3	0.0	0.2	0.0	0.3	0.0	0.3	0.1
OK220707-1B-5	0.8	0.3	1.8	0.3	0.0	0.4	0.1	0.4	0.5	0.1	0.2	0.1	0.4	0.1	0.3	0.1
OK220707-1C-1	4.7	0.2	2.0	0.0	0.1	0.6	0.0	0.2	0.2	0.1	0.3	0.0	0.3	0.0	0.3	0.1
OK220707-1C-1-A	-	-	-	-	-	-	-	-	-	-	-	-	-	-	-	-
OK220707-1C-2	0.6	0.2	0.7	0.5	0.0	0.1	0.0	0.2	0.2	0.1	0.2	0.0	0.1	0.0	0.2	0.0
OK220707-1C-3	2.1	0.2	0.7	0.1	0.0	0.4	0.0	0.1	0.2	0.1	0.0	0.0	0.2	0.0	0.2	0.0
OK220707-1C-4	3.9	0.2	0.7	0.1	0.1	0.4	0.0	0.3	0.3	0.1	0.2	0.0	0.1	0.0	0.3	0.0
OK220707-1C-5	3.0	0.2	1.1	0.2	0.0	0.2	0.0	0.3	0.2	0.1	0.2	0.0	0.1	0.0	0.1	0.0
WHAK432A-1	2.5	0.3	3.7	0.7	0.1	0.7	0.1	0.7	0.5	0.0	0.3	0.1	0.3	0.0	0.2	0.1
WHAK432A-2	-	-	-	-	-	-	-	-	-	-	-	-	-	-	-	-
WHAK432A-3	1.0	0.4	1.9	0.8	0.0	0.4	0.1	0.8	0.4	0.1	0.1	0.0	0.6	0.1	1.1	0.1
WHAK432A-4	1.9	0.1	0.6	0.6	0.1	0.4	0.0	0.2	0.4	0.1	0.2	0.0	0.2	0.0	0.3	0.1
WHAK432A-5	1.4	1.8	1.1	0.7	0.1	0.3	0.1	0.1	0.6	0.1	0.1	0.0	0.8	0.0	0.4	0.1
WHAK432A-6	3.3	0.9	1.4	0.6	0.1	0.1	0.1	0.2	0.6	0.1	0.3	0.0	0.1	0.0	0.1	0.1
WHAK432B-1	1.7	0.2	1.2	0.2	0.1	0.2	0.0	0.1	0.1	0.0	0.2	0.0	0.2	0.0	0.2	0.0
WHAK432B-2	0.9	0.2	1.4	0.3	0.0	0.2	0.0	0.3	0.4	0.1	0.3	0.1	0.5	0.0	0.2	0.0
WHAK432B-3	0.8	0.3	0.6	0.3	0.0	0.2	0.0	0.3	0.1	0.1	0.2	0.0	0.3	0.0	0.3	0.1
WHAK432B-4	1.9	0.2	0.9	0.3	0.1	0.1	0.1	0.2	0.3	0.0	0.2	0.0	0.2	0.0	0.3	0.0

WHAK432B-5	1.3	0.3	1.1	0.2	0.0	0.3	0.0	0.2	0.4	0.0	0.1	0.0	0.2	0.0	0.3	0.0
OK220707-1E-1	1.0	0.6	2.7	0.4	0.1	0.5	0.1	0.1	0.3	0.2	0.4	0.1	0.7	0.1	0.6	0.0
OK220707-1E-1-A	-	-	-	-	-	-	-	-	-	-	-	-	-	-	-	-
WHAK432C-1	-	-	-	-	-	-	-	-	-	-	-	-	-	-	-	-
WHAK432C-2	2.0	0.7	1.7	0.4	0.1	1.2	0.1	0.6	0.3	0.1	0.3	0.1	0.4	0.1	1.0	0.2
WHAK432C-3	5.1	0.1	1.6	1.4	0.2	0.9	0.1	0.5	0.5	0.1	0.1	0.0	1.0	0.1	0.9	0.1
WHAK432C-4	1.3	0.2	1.6	0.2	0.1	0.4	0.1	0.2	0.3	0.0	0.1	0.0	0.4	0.0	0.5	0.0
WHAK432C-5	1.6	0.3	1.6	0.3	0.1	0.4	0.0	0.3	0.2	0.1	0.2	0.1	0.3	0.0	0.6	0.1
OK220707-1F-1	2.2	0.1	1.9	0.2	0.0	0.2	0.0	0.2	0.1	0.0	0.0	0.0	0.1	0.0	0.2	0.0
OK220707-1F-2	0.7	0.2	1.2	0.2	0.1	0.2	0.1	0.4	0.4	0.0	0.1	0.0	0.2	0.1	0.2	0.0
OK220707-1F-3	1.3	0.1	0.9	0.4	0.1	0.3	0.0	0.1	0.2	0.1	0.1	0.0	0.2	0.0	0.3	0.1
OK220707-1F-4	2.1	0.3	1.5	0.4	0.1	0.3	0.1	0.3	0.3	0.1	0.1	0.0	0.2	0.0	0.3	0.0
OK220707-1F-5	1.8	0.2	0.9	0.2	0.0	0.2	0.0	0.3	0.1	0.0	0.1	0.0	0.3	0.0	0.2	0.0
OK220707-1F-6	-	-	-	-	-	-	-	-	-	-	-	-	-	-	-	-
OK220707-1G-1	15	0.4	3.0	0.5	0.1	0.6	0.1	0.4	0.4	0.0	0.3	0.0	0.4	0.1	0.2	0.1
OK220707-1G-2	4.8	0.6	1.6	0.5	0.1	0.4	0.1	0.5	0.4	0.1	0.1	0.0	0.4	0.0	0.4	0.1
OK220707-1G-3	19	0.3	3.1	0.3	0.0	0.5	0.1	0.4	0.3	0.1	0.1	0.0	0.3	0.0	0.1	0.0
OK220707-1G-4	4.9	0.4	1.8	0.4	0.1	0.2	0.1	0.3	0.2	0.1	0.1	0.1	0.2	0.0	0.2	0.0
OK220707-1G-4-A	-	-	-	-	-	-	-	-	-	-	-	-	-	-	-	-
OK220707-1G-5	4.8	0.4	1.4	0.2	0.0	0.2	0.1	0.3	0.2	0.1	0.1	0.0	0.3	0.0	0.2	0.0
OK220707-1G-6	9.7	0.9	0.9	0.4	0.0	0.3	0.1	0.4	0.3	0.1	0.2	0.1	0.4	0.0	0.3	0.0
WHAK432L-1	1.5	0.2	1.0	0.8	0.1	0.4	0.1	0.1	0.6	0.1	0.4	0.0	0.1	0.1	0.6	0.1
WHAK432L-2	1.7	0.1	1.7	0.2	0.1	0.5	0.1	0.2	0.2	0.2	0.3	0.0	0.3	0.1	0.6	0.1

WHAK432L-3	1.0	0.2	0.9	0.4	0.1	0.3	0.0	0.3	0.3	0.1	0.2	0.0	0.4	0.0	0.3	0.0
WHAK432L-4	1.0	0.2	1.3	0.0	0.2	0.1	0.0	0.2	0.2	0.1	0.2	0.0	0.7	0.0	0.2	0.0
WHAK432L-5	1.4	0.2	1.9	0.7	0.1	0.7	0.2	0.1	0.3	0.1	0.3	0.0	0.3	0.1	0.4	0.1
OK220707-1I-1	3.4	1.0	3.0	0.2	0.0	0.3	0.1	0.4	0.5	0.1	0.1	0.1	0.2	0.0	0.1	0.0
OK220707-1I-2	11	1.3	4.5	1.1	0.1	0.6	0.1	1.1	0.3	0.1	0.3	0.1	0.3	0.1	0.3	0.0
OK220707-1I-3	4.5	0.5	2.8	0.5	0.0	0.3	0.1	0.2	0.4	0.0	0.2	0.0	0.3	0.0	0.3	0.0
OK220707-1I-4	6.3	0.9	2.5	1.0	0.1	0.7	0.2	0.4	0.3	0.1	0.2	0.1	0.1	0.0	0.1	0.1
OK220707-1I-5	1.5	0.3	0.5	0.2	0.1	0.3	0.0	0.2	0.3	0.0	0.0	0.0	0.1	0.0	0.2	0.1
WHAK432D-1	0.6	0.3	2.2	0.3	0.1	0.6	0.0	0.2	0.2	0.0	0.2	0.0	0.2	0.0	0.3	0.1
WHAK432D-2	2.5	0.3	2.1	0.4	0.1	0.1	0.0	0.5	0.7	0.1	0.1	0.0	0.3	0.0	0.4	0.1
WHAK432D-3	3.1	0.3	5.4	0.2	0.0	0.5	0.1	0.7	0.1	0.1	0.3	0.1	0.5	0.1	0.5	0.1
WHAK432D-4	1.1	0.2	1.7	0.2	0.1	0.4	0.1	0.3	0.4	0.1	0.2	0.0	0.2	0.1	0.3	0.0
WHAK432D-5	3.2	0.3	1.3	1.1	0.1	0.2	0.2	0.5	0.4	0.1	0.1	0.1	0.1	0.1	0.3	0.1
WHAK432E-1	13	1.2	5.7	1.0	0.1	0.9	0.0	0.5	0.6	0.1	0.1	0.1	0.4	0.0	0.3	0.1
WHAK432E-2	3.0	0.1	0.6	0.1	0.1	0.5	0.2	0.2	-	0.0	0.1	0.0	0.6	0.0	0.2	0.0
WHAK432E-3	9.4	0.5	2.8	0.5	0.1	0.3	0.0	0.5	0.3	0.1	0.2	0.0	0.4	0.1	0.3	0.0
WHAK432E-4	1.7	0.2	1.1	0.2	0.1	0.1	0.1	0.2	0.2	0.0	0.0	0.0	0.2	0.0	0.4	0.0
WHAK432E-5	7.0	1.7	3.3	0.6	0.1	0.8	0.1	1.0	0.2	0.1	0.3	0.1	0.4	0.1	0.5	0.1
OK220707-1L-1	6.8	0.3	1.3	0.9	0.2	0.2	0.0	0.2	0.3	0.1	0.1	0.1	0.3	0.1	0.4	0.0
OK220707-1L-2	3.9	0.1	1.1	0.1	0.0	0.1	0.1	0.3	0.4	0.1	0.2	0.0	0.1	0.0	0.3	0.1
OK220707-1L-3	2.1	0.3	1.7	0.2	0.0	0.2	0.0	0.3	0.1	0.0	0.1	0.0	0.3	0.1	0.1	0.1
OK220707-1L-4	2.8	0.5	1.7	0.5	0.0	0.2	0.0	0.3	0.3	0.1	0.1	0.0	0.2	0.0	0.2	0.0
OK220707-1L-5	3.4	0.3	1.7	0.3	0.0	0.2	0.0	0.2	0.2	0.1	0.1	0.0	0.2	0.0	0.2	0.1

WHAK432F-1	3.0	0.5	1.7	0.3	0.1	0.2	0.0	0.4	0.5	0.1	0.3	0.1	0.3	0.1	1.0	0.1
WHAK432F-2	2.6	0.4	2.0	0.9	0.1	0.6	0.0	0.6	0.4	0.1	0.1	0.1	0.3	0.1	0.6	0.1
WHAK432F-3	1.6	0.5	0.9	0.7	0.0	0.3	0.0	0.5	0.3	0.1	0.3	0.0	0.3	0.1	0.3	0.1
WHAK432F-4	1.1	0.4	1.5	0.6	0.1	0.5	0.0	0.6	0.5	0.0	0.3	0.1	0.2	0.1	0.6	0.2
WHAK432F-5	2.8	0.2	2.1	0.8	0.1	0.8	0.1	0.3	0.4	0.0	0.3	0.0	0.3	0.0	0.4	0.1
OK220707-1N-1	3.0	0.1	0.7	0.3	0.1	0.3	0.0	0.2	0.2	0.0	0.1	0.0	0.2	0.0	0.2	0.1
OK220707-1N-2	3.9	0.3	0.9	0.4	0.1	0.4	0.1	0.3	0.3	0.1	0.2	0.0	0.4	0.1	0.2	0.1
OK220707-1N-3	2.1	0.3	1.3	0.3	0.0	0.2	0.1	0.4	0.1	0.1	0.2	0.0	0.2	0.1	0.3	0.1
OK220707-1N-4	5.3	0.5	1.5	0.3	0.1	0.4	0.0	0.5	0.5	0.0	0.3	0.0	0.5	0.0	0.4	0.1
OK220707-1N-5	4.6	0.3	1.2	0.4	0.1	0.2	0.1	0.4	0.4	0.1	0.2	0.0	0.3	0.1	0.3	0.1
OK220707-1N-6	4.5	0.4	1.7	0.5	0.1	0.2	0.0	0.3	0.4	0.1	0.2	0.0	0.2	0.0	0.3	0.0
WHAK432G-1	2.2	0.4	0.6	0.2	0.0	0.3	0.1	0.2	0.3	0.1	0.1	0.0	0.2	0.0	0.2	0.1
WHAK432G-2	1.3	0.1	0.6	0.2	0.1	0.2	0.0	0.2	0.3	0.1	0.1	0.0	0.3	0.0	0.3	0.0
WHAK432G-3	3.9	0.1	1.7	0.5	0.1	0.4	0.1	0.4	0.5	0.1	0.3	0.0	0.5	0.0	0.5	0.1
WHAK432G-4	1.2	0.2	0.9	0.3	0.0	0.3	0.0	0.3	0.3	0.0	0.2	0.0	0.2	0.0	0.3	0.0
WHAK432G-5	6.3	0.6	2.5	0.2	0.1	0.2	0.0	0.4	0.4	0.1	0.2	0.1	0.1	0.0	0.4	0.0
OK220707-1O-1	2.3	0.5	1.1	0.6	0.0	0.8	0.1	0.4	0.5	0.1	0.5	0.0	0.4	0.1	0.2	0.1
OK220707-1O-2	7.5	0.7	3.3	1.0	0.0	0.6	0.1	0.5	0.8	0.1	0.5	0.1	0.7	0.1	0.4	0.1
OK220707-1O-3	2.4	0.5	1.4	0.4	0.0	0.3	0.1	0.3	0.4	0.1	0.3	0.0	0.3	0.1	0.7	0.2
OK220707-1O-4	5.9	0.9	2.0	0.5	0.0	0.3	0.1	0.7	0.6	0.1	0.3	0.1	0.6	0.1	0.6	0.3
OK220707-1O-5	3.9	0.3	0.9	0.2	0.0	0.1	0.1	0.3	0.1	0.1	0.1	0.0	0.1	0.0	0.3	0.1
OK220707-1O-6	5.9	0.4	1.4	0.3	0.0	0.2	0.0	0.3	0.4	0.0	0.1	0.0	0.3	0.1	0.4	0.2
OK220707-1O-7	3.0	0.2	0.7	0.4	0.0	0.1	0.1	0.3	0.2	0.1	0.2	0.0	0.2	0.1	0.1	0.1

OK220707-1P-1	3.0	0.3	0.8	0.2	0.0	0.1	0.0	0.3	0.2	0.1	0.2	0.0	0.2	0.0	0.4	0.0
OK220707-1P-2	3.5	0.4	1.0	0.3	0.0	0.3	0.0	0.2	0.3	0.0	0.1	0.0	0.2	0.0	0.3	0.0
OK220707-1P-3	2.5	0.2	1.2	0.4	0.1	0.2	0.1	0.2	0.2	0.1	0.1	0.0	0.2	0.0	0.2	0.0
OK220707-1P-5	3.2	0.3	0.8	0.3	0.1	0.2	0.0	0.4	0.3	0.1	0.2	0.1	0.2	0.0	0.3	0.0
OK220707-1P-6	1.7	0.4	1.3	0.3	0.0	0.2	0.0	0.1	0.2	0.0	0.2	0.0	0.2	0.0	0.2	0.0
OK220707-1Q-1	3.2	0.3	0.9	0.2	0.1	0.3	0.1	0.2	0.3	0.1	0.2	0.0	0.3	0.0	0.1	0.0
OK220707-1Q-2	1.5	0.2	0.6	0.5	0.1	0.1	0.0	0.2	0.3	0.1	0.2	0.0	0.1	0.0	0.2	0.1
OK220707-1Q-3	4.5	0.4	1.3	0.4	0.1	0.4	0.1	0.3	0.3	0.1	0.1	0.1	0.2	0.0	0.2	0.0
OK220707-1Q-4	2.9	0.2	1.2	0.3	0.1	0.3	0.0	0.1	0.2	0.1	0.1	0.0	0.3	0.0	0.2	0.0
OK220707-1Q-5	2.3	0.2	0.8	0.4	0.1	0.3	0.1	0.4	0.3	0.0	0.2	0.0	0.3	0.0	0.3	0.0
WHAK432H-1	1.8	0.2	0.9	0.3	0.1	0.3	0.0	0.3	0.2	0.0	0.1	0.0	0.2	0.0	0.2	0.0
WHAK432H-2	1.3	0.2	0.6	0.3	0.0	0.2	0.0	0.1	0.2	0.1	0.2	0.0	0.1	0.0	0.5	0.0
WHAK432H-3	1.7	0.3	1.9	0.4	0.1	0.6	0.1	0.3	0.2	0.1	0.2	0.0	0.2	0.0	0.4	0.0
WHAK432H-4	2.4	0.2	1.2	0.2	0.1	0.4	0.0	0.1	0.1	0.0	0.2	0.0	0.2	0.0	0.3	0.0
WHAK432H-5	1.4	0.2	0.9	0.3	0.0	0.3	0.1	0.2	0.2	0.0	0.2	0.0	0.2	0.0	0.3	0.0
WHAK432I-1	3.1	0.5	1.8	0.5	0.2	0.4	0.1	0.4	0.4	0.1	0.2	0.1	0.3	0.1	0.4	0.0
WHAK432I-1-A	-	-	-	-	-	-	-	-	-	-	-	-	-	-	-	-
WHAK432I-2	2.2	0.2	0.4	0.3	0.1	0.5	0.1	0.5	0.3	0.1	0.2	0.1	0.3	0.0	0.7	0.0
WHAK432I-2-A	-	-	-	-	-	-	-	-	-	-	-	-	-	-	-	-
WHAK432I-3	1.2	0.2	1.5	0.5	0.1	0.6	0.0	0.3	0.3	0.1	0.2	0.1	0.4	0.1	0.2	0.1
WHAK432I-4	1.3	0.4	1.1	0.7	0.1	0.3	0.1	0.5	0.6	0.0	0.3	0.0	0.5	0.1	0.4	0.1
WHAK432I-5	2.4	0.4	0.9	0.3	0.0	0.6	0.1	0.1	0.3	0.0	0.2	0.0	0.3	0.0	0.2	0.0
WHAK432I-5-A	-	-	-	-	-	-	-	-	-	-	-	-	-	-	-	-

WHAK432J-1	1.9	0.2	0.7	0.3	0.0	0.3	0.0	0.3	0.2	0.0	0.2	0.0	0.2	0.0	0.4	0.0
WHAK432J-2	2.0	0.3	1.4	0.2	0.0	0.7	0.0	0.3	0.2	0.1	0.1	0.0	0.2	0.0	0.3	0.0
WHAK432J-3	1.4	0.3	1.5	0.3	0.1	0.4	0.0	0.2	0.1	0.0	0.2	0.0	0.3	0.0	0.4	0.0
WHAK432J-4	2.1	0.2	1.4	0.4	0.1	0.6	0.1	0.3	0.3	0.1	0.1	0.0	0.2	0.0	0.1	0.0
WHAK432J-5	0.8	0.1	0.7	0.3	0.1	0.4	0.0	0.2	0.2	0.0	0.1	0.0	0.2	0.0	0.2	0.0
OK240707-1A-1	-	-	-	-	-	-	-	-	-	-	-	-	-	-	-	-
OK240707-1A-2	-	-	-	-	-	-	-	-	-	-	-	-	-	-	-	-
OK240707-1A-3	-	-	-	-	-	-	-	-	-	-	-	-	-	-	-	-
OK240707-1A-4	-	-	-	-	-	-	-	-	-	-	-	-	-	-	-	-
OK240707-1A-5	1.8	0.2	0.6	0.3	0.0	0.3	0.0	0.1	0.3	0.0	0.3	0.0	0.2	0.0	0.2	0.1
Ōtarawairere-1	-	-	-	-	-	-	-	-	-	-	-	-	-	-	-	-
Ōtarawairere-2	-	-	-	-	-	-	-	-	-	-	-	-	-	-	-	-
Ōtarawairere-3	-	-	-	-	-	-	-	-	-	-	-	-	-	-	-	-
Ōtarawairere-4	-	-	-	-	-	-	-	-	-	-	-	-	-	-	-	-
Ōtarawairere-5	-	-	-	-	-	-	-	-	-	-	-	-	-	-	-	-
OK240707-1C-1	1.6	0.2	2.0	0.4	0.1	0.3	0.1	0.4	0.2	0.2	0.2	0.0	0.3	0.1	0.2	0.1
OK240707-1C-2	1.4	0.1	3.0	0.4	0.0	0.1	0.0	0.0	0.7	0.1	0.1	0.1	0.1	0.1	0.4	0.0
OK240707-1C-3	5.0	0.2	1.5	0.4	0.0	0.4	0.1	0.3	0.1	0.1	0.2	0.1	0.5	0.0	0.2	0.1
OK240707-1C-4	2.4	0.6	2.0	0.4	0.1	0.1	0.0	0.5	0.5	0.0	0.3	0.1	0.4	0.1	0.1	0.1
OK240707-1C-5	4.2	0.1	0.9	0.4	0.1	0.3	0.0	0.2	0.1	0.1	0.1	0.0	0.2	0.1	0.4	0.0
OK240707-1D-1	1.5	0.4	0.6	0.6	0.1	0.1	0.0	0.0	0.2	0.0	0.2	0.0	0.1	0.0	0.3	0.1
OK240707-1D-2	1.5	0.2	0.2	0.4	0.1	0.3	0.0	0.2	0.2	0.0	0.1	0.0	0.1	0.1	0.3	0.1
OK240707-1D-3	5.5	0.5	1.8	0.6	0.1	0.4	0.0	0.2	0.1	0.1	0.2	0.0	0.2	0.0	0.4	0.0

OK240707-1E-2	4.8	0.1	1.7	0.2	0.2	0.4	0.0	0.3	0.4	0.1	0.3	0.1	0.3	0.0	0.6	0.0
OK240707-1E-5-B	-	-	-	-	-	-	-	-	-	-	-	-	-	-	-	-
OK240707-1F-1	4.1	0.4	2.5	0.6	0.1	0.4	0.1	0.7	0.6	0.1	0.4	0.1	0.2	0.1	0.3	0.1
OK240707-1F-2	7.4	0.5	2.0	0.7	0.1	0.6	0.0	0.4	0.4	0.1	0.5	0.0	0.2	0.1	0.5	0.1
OK240707-1F-3	2.0	0.5	0.7	0.5	0.0	0.6	0.0	0.2	0.5	0.0	0.3	0.1	0.3	0.0	0.2	0.0
OK240707-1F-4	4.2	0.4	2.1	0.6	0.1	0.5	0.1	0.2	0.2	0.0	0.1	0.1	0.6	0.1	0.2	0.1
OK240707-1F-5	4.1	0.5	1.7	0.5	0.1	0.4	0.1	0.4	0.5	0.1	0.3	0.1	0.4	0.0	0.3	0.0
OK240707-1F-6	5.3	0.4	2.0	0.5	0.0	0.3	0.0	0.2	0.3	0.0	0.2	0.0	0.2	0.0	0.6	0.1
OK240707-1J-1	1.5	0.1	1.0	0.1	0.0	0.3	0.0	0.2	0.2	0.0	0.1	0.0	0.1	0.0	0.3	0.0
OK240707-1J-2	2.4	0.4	1.8	0.3	0.1	0.3	0.0	0.2	0.1	0.1	0.4	0.0	0.2	0.0	0.3	0.1
OK240707-1J-4	3.1	0.4	1.5	0.4	0.0	0.3	0.0	0.2	0.3	0.1	0.2	0.0	0.3	0.0	0.2	0.0
OK240707-1L-1	3.3	0.5	2.7	0.8	0.1	0.3	0.0	0.4	0.2	0.0	0.3	0.0	0.3	0.0	0.3	0.1
OK240707-1L-2	2.0	0.3	1.1	0.4	0.1	0.1	0.1	0.3	0.4	0.1	0.1	0.0	0.2	0.1	0.3	0.0
OK240707-1L-3	1.6	0.5	0.6	0.3	0.0	0.2	0.1	0.2	0.2	0.1	0.2	0.0	0.1	0.1	0.2	0.0
OK240707-1L-3-A	-	-	-	-	-	-	-	-	-	-	-	-	-	-	-	-
OK240707-1L-4	2.7	0.4	1.0	0.2	0.0	0.2	0.1	0.2	0.1	0.0	0.2	0.0	0.4	0.0	0.2	0.0
OK240707-1L-5	-	-	-	-	-	-	-	-	-	-	-	-	-	-	-	-

Table 2.15: Lapilli glass trace element standard deviations of the mean compositions (Tl203-U238)

Lapilli-subgroup	Tl203	Tl205	Pb206	Pb207	Th232	U235	U238
OK220707-1B-1	0.1	0.1	0.9	0.7	0.3	2.5	0.2
OK220707-1B-2	0.0	0.0	1.2	0.8	0.5	3.6	0.2
OK220707-1B-3	0.1	0.0	0.4	0.1	0.5	2.6	0.1
OK220707-1B-4	0.1	0.0	1.2	1.1	0.4	3.5	0.2
OK220707-1B-5	0.1	0.1	1.3	1.4	0.4	3.8	0.2
OK220707-1C-1	0.1	0.1	1.0	0.5	0.5	2.4	0.2
OK220707-1C-1-A	-	-	-	-	-	-	-
OK220707-1C-2	0.0	0.0	0.7	0.3	0.4	2.1	0.1
OK220707-1C-3	0.1	0.0	1.2	0.5	0.3	3.2	0.2
OK220707-1C-4	0.0	0.1	0.8	0.8	0.7	1.0	0.2
OK220707-1C-5	0.1	0.1	0.9	0.5	0.6	3.0	0.0
WHAK432A-1	0.0	0.0	1.2	1.0	0.4	5.2	0.1
WHAK432A-2	-	-	-	-	-	-	-
WHAK432A-3	0.1	0.0	0.9	1.0	0.4	4.0	0.3
WHAK432A-4	0.0	0.0	0.2	0.4	0.7	2.9	0.1
WHAK432A-5	0.1	0.0	0.9	0.7	0.8	1.8	0.1
WHAK432A-6	0.1	0.1	0.8	1.7	2.3	4.1	0.1
WHAK432B-1	0.1	0.1	0.7	0.5	0.4	2.8	0.1
WHAK432B-2	0.1	0.0	0.8	0.1	0.4	1.7	0.1
WHAK432B-3	0.0	0.1	0.8	0.4	0.7	4.5	0.2
WHAK432B-4	0.0	0.1	0.5	0.8	0.5	2.8	0.1

WHAK432B-5	0.1	0.1	0.5	0.8	0.5	1.9	0.1
OK220707-1E-1	0.2	0.0	1.3	1.4	1.6	3.4	0.3
OK220707-1E-1-A	-	-	-	-	-	-	-
WHAK432C-1	-	-	-	-	-	-	-
WHAK432C-2	0.1	0.1	0.9	1.2	0.8	6.4	0.1
WHAK432C-3	0.1	0.0	1.5	0.9	0.4	-	0.3
WHAK432C-4	0.0	0.1	0.6	0.6	0.2	2.6	0.1
WHAK432C-5	0.2	0.1	0.7	0.3	0.6	6.8	0.3
OK220707-1F-1	0.0	0.1	0.2	0.2	0.3	2.1	0.0
OK220707-1F-2	0.1	0.1	1.5	1.1	0.8	0.7	0.3
OK220707-1F-3	0.1	0.0	0.8	0.7	0.3	2.0	0.1
OK220707-1F-4	0.1	0.1	0.8	0.6	0.2	1.2	0.1
OK220707-1F-5	0.1	0.1	0.8	0.6	0.4	1.6	0.1
OK220707-1F-6	-	-	-	-	-	-	-
OK220707-1G-1	0.1	0.1	1.4	1.2	1.4	2.8	0.5
OK220707-1G-2	0.1	0.1	0.6	0.6	0.8	3.5	0.2
OK220707-1G-3	0.1	0.1	1.5	0.8	0.6	5.0	0.3
OK220707-1G-4	0.1	0.1	1.6	1.4	1.1	0.7	0.1
OK220707-1G-4-A	-	-	-	-	-	-	-
OK220707-1G-5	0.1	0.1	1.6	0.9	0.7	4.6	0.2
OK220707-1G-6	0.1	0.1	1.6	1.3	1.7	4.0	0.5
WHAK432L-1	0.1	0.1	1.3	0.4	0.7	7.3	0.3
WHAK432L-2	0.2	0.2	1.8	1.0	0.7	5.4	0.3

WHAK432L-3	0.1	0.0	1.1	0.7	0.3	4.5	0.2
WHAK432L-4	0.2	0.1	0.9	1.7	0.6	1.3	0.1
WHAK432L-5	0.2	0.1	1.5	1.2	0.6	3.4	0.4
OK220707-1I-1	0.1	0.0	1.7	1.6	0.5	3.5	0.3
OK220707-1I-2	0.0	0.0	0.0	0.4	1.8	0.5	0.5
OK220707-1I-3	0.0	0.1	1.1	0.8	0.7	3.9	0.4
OK220707-1I-4	0.3	0.9	16	1.2	0.3	24	3.6
OK220707-1I-5	0.1	0.0	0.9	1.1	1.2	2.1	0.1
WHAK432D-1	0.2	0.1	2.1	1.7	0.6	3.0	0.2
WHAK432D-2	0.2	0.0	1.8	1.2	1.3	3.5	0.0
WHAK432D-3	0.3	0.3	2.7	1.8	1.9	3.2	0.6
WHAK432D-4	0.2	0.1	0.5	0.8	0.8	6.3	0.3
WHAK432D-5	0.1	0.1	2.6	0.9	1.2	5.8	0.3
WHAK432E-1	0.1	0.0	1.0	0.8	1.2	3.3	0.3
WHAK432E-2	0.1	0.1	0.9	0.2	0.8	2.4	0.1
WHAK432E-3	0.1	0.1	1.0	1.1	1.1	4.7	0.2
WHAK432E-4	0.2	0.1	1.0	0.9	0.6	4.7	0.1
WHAK432E-5	0.2	0.1	1.2	1.3	2.1	7.4	0.2
OK220707-1L-1	0.1	0.1	0.8	1.1	0.8	5.6	0.2
OK220707-1L-2	0.1	0.1	0.8	2.0	0.8	1.9	0.2
OK220707-1L-3	0.1	0.1	0.4	1.2	1.1	3.0	0.2
OK220707-1L-4	0.1	0.0	0.3	0.7	1.5	3.5	0.2
OK220707-1L-5	0.1	0.0	0.5	0.7	0.6	2.2	0.3

WHAK432F-1	0.2	0.1	1.6	4.5	4.5	9.3	0.2
WHAK432F-2	0.2	0.1	2.7	2.5	0.8	9.4	0.2
WHAK432F-3	0.2	0.1	1.4	0.9	0.2	3.6	0.2
WHAK432F-4	0.1	0.1	1.4	1.5	0.5	5.4	0.3
WHAK432F-5	0.2	0.2	1.2	1.7	1.6	4.7	0.6
OK220707-1N-1	0.1	0.0	1.1	0.7	0.9	4.1	0.1
OK220707-1N-2	0.1	0.1	2.2	1.5	0.8	4.7	0.2
OK220707-1N-3	0.1	0.1	0.9	1.0	0.9	5.6	0.3
OK220707-1N-4	0.0	0.1	0.9	1.4	1.6	2.5	0.7
OK220707-1N-5	0.1	0.1	0.9	1.5	0.5	2.9	0.1
OK220707-1N-6	0.1	0.1	0.9	1.4	1.3	3.4	0.1
WHAK432G-1	0.1	0.1	1.0	0.5	1.6	3.9	0.3
WHAK432G-2	0.0	0.1	1.6	1.5	0.9	0.9	0.1
WHAK432G-3	0.2	0.1	2.0	0.7	2.1	3.4	0.3
WHAK432G-4	0.1	0.1	1.2	1.1	1.2	0.9	0.1
WHAK432G-5	0.1	0.0	2.3	0.9	1.8	4.0	0.2
OK220707-1O-1	0.1	0.1	1.7	0.9	1.5	4.9	0.5
OK220707-1O-2	0.1	0.2	0.8	2.3	2.4	2.9	0.7
OK220707-1O-3	0.1	0.1	4.6	2.5	2.8	2.6	0.1
OK220707-1O-4	0.1	0.1	4.6	5.3	3.1	1.6	0.3
OK220707-1O-5	0.1	0.1	0.9	0.6	0.8	3.7	0.5
OK220707-1O-6	0.1	0.1	2.0	1.7	1.9	5.1	0.5
OK220707-1O-7	0.1	0.0	2.2	2.1	1.0	2.2	0.4

OK220707-1P-1	0.1	0.0	0.7	0.8	0.7	2.3	0.1
OK220707-1P-2	0.1	0.1	1.0	0.4	0.4	1.9	0.2
OK220707-1P-3	0.1	0.1	0.6	0.4	0.5	3.5	0.2
OK220707-1P-5	0.1	0.0	1.2	0.5	1.0	3.0	0.1
OK220707-1P-6	0.1	0.1	0.6	0.6	0.7	1.8	0.1
OK220707-1Q-1	0.1	0.1	1.3	0.7	0.8	2.5	0.3
OK220707-1Q-2	0.1	0.1	1.4	0.4	0.9	3.2	0.1
OK220707-1Q-3	0.1	0.1	1.0	1.1	1.1	3.6	0.2
OK220707-1Q-4	0.1	0.1	1.0	0.8	0.7	1.3	0.2
OK220707-1Q-5	0.1	0.1	1.0	1.3	0.5	3.2	0.2
WHAK432H-1	0.0	0.0	0.5	0.6	0.2	2.3	0.1
WHAK432H-2	0.0	0.0	0.3	1.2	0.4	2.1	0.2
WHAK432H-3	0.1	0.0	0.8	0.7	0.5	1.4	0.1
WHAK432H-4	0.1	0.0	0.8	0.7	0.7	2.3	0.1
WHAK432H-5	0.1	0.1	0.8	0.6	0.5	2.1	0.1
WHAK432I-1	0.1	0.1	1.3	1.0	0.7	5.0	0.2
WHAK432I-1-A	-	-	-	-	-	-	-
WHAK432I-2	0.1	0.1	1.5	0.8	0.6	4.7	0.2
WHAK432I-2-A	-	-	-	-	-	-	-
WHAK432I-3	0.2	0.1	0.8	0.7	0.4	4.5	0.2
WHAK432I-4	0.1	0.1	0.7	1.2	0.8	5.7	0.2
WHAK432I-5	0.0	0.0	0.5	0.8	0.7	3.4	0.1
WHAK432I-5-A	-	-	-	-	-	-	-

WHAK432J-1	0.0	0.0	0.4	0.4	0.5	2.6	0.1
WHAK432J-2	0.0	0.0	0.9	1.2	0.5	1.0	0.1
WHAK432J-3	0.0	0.0	0.5	1.0	0.6	2.8	0.1
WHAK432J-4	0.1	0.1	0.7	0.4	0.9	1.2	0.1
WHAK432J-5	0.0	0.0	0.5	0.5	0.5	1.5	0.1
OK240707-1A-1	-	-	-	-	-	-	-
OK240707-1A-2	-	-	-	-	-	-	-
OK240707-1A-3	-	-	-	-	-	-	-
OK240707-1A-4	-	-	-	-	-	-	-
OK240707-1A-5	0.1	0.1	1.2	1.0	0.8	2.0	0.1
Ōtarawairere-1	-	-	-	-	-	-	-
Ōtarawairere-2	-	-	-	-	-	-	-
Ōtarawairere-3	-	-	-	-	-	-	-
Ōtarawairere-4	-	-	-	-	-	-	-
Ōtarawairere-5	-	-	-	-	-	-	-
OK240707-1C-1	0.1	0.4	4.9	1.0	1.2	5.4	0.8
OK240707-1C-2	0.1	0.3	1.7	3.2	2.2	5.1	0.2
OK240707-1C-3	0.1	0.1	1.5	1.3	1.2	4.8	0.3
OK240707-1C-4	0.0	0.1	0.6	0.7	2.0	5.5	0.7
OK240707-1C-5	0.1	0.1	0.5	0.9	1.2	3.7	0.4
OK240707-1D-1	0.1	0.1	1.3	2.4	1.1	1.0	0.1
OK240707-1D-2	0.1	0.1	0.3	1.1	0.3	5.3	0.2
OK240707-1D-3	0.1	0.0	0.9	0.6	0.9	2.0	0.1

OK240707-1E-2	0.2	0.2	1.2	0.6	2.0	1.8	0.6
OK240707-1E-5-B	-	-	-	-	-	-	-
OK240707-1F-1	0.1	0.1	3.3	0.8	1.9	12	1.2
OK240707-1F-2	0.1	0.1	1.1	1.3	2.1	5.0	0.5
OK240707-1F-3	0.2	0.0	1.5	1.9	0.8	4.5	0.5
OK240707-1F-4	0.1	0.1	2.0	1.7	1.8	16	4.8
OK240707-1F-5	0.1	0.1	1.3	1.6	1.4	4.2	0.5
OK240707-1F-6	0.1	0.1	2.7	1.8	1.8	8.1	0.2
OK240707-1J-1	0.1	0.0	1.2	0.7	0.4	1.5	0.1
OK240707-1J-2	0.1	0.1	1.0	0.4	0.6	5.2	0.1
OK240707-1J-4	0.0	0.1	1.0	0.4	0.6	4.2	0.3
OK240707-1L-1	0.2	0.1	1.3	1.2	1.1	3.5	0.1
OK240707-1L-2	0.1	0.1	1.0	0.6	0.6	3.5	0.1
OK240707-1L-3	0.1	0.1	1.3	1.1	1.2	3.5	0.1
OK240707-1L-3-A	-	-	-	-	-	-	-
OK240707-1L-4	0.1	0.1	1.0	0.2	0.8	3.5	0.1
OK240707-1L-5	-	-	-	-	-	-	-

2.7 References

Alloway, B. v, Pillans, B. J., Sandhu, A. S., & Westgate, J. A. (1993). Expressed Revision of the marine chronology in the Wanganui Basin, New Zealand, based on the isothermal plateau fission-track dating of tephra horizons. In Sedimentary Geology (Vol. 82).

Bachmann, O., & Bergantz, G. W. (2004). On the origin of crystal-poor rhyolites: Extracted from batholithic crystal mushes. Journal of Petrology, 45(8), 1565–1582. https://doi.org/10.1093/petrology/egh019

Bachmann, O., & Bergantz, G. W. (2008). The magma reservoirs that feed supereruptions. Elements, 4(1), 17–21. https://doi.org/10.2113/GSELEMENTS.4.1.17

Barboni, M., Annen, C., & Schoene, B. (2015). Evaluating the construction and evolution of upper crustal magma reservoirs with coupled U/Pb zircon geochronology and thermal modeling: A case study from the Mt. Capanne pluton (Elba, Italy). Earth and Planetary Science Letters, 432, 436–448. https://doi.org/10.1016/j.epsl.2015.09.043

Bégué, F., Deering, C. D., Gravley, D. M., Kennedy, B. M., Chambefort, I., Gualda, G. A. R., & Bachmann, O. (2014). Extraction, storage and eruption of multiple isolated magma batches in the paired Mamaku and Ohakuri eruption, Taupō volcanic zone, New Zealand. Journal of Petrology, 55(8), 1653–1684. https://doi.org/10.1093/petrology/egu038

Bégué, F., Gualda, G. A. R., Ghiorso, M. S., Pamukcu, A. S., Kennedy, B. M., Gravley, D. M., Deering, C. D., & Chambefort, I. (2014). Phase-equilibrium geobarometers for silicic rocks based on rhyolite-MELTS. Part 2: application to Taupō Volcanic Zone rhyolites. Contributions to Mineralogy and Petrology, 168, 1–16. https://doi.org/10.1007/s00410-014-1082-7

Blundy, J. D., & Cashman, K. v. (2008). Petrologic reconstruction of Magmatic System Variables and Processes. Reviews in Mineralogy & Geochemistry, 69, 179–239. https://doi.org/10.2138/rmg.2008.69.6

Boehnke, P., Watson, E. B., Trail, D., Harrison, T. M., & Schmitt, A. K. (2013). Zircon saturation re-revisited. Chemical Geology, 351, 324–334. https://doi.org/10.1016/j.chemgeo.2013.05.028

Bonadonna, C., Costa, A., Folch, A., & Koyaguchi, T. (2015). Chapter 33 - Tephra Dispersal and Sedimentation. In H. Sigurdsson (Ed.), The Encyclopedia of Volcanoes (Second Edition) (pp. 587–597). Academic Press. https://doi.org/10.1016/B978-0-12-385938-9.00033-X

Bonadonna, C., & Phillips, J. C. (2003). Sedimentation from strong volcanic plumes. Journal of Geophysical Research: Solid Earth, 108(B7). https://doi.org/10.1029/2002jb002034

Briggs, N. D. (1976a). Recognition and correlation of subdivisions within the Whakamaru ignimbrite, central North Island, New Zealand. New Zealand Journal of Geology and Geophysics, 19(4), 463–501. https://doi.org/10.1080/00288306.1976.10423540

Briggs, N. D. (1976b). Welding and crystallisation zonation in Whakamaru Ignimbrite, central North Island, New Zealand. New Zealand Journal of Geology and Geophysics, 19(2), 189–212. https://doi.org/10.1080/00288306.1976.10423517

Brown, R. J., Bonadonna, C., & Durant, A. J. (2012). A review of volcanic ash aggregation. Physics and Chemistry of the Earth, 45–46, 65–78. https://doi.org/10.1016/j.pce.2011.11.001

Brown, R. J., & D. M. Andrews, G. (2015). Chapter 36 - Deposits of Pyroclastic Density Currents. In H. Sigurdsson (Ed.), The Encyclopedia of Volcanoes (Second Edition) (pp. 631–648). Academic Press.

https://doi.org/://doi.org/10.1016/B978-0-12-385938-9.00036-5

Brown, S. J. A. (1994). Geology and geochemistry of the Whakamaru Group ignimbrites, and associated rhyolite domes, Taupō Volcanic Zone, New Zealand.

Brown, S. J. A., & Fletcher, I. R. (1999). SHRIMP U-Pb dating of the preeruption growth history of zircons from the 340 ka Whakamaru Ignimbrite, New Zealand: Evidence for >250 k.y. magma residence times. Geology, 27(11), 1035–1038. https://doi.org/10.1130/0091-7613(1999)027<1035:supdot>2.3.co;2

Brown, S. J. A., Wilson, C. J. N., Cole, J. W., & Wooden, J. L. (1998). THIS ONE The Whakamaru group ignimbrites, Taupō Volcanic Zone, New Zealand: Evidence for reverse tapping of a zoned silicic magmatic system. Journal of Volcanology and Geothermal Research, 84(1–2), 1–37. https://doi.org/10.1016/S0377-0273(98)00020-1

Carr, R. G. (1994). Physical geology and eruptive history of the Matahina Ignimbrite, Taupō Volcanic Zone, North Island, New Zealand. New Zealand Journal of Geology and Geophysics, 37(3), 319–344. https://doi.org/10.1080/00288306.1994.9514624

Cashman, K. v., & Giordano, G. (2014). Calderas and magma reservoirs. Journal of Volcanology and Geothermal Research, 288, 28–45. https://doi.org/10.1016/j.jvolgeores.2014.09.007

Chamberlain, K. J., Wilson, C. J. N., Wallace, P. J., & Millet, M. A. (2015). Micro-analytical perspectives on the bishop tuff and its magma chamber. Journal of Petrology, 56(3), 605–640. https://doi.org/10.1093/petrology/egv012

Charlier, B. L. A., Bachmann, O., Davidson, J. P., Dungan, M. A., & Morgan, D. J. (2007). The Upper Crustal Evolution of a Large Silicic Magma Body: Evidence from Crystal-scale Rb-Sr Isotopic Heterogeneities in the Fish Canyon Magmatic System, Colorado. Journal of Petrology, 48(10), 1875–1894. https://doi.org/10.1093/petrology/egm043

Cooper, G. F., Morgan, D. J., & Wilson, C. J. N. (2017). Rapid assembly and rejuvenation of a large silicic magmatic system: Insights from mineral diffusive profiles in the Kidnappers and Rocky Hill deposits, New Zealand. Earth and Planetary Science Letters, 473, 1–13. https://doi.org/10.1016/j.epsl.2017.05.036

Cooper, G. F., Wilson, C. J. N., Millet, M. A., Baker, J. A., & Smith, E. G. C. (2012). Systematic tapping of independent magma chambers during the 1Ma Kidnappers supereruption. Earth and Planetary Science Letters, 313–314(1), 23–33. https://doi.org/10.1016/j.epsl.2011.11.006

Cooper, K. M. (2017). What Does a Magma Reservoir Look Like? The "Crystal's-Eye" View. ElEmEnts, 13, 23–28. https://doi.org/10.2113/gselements.13.1.23

Cooper, K. M., & Kent, A. J. R. (2014). Rapid remobilization of magmatic crystals kept in cold storage. Nature, 506(7489), 480–483. https://doi.org/10.1038/nature12991

Costa, A., Folch, A., Macedonio, G., Giaccio, B., Isaia, R., & Smith, V. C. (2012). Quantifying volcanic ash dispersal and impact of the Campanian Ignimbrite super-eruption. Geophysical Research Letters, 39(10). https://doi.org/10.1029/2012GL051605

Deering, C. D., Bachmann, O., & Vogel, T. A. (2011). The Ammonia Tanks Tuff: Erupting a melt-rich rhyolite cap and its remobilized crystal cumulate. Earth and Planetary Science Letters, 310, 518–525. https://doi.org/10.1016/j.epsl.2011.08.032

Deering, C. D., Gravley, D. M., Vogel, T. A., Cole, J. W., & Leonard, G. S. (2010). Origins of cold-wet-oxidizing to hot-dry-reducing rhyolite magma cycles and distribution in the Taupō Volcanic Zone, New Zealand. Contributions to Mineralogy and Petrology, 160(4), 609–629. https://doi.org/10.1007/s00410-010-0496-0

Downs, D. T., Wilson, C. J. N., Cole, J. W., Rowland, J. v., Calvert, A. T., Leonard, G. S., & Keall, J. M. (2014). Age and eruptive center of the Paeroa Subgroup ignimbrites (Whakamaru Group) within the Taupō Volcanic Zone of New Zealand. Bulletin of the Geological Society of America, 126(9–10), 1131–1144. https://doi.org/10.1130/B30891.1

Eastwood, A. A., Gravley, D. M., Wilson, C. J. N., Chambefort, I., Oze, C., Cole, J. W., & Ireland, T. R. (2013). U-Pb Dating of Subsurface Pyroclastic Deposits (Tahorakuri Formation) at Ngatamariki and Rotokawa Geothermal Fields. 35th New Zealand Geothermal Workshop.

Ewart, A. (1965). Mineralogy and Petrogenesis of the Whakamaru Ignimbrite in the Maraetai area of the Taupō volcanic zone, New Zealand. New Zealand Journal of Geology and Geophysics, 8(4), 611–679. https://doi.org/10.1080/00288306.1965.10423194

Ewart, A. (1967a). Pyroxene and magnetite phenocrysts from the Taupō quaternary rhyolitic pumice deposits, New Zealand. Mineralogy Magazine, 36, 180–194.

Ewart, A. (1967b). The Petrography of the Central North Island Rhyolitic Lavas. New Zealand Journal of Geology and Geophysics, 10(1), 182–197. https://doi.org/10.1080/00288306.1967.10428189

Ewart, A., & Healy, J. (1966). Te Whaiti ignimbrites at Murupara. In B. Thompson, L. Kermode, & A. Ewart (Eds.), New Zealand Volcanology, Central Volcanic Region (Vol. 50, pp. 121–125). New Zealand Department of Scientific and Industrial Research Information.

Folch, A., & Felpeto, A. (2005). A coupled model for dispersal of tephra during sustained explosive eruptions. Journal of Volcanology and Geothermal Research, 145(3–4), 337–349. https://doi.org/10.1016/j.jvolgeores.2005.01.010

Foley, M. L., Miller, C. F., & Gualda, G. A. R. (2020). Architecture of a Super-sized Magma Chamber and Remobilization of its Basal Cumulate (Peach Spring Tuff, USA). Journal of Petrology, 61(1). https://doi.org/10.1093/petrology/egaa020

Froggatt, P., Nelson, C., Carter, L., Griggs, G., & Black, K. (1986). An exceptionally large late Quaternary eruption from New Zealand. Nature, 319(February), 578–582.

Gravley, D. M., Deering, C. D., Leonard, G. S., & Rowland, J. v. (2016). Ignimbrite flare-ups and their drivers: A New Zealand perspective. Earth-Science Reviews, 162, 65–82. https://doi.org/10.1016/j.earscirev.2016.09.007

Gravley, D. M., Wilson, C. J. N., Leonard, G. S., & Cole, J. W. (2007). Double trouble: Paired ignimbrite eruptions and collateral subsidence in the Taupō Volcanic Zone, New Zealand. Bulletin of the Geological Society of America, 119(1–2), 18–30. https://doi.org/10.1130/B25924.1

Griffin, W., Powell, W., Pearson, N. J., & O'Reilly, S. (2008). GLITTER: data reduction software for laser ablation ICP-MS. Short Course Series, 40, 308–311.

Grindley, G. (1960). Geological Map of New Zealand 1:250,000. In NZ Department of Scientific and Industrial Research: Vol. Sheet 8 (Issue Taupō).

Gualda, G. A. R., & Ghiorso, M. S. (2013). The Bishop Tuff giant magma body: an alternative to the

Standard Model. 2Contributions to Mineralogy and Petrology, 166, 755–775. https://doi.org/10.1007/s00410-013-0901-6

Gualda, G. A. R., & Ghiorso, M. S. (2014). Phase-equilibrium geobarometers for silicic rocks based on rhyolite-MELTS. Part 1: Principles, procedures, and evaluation of the method. Contributions to Mineralogy and Petrology, 168(1), 1–17. https://doi.org/10.1007/s00410-014-1033-3

Gualda, G. A. R., & Ghiorso, M. S. (2015). MELTS-Excel: A Microsoft Excel-based MELTS interface for research and teaching of magma properties and evolution. Geochemistry, Geophysics, Geosystems, 16(1), 315–324. https://doi.org/10.1002/2014GC005545

Gualda, G. A. R., Ghiorso, M. S., Lemons, R. v., & Carley, T. L. (2012). Rhyolite-MELTS: a Modified Calibration of MELTS Optimized for Silica-rich, Fluid-bearing Magmatic Systems. Journal of Petrology, 53(5), 875–890. https://doi.org/10.1093/petrology/egr080

Gualda, G. A. R., Gravley, D. M., Conner, M., Hollmann, B., Pamukcu, A. S., Bégué, F., Ghiorso, M. S., & Deering, C. D. (2018). Climbing the crustal ladder: Magma storage-depth evolution during a volcanic flare-up. Science Advances, 4(10). https://doi.org/10.1126/sciadv.aap7567

Gualda, G. A. R., Pamukcu, A. S., Ghiorso, M. S., Anderson Jr, A. T., Sutton, S. R., Rivers, M. L., & Houlie, N. (2012). Timescales of Quartz Crystallization and the Longevity of the Bishop Giant Magma Body. PLoS ONE, 7(5). https://doi.org/10.1371/journal.pone.0037492

Gualda, G. A. R., & Sutton, S. R. (2016). The year leading to a supereruption. PLoS ONE, 11(7), 1–18. https://doi.org/10.1371/journal.pone.0159200

Harmon, L. J., Cowlyn, J., Gualda, G. A. R., & Ghiorso, M. S. (2018). Phase-equilibrium geobarometers for silicic rocks based on rhyolite-MELTS. Part 4: Plagioclase, orthopyroxene, clinopyroxene, glass geobarometer, and application to Mt. Ruapehu, New Zealand. Contributions to Mineralogy and Petrology, 173(1). https://doi.org/10.1007/s00410-017-1428-z

Healy, J., Schofield, J., & Thompson, B. (1964). Sheet 5, Rotorua. Geological Map of New Zealand 1:250,000.

Hildreth, W. (1979). The Bishop Tuff: Evidence for the origin of compositional zonation in silicic magma chambers. Geological Society of America, Special Paper 180. http://specialpapers.gsapubs.org.proxy.library.vanderbilt.edu/content/180/43.full.pdf

Hildreth, W., & Wilson, C. J. N. (2007). Compositional zoning of the bishop tuff. Journal of Petrology, 48(5), 951–999. https://doi.org/10.1093/petrology/egm007

Houghton, B. F., & Carey, R. J. (2015). Chapter 34 - Pyroclastic Fall Deposits. In H. Sigurdsson (Ed.), The Encyclopedia of Volcanoes (Second Edition) (pp. 599–616). Academic Press. https://doi.org/://doi.org/10.1016/B978-0-12-385938-9.00034-1

Houghton, B. F., Wilson, C. J. N., Mcwilliams, M. O., Lanphere, M. A., Weaver, S. D., Briggs, R. M., & Pringle, M. S. (1995). Volcanic Zone , New Zealand Chronology and dynamics of a large silicic magmatic system: Central Taupō Volcanic Zone , New Zealand. Geology, 23(1), 13–16. https://doi.org/10.1130/0091-7613(1995)023<0013

Kaiser, J. F., de Silva, S., Schmitt, A. K., Economos, R., & Sunagua, M. (2017). Million-year melt–presence in monotonous intermediate magma for a volcanic–plutonic assemblage in the Central Andes: Contrasting histories of crystal-rich and crystal-poor super-sized silicic magmas. Earth and Planetary Science Letters, 457, 73–86. https://doi.org/10.1016/j.epsl.2016.09.048

Kohn, B. P., Pillans, B., & Mcglone, M. S. (1992). Zircon fission track age for middle Pleistocene Rangitawa Tephra, New Zealand: stratigraphic and paleoclimatic significance. Palaeogeography, Palaeoclimatology, Palaeoecology, 95, 73–94.

Leonard, G. S., Begg, J. G., & Wilson, C. J. N. (2010). Geology of the Rotorua area. GNS Science. https://www.researchgate.net/publication/285598682

Lowe, D., Tippett, J., Kamp, P., Liddell, I., Briggs, R., & Horrocks, J. (2001). Tephras: Chronology, Archaeology (E. Juvigné & J.-P. Raynal, Eds.). CDERAD.

Manning, D. A. (1995). Late Pleistocene Tephrostratigraphy of the Eastern Bay of Plenty Region, New Zealand.

Manning, D. A. (1996). Middle-late Pleistocene tephrastratigraphy of the eastern Bay of Plenty, New Zealand. Quaternary International, 34–36, 3–12. https://doi.org/1040-6182(95)00064-X

Martin, R. C. (1961). Stratigraphy and structural outline of the Taupō Volcanic Zone. New Zealand Journal of Geology and Geophysics, 4(4), 449–478. https://doi.org/10.1080/00288306.1961.10420134

Martin, R. C. (1965). Lithology and eruptive history of the Whakamaru ignimbrites in the Maraetai area of the Taupō volcanic zone, New Zealand. New Zealand Journal of Geology and Geophysics, 8(4), 680–705. https://doi.org/10.1080/00288306.1965.10423195

Matthews, N. E. (2011). Magma chamber assembly and dynamics of a supervolcano: Whakamaru, Taupō Volcanic Zone, New Zealand.

Matthews, N. E., Pyle, D. M., Smith, V. C., Wilson, C. J. N., Huber, C., & van Hinsberg, V. (2012). Quartz zoning and the pre-eruptive evolution of the 340-ka Whakamaru magma systems, New Zealand. Contributions to Mineralogy and Petrology, 163(1), 87–107. https://doi.org/10.1007/s00410-011-0660-1

Matthews, N. E., Smith, V. C., Costa, A., Durant, A. J., Pyle, D. M., & Pearce, N. J. G. (2012). Ultra-distal tephra deposits from super-eruptions: Examples from Toba, Indonesia and Taupō Volcanic Zone, New Zealand. Quaternary International, 258, 54–79. https://doi.org/10.1016/j.quaint.2011.07.010

Pamukcu, A. S., Gualda, G. A. R., Bégué, F., & Gravley, D. M. (2015). Melt inclusion shapes: Timekeepers of short-lived giant magma bodies. Geology, 43(11), 947–950. https://doi.org/10.1130/G37021.1

Pamukcu, A. S., Gualda, G. A. R., Ghiorso, M. S., Miller, C. F., & McCracken, R. G. (2015). Phase-equilibrium geobarometers for silicic rocks based on rhyolite-MELTS, Part 3: Application to the Peach Spring Tuff (Arizona, California, Nevada, USA). Contributions to Mineralogy and Petrology, 169(33). https://doi.org/10.1007/s00410-015-1122-y

Pillans, B., Kohn, B. P., Berger, G., Froggatt, P., Duller, G., Alloway, B., & Hesset, P. (1996). Multi-method dating comparison for mid-Pleistocene Rangitawa Tephra, New Zealand. Quaternary Science Reviews, 15, 641–653.

Pitcher, B. W., Gualda, G. A. R., & Hasegawa, T. (2021). Repetitive Duality of Rhyolite Compositions, Timescales, and Storage and Extraction Conditions for Pleistocene Caldera-forming Eruptions, Hokkaido, Japan. Journal of Petrology, 62(2). https://doi.org/10.1093/petrology/egaa106

Reid, M. R., & Vazquez, J. A. (2017). Fitful and protracted magma assembly leading to a giant eruption, Youngest Toba Tuff, Indonesia. Geochemistry Geophysics Geosystems, 18, 156–177. https:

//doi.org/10.1002/2016GC006406

Saunders, K., Morgan, D. J., Baker, J. A., & Wysoczanski, R. J. (2010). The Magmatic Evolution of the Whakamaru Supereruption, New Zealand, Constrained by a Microanalytical Study of Plagioclase and Quartz. Journal of Petrology, 51(12), 2465–2488. https://doi.org/10.1093/petrology/egq064

Shamloo, H. I., & Till, C. B. (2019). Decadal transition from quiescence to supereruption: petrologic investigation of the Lava Creek Tuff, Yellowstone Caldera, WY. Contributions to Mineralogy and Petrology, 174(4). https://doi.org/10.1007/s00410-019-1570-x

Shoji, S., Nanzyo, M., & Dahlgren, R. (1994). Volcanic Ash Soils: Genesis, Properties and Utilization. Elsevier.

Simon, J. I., & Reid, M. R. (2005). The pace of rhyolite differentiation and storage in an "archetypical" silicic magma system, Long Valley, California. Earth and Planetary Science Letters, 235(1–2), 123–140. https://doi.org/10.1016/j.epsl.2005.03.013

Stelten, M. E., Cooper, K. M., Vazquez, J. A., Calvert, A. T., & Glessner, J. J. G. (2014). Mechanisms and timescales of generating eruptible rhyolitic magmas at Yellowstone Caldera from Zircon and sanidine geochronology and geochemistry. Journal of Petrology, 56(8), 1607–1642. https://doi.org/10.1093/petrology/egv047

Swallow, E. J., Wilson, C. J. N., Myers, M. L., Wallace, P. J., Collins, K. S., & Smith, E. G. C. (2018). Evacuation of multiple magma bodies and the onset of caldera collapse in a supereruption, captured in glass and mineral compositions. Contributions to Mineralogy and Petrology, 173(4), 1–22. https://doi.org/10.1007/s00410-018-1459-0

van Achterbergh, E., Ryan, C. G., Jackson, S. E., & Griffen, W. L. (2001). Data reduction software for LAICPMS: appendix. In P. J. Sylvester (Ed.), Laser ablation ICPMS in the Earth Sciences: Principles and Applications (29th ed., Vol. 29, pp. 224–239). Mineralogy Association Canada Short Course Series.

Wilson, C. J. N., & Charlier, B. L. A. (2016). The life and times of silicic. Elements, 12(2), 103–108. https://doi.org/10.2113/gselements.12.2.103

Wilson, C. J. N., Gravley, D. M., Leonard, G. S., & Rowland, J. v. (2009). Volcanism in the central Taupō Volcanic Zone, New Zealand: tempo styles and controls. In T. Thordarson, S. Self, G. Larsen, S. K. Rowland, & A. Hoskuldsson (Eds.), Studies in Volcanology: The Legacy of George Walker. Special Publications of IAVCEI (pp. 225–247).

Wilson, C. J. N., Houghton, B. F., & Lloyd, E. F. (1986). Volcanic history and evolution of the Maroa Taupō area.

Wilson, C. J. N., Houghton, B. F., Mcwilliams, M. O., Lanphere, M. A., Weaver, S. D., & Briggs, R. M. (1995). Volcanic and structural evolution of Taupō Volcanic Zone, New Zealand: a review. Journal of Volcanology and Geothermal Research, 68(68), 1–28. https://doi.org/10.1016/0377-0273(95)00006-G

Wilson, C. J. N., Rogan, A. M., Smith, I. E. M., Northey, D. J., Nairn, I. A., & Houghton, B. F. (1984). Caldera volcanoes of the Taupō volcanic zone, New Zealand. Journal of Geophysical Research, 89(B10), 8463–8484. https://doi.org/10.1029/JB089iB10p08463

CHAPTER 3

Untangling the Magmas and Timing of the Whakamaru Group Ignimbrites

3.1 Introduction

Large, explosive volcanic eruptions imply that the crust must create and accommodate large volumes of eruptible magma prior to eruption. Eruptible magma bodies that source these extreme volcanic events are known to be ephemeral features (Gualda, Pamukcu, *et al.*, 2012; Pamukcu, Gualda, Bégué, *et al.*, 2015). Substantial advances have been made to understand the pre-eruptive conditions of the eruptible magma bodies (Cashman & Giordano, 2014)(Cashman & Giordano, 2014), including work on timescales (K. M. Cooper & Kent, 2014; Gualda & Sutton, 2016; Pamukcu, Gualda, Bégué, *et al.*, 2015; Shamloo & Till, 2019); storage pressures (Bégué, Deering, *et al.*, 2014; Gualda *et al.*, 2018; Gualda & Ghiorso, 2013a; Pitcher *et al.*, 2021); and volatile content and oxygen fugacity (f_{O_2}) conditions (Pitcher *et al.*, 2021). These eruptions have a variety of possible pre-eruptive storage configurations as they can erupt from one (Bachmann & Bergantz, 2008, 2004; Chamberlain *et al.*, 2015; Deering *et al.*, 2011; Foley *et al.*, 2020; Hildreth, 1979; Hildreth & Wilson, 2007; Pamukcu *et al.*, 2013) or multiple eruptible magma bodies (Bégué, Deering, *et al.*, 2014; Cashman & Giordano, 2014; G. F. Cooper *et al.*, 2012; Gualda & Ghiorso, 2013b; Swallow *et al.*, 2018). This precludes a one-model-fits-all approach to understanding eruptible magmatic bodies.

Here, we use the same terminology as Chapter 2 and demonstrated schematically in Figure 1. A magma body is a parcel of magma that is in contact with rocks or other magmas, with clear boundaries. We define eruptible magma bodies and magma mush bodies. An eruptible magma body is composed of crystal-poor magma that is melt dominated and typically has a suspension of crystals and bubbles. It can be erupted imminently. A magma mush body is composed of crystal-rich magma that contains a framework of touching crystals, possibly with bubbles present. The magma mush resists shear and is unlikely to be readily erupted. The collection of magma bodies that coexist in the crust at any given point in time defines the magma reservoir. The details of the compositions and distribution of magma bodies within the reservoir can be well or poorly defined. The magma system includes all magma bodies through time.

In contrast to the pre-eruptive conditions of the eruptible magma bodies, the magma mush bodies are not as well understood. It is only recently that we have begun to probe where and how eruptible magma is extracted from the crystal-rich magma mush body (Figure 1) (Gualda *et al.*, 2019). By understanding both the conditions of pre-eruptive magma storage and extraction from the magma mush body, we extend our understanding of magmatic reservoirs deeper into the crust (Kodaira *et al.*, 2021).

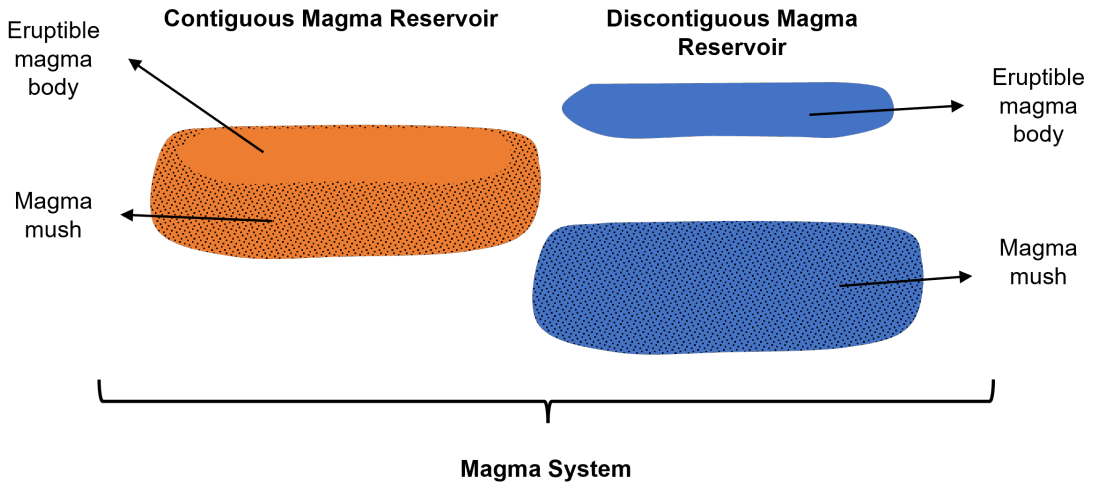

Figure 3.1: Schematic of a magma system. There are both eruptible magma bodies and magma mush bodies. The eruptible magma can be stored in contact with the magma mush from which it is extracted (contiguous magma reservoir), or it can be extracted, migrate, and be stored at a shallower crustal depth (discontiguous magma reservoir).

In addition to looking at a snapshot of the magma reservoir just prior to eruption, we want to understand the longer timeline of the magmatic system in areas that have multiple eruptions through time (Gravley *et al.*, 2016; Gualda *et al.*, 2018; Pitcher *et al.*, 2021). The magma systems from which the magma bodies form can exist over much longer timescales (Kaiser *et al.*, 2017; Reid, 2008; Reid & Vazquez, 2017; Simon & Reid, 2005). The Whakamaru group ignimbrites (Brown *et al.*, 1998; Ewart & Healy, 1966; Grindley, 1960; Wilson *et al.*, 1986) and later flare-up eruptions of the Taupo Volcanic Zone, New Zealand (Gravley *et al.*, 2016; Gualda *et al.*, 2018; Houghton *et al.*, 1995; Wilson *et al.*, 1995) are ideal for this task. The Whakamaru eruptions are known to have multiple compositions of pumice (Brown *et al.*, 1998) and the group of ignimbrites initiates the highly active ignimbrite flare-up period (Gravley *et al.*, 2016). Here, we try to elucidate the pre-eruptive magmatic conditions of the magma bodies' storage and extraction, as well as understand the crustal maturation leading up to and response following the evacuation of large volumes of magma.

We investigate the pre-eruptive conditions of the magma system, which includes the eruptible magma bodies and magma mush bodies that sourced and erupted the Whakamaru group ignimbrites using erupted pumice clasts. Glass and whole rock compositions from erupted ignimbrite pumice elucidate the relationships between the different ignimbrites and magma bodies. We use glass compositions from co-erupted pyroclastic fall deposits to constrain the timing of the eruptions. The ultimate goal is to understand what the crust looks like prior to volcanic eruptions and how the crust can produce such active magmatic and volcanic systems.

3.1.1 Geologic Background

The Taupō Volcanic Zone (TVZ) is a rifted arc (Wilson *et al.*, 1995) situated in the central North Island of Aotearoa New Zealand and is one of the most active silicic volcanic regions in the world (Houghton *et al.*, 1995; Wilson *et al.*, 1995). There have been several pulses of intense volcanic activity (Gravley *et al.*, 2007, 2016; Houghton *et al.*, 1995), known as ignimbrite flare-ups, over the TVZ's 1.9 Ma history of silicic volcanism (Eastwood *et al.*, 2013). The most intense ignimbrite flare-up, from ∼350 to ∼280 ka, included 8 large ignimbrite-forming eruptions and began with the largest Whakamaru eruptions (Gravley *et al.*, 2016; Leonard *et al.*, 2010) and references therein). The Whakamaru magma system explosively erupted >2000 km3 (Downs *et al.*, 2014; Matthews, Smith, *et al.*, 2012; Wilson *et al.*, 1986) of relatively crystal-rich eruptible magma (10-40 wt.% crystals) (Brown *et al.*, 1998) after a ∼ 200 ka hiatus in caldera-forming volcanism (Deering *et al.*, 2010). The Whakamaru eruptions are unique within the TVZ as they sometimes contain sanidine (Brown *et al.*, 1998; Ewart, 1965), and are described as having a "cold, wet, oxidizing" signature (Deering *et al.*, 2010). These subsequent eruptions show a stark transition in composition and style (Gravley *et al.*, 2016; Wilson *et al.*, 2009a) as they are smaller by an order of magnitude (50-150 km3), crystal poor, and exhibit a "hot, dry, reducing" magmatic signature (Deering *et al.*, 2010; Ewart, 1967b, 1967a; Leonard *et al.*, 2010; Wilson *et al.*, 2009b).

The Whakamaru magmas erupted from relatively shallow storage depths (∼100-150 MPa Chapter 2 of this thesis and (Brown *et al.*, 1998; Matthews, 2011), typical of the TVZ (Bégué, Gualda, *et al.*, 2014; Gualda *et al.*, 2018). The subsequent flare-up magmas erupted from much deeper storage conditions (Gualda *et al.*, 2018) before a progressive shallowing through the flare-up. Typical shallow storage pressures were only restored with the youngest flare-up eruption ∼ 70 ka later (Gualda *et al.*, 2018). In contrast to the shallowing storage pressures, the extraction pressures are consistently 200-400 MPa for all of the younger flare-up magmas (Chimpanzee, Pokai, Mamaku, and Ohakuri) (Gualda *et al.*, 2019). Together, the storage and extraction pressures of eruptible magma from magma mush bodies show a transition from contiguous extraction with deep storage pressures of eruptible magma bodies to non-contiguous extraction with shallow storage pressures for eruptible magma bodies (Gualda *et al.*, 2019). In the case of contiguous extraction and storage, the crystal-rich mush body is in contact with the eruptible magma body (the "Mush Model") (Bachmann & Bergantz, 2008, 2004; Hildreth, 1979), while in non-contiguous extraction and storage, the eruptible magma is separated from the magma mush body, and is transported through the crust before storage at a shallower crustal level (Gualda *et al.*, 2019). The change in extraction and storage pressures shows the establishment and evolution of a post-Whakamaru flare-up magma system (Gravley *et al.*, 2016; Gualda *et al.*, 2018). In the context of the flare-up, the Whakamaru eruptions initiate a pronounced change in the storage

of large TVZ magma bodies. We explore the crustal conditions of the Whakamaru magma system and how that may have influenced subsequent eruptions.

3.1.2 Previous Work on the Whakamaru Group Ignimbrites

The Whakamaru eruptions have long been recognized as a major volcanic event in the central TVZ (Briggs, 1976a, 1976b; Ewart & Healy, 1966; Grindley, 1960; Martin, 1965; Wilson *et al.*, 1984, 1986, 2009a). Previous field, petrographic, and compositional work on the Whakamaru group ignimbrites demonstrates that >2000 km3 (Downs *et al.*, 2014; Matthews, Smith, *et al.*, 2012; Wilson *et al.*, 1986) erupted and crops out as multiple ignimbrite deposits (Briggs, 1976a, 1976b; Brown *et al.*, 1998; Ewart & Healy, 1966; Grindley, 1960; Wilson *et al.*, 1986) with different textural signatures which erupted multiple compositionally distinct types of magma (Briggs, 1976a; Brown *et al.*, 1998) over a short period of time (Downs *et al.*, 2014). There are four mappable ignimbrite units that make up the Whakamaru eruptions – the Whakamaru, Manunui, Rangitaiki, and Te Whaiti ignimbrites (Figure 2). The Manunui and Whakamaru ignimbrites crop out to the west of the caldera, and the Te Whaiti and Rangitaiki ignimbrites outcrop to the east of the caldera (Grindley, 1960; Wilson *et al.*, 1986). There is a fifth, younger ignimbrite, the Paeroa subgroup 339± 5 ka (Downs *et al.*, 2014), that is interpreted to have erupted from a nearby source (Figure 2). However, we focus on the four main ignimbrites of the Whakamaru group eruptions. The four ignimbrites are described in Table 1 based on previous work (predominantly by Brown *et al.* (1998)) including welding, crystal contents, and compositional types of pumice found in each ignimbrite. The Whakamaru system is complex, and the ignimbrites are notoriously difficult to put in stratigraphic order, as overlap in the field is insufficient to definitively determine the relative ages of the ignimbrites (Wilson *et al.*, 1986), and age dating cannot determine a time break between the Whakamaru, Rangitaiki, and Te Whaiti ignimbrites (349 ± 4 ka) (Downs *et al.*, 2014). Wilson *et al.* (1986) proposed that the Manunui and Te Whaiti ignimbrites erupted first and could be correlative, and then the Whakamaru and Rangitaiki ignimbrites erupted second and could be correlative. Multiple pulses have been established in both the Rangitaiki and Te Whaiti ignimbrites (Briggs, 1976b), further demonstrating the complex eruptive history of the ignimbrites.

Brown *et al.* (1998) defines four compositional types of rhyolite pumice– Types A, B, C, and D – with a minor amount of mingled basalt. The four types are categorized by mineralogy and whole-rock chemical composition, see Table 2.1. In the Whakamaru ignimbrite, all four pumice types are found, while in the other ignimbrites, a more restricted pumice population is observed (Brown *et al.*, 1998; Matthews, 2011). We attempt to constrain the eruption timing of the different magma types and their relationships to the different ignimbrites.

The Whakamaru reservoir constituents and maturation have been described from the zircon (Brown &

Table 3.1: Description of Whakamaru group ignimbrites after Brown *et al.* (1998)

Ignimbrite	General Location	Pumice Types Present	General Description
Whakamaru	west TVZ	A, B, C, D	xtl rich texture; large, resorbed qtz; qtz-rich, welded ign lithic fragments; increasing xtl content from 10-35+ wt% in lowest unit A with increasing phenocryst size in units B-D; qtz-absent in lowest 30 m; size, abundance, and resorption of qtz increases with strat height; increase in bt with bt>hbl at the top of the ign; opx present throughout ign; sanidine absent for base and units A-B; sanidine appears in units D-F (unclear if it's present in unit C)
Manunui	west TVZ, further south	C, D	intensely welded, less xtl and pumice rich; metased lithic fragments
Rangitaiki	east TVZ	A; Brown 1998 notes that lack of bt-rich Type B and C; Matthews finds one Rangitaiki that has sanidine in thin section, but does not study it further (no XRF)	xtl rich texture; large, resorbed qtz; qtz-rich, welded ign lithic fragments; petrographically similar to Whakamaru ign; poorer in bt than Whakamaru ign
Te Whaiti	east TVZ, further south		intensely welded, less xtl and pumice rich; metasedimentary lithic fragments

Fletcher, 1999; Matthews, 2011) and plagioclase (Saunders *et al.*, 2010) records. The ubiquitous presence of zircon (Brown & Fletcher, 1999; Matthews, 2011) indicates that zircon was saturated at the time of eruption and also recorded the early history of the magma system. Zircon ages from Type A and D pumice clasts show a long-lived and complex history of magma evolution (Brown & Fletcher, 1999; Matthews, 2011). There is debate about the timing of the initiation of the Whakamaru system, as Brown *et al.* 1999 (Brown & Fletcher, 1999) purports a 250 ka history while Matthews (2011) more extensive data set claims to show a peak of zircon ages that imply a ∼50-100 ka history for most of the magma system. However, both studies show the protracted history of the magma system that fed the Whakamaru eruptions likely did not interact with the Utu system (∼549 ka eruption age) (Deering *et al.*, 2010) or any other caldera-forming eruption. Compositional and textural evidence from plagioclase crystals indicate multiple sources for the magma system and a complex history of mingling, mixing, and homogenization ultimately yielded the Whakamaru magmas (Saunders *et al.*, 2010). The compositions (i.e., An content, Ba, Sr, La) of plagioclase crystals suggest

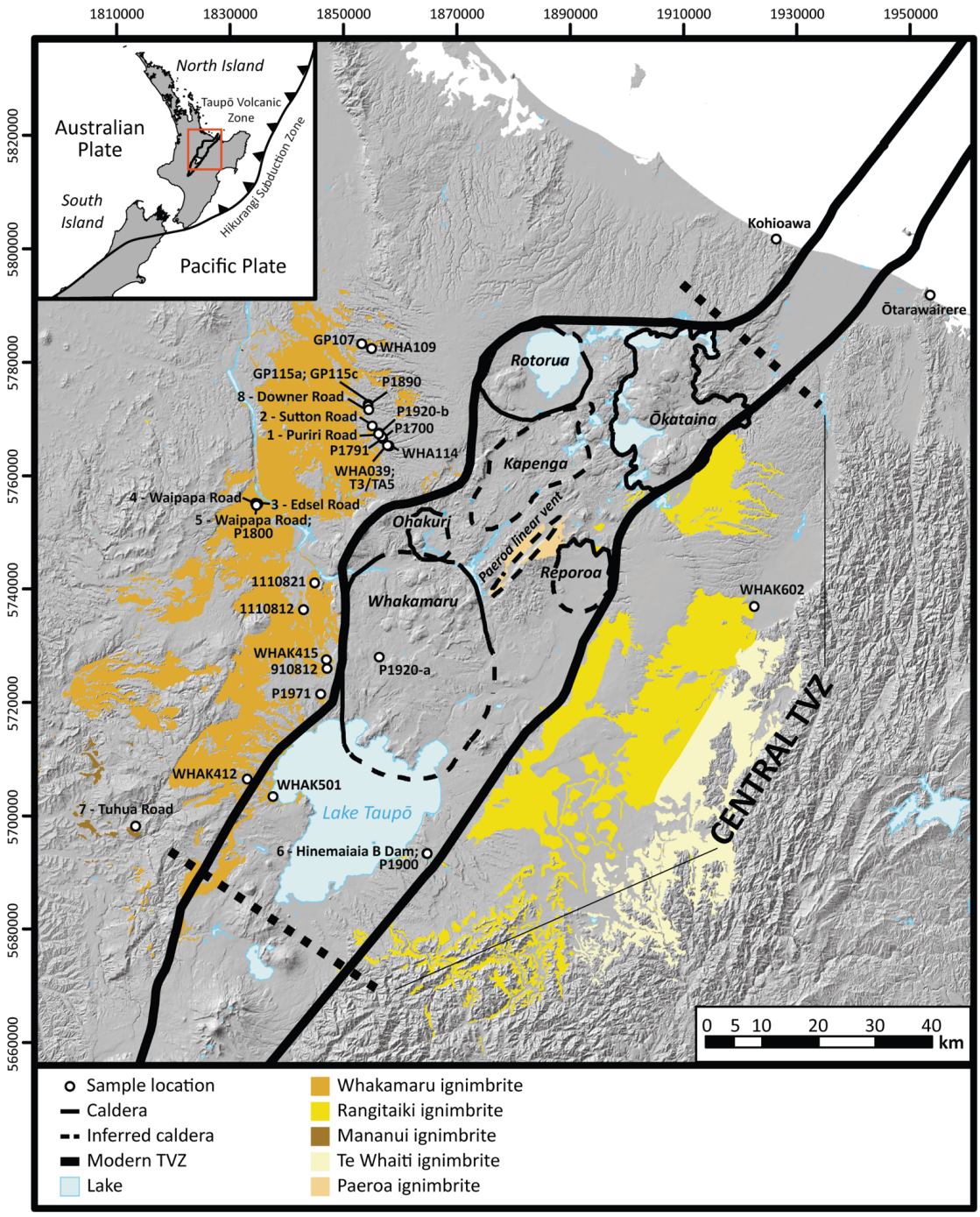

Figure 3.2: - The Whakamaru eruptions include the Whakamaru and Manunui ignimbrites to the west of the caldera and the Rangitaiki and Te Whaiti ignimbrites to the east of the caldera. Sample locations are marked with circles. The two sample locations at the coast, Kohioawa and Ōtarawairere are the locations of the pyroclastic fall deposits (PFDs).

that both crustal melts of the underlying greywacke basement rock and mantle-derived melts are the ultimate sources of magma for the Whakamaru magma system (Saunders *et al.*, 2010).

Quartz diffusional timescales allow us to estimate the maximum crystallization time of the eruptible rhyolite magma body (Gualda, Pamukcu, *et al.*, 2012; Gualda & Sutton, 2016; Pamukcu, Gualda, Bégué, *et al.*, 2015). Timescales derived from Ti diffusion in quartz show 1-10 ka timescales for Types A and D pumice clasts from the Whakamaru and Rangitaiki ignimbrites (Matthews, Huber, *et al.*, 2012). The work by Matthews *et al.* (Matthews, Huber, *et al.*, 2012) suggest that the eruptible magmas that fed the Whakamaru eruptions existed for no longer than 10 ka, but possibly for as little as 1 ka. Quartz rims indicate that the final pulse of crystallization was < 300 a prior to eruption (Saunders *et al.*, 2010). Evidence from quartz agrees with the general observation that large eruptible magma bodies are ephemeral crustal features (Gualda, Pamukcu, *et al.*, 2012). To summarize, evidence from both zircons (Brown & Fletcher, 1999; Matthews, 2011) and plagioclase (Saunders *et al.*, 2010) crystals indicates that the Whakamaru magma system was established over a longer time from a variety of magma sources, and evidence from quartz (Matthews, Pyle, *et al.*, 2012; Saunders *et al.*, 2010) shows short storage time of eruptible magma bodies.

3.1.3 Nomenclature

The Whakamaru magma system refers to all eruptible magma bodies and magma mush bodies that were involved in the Whakamaru magma system. We use Whakamaru group ignimbrites when referring to the material erupted in the ignimbrites. We specify the single Whakamaru ignimbrite when it is necessary to distinguish it from the other ignimbrites.

3.2 Methods

3.2.1 Field Observations and Sampling

Pumice samples were collected from locations detailed in Figure 2 and Table 2. We chose the largest and freshest pumice clasts available at the outcrops. Due to the predominantly welded nature of the ignimbrites (Briggs, 1976a), finding unwelded pumice with pristine glass is challenging. We tried to sample from a variety of locations and ignimbrites, although the quality of exposures and the existence of unwelded pumice led us to sample predominantly from the Whakamaru ignimbrite. Each pumice clast was brushed lightly in water to remove bulk tephra and then dried in an oven at $\sim$50 °C for $\sim$24 hours. After cleaning, each pumice clast was stored individually to minimize contamination.

3.2.2 Pumice Glass Geochemistry

Major and trace-element glass compositions were obtained using the same methods as detailed in Chapter 2 on all 39 pumice clasts. The methods are also summarized below. For every pumice clast, we picked a small (< 1 cm3) piece of the interior of the pumice clast, to make sure no bulk ignimbrite was incorporated

in analyses. We mounted the pumice pieces in epoxy, before being polished and carbon coated for analysis.

The glass major-element compositions were obtained at Vanderbilt University using an Oxford X-max 50-mm2 Energy Dispersive Spectrometer (EDS) attached to a Tescan Vega 3 LM Variable Pressure Scanning Electron Microscope (SEM). Most glass analyses were obtained using 15 kV accelerating voltage (with several obtained with an accelerating voltage of 18-20 kV to achieve a higher output count rate) and a specimen current of $\sim$4 nA at a working distance of 15 mm. The USGS-Rhyolite Glass Mountain (RGM-1) standard was measured at the beginning of each SEM session as a secondary standard. Data reduction for all SEM-EDS analyses was performed using the Aztec Oxford software, which uses internal standards for calibration.

We analyzed $\sim$15 spots of the largest, most pristine sections of glass, far from crystals. Analyses were excluded if 1) a mineral (usually feldspar or a Fe-Ti oxide) was encountered; 2) the SiO_2 was > 82 wt%; 3) the composition lied outside 1.5 times the interquartile range (IQR) for that individual lapillus. This IQR test was performed once, and not iteratively, to identify and remove outliers that fall outside the natural variability of the glass (see Chapter 2).

The trace element glass compositions were obtained via laser ablation inductively coupled plasma mass spectrometry (LA-ICP-MS) at Vanderbilt University. The system is a Photon Machines Excite 193 nm excimer laser attached to a Thermo iCAP Q quadrupole ICP-MS system. For each analysis, a 50 μm × 50 μm square laser spot size was ablated for 25 s at a pulse frequency of 10 Hz. NIST 610 was used as the primary standard and NIST 612 and RGM-1 were used as secondary standards. The isotope 28Si was used as an internal standard, using average SiO_2 contents determined for each sample by SEM-EDS analysis prior to trace element collection. Concentrations were processed through the data reduction program Glitter (Griffin *et al.*, 2008; van Achterbergh *et al.*, 2001).

We analyzed $\sim$ 15 spots per pumice clast for trace-element compositions, where the spot locations were not the same as those analyzed for major-element compositions. Trace-element analyses were discarded if a mineral (usually feldspar or a Fe-Ti oxide) was encountered or if an analysis had at least 5 elements below the detection limit; individual analytes were discarded if they failed the same IQR method as the major element data; trace element data from individual pumice clasts were discarded if there were fewer than 3 analyses to average.

3.2.3 Pumice Whole Rock Geochemistry

A subset of the larger pumice clasts (16) was analyzed via x-ray fluorescence (XRF) spectrometry to determine their whole rock compositions. Pumice clasts chosen for whole rock XRF were the largest clasts, and we chose clasts that exhibited different glass compositions to span the different pumice types. Analysis was

completed by Hamilton Analytical Lab (Hamilton Analytical Lab – Hamilton College), using a Thermo Scientific ARL Perform'X sequential XRF spectrometer. Routine operating conditions of the spectrometer are 45 kV accelerating voltage at 45 mA. A total of 72 reference materials (RMs) are used for calibration. Drift is monitored with in-house standards that are run every 3-4 weeks. One duplicate unknown was prepared and analyzed for each analytical session to check for sample homogeneity and reproducibility of data. Loss on Ignition (LOI)-eliminated influence coefficients are used for matrix correction. Calibration RMs are chiefly those issued by the USGS and GSJ, but also including RMs from the CRPG, GIT-IWG, NIST, BAS, Mintek, and other sources. The revised USGS, GSJ, and CRPG RM values provided in Jochum *et al.* (Jochum *et al.*, 2016) were employed and weighted more heavily than the values from other RMs.

3.2.4 Geobarometry

We use the glass and whole-rock pumice compositions to calculate rhyolite-MELTS pre-eruptive storage pressures of the eruptible magma bodies and extraction pressures from where the eruptible magma is extracted from the magma mush bodies, respectively (Figure 1). We model the storage and extraction pressures using the methods outlined in previous papers and in Chapter 2 (Bégué, Gualda, *et al.*, 2014; Gualda & Ghiorso, 2014; Harmon *et al.*, 2018; Pamukcu, Gualda, Ghiorso, *et al.*, 2015). Similar to Chapter 2, we set MnO and P2O5 to 0 wt%, and – for glass compositions – we set MgO to 0.05 wt% if the measured value is below the analytical detection limit. For both glass and whole-rock compositions, we model from 500-25 MPa in 25 MPa steps, from 1100-700 °C in 1 °C steps, with 10 wt% H2O to impose fluid saturated in all calculations. Gualda and Ghiorso (2014) and Ghiorso and Gualda (2015) show that H2O does not have a substantial effect on pressure calculations. For the glass compositions, we fixed the f_{O_2} to the NNO buffer (Δ NNO 0) in rhyolite-MELTS calculations; for the whole-rock compositions, we explored a range of f_{O_2} parameters from f_{O_2} equal to the NNO buffer Δ NNO 0 to 1.5 log units above NNO in half log unit steps (Δ NNO +0.5, +1, +1.5), which encompasses the reasonable ranges of f_{O_2} for the system (Deering *et al.*, 2010; Matthews, 2011). We consider the storage assemblages of 1) quartz + feldspar (qtz-1feld) and 2) quartz + plagioclase + sanidine (qtz-2feld) (Gualda & Ghiorso, 2014). For the extraction calculations, we consider the extraction assemblages of 1) quartz + feldspar (qtz-1feld) and 2) feldspar + orthopyroxene (feld-opx) (Bégué, Deering, *et al.*, 2014; Harmon *et al.*, 2018; Pitcher *et al.*, 2021).

3.2.5 Zircon Geothermometry

Zircon saturation temperatures are calculated using the mean major element glass compositions and mean Zr concentrations in the glass of the pumice clasts using the formulations of Watson and Harrison (1983) and Boehnke *et al.* (2013). If zircon is saturated, the temperature represents the temperature of zircon-melt

equilibrium (likely a pre-eruptive storage temperature); if zircon is undersaturated, the calculations return a minimum temperature. Previous work (Brown, 1994; Brown & Fletcher, 1999; Matthews, 2011), as well as glass chemistry,(Brown, 1994; Brown & Fletcher, 1999; Matthews, 2011), as well as glass chemistry,(Brown, 1994; Brown & Fletcher, 1999; Matthews, 2011(Brown, 1994; Brown & Fletcher, 1999; Matthews, 2011), as well as glass chemistry,(Brown, 1994; Brown & Fletcher, 1999; Matthews, 2011 suggests zircon is ubiquitously saturated in the Whakamaru group ignimbrites.

3.3 Results

This section is organized by the data sets of field observations and sampling, whole rock compositions of pumice clasts, major element glass compositions, trace element glass compositions, zircon saturation geothermometry, and rhyolite-MELTS glass geobarometry.

3.3.1 Sampling

We sampled from a total of eight outcrops throughout the Whakamaru group ignimbrites. The majority of our samples (35) are from the Whakamaru ignimbrite with an additional four samples from the Rangitaiki ignimbrite. The Whakamaru ignimbrite samples are from six different outcrops within the Kinleith forest (the northern most samples on the west side of the TVZ), and an additional location to the North of Lake Taupō (Figure 2). We collected four samples from the Rangitaiki ignimbrite from one location. We found no fresh, glassy pumice in neither the Manunui nor the highly welded Te Whaiti ignimbrite deposits, so we did not analyze any Manunui or Te Whaiti pumice. In the future, analyzing glass from the Manunui and Te Whaiti bulk ignimbrites could allow us to further analyze these ignimbrites. We supplement our data with whole rock data from Brown *et al.* (1998) and Matthews (2011).

3.3.2 Pumice Geochemistry

Brown *et al.* (1998) defines four predominant compositional pumice types – Types A, B, C, and D, which are distinguished based on whole rock Rb and Sr values (Brown *et al.*, 1998). Our whole-rock data contain pumice from all four magma types, which is confirmed by comparing our whole-rock data to Brown *et al.* (1998) and Matthews (2011) (Tables 3-5 and Figure 3).

In addition to the whole-rock compositions, we can distinguish Types A, B, and C by their matrix glass compositions, (Tables 7-14). Following the classification for the tephra in Chapter 2, we can distinguish Type A from Types B and C by CaO and TiO_2 major-element glass compositions, and we can distinguish Types A, B, and C (especially Type B from Type C) by the Ba and Sr trace element glass compositions. Using matching whole-rock and glass pairs for several pumice clasts presented in this study, we confirm that the

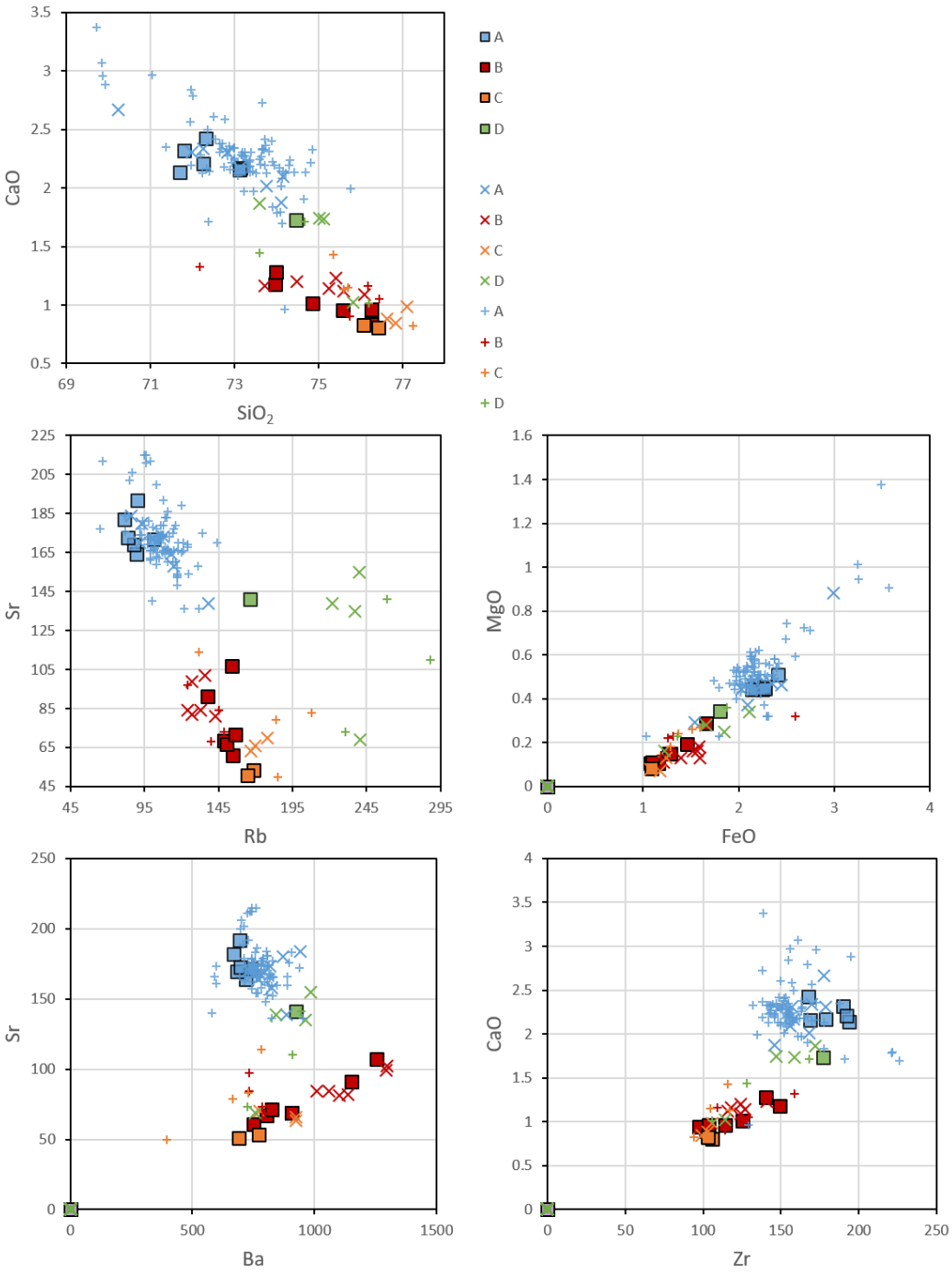

Figure 3.3: Whole rock compositions from ignimbrite pumice. Data presented here are represented by filled-in squares; The X's are literature data from Brown *et al.* (1998); the plusses are literature data from Matthews (2011). The four compositional groups (A, B, C, D) are established from the Brown *et al.* (1998); types A and D are plagioclase-bearing but do not contain sanidine (data in blue and green); types B and C contain sanidine (data in red and orange).

classification of Whakamaru compositional types developed in Chapter 2 using glass compositions. Type D pumice is distinguishable from other pumice types in whole rock but is not readily distinguished by the glass composition. Since we have whole-rock data for only one Type D pumice, we cannot definitively distinguish Type D glass. However, we can distinguish Types A, B, and C using whole-rock and glass compositions, so we can determine the pumice type when clasts are not big enough for whole-rock analysis. We compare these glass compositions to glass compositions of Matthews (2011), Gualda *et al.* (2018), and in Chapter 2.

3.3.2.1 Pumice Whole Rock Geochemistry

All pumice compositions range from 71.7-76.4 wt% SiO_2, 0.8-2.4 wt% CaO, 81-169 ppm Rb, and 51-192 ppm Sr. Using the Brown *et al.* (1998) classification discussed above, there are 6 Type A pumice clasts, 7 Type B pumice clasts, 2 Type C pumice clasts, and 1 Type D pumice clast (16 total). Their compositional signatures are highlighted in Figure 3 and Tables 1 and 3-5.

3.3.2.2 Pumice Glass Geochemistry

We analyzed the glass of 41 pumice clasts (Tables 7-14), with two showing altered glass compositions with SiO_2 > 82 wt% that are not further discussed. For the 15 pumice clasts that have both whole-rock and glass data (all except WHAK415-A2), we use the whole-rock classification from Brown *et al.* (Brown *et al.*, 1998) in addition to the tephra classification for glass (Chapter 2) to determine the pumice type. For the pumice clasts that do not have matching whole-rock data, we rely on the Chapter 2 tephra glass classification (Figures 4 and 5). There are 16 Type A samples (1 of which does not have trace elements due to culling the analyses detailed in the methods), 14 Type B samples (4 of which do not have trace element compositions), 4 Type C samples, and 1 Type D sample. The four pumice clasts from the Rangitaiki ignimbrite do not fall into any of the categories defined by Brown *et al.* (1998), and do not have similar compositions. Their anomalously high Rb content and low Sr content indicate that they are likely do not represent pristine glass compositions. We refer to these pumice clasts as "unclassified". They are plotted, but are not discussed further.

3.3.3 Zircon Saturation Temperatures

From previous work on zircon chemistry and age dating, zircon has been studied extensively in Types A and D pumice from the Whakamaru and Rangitaiki ignimbrites (Brown & Fletcher, 1999; Matthews, 2011). Zircon is likely saturated in all magma types (Brown, 1994), which is supported by our whole-rock and glass pairs, showing lower Zr concentrations in glass when compared to whole-rock, indicating that some Zr is stored in zircon (Figure 5). Using the average glass compositions, we calculate zircon saturation temperatures of 791 ± 28 °C (1-sigma) for Type A, 750 ± 17 °C for Type B, 741 ± 9 °C for Type C, 752 °C for Type D, and 795

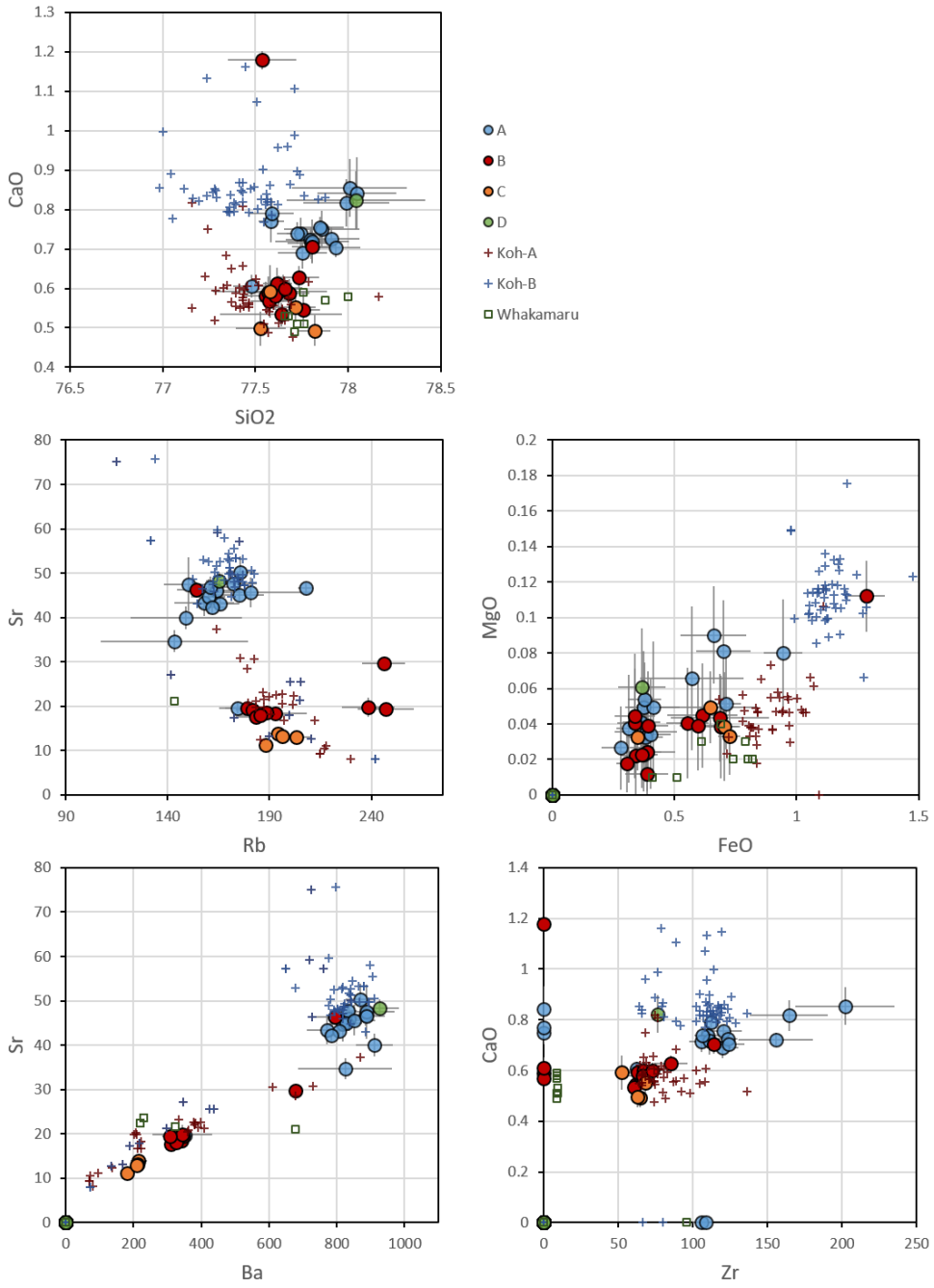

Figure 3.4: Glass compositions from ignimbrite pumice clasts. The four groups (A, B, C, D) are established from whole-rock composition data. Data from the PFDs are represented by small plusses, and literature ignimbrite data from the Whakamaru ignimbrite from Gualda *et al.* (2018) are represented by small squares labeled "Whakamaru".

± 1 °C for the unclassified samples using the Watson and Harrison (1983) calculation (Watson & Harrison, 1983). Using the Boehnke *et al.* (2013) formula, the average zircon saturation temperatures are 759 ± 33 °C

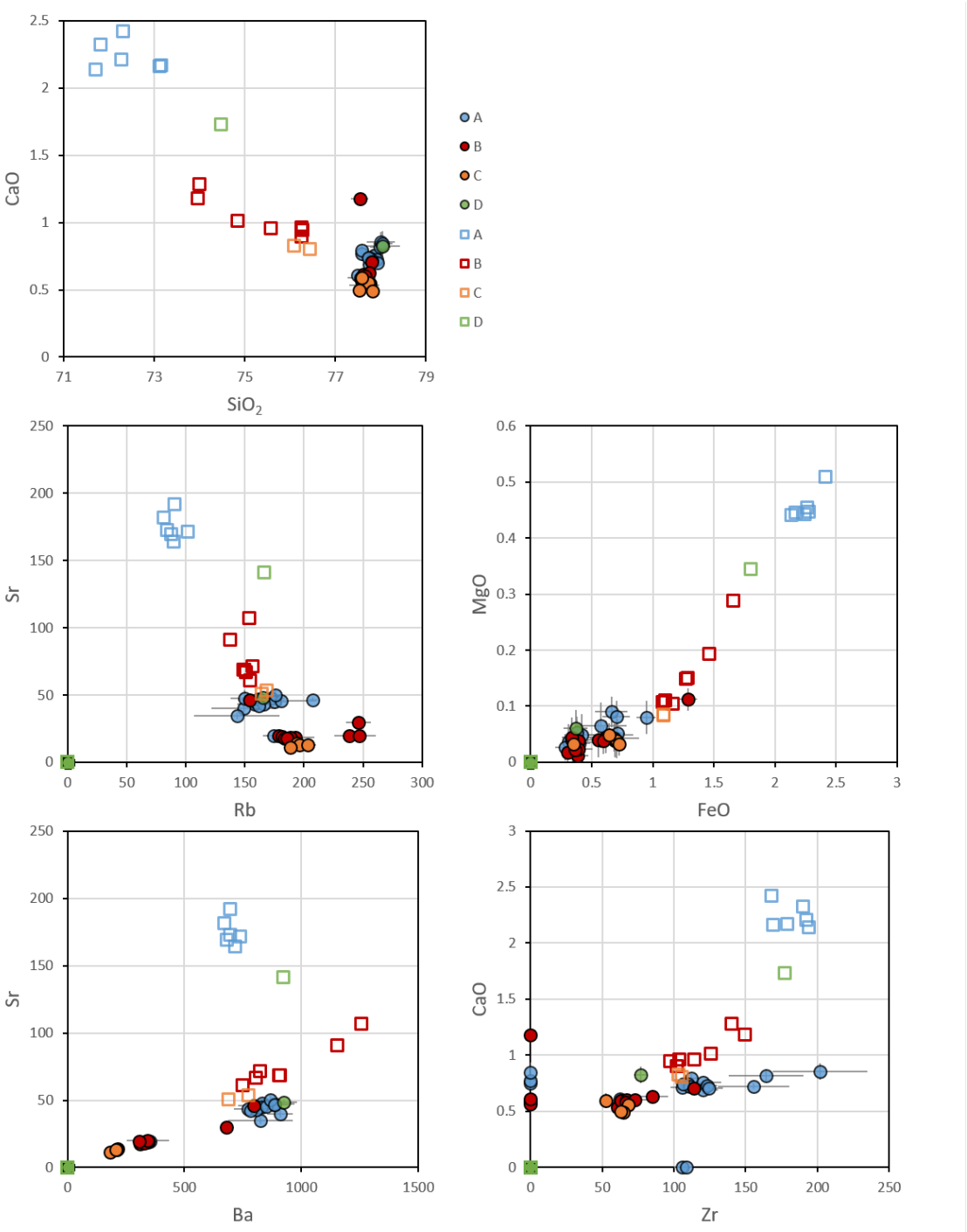

Figure 3.5: Glass and whole rock compositional data from ignimbrite pumice clasts. Whole rock data are represented by squares; glass data are represented by filled circles Data show the differences in compositions between the whole rock compositions. The glass data converging to high SiO_2 values indicates that all magma types have high silica rhyolite melt compositions.

(1-sigma) for Type A, 711 ± 19 °C for Type B, 701 ± 11 °C for Type C, 712 °C for Type D, and 768 ± 1 °C. All individual calculations are reported in Table 15. Generally, we see that Types A and unclassified samples are hotter, while Types B, C, and D are cooler.

3.3.4 Ignimbrites and Pumice Type

The different ignimbrites show different pumice populations that can help us reconstruct the pre-eruptive conditions of the magma bodies.

From our pumice data and data from Matthews (2011) and Brown *et al.* (1998), the Whakamaru ignimbrite has pumice from all four compositional types (Types A, B, C, D). The Manunui ignimbrite has only four samples, two Type A samples, 1 Type C, and 1 Type D sample. The Rangitaiki ignimbrite contains exclusively Type A from the pumice analyzed in previous studies. The Rangitaiki pumice clasts in this study all fall into the "unclassified" pumice category. We did not analyze pumice clasts from Te Whaiti pumice.

The Whakamaru ignimbrite samples from the different outcrops show some variation in pumice proportion (Figure 6). Within the Whakamaru ignimbrite deposit, in the northwest deposits (in the Kinleith forest), there is a concentration of deposits that have Type C pumice. The majority of the western and southern Whakamaru deposits are dominated by type A and B pumice, with minor numbers of Type D pumice. The other type C sample is in the southern Manunui ignimbrite. To the east, the Rangitaiki ignimbrite has exclusively Type A pumice, Table 2.

3.3.5 Geobarometry

Recent work focusing on storage pressures of magma bodies demonstrate that it is possible to use measured glass composition with a known (or inferred) mineral assemblage to constrain storage pressures of pyroclastic rocks (Bégué, Gualda, *et al.*, 2014; Gualda, Ghiorso, *et al.*, 2012; Gualda & Ghiorso, 2014; Harmon *et al.*, 2018; Pamukcu, Gualda, Ghiorso, *et al.*, 2015).

3.3.5.1 Storage Assemblages and Pressures

Overall, storage pressures calculated from glass compositions are shallow, ranging from 40-270 MPa (1.5-10 km). We report the results of each pumice type below, with results summarized in Table 15 and Figure 8.

Of the 16 Type A glass compositions, ten returned storage pressures. One (1/16) composition returns a qtz-2feld pressure and the other (9/16) calculations returned qtz-1feld pressures. Of the 13 Type B glass compositions, nine (9/13) returned qtz-2feld pressures and an additional (3/13) returned qtz-1feld storage pressures. Of the 4 Type C glass compositions, three (3/4) returned qtz-2feld pressures, and the other (1/4) returned a qtz-1feld storage pressure. The one Type D sample and the unclassified samples return qtz-1feld

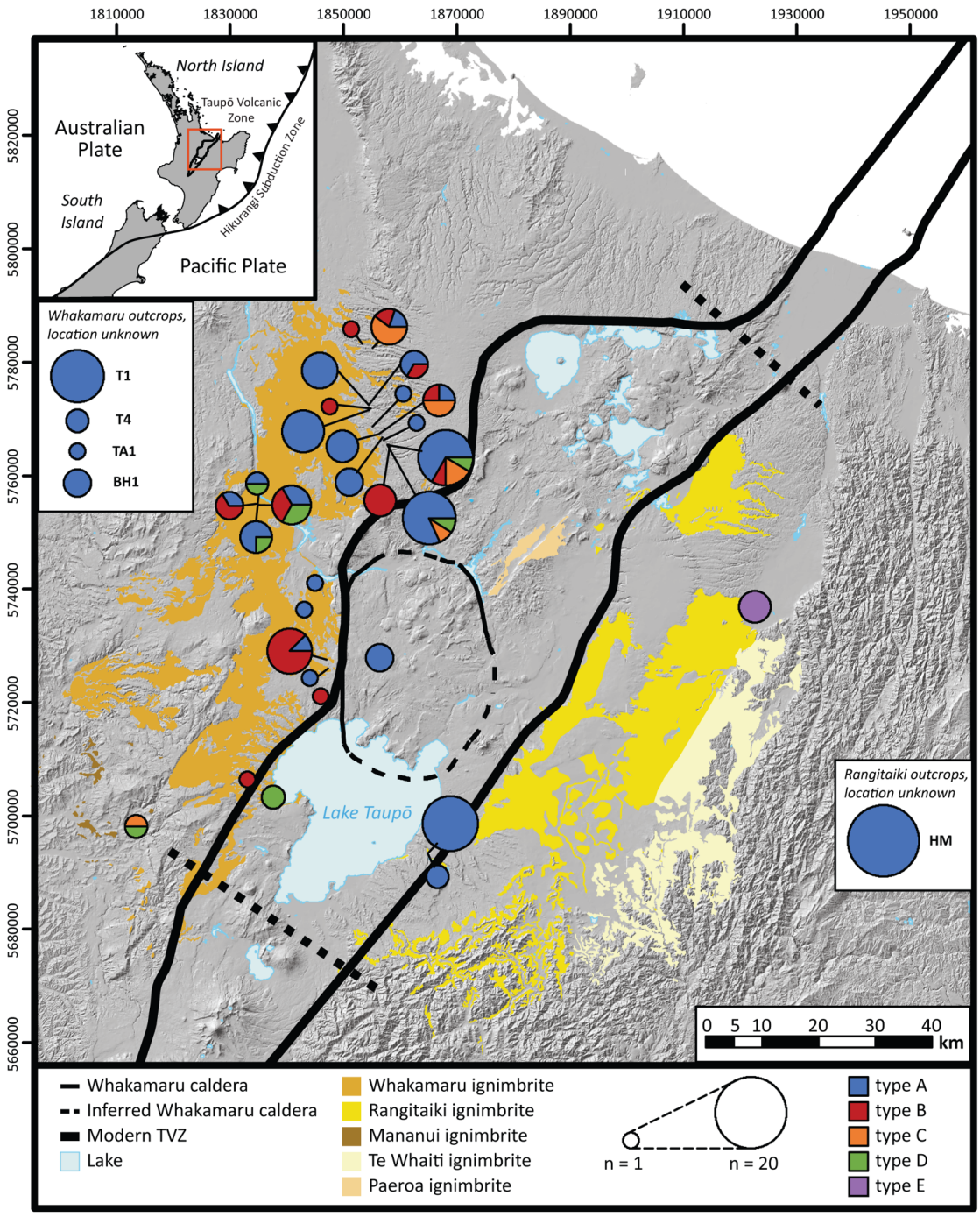

Figure 3.6: The distribution of pumice types within the different Whakamaru group ignimbrites. The colors represent the different pumice types, and the size of the circle represents how many pumice clasts are present at each location. The Kinleith forest area, to the north of the caldera within the Whakamaru ignimbrite, has the highest sampling density.

storage pressure assemblage.

We calculate mean storage pressures of 93 ± 23 MPa (1-sigma) (3.5 ± 0.8 km) for Type A, 110 ± 24 MPa

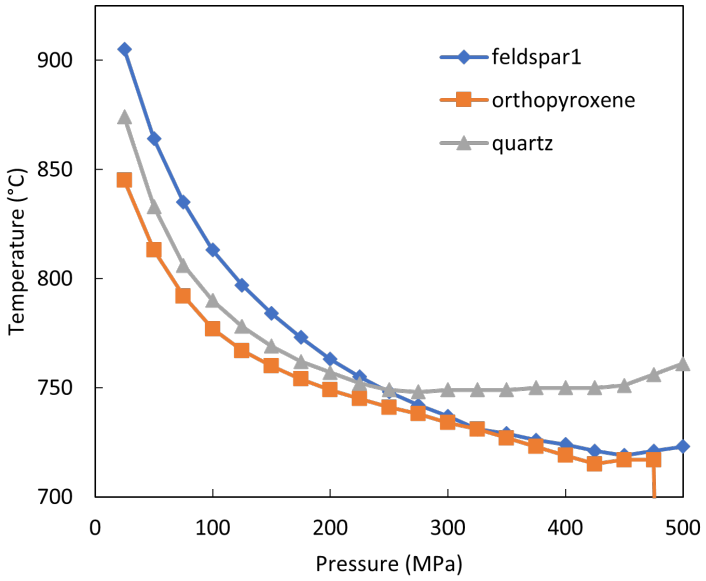

Figure 3.7: Representative Rhyolite-MELTS geobarometry extraction pressure calculation. The saturation surfaces of quartz, sanidine, and plagioclase are plotted in temperature (left vertical axis) vs pressure (x-axis). The feldspar1 and quartz saturation surfaces cross at $\sim$ 240 MPa, so a qtz-1feld pressure is calculated. While the feldspar1 and orthopyroxene saturation surfaces cross at $\sim$ 325 MPa, this is an invalid extraction pressure, since the quartz saturation surface is at a higher temperature than the feldspar1-orthopyroxene intersection. This indicates that the feldspar1-orthopyroxene intersection would not be in equilibrium with the input glass composition. We perform this calculation on all whole rock compositions to determine the extraction pressures.

(4.1 ± 0.9 km) for Type B, 85 ± 35 MPa (3.1 ± 1.3 km) for Type C, where the larger standard deviation for Type C is due mostly to the single shallow 38 MPa (1.4 km) qtz-1feld storage pressure. By excluding this pressure, the Type C storage pressures are 100 ± 18 MPa (3.7 ± 0.7 km), very similar to what is observed for Type B. The mean storage pressures for the Type D glass composition is 52 MPa (1.9 km) and 228 ± 29 MPa (8.5 ± 1.1 km) for the unclassified samples.

Using the mineralogy of previous studies (Briggs, 1976a; Brown *et al.*, 1998; Ewart, 1965; Martin, 1965), pumice Types A and D do not have sanidine, while Types B and C do have sanidine. Therefore, Types A and D should not produce qtz-2feld storage pressures, and the qtz-1feld storage pressures are expected. Types B and C should produce qtz-2feld pressures, which is reflected by the majority of the storage pressures calculated via rhyolite-MELTS. For the Type B and C compositions that only produce qtz-1feld pressures, we accept that the qtz-1feld pressures have a larger uncertainty of 38 MPa, while qtz-2feld pressures have a smaller uncertainty of 24 MPa (Pitcher *et al.*, 2021). The several samples that do not produce pressures likely reflect the sensitivity of rhyolite-MELTS, which has been used to distinguish altered or otherwise imperfect glass compositions (Bégué, Gualda, *et al.*, 2014; Gualda & Ghiorso, 2014; Pamukcu, Gualda, Ghiorso, *et al.*,

2015). The rhyolite-MELTS calculations mostly reflect the expected mineralogy in the pumice types. Types B and C mostly give qtz-2feld pressures, while Types A and D give qtz-1feld, as expected. The success yield in type A is lower than in other types, which could suggest alteration, perhaps due to Na-K exchange.

3.3.5.2 Extraction Assemblages and Pressures

We consider two possible extraction assemblages – quartz-plagioclase (qtz-1feld) or plagioclase-orthopyroxene (feld-opx) – both of which are potential extraction assemblages from the quartzo-feldspathic lower crust of New Zealand, which is the ultimate magma source (Gualda *et al.*, 2019). In New Zealand, there is a sharp density transition at 16 km, which is inferred to be the Moho (Stern *et al.*, 2006) or heavily intruded lower crust (Harrison & White, 2006). Therefore, the maximum crustal extraction pressures would be ∼450 MPa, assuming a crustal density of 2.75 g/cm3. All of the calculated extraction pressures are < 400 MPa, but the calculated extraction pressures depend on the extraction assemblage considered and oxygen fugacity (f_{O_2}). Extraction pressures and assemblages are reported in Table 6 and Figure 8.

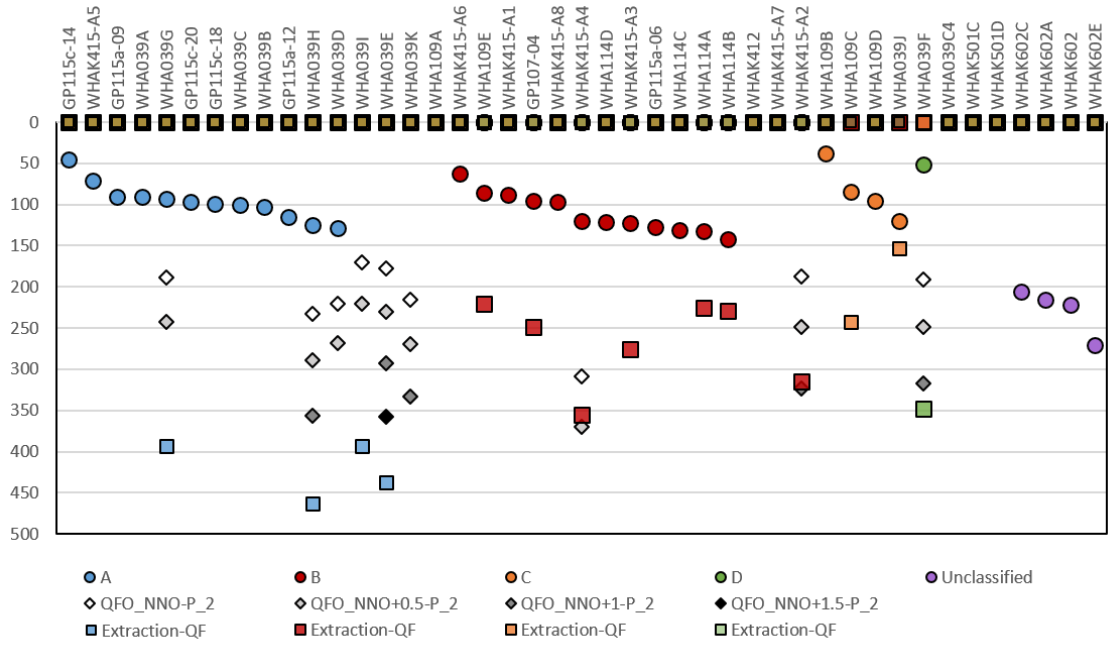

Figure 3.8: Pre-eruptibe storage pressures from rhyolite-MELTS calculations using the glass compositions and extraction pressures of the melt from rhyolite-MELTS calculations using the whole rock compositions. Pre-eruptive storage pressures are represented by circles, and show the final storage pressures of the eruptible magma bodies prior to eruptions. The extraction pressures represented by diamonds and quares show from what level the melt is extracted from the magma mush bodies. The extraction pressures are dependent on f_{O_2}. The diamonds represent the feld-opx extraction pressures at increasing f_{O_2} (Δ NNO 0 = white, Δ NNO +0.5 = light gray, Δ NNO +1 = medium gray, and Δ NNO + 1.5 = black). The colored squares represent the qtz-1feld extraction pressures, which are not dependent on f_{O_2}. These represent the deepest possible extraction pressures. Types A and D have an extraction assemblage of feld-opx at lower f_{O_2} and feld-opx±qtz at f_{O_2} of Δ NNO +1.5 or Δ NNO +2.

All seven of the whole-rock analyses for Types A and D produce extraction pressures. The feld-opx extraction pressures range between 170-230 MPa for f_{O_2} equal to NNO (Δ NNO 0). The extraction pressures increase with increasing f_{O_2}. However, fewer valid extraction pressures are calculated with increasing f_{O_2}. Both Δ NNO 0 and Δ NNO +0.5 produce 7 extraction pressures; Δ NNO +1 produces 4 extraction pressures; Δ NNO +1.5 produces 1 extraction pressure. We calculate the following range of extraction pressures: 170-230 MPa for Δ NNO 0, 220-270 MPa for Δ NNO +0.5, 290-330 MPa for Δ NNO +1, 290-360 MPa for Δ NNO +1.5, and 360 MPa for Δ NNO +1.5. At f_{O_2} Δ NNO +1 to Δ NNO +1.5, two compositions produce quartz-plagioclase-orthopyroxene (qtz-1feld-opx) pressures. For the other compositions, the quartz saturation curve generally comes very close to the feld-opx intersection, indicating that there could be quartz present at the source if the f_{O_2} is Δ NNO +1 to Δ NNO +1.5, which agrees with some of the existing f_{O_2} estimates (Brown *et al.*, 1998; Deering *et al.*, 2010). However, Matthews *et al.* (Matthews, 2011) estimates f_{O_2} between NNO and NNO +0.5, Types A and D would have been extracted from a feld-opx mineral assemblage at shallower pressures.

All nine whole-rock compositions for Types B and C produce extraction pressures. There are only two compositions that yield feld-opx extraction pressures - WHAK415-A4 has a feld-opx extraction pressure of 310 MPa at an f_{O_2} of Δ NNO 0, while WHAK415-A2 has a feld-opx extraction pressures of 190 MPa at an f_{O_2} of Δ NNO 0 and 250 MPa for an f_{O_2} of Δ NNO +0.5. All compositions produce qtz-1feld extraction pressures, with a range of 150 MPa to 360 MPa with most pressures between 220 and 310 MPa. None of the other compositions yield viable feld-opx pressures – in all cases, the orthopyroxene saturation curve is below the quartz or feldspar saturation curve. The valid pressure estimate cannot have a phase saturating at higher temperature (Figure 7). Since the qtz-1feld extraction pressures are shallower than the feld-opx pressures, and the quartz saturation curve is above the feld-opx intersection, we can disregard the feld-opx pressures (Figure 7). The WHA039J sample has the shallowest pressure (150 MPa), which is just slightly deeper than the Type C storage pressure.

3.4 Discussion

3.4.1 The Eruptible Magma Bodies (Multiple Magma Bodies and their Pre-Eruptive Storage Conditions)

Our data suggest that three to four distinct types of magma sourced the Whakamaru eruptions. Our samples can be placed in two overarching groups based on whole rock and glass compositions, as well as mineralogy. Samples of pumice types A and D have higher Sr and CaO in whole rock compositions and higher Sr, Ba, and Zr in glass compositions in common, and previous work has shown that these magmas do not contain sanidine. Results from rhyolite-MELTS supports this observation, as most storage pressure results are not

sanidine-bearing (quartz-plagioclase pressures). Samples of Types B and C form a second group, having lower Sr and Zr in whole rock and generally more fractionated glass compositions with lower Ba and Sr and slightly higher Rb compositional aspects in common and bear sanidine (Brown *et al.*, 1998); this is also supported by the rhyolite-MELTS results, as most storage pressures are sanidine-bearing (quartz + 2 feldspars). Zircon saturation geothermometry helps to further parse these groups. Results suggest that Type A was stored at a hotter temperature than Types B, C, and D. Together, these results suggest at least 3 distinct eruptible magma bodies (A, B+C, D). Given their compositions and storage temperatures, Types B and C were likely distinct eruptible magma bodies. Since there is little overlap in either whole-rock or glass compositions among the different magma types, the eruptible magma bodies likely did not mix prior to eruption.

Considering our rhyolite-MELTS geobarometry results in more detail also provides some insights into the arrangement of these magma bodies in the crust. The rhyolite-MELTS storage pressures are all similarly shallow for Types A-D (Figure 8) indicating that each magma type occupies a narrow range of storage depths in the upper crust. This is consistent with the predominantly shallow storage pressures of the TVZ (Bégué *et al.* 2014), which may be at least partly tectonically controlled (Gravley *et al.*, 2016 and references therein).

Our results suggest a model that contrasts with that of Brown *et al.* (1998), who suggested the system was comprised of a single, zoned magma body. Rather, the differences in composition, storage temperature, and storage pressure we see in our data suggests that the different magma types were likely independent, adjacent eruptible magma bodies. From the tephra data of Chapter 2, Type A erupts at the beginning and then continuously through the Whakamaru eruptions, while Type B is present in the second and third units, and Type C is present only in the final unit, and Type D compositions are not distinguished in the tephra. While we do not know the residence times for these magmas, we know that magma bodies of all three compositions represented in the tephra (Types A, B, and C) must be present in the crust at least for the final stages of the Whakamaru eruptions, see Chapter 2.

3.4.2 The Magma Mush Bodies

Extraction pressures can give clues about the organization of the magma mush bodies (Gualda *et al.*, 2019), which provides information on the integrated larger magma system scale. Previous work in the TVZ shows that both contiguous and noncontiguous extraction has occurred in the region (Gualda *et al.* 2019). Since we have established that there must be multiple eruptible magma bodies that feed the Whakamaru eruptions, understanding the extraction from the magma mush lets us interrogate the different magma source(s). As well as the depth of extraction, we can also constrain mineral assemblage during extraction (Gualda *et al.* 2019).

Type B and C magmas were extracted from similar levels with a qtz-1feld assemblage, which is consistent with their compositional and mineralogical similarities. Type B magma extraction occurred at a depth of 260

MPa ± 50 MPa, and Type C extraction occurred at 200 MPa ± 60 MPa. Since the qtz-1feld pressures are not affected by f_{O_2} and the orthopyroxene curve does not intersect the qtz-1feld pressures at any reasonable f_{O_2} (Δ NNO 0 to Δ NNO +1.5) in our rhyolite-MELTS calculations, we can definitively determine that orthopyroxene is not saturated at the source for Type B or Type C magmas, and that they are extracted with a qtz-1feld assemblage with most pressures coming from a narrow, relatively shallow range (220-280 MPa).

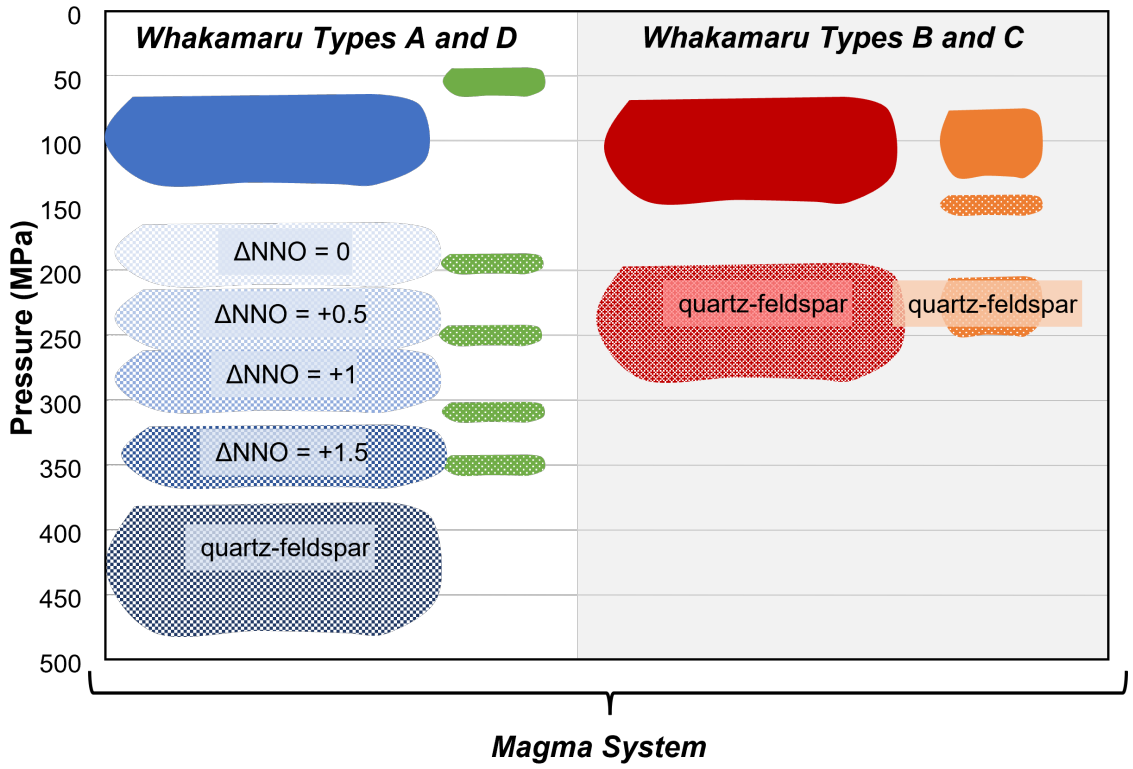

Figure 3.9: Schematic of eruptible magma bodies and magma mush bodies that make up the Whakamaru magma system. The lighter gray area represent the storage pressures and the darker gray area represent extraction pressures. The colored rectangles in the storage area represent the different eruptible magma types. It is unclear if Types B and C constitute the same or different eruptible magma bodies. The unclassified pumice clasts give deeper storage pressures, in purple. From the extraction assemblages, Types A and D make up one magma subsystem with an extraction assemblage of feld-opx±qtz, and Types B and C make up the other subsystem with an extraction assemblage of qtz-1feld. The extraction pressures for Types A and D are dependent on f_{O_2}, with the shallower magma mush body representative of a lower f_{O_2}, and the deeper extraction depth representing a higher f_{O_2} and a feld-opx±qtz extraction assemblage. For Types B and C, only the qtz-1feld extraction assemblage gives valid extraction pressures. There are three different extraction pressures, although extraction could occur throughout the two deeper areas. Note that the number of magma bodies represents the gaps in storage data, and we do not know how many individual magma bodies exist prior to and during eruptions.

Type A and Type D magmas are distinct in their extraction characteristics. For f_{O_2} between Δ NNO 0 and Δ NNO +1.5, a feld-opx extraction assemblage is required. Since orthopyroxene is sensitive to f_{O_2}, the calculations at different f_{O_2} give rise to different extraction pressures. For Δ NNO 0, the extraction pressures

are 200 MPa ± 25 MPa for Type A and 190 MPa for the single Type D sample. The pressures increase with increasing f_{O_2} until Δ NNO +1.5, which exhibit a feld-opx pressure of 360 MPa; however, there are several compositions that show the pressure converging to a qtz-1feld-opx assemblage of 390-460 MPa.

In contrast to Type B and Type C, Type A and D require orthopyroxene to be present at extraction. This leads to two competing hypotheses: 1. All magma types are extracted from the same/similar shallower depth with two different assemblages (Type A and D extracted with feld-opx; Type B and C extracted with qtz-1feld) 2. The magmas are extracted from different depths with different assemblages (Type A and D extracted from up to $\sim$ 300-460 MPa with feld-opx±qtz and Type B and C extracted from $\sim$ 200-260 MPa with qtz-1feld)

If scenario one is valid, the f_{O_2} would be estimated to be Δ NNO 0 to Δ NNO +0.5, which agrees with the estimates by Matthews (Matthews, 2011). This would imply that XYZ. If the f_{O_2} is higher (Δ NNO +1 to Δ NNO +1.5), which agrees with the estimates by Brown *et al.* (Brown *et al.*, 1998) and Deering *et al.* (Deering *et al.*, 2010), then the source of Type A and D magmas likely included quartz+plagioclase+orthopyroxene at deep pressures. in the crust. In both scenarios, the extraction of Types A and D occurs over a narrow range.

In either scenario there must be two independent magma subsystems that source the Whakamaru magma system – one subsystem is responsible for the Types A and D magmas, and the other is linked to Types B and C magmas. Results for all four magma types indicate noncontiguous storage and require that magma migrated through the crust between extraction from a magma mush body and storage as eruptible magma bodies. This further shows that the magma system is vertically extensive and that the Whakamaru system cannot be sourced by a single eruptible magma body. If Type A and D magmas are extracted from a deeper source, the migration of the magma from extraction to storage would be $\sim$ 300 MPa. The overlapping storage conditions of all eruptible magma bodies shows that there could be a structural or tectonic control on the storage depths of the eruptible magma bodies, regardless of their extraction pressures or assemblages. Two options for the control are that the rifted nature of the crust allows magmas to be stored shallower in the TVZ than other places, or that the magmas could reach neutral buoyancy at these storage levels.

Zircon saturation temperatures can help further constrain which of these extraction scenarios is more likely. Since Type A magma shows hotter storage temperatures, it implies that Type A eruptible magma is likely sourced from shallower magma mush bodies that have a feld-opx assemblage. If the eruptible magmas were sourced from deeper magma mush bodies with a feld-opx-qtz assemblage, the eruptible magma would likely be cooler than the shallower qtz-1feld magma mush bodies that sourced Type B and C eruptible magma bodies (at least if water activity is similar for both magma types). Therefore, a plag-opx-bearing assemblage is slightly favored for the magma mush bodies that source Types A and D.

The relationship between Type B and Type C magmas is potentially illuminated by the extraction pres-

sures. The Type C pumice clasts have two valid extraction pressures, one that overlaps with Type B extraction, while the other is shallower and overlaps with the Type B storage pressures (150 MPa). It is possible that there is a vertically extensive magma mush system sourcing the Type B and C magmas, where some of the Type C magma is extracted from a developing Type B mush at the base of the Type B magma body. Since Type C is erupted only in the final unit, it is possible that it is more evolved and Ba and Sr compositions are a consequence of extraction from the Type B magma body following crystallization of two feldspars. The similarity in the whole rock and glass composition, mineral assemblage, and extraction pressure indicates that Types B and C are likely geochemically related to the same source. However, the slight differences in whole-rock and glass compositions show that a more evolved signature for Type C could indicate that Type C magma is extracted from Type B in a two-part extraction and storage. This is consistent with observations from the tephra sequences studied in Chapter 2, which show that Type C magmas only appear late in the erupted sequence. A summary cartoon of the pre-eruptive magma bodies and reservoirs is shown in Figure 9.

3.4.3 The Timing of the Whakamaru Eruptions

Understanding the temporal relations of the Whakamaru group ignimbrites is difficult given the lack of distinctive field relationships between the different ignimbrites (Briggs, 1976a, 1976b; Brown *et al.*, 1998; Leonard *et al.*, 2010; Wilson *et al.*, 1986). However, we can take advantage of the pyroclastic fall deposits (PFDs), deposited in tephra sequences (Manning, 1995) studied in Chapter 2 to constrain the relative timing of the ignimbrites by correlating magma types, mineralogy and glass compositions from the tephra with the characteristics of the ignimbrites. Evidence from the tephras shows that there are three main phases of the Whakamaru eruptions (see Chapter 2): 1. In the initial stages of the Whakamaru eruptions, eruptions included exclusively Type A pumice, likely from one eruptible magma body. The initial stages of the eruption being sourced by only Type A magma is supported by a lack of sanidine in the lowest drill core data from Whakamaru ignimbrite deposits (Ewart, 1965; Martin, 1965), which has been interpreted as the first pulse of ignimbrite eruption. 2. For the thickest, massive unit of the tephras, both magma Types A and B erupt in all horizons. This indicates that two magma types from at least two different eruptible magma bodies erupt through the majority of the Whakamaru eruptions. From both the ignimbrite mineralogy by Brown *et al.* (1998) and from the mineralogy inferred by rhyolite-MELTS for tephras and ignimbrites, Type B magma is shown to be saturated in sanidine (qtz-2feld storage pressures), while Type A is sanidine-absent (only qtz-1feld storage pressures), which indicates two separate, eruptible magma bodies. 3. Type C pumice is only present in the upper tephra unit. It is marked by a change in field characteristics from massive to interbedded fine and coarse layers that contains glass from Types A, B, and C, with most of the lapilli clasts exhibiting Type C glass compositions. The appearance of Type C in the top unit indicates that this Type C magma only

erupts at the end of the Whakamaru tephra sequence. This can be attributed either to a shift in composition of the Type B magma or to a third magma body that erupts Type C. Any ignimbrite that contains Type C pumice must be a later erupted unit, evidenced by the interbedded layers of tephra. The presence of the Type C magma suggests a shift in the latest stage of eruption to being sourced by magma from Type A and Type B and C. This could either indicate a compositional change to the Type B magma or suggest mobilization of three eruptible magma bodies (Types A, B, and C).

To summarize, Type A continuously erupts throughout the Whakamaru eruptions, while Type B appears in the second and third tephra units. Type C is a late-erupted magma type that only erupts in the third unit of the tephras – it is the dominant magma type at that stage. Since we cannot distinguish Type A from Type D using only glass compositions, we cannot determine where in the stratigraphy Type D magma erupts.

Evidence from the tephras requires that no sanidine-bearing magma is erupted in the beginning of the eruptions. This implies that only Types A and D can erupt in the beginning. Since the Rangitaiki ignimbrite only exhibits Type A, it is most likely erupted early in the sequence. In contrast, evidence from the tephras shows Type C is only erupted in the final horizons. Both the Manunui ignimbrite and the Whakamaru ignimbrite in the northernmost samples on the west side of the TVZ (the Kinleith area) have Type C, indicating that these ignimbrites erupted during the final stages of the eruptive sequence. The somewhat narrow range of Type C demonstrates that it is somewhat restricted in both time and space (Figure 6). This implies that the ignimbrites preserved in the east likely erupted first and that the ignimbrites to the west were later erupted, with a final tongue of ignimbrite erupted and emplaced in the north, on the western side of the TVZ.

We propose that Rangitaiki is an early eruptive deposit that only shows Type A in the deposits, before Manunui and Whakamaru ignimbrites erupt Types A, B, C, and D in multiple pulses, as seen in the interbedded morphology of the tephras. Due to the variation in pumice preservation, the Kinleith forest is where we collected the majority of the pumice. There is a large abundance of Type C pumice in several Kinleith sampling locations, indicating that the northeast portion of the Kinleith area is likely one of the later erupted ignimbrites, representing the youngest pulses of the Whakamaru ignimbrite. The older section of Whakamaru ignimbrite (e.g. at the Maraetai dam) should be analyzed to determine at what stratigraphic level Type C appears within the Whakamaru ignimbrite.

The tephra deposits show the chronology of the eruptions, and the ignimbrites provide additional compositional information. The combination allows us to better understand the magma system, including the eruptible magma bodies, magma mush bodies, and the timing of eruptions. While only $\sim$40 samples are a tiny minority of the erupted material (> 2000 km3) it is the combination with the tephra data that allows us to constrain the timing of the ignimbrites for this system. The larger pumice clasts of the ignimbrites provide valuable information on the storage and extraction of the magmas, which, combined with the tephra data, can

provide a time-integrated view of the magma system.

The idea of multiple magma bodies feeding the Whakamaru eruptions confirms the interpretation from the tephra and contrasts with the model of a zoned magma body proposed by Brown *et al.* (1998). The overlapping storage pressures of the different magma types indicate that it is not a zoned magma body, and is more likely to be multiple, adjacent eruptible magma bodies. Further, since the Whakamaru and Manunui ignimbrites contain multiple pumice types, the compositionally distinct eruptible magma bodies must have coexisted in the crust prior to eruption, and a single magma body cannot have sourced the Whakamaru eruptions. The different pumice types appear in multiple ignimbrites (Brown *et al.*, 1998), which precludes a simple model of sourcing each ignimbrite from an individual magma body. Further, the two magma subsystems indicate that the Whakamaru system was complex, with multiple sources of eruptible magma.

3.4.4 Whakamaru System and the Greater Taupo Volcanic Zone

The Whakamaru eruptions mark a significant transition in the TVZ. There are very few major eruptions leading up to the Whakamaru eruptions (Gravley *et al.*, 2016)(Gravley *et al.*, 2016)with no major eruptions for $\sim$200 ka prior to the Whakamaru eruptions (Deering *et al.*, 2010). The Whakamaru eruptions are the first in a series of large eruptions, which is the most productive period of volcanism in TVZ history (Gravley *et al.*, 2016). After the catastrophic Whakamaru eruptions, there is a crustal reorganization in the later flare-up magmas (Deering *et al.*, 2010; Gravley *et al.*, 2016; Gualda *et al.*, 2018), as if the Whakamaru magma system emptied itself before a new magma system developed, giving rise to the "hot-dry" flare-up (Deering *et al.*, 2010; Gravley *et al.*, 2016; Gualda *et al.*, 2018). The magma production fed the Whakamaru eruptions and then the ability of the crust to erupt large volumes of magma continued through the flare-up. The changes in composition and style of eruption between the Whakamaru and subsequent flare-up eruptions (Deering *et al.*, 2010; Gravley *et al.*, 2016) indicates that the Whakamaru system created a substantial change in the crust where the magma mush bodies are created and where the eruptible magma bodies are stored.

The Whakamaru magma system is interpreted to be a mature magma system, with a narrow, consistent range of extraction pressures where it is interpreted that magma mush bodies exist for protracted periods of time, and shallow, consistent storage pressures, where it is interpreted that the eruptible magma bodies exist on short timescales prior to eruption. The sanidine present in the Type B and C magmas also indicates a more mature, near-invariant assemblage. In contrast, the subsequent flare-up magmas begin with immature extraction and storage before progressing to a more mature system, since the relationship between the magma mush bodies and the eruptible magma bodies change from contiguous and deep to non-contiguous and shallow (Bégué, Deering, *et al.*, 2014). It is not until the youngest flare-up magmas that the typical shallow TVZ storage pressures are recovered (Gualda *et al.*, 2018).

This transition from shallow mature Whakamaru magma bodies to the deeper immature flare-up magma bodies resembles the same transition shown with the Oruanui eruption to Taupō eruption. It could be that the large eruptions (Whakamaru and Oruanui) have a substantial influence on the subsequent development of magma systems and eruptible magma bodies.

3.5 Implications, Conclusions, and Future Work

The Whakamaru magma system is composed of two magma subsystems, that have different magma mush extraction mineralogies, and potentially different extraction pressures. The two magma subsystems produced eruptible magma bodies that differ in composition and temperature. The eruptible magma bodies were stored at consistent storage pressures, indicating a possible tectonic or structural control on where the eruptible magma bodies are stored. The four different types of eruptible magma were stored in at least three magma bodies adjacent to one another in the upper crust. There has been substantial debate about the timing of the different eruptions. Using the co-erupted tephras, we hypothesize that the ignimbrites to the east erupted first, before the Manunui and Whakamaru eruptions erupted in a later stage. The Whakamaru magma system kicked off the ignimbrite flare-up period of the TVZ, indicating the massive Whakamaru magma system yielded a reorganization in the TVZ crust after eruption. Several aspects of the Whakamaru magma system are still unknown. The timing and composition of the Te Whaiti ignimbrite remains mysterious and could test our hypothesis that the eastern ignimbrites erupted before the western ignimbrites. Also, the extraction of eruptible magma from the magma mush bodies are currently the deepest level that we can confidently estimate as we have not yet developed techniques to query deeper within the magma system. Finding a way to look at the roots of the magma systems is necessary to understand how the magma system ultimately develops and how the crust responds to large magmatic volcanic events through time.

Table 3.2: Pumice clast information

Sample Name	Sample Location	Location	Magma Type	Ignimbrite	Whole-Rock	Glass-Major	Glass-Trace
GP107-04	GP107	Kinleith	B	Whakamaru	X	X	X
GP115a-06	GP115a	Kinleith	B	Whakamaru		X	X
GP115a-09	GP115a	Kinleith	A	Whakamaru		X	X
GP115a-12	GP115a	Kinleith	A	Whakamaru		X	X
GP115c-14	GP115c	Kinleith	A	Whakamaru		X	X
GP115c-18	GP115c	Kinleith	A	Whakamaru		X	X
GP115c-20	GP115c	Kinleith	A	Whakamaru		X	X
WHA039A	WHA039	Pokai Road	A	Whakamaru		X	X
WHA039B	WHA039	Pokai Road	A	Whakamaru		X	X
WHA039C	WHA039	Pokai Road	A	Whakamaru		X	X
WHA039D	WHA039	Pokai Road	A	Whakamaru	X	X	X
WHA039E	WHA039	Pokai Road	A	Whakamaru	X	X	X
WHA039F	WHA039	Pokai Road	D	Whakamaru	X	X	X
WHA039G	WHA039	Pokai Road	A	Whakamaru	X	X	X
WHA039H	WHA039	Pokai Road	A	Whakamaru	X	X	X
WHA039I	WHA039	Pokai Road	A	Whakamaru	X	X	X
WHA039J	WHA039	Pokai Road	C	Whakamaru	X	X	X
WHA039K	WHA039	Pokai Road	A	Whakamaru	X	X	
WHA109A	WHA109	Tunnel	A	Whakamaru		X	X
WHA109B	WHA109	Tunnel	C	Whakamaru		X	X
WHA109C	WHA109	Tunnel	C	Whakamaru	X	X	X

WHA109D	WHA109	Tunnel	C	Whakamaru		X	X
WHA109E	WHA109	Tunnel	B	Whakamaru	X	X	X
WHA114A	WHA114	Epic	B	Whakamaru	X	X	X
WHA114B	WHA114	Epic	B	Whakamaru	X	X	X
WHA114C	WHA114	Epic	B	Whakamaru		X	X
WHA114D	WHA114	Epic	B	Whakamaru		X	X
WHAK412	WHAK412	W Taupo	B	Whakamaru		X	
WHAK415-A1	WHAK415	N Taupo	B	Whakamaru		X	
WHAK415-A2	WHAK415	N Taupo	B	Whakamaru	X		
WHAK415-A3	WHAK415	N Taupo	B	Whakamaru	X	X	
WHAK415-A4	WHAK415	N Taupo	B	Whakamaru	X	X	
WHAK415-A5	WHAK415	N Taupo	A	Whakamaru		X	X
WHAK415-A6	WHAK415	N Taupo	B	Whakamaru		X	X
WHAK415-A7	WHAK415	N Taupo	B	Whakamaru		X	X
WHAK415-A8	WHAK415	N Taupo	B	Whakamaru		X	X
WHAK602	WHAK602	Murupara	Unclassified	Rangitaiki		X	
WHAK602A	WHAK602	Murupara	Unclassified	Rangitaiki		X	X
WHAK602C	WHAK602	Murupara	Unclassified	Rangitaiki		X	X
WHAK602E	WHAK602	Murupara	Unclassified	Rangitaiki		X	X

Table 3.3: Pumice whole rock major element compositions

Sample Name	Sample Location	SiO_2	Al_2O_3	TiO_2	MgO	FeO	MnO	CaO	Na_2O	K_2O	P2O5
GP107-04	GP107	75.6	14.0	0.17	0.15	1.27	0.06	0.96	3.24	4.59	0.01
WHA039D	WHA039	72.3	15.5	0.33	0.44	2.17	0.05	2.42	3.72	2.99	0.02
WHA039E	WHA039	71.7	16.6	0.36	0.51	2.41	0.06	2.14	3.42	2.80	0.02
WHA039F	WHA039	74.5	14.6	0.30	0.34	1.81	0.04	1.73	3.41	3.30	0.02
WHA039G	WHA039	73.2	15.3	0.34	0.44	2.24	0.05	2.17	3.51	2.82	0.02
WHA039H	WHA039	71.8	16.6	0.35	0.45	2.27	0.06	2.32	3.55	2.58	0.02
WHA039I	WHA039	73.1	14.9	0.32	0.44	2.14	0.06	2.16	3.44	3.44	0.02
WHA039J	WHA039	76.4	13.7	0.14	0.08	1.09	0.04	0.81	3.04	4.64	0.01
WHA039K	WHA039	72.3	16.2	0.35	0.45	2.28	0.06	2.21	3.46	2.67	0.02
WHA109C	WHA109	76.1	13.5	0.12	0.08	1.09	0.05	0.83	3.56	4.66	0.01
WHA109E	WHA109	76.3	13.4	0.14	0.11	1.16	0.05	0.90	3.53	4.42	0.01
WHA114A	WHA114	76.3	13.4	0.14	0.11	1.08	0.04	0.95	3.51	4.46	0.01
WHA114B	WHA114	76.3	13.4	0.14	0.11	1.10	0.04	0.96	3.52	4.43	0.01
WHAK415-A2	WHAK415	74.0	15.8	0.24	0.29	1.66	0.05	1.18	2.85	3.92	0.03
WHAK415-A3	WHAK415	74.8	15.0	0.17	0.15	1.29	0.04	1.01	2.90	4.59	0.03
WHAK415-A4	WHAK415	74.0	15.4	0.21	0.19	1.46	0.05	1.28	3.12	4.29	0.03

Table 3.4: Pumice whole rock trace element compositions (Ni-Hf)

Sample Name	Ni	Cr	V	Sc	Cu	Zn	Ga	Ba	Rb	Cs	Sr	Y	Zr	Hf
GP107-04	0.9	3.1	7.5	3.5	1.1	32	14	906	150	9.5	69	23	114	4.4
WHA039D	2.2	9.9	27	7.0	-	34	15	695	91	5.4	192	15	168	3.3
WHA039E	1.9	5.5	26	5.9	5.8	40	16	718	90	3.5	164	20	194	4.3
WHA039F	2.7	6.5	19	4.1	18	41	14	924	166	11	141	18	177	4.8
WHA039G	1.6	4.6	27	5.7	-	32	16	682	88	2.6	169	16	179	4.8
WHA039H	3.2	7.6	28	7.0	12	41	16	669	81	7.4	182	15	190	4.8
WHA039I	0.4	3.7	25	4.0	-	31	14	738	102	2.2	172	17	169	5.1
WHA039J	0.8	5.6	6.1	4.0	25	34	13	774	169	9.7	53	21	106	4.0
WHA039K	1.4	7.5	28	6.9	6.5	35	15	697	84	4.2	173	18	192	4.8
WHA109C	1.0	3.4	4.2	1.4	112	86	14	690	165	5.0	51	24	103	3.8
WHA109E	0.2	5.3	5.3	2.7	43	55	12	750	155	6.6	61	21	102	2.7
WHA114A	1.0	5.4	7.0	2.7	62	60	13	907	149	8.2	69	21	98	4.0
WHA114B	2.0	5.3	5.6	2.2	29	42	13	804	151	6.3	67	21	103	3.3
WHAK415-A2	0.2	1.7	14	4.2	0.7	26	14	1152	137	8.3	91	18	149	4.6
WHAK415-A3	2.5	4.0	8.4	3.8	13	23	14	825	157	7.2	72	22	126	3.3
WHAK415-A4	4.6	9.4	12	3.9	3.5	19	14	1256	154	8.8	107	18	140	3.3

Table 3.5: Pumice whole rock trace element compositions (Nb-Bi)

Sample Name	Nb	Ta	Mo	La	Ce	Nd	Sm	Dy	Yb	Th	U	Tl	Pb	Sn	Bi
GP107-04	8.6	1.0	3.2	28	57	20	4.4	3.3	2.5	17	2.6	0.7	11	2.9	0.1
WHA039D	6.9	0.7	2.3	17	34	14	2.7	2.4	1.4	11	2.5	1.0	7.6	3.1	0.4
WHA039E	7.8	1.0	1.2	24	41	16	3.2	3.1	2.1	12	4.5	0.6	7.2	3.0	0.1
WHA039F	6.1	0.9	0.8	26	42	15	2.4	2.8	1.8	10	2.2	1.3	7.9	3.1	0.4
WHA039G	6.8	1.0	2.1	18	34	13	2.9	2.4	1.8	11	2.7	0.7	6.8	3.0	0.0
WHA039H	8.0	1.6	1.1	18	35	11	2.0	2.4	1.7	10	2.4	0.6	7.7	3.1	-
WHA039I	6.7	0.5	2.3	18	41	15	3.0	2.2	1.8	12	2.2	0.7	7.3	3.0	0.1
WHA039J	7.3	1.5	2.3	26	59	18	3.8	3.0	2.0	16	4.1	1.0	7.8	3.1	0.3
WHA039K	6.8	0.9	1.2	22	47	16	3.3	3.0	2.0	12	2.6	1.0	7.7	3.1	0.3
WHA109C	8.1	0.8	2.3	29	53	19	4.0	3.4	2.4	18	3.6	0.6	11	3.1	0.0
WHA109E	7.0	1.2	2.9	29	53	18	3.4	3.1	2.2	15	4.2	1.8	7.7	3.1	0.1
WHA114A	7.3	0.7	0.8	23	49	17	3.4	3.1	2.2	15	3.1	1.1	9.3	3.1	0.4
WHA114B	7.8	1.3	3.7	28	53	20	3.7	3.1	2.1	15	3.0	1.0	9.9	3.1	0.2
WHAK415-A2	8.0	0.9	1.0	24	47	18	3.6	2.8	1.7	17	3.5	0.4	4.3	2.7	0.1
WHAK415-A3	7.5	0.9	1.0	25	52	19	3.6	3.3	2.1	18	2.6	1.1	3.3	3.1	0.3
WHAK415-A4	7.7	1.2	1.6	26	49	18	3.3	2.7	1.9	15	2.9	1.4	0.8	3.1	0.2

Table 3.6: Pumice whole rock extraction pressures (MPa)

Sample Name	Q2F P_2	Q2F P_3	QFO NNO P_2	QFO NNO P_3	QFO NNO+0.5 P_2	QFO NNO+0.5 P_3	QFO NNO+1 P_2	QFO NNO+1 P_3	QFO NNO+1.5 P_2	QFO NNO+1.5 P_3	QFO NNO+2 P_2	QFO NNO+2 P_3
GP107-04	249	-	309	-	397	-	323	-	-	-	-	-
WHA039D	-	-	220	-	268	-	-	-	-	-	-	-
WHA039E	438	-	178	-	230	-	292	-	358	-	-	-
WHA039F	349	-	192	-	248	-	318	316	-	347	-	-
WHA039G	393	-	189	-	242	-	-	-	-	-	-	-
WHA039H	463	-	233	-	289	-	356	-	-	-	-	-
WHA039I	393	-	171	-	221	-	-	-	-	-	-	-
WHA039J	153	-	-	-	364	-	-	-	-	-	-	-
WHA039K	-	-	215	-	270	-	333	-	-	-	-	-
WHA109C	242	-	331	-	328	-	308	-	-	-	-	-
WHA109E	220	-	369	-	411	-	298	-	147	-	-	-
WHA114A	226	-	366	-	381	-	298	-	-	-	-	-
WHA114B	229	-	364	-	391	-	298	-	-	-	-	-
WHAK415-A2	315	-	187	-	248	-	324	-	-	-	-	-
WHAK415-A3	276	-	313	-	407	-	-	-	-	-	-	-
WHAK415-A4	355	-	308	-	369	-	-	-	-	-	-	-

Table 3.7: Pumice glass major element mean compositions

Sample Name	Sample Location	SiO_2	Al_2O_3	TiO_2	MgO	FeO	MnO	CaO	Na_2O	K_2O
GP107-04	GP107	77.8	12.6	0.17	0.04	0.39	0.01	0.70	3.33	4.95
GP115a-06	GP115a	77.8	12.7	0.09	0.01	0.39	0.04	0.55	3.53	4.98
GP115a-09	GP115a	77.9	12.5	0.19	0.07	0.57	0.02	0.75	3.40	4.67
GP115a-12	GP115a	77.6	12.6	0.18	0.09	0.66	0.04	0.77	3.39	4.72
GP115c-14	GP115c	77.8	12.5	0.19	0.05	0.37	0.03	0.75	2.92	5.35
GP115c-18	GP115c	77.6	12.6	0.18	0.08	0.70	0.04	0.79	3.34	4.68
GP115c-20	GP115c	77.7	12.6	0.16	0.04	0.38	0.03	0.74	3.22	5.11
WHA039A	WHA039	77.8	12.6	0.17	0.03	0.38	0.04	0.69	3.28	5.01
WHA039B	WHA039	77.8	12.7	0.18	0.02	0.38	0.02	0.72	3.42	4.81
WHA039C	WHA039	78.0	12.6	0.18	0.02	0.39	0.02	0.82	3.25	4.77
WHA039D	WHA039	77.5	12.6	0.08	0.05	0.71	0.05	0.61	3.59	4.82
WHA039E	WHA039	78.0	12.5	0.22	0.05	0.42	0.01	0.85	2.75	5.17
WHA039F	WHA039	78.0	12.6	0.13	0.06	0.37	0.04	0.82	3.03	4.94
WHA039G	WHA039	77.8	12.6	0.19	0.03	0.40	0.01	0.71	3.33	4.90
WHA039H	WHA039	77.9	12.7	0.16	0.04	0.31	0.02	0.73	3.13	4.98
WHA039I	WHA039	77.9	12.7	0.18	0.03	0.28	0.05	0.70	2.52	5.59
WHA039J	WHA039	77.7	12.7	0.08	0.03	0.35	0.04	0.55	3.44	5.06
WHA039K	WHA039	78.0	12.5	0.16	0.04	0.36	0.03	0.84	2.80	5.24
WHA109A	WHA109	77.8	12.5	0.17	0.08	0.95	0.04	0.72	3.17	4.61
WHA109B	WHA109	77.8	12.5	0.08	0.04	0.70	0.06	0.49	3.37	4.98
WHA109C	WHA109	77.6	12.6	0.06	0.05	0.65	0.04	0.59	3.02	5.42

WHA109D	WHA109	77.5	12.6	0.06	0.03	0.72	0.06	0.50	3.25	5.29
WHA109E	WHA109	77.6	12.6	0.06	0.04	0.69	0.06	0.53	3.12	5.25
WHA114A	WHA114	77.6	12.6	0.07	0.04	0.69	0.06	0.58	3.58	4.88
WHA114B	WHA114	77.6	12.6	0.09	0.04	0.61	0.03	0.59	3.61	4.88
WHA114C	WHA114	77.6	12.6	0.07	0.04	0.55	0.05	0.59	3.55	4.90
WHA114D	WHA114	77.6	12.6	0.10	0.04	0.60	0.03	0.60	3.55	4.84
WHAK412	WHAK412	77.5	12.5	0.17	0.11	1.29	0.07	1.18	4.04	3.12
WHAK415-A1	WHAK415	77.7	12.6	0.09	0.04	0.34	0.04	0.59	2.93	5.65
WHAK415-A3	WHAK415	77.6	12.6	0.08	0.02	0.34	0.03	0.57	3.04	5.71
WHAK415-A4	WHAK415	77.6	12.6	0.11	0.02	0.31	0.03	0.61	2.99	5.74
WHAK415-A5	WHAK415	77.7	12.6	0.12	0.05	0.38	0.05	0.74	2.75	5.61
WHAK415-A6	WHAK415	77.7	12.6	0.10	0.04	0.34	0.02	0.63	2.72	5.78
WHAK415-A7	WHAK415	77.6	12.6	0.08	0.02	0.39	0.04	0.58	2.79	5.90
WHAK415-A8	WHAK415	77.7	12.6	0.06	0.02	0.37	0.02	0.60	2.88	5.76
WHAK602	WHAK602	77.6	12.5	0.17	0.01	0.21	0.03	0.34	2.46	6.75
WHAK602A	WHAK602	77.5	12.5	0.19	0.01	0.25	-	0.39	2.39	6.76
WHAK602C	WHAK602	77.5	12.4	0.16	0.03	0.47	0.01	0.25	2.63	6.56
WHAK602E	WHAK602	77.2	12.4	0.13	0.06	0.68	0.00	0.24	2.88	6.37

Table 3.8: Pumice glass major element standard deviations of the mean compositions

Sample Name	Sample Location	SiO_2	Al_2O_3	TiO_2	MgO	FeO	MnO	CaO	Na_2O	K_2O
GP107-04	GP107	0.11	0.03	0.08	0.01	0.03	0.08	0.04	0.08	0.13
GP115a-06	GP115a	0.09	0.03	0.09	0.04	0.01	0.09	0.05	0.15	0.17
GP115a-09	GP115a	0.20	0.04	0.05	0.03	0.04	0.21	0.05	0.08	0.13
GP115a-12	GP115a	0.07	0.04	0.07	0.04	0.03	0.14	0.05	0.07	0.11
GP115c-14	GP115c	0.13	0.04	0.07	0.03	0.03	0.08	0.03	0.23	0.31
GP115c-18	GP115c	0.12	0.04	0.06	0.04	0.03	0.11	0.04	0.05	0.06
GP115c-20	GP115c	0.07	0.05	0.05	0.03	0.02	0.13	0.04	0.14	0.26
WHA039A	WHA039	0.13	0.01	0.05	0.03	0.03	0.07	0.04	0.10	0.10
WHA039B	WHA039	0.14	0.04	0.08	0.02	0.02	0.06	0.03	0.07	0.08
WHA039C	WHA039	0.23	0.07	0.16	0.03	0.02	0.12	0.06	0.09	0.10
WHA039D	WHA039	0.10	0.05	0.04	0.04	0.03	0.06	0.03	0.04	0.05
WHA039E	WHA039	0.31	0.05	0.22	0.01	0.04	0.10	0.07	0.44	0.30
WHA039F	WHA039	0.37	0.05	0.19	0.04	0.03	0.10	0.07	0.46	0.40
WHA039G	WHA039	0.13	0.04	0.05	0.02	0.03	0.08	0.04	0.07	0.10
WHA039H	WHA039	0.15	0.06	0.05	0.02	0.03	0.05	0.03	0.17	0.09
WHA039I	WHA039	0.13	0.04	0.13	0.04	0.02	0.08	0.03	0.18	0.15
WHA039J	WHA039	0.11	0.05	0.08	0.04	0.02	0.05	0.04	0.10	0.11
WHA039K	WHA039	0.21	0.07	0.25	0.03	0.02	0.08	0.09	0.41	0.34
WHA109A	WHA109	0.20	0.04	0.11	0.04	0.03	0.08	0.06	0.14	0.07
WHA109B	WHA109	0.08	0.06	0.04	0.04	0.03	0.07	0.04	0.11	0.07
WHA109C	WHA109	0.31	0.05	0.22	0.03	0.02	0.19	0.07	0.55	0.52

WHA109D	WHA109	0.13	0.04	0.09	0.04	0.02	0.05	0.04	0.12	0.14
WHA109E	WHA109	0.33	0.04	0.11	0.05	0.02	0.20	0.03	0.47	0.36
WHA114A	WHA114	0.12	0.03	0.08	0.04	0.03	0.07	0.04	0.06	0.04
WHA114B	WHA114	0.10	0.06	0.07	0.03	0.03	0.14	0.04	0.04	0.08
WHA114C	WHA114	0.09	0.04	0.03	0.05	0.03	0.09	0.04	0.05	0.07
WHA114D	WHA114	0.11	0.05	0.10	0.04	0.02	0.07	0.03	0.05	0.06
WHAK412	WHAK412	0.19	0.05	0.06	0.05	0.02	0.08	0.02	0.06	0.05
WHAK415-A1	WHAK415	0.11	0.02	0.05	0.03	0.03	0.07	0.03	0.03	0.07
WHAK415-A3	WHAK415	0.10	0.05	0.04	0.03	0.02	0.06	0.03	0.06	0.07
WHAK415-A4	WHAK415	0.08	0.05	0.07	0.03	0.02	0.04	0.04	0.05	0.09
WHAK415-A5	WHAK415	0.11	0.05	0.08	0.05	0.02	0.07	0.03	0.05	0.07
WHAK415-A6	WHAK415	0.11	0.05	0.06	0.02	0.04	0.08	0.03	0.05	0.06
WHAK415-A7	WHAK415	0.08	0.04	0.04	0.04	0.02	0.06	0.04	0.04	0.04
WHAK415-A8	WHAK415	0.10	0.04	0.03	0.02	0.02	0.05	0.03	0.04	0.05
WHAK602	WHAK602	0.16	0.03	0.05	0.03	0.01	0.05	0.05	0.14	0.06
WHAK602A	WHAK602	0.17	0.04	0.06	-	0.02	0.07	0.04	0.13	0.05
WHAK602C	WHAK602	0.19	0.05	0.04	0.02	0.03	0.15	0.02	0.06	0.07
WHAK602E	WHAK602	0.13	0.02	0.12	0.01	0.06	0.15	0.08	0.12	0.12

Table 3.9: Pumice glass trace element mean compositions (Li-Nb)

Sample Name	Li	Al	Si	Sc	V	Fe	Ni	Zn	Ga	Rb	Sr	Y	Zr	Nb
GP107-04	43	64149	363574	9.6	2.7	39	0.3	15	67	154	46	18	114	7.7
GP115a-06	55	61479	363528	15	0.4	37	0.6	27	39	193	18	20	62	7.9
GP115a-09	42	61509	363761	9.5	2.8	45	0.0	22	70	164	46	17	106	7.5
GP115a-12	45	61073	362639	11	2.8	47	0.5	21	67	158	43	17	109	6.9
GP115c-14	23	67191	363902	10	3.0	58	0.8	11	73	160	45	18	120	7.0
GP115c-18	40	62348	362593	9.6	2.6	52	0.2	22	70	172	48	19	112	7.1
GP115c-20	39	61546	363434	11	2.9	43	0.3	17	69	161	47	19	110	7.5
WHA039A	36	68776	363200	14	2.9	34	0.1	9.5	89	175	45	18	120	7.1
WHA039B	39	113900	363200	15	4.0	85	0.6	19	103	149	40	27	155	11
WHA039C	31	97773	363200	14	3.0	97	0.4	23	103	150	48	19	164	9.1
WHA039D	49	62862	362266	10.0	0.4	50	0.4	23	34	174	20	20	62	7.5
WHA039E	32	111688	363060	20	3.8	136	1.9	27	90	143	35	29	202	12
WHA039F	49	62004	363574	14	1.0	45	0.4	29	90	165	48	14	76	6.3
WHA039G	41	66575	363528	15	2.6	42	0.2	12	85	166	43	17	106	6.8
WHA039H	29	72738	363761	17	3.0	37	0.5	7.5	85	162	42	17	123	6.6
WHA039I	25	70116	362920	16	3.0	87	1.3	9.8	89	181	46	18	124	7.8
WHA039J	41	69986	363247	15	0.5	39	0.5	15	34	194	14	23	68	8.9
WHA039K	-	-	-	-	-	-	-	-	-	-	-	-	-	-
WHA109A	20	66955	362266	14	2.5	51	0.2	18	91	176	50	18	111	6.4
WHA109B	26	65292	362266	13	0.3	43	0.1	16	31	196	13	22	64	7.8
WHA109C	18	56255	361985	14	0.4	38	0.2	20	27	188	11	18	52	8.0

WHA109D	36	64139	362265	14	0.4	49	0.2	28	31	203	13	21	63	8.1
WHA109E	52	62681	362125	15	0.5	53	0.3	30	44	188	19	20	61	7.4
WHA114A	52	62203	362686	9.2	0.5	50	0.4	24	37	179	20	20	64	7.7
WHA114B	52	62560	362593	14	0.5	41	0.3	21	45	182	19	20	63	7.7
WHA114C	44	64277	362733	13	0.6	36	0.1	16	42	183	18	20	63	7.5
WHA114D	48	64513	362733	14	0.4	36	0.1	16	44	185	18	21	67	8.0
WHAK412	-	-	-	-	-	-	-	-	-	-	-	-	-	-
WHAK415-A1	-	-	-	-	-	-	-	-	-	-	-	-	-	-
WHAK415-A3	-	-	-	-	-	-	-	-	-	-	-	-	-	-
WHAK415-A4	-	-	-	-	-	-	-	-	-	-	-	-	-	-
WHAK415-A5	35	82018	363154	16	1.5	37	0.8	7.7	101	208	47	17	106	7.4
WHAK415-A6	44	79001	363200	15	0.6	31	0.5	6.2	79	246	30	18	85	8.0
WHAK415-A7	47	64176	362733	15	0.5	34	0.5	12	42	239	20	22	66	8.1
WHAK415-A8	40	68052	362967	14	0.6	28	0.1	7.0	40	247	19	22	73	8.7
WHAK602	-	-	-	-	-	-	-	-	-	-	-	-	-	-
WHAK602A	32	67629	362078	19	2.6	27	0.1	7.4	79	502	14	18	115	6.8
WHAK602C	83	63220	361985	17	3.4	53	0.7	12	44	781	7.0	18	109	7.1
WHAK602E	135	67065	360957	16	2.9	30	0.1	7.2	35	972	5.5	18	108	7.2

Table 3.10: Pumice glass trace element mean compositions (Cs-Tm)

Sample Name	Cs	Ba	La	Ce	Pr	Nd	Sm	Eu	Tb	Gd	Dy	Ho	Er	Tm
GP107-04	6.7	795	23	45	4.6	17	3.2	0.3	0.5	2.7	2.8	0.6	1.8	0.3
GP115a-06	8.9	319	26	53	5.0	18	3.7	0.2	0.5	3.0	3.3	0.6	1.9	0.3
GP115a-09	7.4	836	22	43	4.3	16	3.2	0.3	0.4	2.5	2.9	0.6	1.8	0.3
GP115a-12	7.0	770	22	42	4.2	15	3.2	0.3	0.4	2.7	2.8	0.6	1.8	0.3
GP115c-14	7.5	817	25	41	4.7	17	2.6	0.3	0.4	3.0	3.1	0.6	1.9	0.3
GP115c-18	7.5	832	25	44	4.5	16	3.3	0.4	0.5	2.7	2.8	0.6	1.8	0.3
GP115c-20	7.3	884	25	40	4.5	18	3.2	0.4	0.5	2.9	3.0	0.6	1.9	0.3
WHA039A	7.8	829	24	44	4.5	17	3.1	0.3	0.5	2.7	2.9	0.6	1.9	0.3
WHA039B	8.0	910	36	48	6.4	22	4.2	0.5	0.7	4.0	4.3	0.9	2.7	0.4
WHA039C	7.4	887	29	39	4.8	16	3.1	0.4	0.5	2.7	3.0	0.7	1.9	0.3
WHA039D	8.7	351	27	52	4.9	19	3.5	0.2	0.5	2.9	3.3	0.7	2.1	0.3
WHA039E	9.1	824	35	45	6.7	25	4.6	0.7	0.8	4.8	4.4	1.0	2.6	0.4
WHA039F	6.6	926	21	42	3.9	14	2.7	0.4	0.4	2.3	2.3	0.5	1.5	0.2
WHA039G	7.5	808	22	42	4.3	16	3.2	0.4	0.5	2.8	2.7	0.6	1.7	0.3
WHA039H	7.4	783	22	42	3.9	17	3.2	0.4	0.4	2.7	2.9	0.6	1.6	0.3
WHA039I	8.2	850	24	44	4.0	17	3.1	0.3	0.5	3.0	3.0	0.6	1.8	0.3
WHA039J	10	215	26	54	5.2	19	3.6	0.2	0.6	3.3	3.7	0.8	2.4	0.4
WHA039K	-	-	-	-	-	-	-	-	-	-	-	-	-	-
WHA109A	7.4	868	25	45	4.5	17	3.1	0.2	0.5	2.8	2.9	0.6	1.9	0.3
WHA109B	9.3	211	26	52	5.2	18	3.8	0.1	0.6	3.2	3.6	0.8	2.2	0.4
WHA109C	8.6	181	22	49	4.4	17	4.0	0.2	0.6	3.0	3.1	0.6	2.0	0.3

WHA109D	9.5	209	26	54	5.1	19	3.5	0.1	0.5	3.1	3.5	0.8	2.3	0.4
WHA109E	8.4	342	25	52	4.9	18	3.1	0.2	0.5	3.1	3.0	0.7	1.9	0.3
WHA114A	8.8	346	27	53	5.2	20	3.7	0.2	0.5	2.8	3.3	0.7	2.1	0.3
WHA114B	8.8	333	27	54	5.2	18	3.6	0.2	0.5	2.9	3.1	0.7	2.0	0.3
WHA114C	8.5	311	26	53	4.9	18	3.5	0.2	0.5	3.0	3.2	0.7	2.0	0.3
WHA114D	8.7	327	29	55	5.4	19	3.7	0.2	0.5	3.2	3.4	0.7	2.1	0.3
WHAK412	-	-	-	-	-	-	-	-	-	-	-	-	-	-
WHAK415-A1	-	-	-	-	-	-	-	-	-	-	-	-	-	-
WHAK415-A3	-	-	-	-	-	-	-	-	-	-	-	-	-	-
WHAK415-A4	-	-	-	-	-	-	-	-	-	-	-	-	-	-
WHAK415-A5	11	887	25	46	4.9	19	3.6	0.4	0.5	2.8	2.8	0.6	1.6	0.3
WHAK415-A6	14	678	27	55	5.0	19	3.1	0.3	0.5	2.7	3.1	0.7	1.9	0.3
WHAK415-A7	9.7	344	29	57	5.6	19	3.7	0.2	0.6	3.2	3.5	0.7	2.2	0.4
WHAK415-A8	12	308	30	58	5.7	20	3.9	0.2	0.6	3.3	3.7	0.8	2.2	0.4
WHAK602	-	-	-	-	-	-	-	-	-	-	-	-	-	-
WHAK602A	42	710	23	41	4.3	16	3.1	0.2	0.5	2.8	2.9	0.6	2.0	0.3
WHAK602C	75	348	22	46	4.3	15	3.2	0.1	0.5	2.6	2.9	0.6	1.9	0.3
WHAK602E	93	238	24	46	4.7	17	3.1	0.0	0.4	2.7	3.1	0.7	1.8	0.3

Table 3.11: Pumice glass trace element mean compositions (Yb-U)

Sample Name	Yb	Lu	Hf	Ta	Pb	Th	U
GP107-04	2.3	0.3	3.4	0.6	11	14	3.5
GP115a-06	2.5	0.4	2.5	0.7	12	17	4.6
GP115a-09	2.2	0.3	3.1	0.6	13	14	3.7
GP115a-12	2.2	0.3	3.2	0.6	13	15	3.6
GP115c-14	2.2	0.3	3.4	0.7	13	15	3.5
GP115c-18	2.2	0.3	3.2	0.6	17	15	3.6
GP115c-20	2.2	0.3	3.1	0.6	13	14	3.4
WHA039A	2.2	0.3	3.7	0.7	11	15	3.7
WHA039B	3.0	0.4	4.8	0.8	15	22	4.1
WHA039C	2.1	0.3	4.8	0.9	14	17	3.4
WHA039D	2.4	0.4	2.5	0.7	11	16	4.0
WHA039E	3.1	0.4	5.8	1.1	14	23	4.3
WHA039F	1.9	0.3	2.6	0.5	15	12	3.2
WHA039G	2.1	0.3	3.1	0.6	10	14	3.6
WHA039H	2.1	0.3	3.7	0.6	11	15	2.9
WHA039I	2.2	0.4	3.9	0.7	13	15	3.2
WHA039J	2.8	0.4	2.8	0.9	13	18	4.9
WHA039K	-	-	-	-	-	-	-
WHA109A	2.3	0.3	3.4	0.6	12	15	3.5
WHA109B	2.7	0.4	2.6	0.8	9.4	17	4.5
WHA109C	2.4	0.4	2.1	0.8	11	15	4.5

WHA109D	2.7	0.4	2.6	0.8	10	17	4.9
WHA109E	2.3	0.3	2.4	0.8	12	16	4.2
WHA114A	2.5	0.4	2.3	0.7	11	16	4.3
WHA114B	2.5	0.3	2.4	0.7	11	16	4.3
WHA114C	2.5	0.4	2.5	0.8	13	16	4.2
WHA114D	2.6	0.4	2.6	0.8	12	17	4.3
WHAK412	-	-	-	-	-	-	-
WHAK415-A1	-	-	-	-	-	-	-
WHAK415-A3	-	-	-	-	-	-	-
WHAK415-A4	-	-	-	-	-	-	-
WHAK415-A5	2.1	0.3	3.4	0.7	3.8	16	3.7
WHAK415-A6	2.4	0.4	3.0	0.8	3.7	17	4.1
WHAK415-A7	2.8	0.4	2.7	0.8	3.5	18	4.8
WHAK415-A8	2.6	0.4	2.7	0.9	3.2	18	4.7
WHAK602	-	-	-	-	-	-	-
WHAK602A	2.2	0.4	3.7	0.6	5.1	14	4.1
WHAK602C	2.2	0.4	3.2	0.6	5.4	14	3.5
WHAK602E	2.1	0.3	3.2	0.6	6.3	14	3.6

Table 3.12: Pumice glass trace element standard deviations of the mean compositions (Li-Nb)

Sample Name	Li	Al	Si	Sc	V	Fe	Ni	Zn	Ga	Rb	Sr	Y	Zr	Nb
GP107-04	5.7	4395	0.0	1.1	0.4	12	0.6	7.3	3.2	9.5	1.8	1.4	6.3	0.7
GP115a-06	2.0	3584	0.0	1.1	0.0	6.2	0.2	3.2	2.2	16	1.0	0.8	2.7	0.7
GP115a-09	-	-	-	-	-	-	-	-	-	-	-	-	-	-
GP115a-12	-	-	-	-	-	-	-	-	-	-	-	-	-	-
GP115c-14	7.2	8288	0.0	1.2	0.3	35	0.2	2.3	4.0	8.5	3.9	1.5	12	1.5
GP115c-18	3.2	976	0.0	0.6	0.4	7.6	0.3	7.0	3.4	11	1.4	0.9	5.4	0.5
GP115c-20	12	2596	0.0	1.9	0.2	15	0.5	5.3	3.5	8.6	2.5	1.7	8.8	1.0
WHA039A	5.3	4103	0.0	0.8	0.2	14	0.1	2.3	6.0	12	1.5	0.3	11	0.4
WHA039B	3.7	33718	0.0	1.2	0.8	18	0.3	5.0	10	27	2.6	6.1	25	2.4
WHA039C	2.5	20328	0.0	1.3	0.5	36	0.3	7.5	5.8	12	6.1	1.9	26	1.9
WHA039D	2.5	2394	0.0	0.9	0.1	8.1	0.3	5.4	0.7	8.8	1.3	0.6	1.3	0.2
WHA039E	4.3	29914	0.0	1.7	0.9	75	1.5	9.2	14	36	2.4	4.7	33	3.6
WHA039F	2.2	4320	0.0	0.3	0.1	4.9	0.1	3.4	5.2	6.3	2.0	1.0	4.2	0.4
WHA039G	4.9	6198	0.0	1.1	0.2	10	0.1	0.9	5.2	9.5	1.5	1.0	8.3	0.7
WHA039H	7.7	12063	-	0.3	0.2	12	0.0	6.0	3.5	6.5	1.4	3.8	6.6	1.8
WHA039I	3.7	5921	0.0	1.5	0.4	43	0.4	4.5	5.8	29	3.5	2.4	10	0.9
WHA039J	3.7	4407	0.0	1.5	0.2	11	0.2	1.9	3.9	4.1	1.0	1.7	3.5	0.5
WHA039K	-	-	-	-	-	-	-	-	-	-	-	-	-	-
WHA109A	5.3	2254	0.0	0.9	0.3	9.0	0.2	3.2	4.3	6.8	3.6	1.3	5.2	0.4
WHA109B	3.0	3256	0.0	0.5	0.0	5.1	0.1	4.3	0.7	7.2	0.4	1.2	3.1	0.5
WHA109C	0.5	3081	-	1.7	0.1	4.9	-	1.3	0.8	2.5	1.4	0.6	3.0	0.7

WHA109D	7.3	2769	0.0	0.7	0.1	7.2	0.2	3.9	1.6	7.0	0.4	0.7	2.7	0.3
WHA109E	9.8	721	-	1.2	0.1	2.3	0.1	0.1	0.5	4.2	1.4	0.9	0.4	0.1
WHA114A	2.4	3279	0.0	1.4	0.0	1.1	0.3	4.9	1.3	11	1.1	0.6	2.8	0.3
WHA114B	2.3	5620	0.0	1.2	0.1	7.6	0.6	7.8	2.0	8.2	1.6	1.6	6.4	0.6
WHA114C	5.7	5253	0.0	0.7	0.2	9.5	0.1	2.8	3.1	10	1.0	1.9	7.4	0.7
WHA114D	2.9	7141	0.0	0.6	0.0	8.9	0.1	6.7	5.1	13	1.3	2.5	8.5	0.9
WHAK412	-	-	-	-	-	-	-	-	-	-	-	-	-	-
WHAK415-A1	-	-	-	-	-	-	-	-	-	-	-	-	-	-
WHAK415-A3	-	-	-	-	-	-	-	-	-	-	-	-	-	-
WHAK415-A4	-	-	-	-	-	-	-	-	-	-	-	-	-	-
WHAK415-A5	2.2	1653	-	0.2	0.2	8.6	0.6	0.1	0.2	3.6	1.3	1.1	0.6	1.3
WHAK415-A6	2.3	10693	-	0.7	0.1	5.1	0.2	2.0	5.8	11	0.7	1.6	11	1.0
WHAK415-A7	9.8	5034	0.0	1.1	0.1	4.6	0.0	7.9	10	13	2.2	2.5	9.5	0.8
WHAK415-A8	5.3	7358	0.0	0.7	0.2	4.4	0.1	2.2	4.7	14	1.1	1.6	11	0.7
WHAK602	-	-	-	-	-	-	-	-	-	-	-	-	-	-
WHAK602A	9.4	1708	-	0.7	0.3	8.8	0.2	2.0	6.0	28	1.9	0.9	3.2	0.8
WHAK602C	29	2006	0.0	1.5	0.6	24	0.6	3.2	7.6	50	2.6	1.7	10	0.3
WHAK602E	52	3417	-	0.2	0.1	14	0.1	2.7	7.6	27	2.4	0.2	7.5	0.2

Table 3.13: Pumice glass trace element standard deviations of the mean compositions (Cs-Tm)

Sample Name	Cs	Ba	La	Ce	Pr	Nd	Sm	Eu	Tb	Gd	Dy	Ho	Er	Tm
GP107-04	0.6	67	1.5	3.2	0.7	1.7	0.5	0.1	0.1	0.3	0.5	0.0	0.1	0.1
GP115a-06	0.3	18	2.3	2.9	0.5	0.9	0.2	0.0	0.0	0.3	0.3	0.0	0.2	0.0
GP115a-09	-	-	-	-	-	-	-	-	-	-	-	-	-	-
GP115a-12	-	-	-	-	-	-	-	-	-	-	-	-	-	-
GP115c-14	0.6	45	3.2	2.6	0.2	3.3	0.6	0.0	0.0	0.2	0.2	0.1	0.3	0.0
GP115c-18	0.2	26	1.0	1.7	0.3	1.4	0.7	0.0	0.0	0.2	0.2	0.1	0.1	0.0
GP115c-20	0.5	29	1.0	3.6	0.2	2.2	0.6	0.1	0.1	0.3	0.2	0.0	0.1	0.0
WHA039A	0.5	46	0.9	3.4	0.3	0.8	0.4	0.0	0.0	0.3	0.2	0.0	0.2	0.0
WHA039B	0.6	54	6.9	6.4	1.3	3.8	0.8	0.2	0.2	1.0	1.0	0.2	0.5	0.1
WHA039C	0.5	84	3.6	5.1	0.5	1.8	0.5	0.0	0.1	0.2	0.3	0.1	0.1	0.0
WHA039D	0.4	20	0.7	3.3	0.3	1.4	0.3	0.0	0.0	0.2	0.2	0.1	0.1	0.0
WHA039E	1.6	138	7.8	8.5	1.0	6.1	1.0	0.0	0.1	0.7	1.0	0.0	0.5	0.0
WHA039F	0.4	56	1.8	2.0	0.1	0.3	0.2	0.0	0.0	0.2	0.2	0.1	0.1	0.0
WHA039G	0.5	12	1.8	2.1	0.2	1.4	0.5	0.0	0.0	0.2	0.2	0.0	0.1	0.0
WHA039H	0.1	22	4.8	0.8	1.0	0.6	0.0	-	0.1	0.4	0.2	0.0	0.4	0.0
WHA039I	1.2	64	2.1	6.6	0.2	1.4	0.8	0.0	0.0	0.3	0.2	0.0	0.2	0.1
WHA039J	0.6	24	1.6	2.9	0.5	0.7	0.2	0.0	0.0	0.1	0.2	0.0	0.2	0.0
WHA039K	-	-	-	-	-	-	-	-	-	-	-	-	-	-
WHA109A	0.2	44	1.8	1.5	0.5	1.3	0.4	0.0	0.0	0.3	0.3	0.0	0.1	0.0
WHA109B	0.4	8.9	1.3	2.4	0.3	1.0	0.3	0.0	0.0	0.2	0.2	0.0	0.1	0.0
WHA109C	0.4	3.4	2.4	2.3	0.1	1.4	0.4	0.0	0.0	0.2	0.3	0.0	0.1	0.0

WHA109D	0.4	13	0.9	2.0	0.2	0.9	0.3	0.0	0.0	0.2	0.1	0.0	0.2	0.0
WHA109E	0.5	11	0.4	3.4	0.1	0.3	0.2	0.0	0.0	0.1	0.0	0.0	0.1	0.0
WHA114A	0.3	11	0.5	2.1	0.2	1.5	0.6	0.0	0.0	0.3	0.1	0.1	0.2	0.0
WHA114B	0.5	18	2.4	2.9	0.3	1.5	0.4	0.0	0.1	0.2	0.2	0.1	0.2	0.0
WHA114C	0.3	20	2.0	2.3	0.4	1.3	0.4	0.0	0.0	0.3	0.3	0.1	0.2	0.0
WHA114D	0.5	33	3.7	2.9	0.5	2.3	0.6	0.0	0.1	0.4	0.4	0.1	0.2	0.0
WHAK412	-	-	-	-	-	-	-	-	-	-	-	-	-	-
WHAK415-A1	-	-	-	-	-	-	-	-	-	-	-	-	-	-
WHAK415-A3	-	-	-	-	-	-	-	-	-	-	-	-	-	-
WHAK415-A4	-	-	-	-	-	-	-	-	-	-	-	-	-	-
WHAK415-A5	0.2	55	1.1	8.0	0.9	1.7	0.5	0.1	0.0	0.3	0.2	0.1	0.2	0.0
WHAK415-A6	0.7	12	0.8	2.9	0.3	3.2	0.3	0.0	0.0	0.2	0.2	0.0	0.1	0.0
WHAK415-A7	0.5	89	3.4	5.7	0.7	2.3	0.6	0.0	0.1	0.5	0.6	0.1	0.3	0.1
WHAK415-A8	1.2	24	1.7	1.2	0.3	1.4	0.5	0.0	0.1	0.1	0.2	0.1	0.2	0.0
WHAK602	-	-	-	-	-	-	-	-	-	-	-	-	-	-
WHAK602A	2.9	60	1.3	2.5	0.3	0.9	0.4	0.0	0.0	0.3	0.1	0.1	0.1	0.0
WHAK602C	5.3	79	1.3	6.2	0.2	2.0	0.4	0.0	0.1	0.3	0.5	0.0	0.2	0.0
WHAK602E	7.1	82	2.4	2.1	0.3	1.5	0.1	0.0	0.1	0.1	0.1	0.1	0.3	0.0

Table 3.14: Pumice glass trace element standard deviations of the mean compositions (Yb-U)

Sample Name	Yb	Lu	Hf	Ta	Pb	Th	U
GP107-04	0.2	0.0	0.5	0.1	1.2	0.5	0.3
GP115a-06	0.2	0.0	0.3	0.0	0.5	1.1	0.4
GP115a-09	-	-	-	-	-	-	-
GP115a-12	-	-	-	-	-	-	-
GP115c-14	0.2	0.0	0.3	0.1	1.6	0.5	0.5
GP115c-18	0.1	0.0	0.2	0.1	1.8	0.6	0.3
GP115c-20	0.1	0.0	0.4	0.0	1.9	0.4	0.2
WHA039A	0.2	0.0	0.4	0.1	0.8	0.8	0.3
WHA039B	0.6	0.1	0.8	0.1	2.7	6.8	0.5
WHA039C	0.2	0.0	0.8	0.2	1.4	1.4	0.4
WHA039D	0.2	0.0	0.2	0.1	0.8	0.9	0.4
WHA039E	0.4	0.1	0.9	0.1	0.6	6.0	0.3
WHA039F	0.1	0.0	0.2	0.0	0.6	1.0	0.2
WHA039G	0.1	0.0	0.3	0.0	1.0	1.5	0.3
WHA039H	0.3	0.0	0.1	0.2	0.3	0.6	0.5
WHA039I	0.2	0.0	0.3	0.1	1.7	1.2	0.5
WHA039J	0.1	0.0	0.2	0.1	1.0	0.8	0.5
WHA039K	-	-	-	-	-	-	-
WHA109A	0.2	0.0	0.1	0.1	0.9	1.1	0.1
WHA109B	0.1	0.0	0.1	0.1	0.7	0.4	0.2
WHA109C	0.1	0.0	0.1	0.0	1.6	0.3	0.5

WHA109D	0.0	0.0	0.1	0.0	0.8	0.6	0.2
WHA109E	0.2	0.0	0.1	0.0	3.9	0.3	0.2
WHA114A	0.1	0.0	0.2	0.0	0.7	0.4	0.2
WHA114B	0.1	0.0	0.3	0.1	0.7	1.2	0.3
WHA114C	0.3	0.0	0.3	0.1	1.1	1.3	0.3
WHA114D	0.3	0.0	0.3	0.1	0.6	1.7	0.4
WHAK412	-	-	-	-	-	-	-
WHAK415-A1	-	-	-	-	-	-	-
WHAK415-A3	-	-	-	-	-	-	-
WHAK415-A4	-	-	-	-	-	-	-
WHAK415-A5	0.1	0.0	0.4	0.0	0.8	2.3	0.0
WHAK415-A6	0.2	0.0	0.2	0.1	0.4	2.0	0.1
WHAK415-A7	0.5	0.1	0.3	0.1	0.4	2.6	0.5
WHAK415-A8	0.2	0.0	0.3	0.0	0.2	1.5	0.5
WHAK602	-	-	-	-	-	-	-
WHAK602A	0.2	0.0	0.2	0.0	0.4	0.6	0.2
WHAK602C	0.2	0.0	0.5	0.0	0.8	1.6	0.4
WHAK602E	0.1	0.1	0.3	0.0	1.1	1.1	0.4

Table 3.15: Pumice glass storage pressures and zircon saturation temperatures

Sample Name	qtz-2feld	qtz-1feld	P plag-opx-qtz	Best Pressure	Pressure Type	Zircon Sat Temp (°C) T-Boehnke	Zircon Sat Temp (°C) T-W&H
GP107-04	-	96	-	96	qtz-1feld	754	787
GP115a-06	127	121	-	127	qtz-2feld	700	740
GP115a-09	-	90	-	90	qtz-1feld	780	745
GP115a-12	-	115	-	115	qtz-1feld	782	747
GP115c-14	-	45	-	45	qtz-1feld	759	791
GP115c-18	-	99	-	99	qtz-1feld	750	784
GP115c-20	-	97	-	97	qtz-1feld	749	783
WHA039A	-	91	-	91	qtz-1feld	761	793
WHA039B	-	103	-	103	qtz-1feld	788	815
WHA039C	-	-	-	-	qtz-2feld	790	818
WHA039D	-	129	-	129	qtz-1feld	697	739
WHA039E	-	-	-	-	qtz-2feld	815	838
WHA039F	-	52	-	52	qtz-1feld	712	752
WHA039G	-	93	-	93	qtz-1feld	747	781
WHA039H	-	-	-	-	qtz-2feld	765	796
WHA039I	-	-	-	-	qtz-2feld	770	799
WHA039J	120	111	-	120	qtz-2feld	710	748
WHA039K	-	-	-	-	qtz-2feld		
WHA109A	-	-	-	-	qtz-2feld	754	787
WHA109B	-	37	-	37	qtz-1feld	707	745
WHA109C	85	54	-	85	qtz-2feld	684	727

WHA109D	96	93	-	96	qtz-2feld	704	743
WHA109E	85	37	-	85	qtz-2feld	701	740
WHA114A	132	124	-	132	qtz-2feld	701	742
WHA114B	142	130	-	142	qtz-2feld	699	740
WHA114C	131	124	-	131	qtz-2feld	699	740
WHA114D	-	122	-	122	qtz-1feld	705	745
WHAK412	-	158	-	158	qtz-1feld		
WHAK415-A1	88	57	-	88	qtz-2feld		
WHAK415-A3	122	127	-	122	qtz-2feld		
WHAK415-A4	120	129	-	120	qtz-2feld		
WHAK415-A5	71	47	-	71	qtz-2feld	747	781
WHAK415-A6	-	63	-	63	qtz-1feld	730	766
WHAK415-A7	-	-	-	-	qtz-2feld	706	745
WHAK415-A8	97	89	-	97	qtz-2feld	714	753
WHAK602	-	221	-	221	qtz-1feld		
WHAK602A	-	215	-	215	qtz-1feld	768	796
WHAK602C	-	206	-	206	qtz-1feld	768	795
WHAK602E	-	271	-	271	qtz-1feld	766	793

3.6 References

Bachmann, O., & Bergantz, G. (2008). The magma reservoirs that feed supereruptions. Elements, 4(1), 17–21. https://doi.org/10.2113/GSELEMENTS.4.1.17

Bachmann, O., & Bergantz, G. W. (2004). On the origin of crystal-poor rhyolites: Extracted from batholithic crystal mushes. Journal of Petrology, 45(8), 1565–1582. https://doi.org/10.1093/petrology/egh019

Bégué, F., Deering, C. D., Gravley, D. M., Kennedy, B. M., Chambefort, I., Gualda, G. A. R., & Bachmann, O. (2014). Extraction, storage and eruption of multiple isolated magma batches in the paired Mamaku and Ohakuri eruption, Taupo volcanic zone, New Zealand. Journal of Petrology, 55(8), 1653–1684. https://doi.org/10.1093/petrology/egu038

Bégué, F., Gualda, G. A. R., Ghiorso, M. S., Pamukcu, A. S., Kennedy, B. M., Gravley, D. M., Deering, C. D., & Chambefort, I. (2014). Phase-equilibrium geobarometers for silicic rocks based on rhyolite-MELTS. Part 2: application to Taupo Volcanic Zone rhyolites. Contributions to Mineralogy and Petrology, 168, 1–16. https://doi.org/10.1007/s00410-014-1082-7

Boehnke, P., Watson, E. B., Trail, D., Harrison, T. M., & Schmitt, A. K. (2013). Zircon saturation re-revisited. Chemical Geology, 351, 324–334. https://doi.org/10.1016/j.chemgeo.2013.05.028

Briggs, N. D. (1976a). Welding and crystallisation zonation in whakamaru ignimbrite, central north island, new zealand. New Zealand Journal of Geology and Geophysics, 19(2), 189–212. https://doi.org/10.1080/00288306.1976.10423517

Briggs, N. D. (1976b). Recognition and correlation of subdivisions within the whakamaru ignimbrite, central north island, new zealand. New Zealand Journal of Geology and Geophysics, 19(4), 463–501. https://doi.org/10.1080/00288306.1976.10423540

Brown, S. J. A. (1994). Geology and geochemistry of the Whakamaru Group ignimbrites, and associated rhyolite domes, Taupo Volcanic Zone, New Zealand.

Brown, S. J. A., & Fletcher, I. R. (1999). SHRIMP U-Pb dating of the preeruption growth history of zircons from the 340 ka Whakamaru Ignimbrite, New Zealand: Evidence for >250 k.y. magma residence times. Geology, 27(11), 1035–1038. https://doi.org/10.1130/0091-7613(1999)027<1035:supdot>2.3.co;2

Brown, S. J. A., Wilson, C. J. N., Cole, J. W., & Wooden, J. L. (1998). The Whakamaru group ignimbrites, Taupo Volcanic Zone, New Zealand: Evidence for reverse tapping of a zoned silicic magmatic system. Journal of Volcanology and Geothermal Research, 84(1–2), 1–37. https://doi.org/10.1016/S0377-0273(98)00020-1

Cashman, K. v., & Giordano, G. (2014). Calderas and magma reservoirs. Journal of Volcanology and Geothermal Research, 288, 28–45. https://doi.org/10.1016/j.jvolgeores.2014.09.007

Chamberlain, K. J., Wilson, C. J. N., Wallace, P. J., & Millet, M. A. (2015). Micro-analytical perspectives on the bishop tuff and its magma chamber. Journal of Petrology, 56(3), 605–640. https://doi.org/10.1093/petrology/egv012

Cooper, G. F., Wilson, C. J. N., Millet, M. A., Baker, J. A., & Smith, E. G. C. (2012). Systematic tapping of independent magma chambers during the 1Ma Kidnappers supereruption. Earth and Planetary Science Letters, 313–314(1), 23–33. https://doi.org/10.1016/j.epsl.2011.11.006

Cooper, K. M., & Kent, A. J. R. (2014). Rapid remobilization of magmatic crystals kept in cold storage. Nature, 506(7489), 480–483. https://doi.org/10.1038/nature12991

Deering, C. D., Bachmann, O., & Vogel, T. A. (2011). The Ammonia Tanks Tuff: Erupting a melt-rich rhyolite cap and its remobilized crystal cumulate. Earth and Planetary Science Letters, 310, 518–525. https://doi.org/10.1016/j.epsl.2011.08.032

Deering, C. D., Gravley, D. M., Vogel, T. A., Cole, J. W., & Leonard, G. S. (2010). Origins of cold-wet-oxidizing to hot-dry-reducing rhyolite magma cycles and distribution in the Taupo Volcanic Zone, New Zealand. Contributions to Mineralogy and Petrology, 160(4), 609–629. https://doi.org/10.1007/s00410-010-0496-0

Downs, D. T., Wilson, C. J. N., Cole, J. W., Rowland, J. v., Calvert, A. T., Leonard, G. S., & Keall, J. M. (2014). Age and eruptive center of the Paeroa Subgroup ignimbrites (Whakamaru Group) within the Taupo Volcanic Zone of New Zealand. Bulletin of the Geological Society of America, 126(9–10), 1131–1144. https://doi.org/10.1130/B30891.1

Eastwood, A. A., Gravley, D. M., Wilson, C. J. N., Chambefort, I., Oze, C., Cole, J. W., & Ireland, T. R. (2013). U-Pb Dating of Subsurface Pyroclastic Deposits (Tahorakuri Formation) at Ngatamariki and Rotokawa Geothermal Fields. 35th New Zealand Geothermal Workshop.

Ewart, A. (1965). Mineralogy and Petrogenesis of the Whakamaru Ignimbrite in the Maraetai area of the Taupo volcanic zone, New Zealand. New Zealand Journal of Geology and Geophysics, 8(4), 611–679. https://doi.org/10.1080/00288306.1965.10423194

Ewart, A. (1967a). Pyroxene and magnetite phenocrysts from the Taupo quaternary rhyolitic pumice deposits, New Zealand. Mineralogy Magazine, 36, 180–194.

Ewart, A. (1967b). The Petrography of the Central North Island Rhyolitic Lavas. New Zealand Journal of Geology and Geophysics, 10(1), 182–197. https://doi.org/10.1080/00288306.1967.10428189

Ewart, A., & Healy, J. (1966). Te Whaiti ignimbrites at Murupara. In B. Thompson, L. Kermode, & A. Ewart (Eds.), New Zealand Volcanology, Central Volcanic Region (Vol. 50, pp. 121–125). New Zealand Department of Scientific and Industrial Research Information.

Foley, M. L., Miller, C. F., & Gualda, G. A. R. (2020). Architecture of a Super-sized Magma Chamber and Remobilization of its Basal Cumulate (Peach Spring Tuff, USA). Journal of Petrology, 61(1). https://doi.org/10.1093/petrology/egaa020

Ghiorso, M. S., & Gualda, G. A. R. (2015). An H2O–CO2 mixed fluid saturation model compatible with rhyolite-MELTS. Contributions to Mineralogy and Petrology, 169(53). https://doi.org/10.1007/s00410-015-1141-8

Gravley, D. M., Deering, C. D., Leonard, G. S., & Rowland, J. v. (2016). Ignimbrite flare-ups and their drivers: A New Zealand perspective. Earth-Science Reviews, 162, 65–82. https://doi.org/10.1016/j.earscirev.2016.09.007

Gravley, D. M., Wilson, C. J. N., Leonard, G. S., & Cole, J. W. (2007). Double trouble: Paired ignimbrite eruptions and collateral subsidence in the Taupo Volcanic Zone, New Zealand. Bulletin of the Geological Society of America, 119(1–2), 18–30. https://doi.org/10.1130/B25924.1

Griffin, W., Powell, W., Pearson, N. J., & O'Reilly, S. (2008). GLITTER: data reduction software for laser ablation ICP-MS. Short Course Series, 40, 308–311.

Grindley, G. (1960). Geological Map of NewZealand 1:250,000. In NZ Department of Scientific and Industrial Research: Vol. Sheet 8 (Issue Taupo).

Gualda, G. A. R., & Ghiorso, M. S. (2013a). Low-Pressure Origin of High-Silica Rhyolites and Granites. The Journal of Geology, 121, 537–545. https://doi.org/10.1086/671395

Gualda, G. A. R., & Ghiorso, M. S. (2013b). The Bishop Tuff giant magma body: an alternative to the Standard Model. 2Contributions to Mineralogy and Petrology, 166, 755–775. https://doi.org/10.1007/s00410-013-0901-6

Gualda, G. A. R., & Ghiorso, M. S. (2014). Phase-equilibrium geobarometers for silicic rocks based on rhyolite-MELTS. Part 1: Principles, procedures, and evaluation of the method. Contributions to Mineralogy and Petrology, 168(1), 1–17. https://doi.org/10.1007/s00410-014-1033-3

Gualda, G. A. R., Ghiorso, M. S., Lemons, R. v., & Carley, T. L. (2012). Rhyolite-MELTS: a Modified Calibration of MELTS Optimized for Silica-rich, Fluid-bearing Magmatic Systems. Journal of Petrology, 53(5), 875–890. https://doi.org/10.1093/petrology/egr080

Gualda, G. A. R., Gravley, D. M., Conner, M., Hollmann, B., Pamukcu, A. S., Bégué, F., Ghiorso, M. S., & Deering, C. D. (2018). Climbing the crustal ladder: Magma storage-depth evolution during a volcanic flare-up. Science Advances, 4(10). https://doi.org/10.1126/sciadv.aap7567

Gualda, G. A. R., Gravley, D. M., Deering, C. D., & Ghiorso, M. S. (2019). Magma extraction pressures and the architecture of volcanic plumbing systems. Earth and Planetary Science Letters, 522, 118–124. https://doi.org/10.1016/j.epsl.2019.06.020

Gualda, G. A. R., Pamukcu, A. S., Ghiorso, M. S., Anderson Jr, A. T., Sutton, S. R., Rivers, M. L., & Houlie, N. (2012). Timescales of Quartz Crystallization and the Longevity of the Bishop Giant Magma Body. PLoS ONE, 7(5). https://doi.org/10.1371/journal.pone.0037492

Gualda, G. A. R., & Sutton, S. R. (2016). The year leading to a supereruption. PLoS ONE, 11(7), 1–18. https://doi.org/10.1371/journal.pone.0159200

Harmon, L. J., Cowlyn, J., Gualda, G. A. R., & Ghiorso, M. S. (2018). Phase-equilibrium geobarometers for silicic rocks based on rhyolite-MELTS. Part 4: Plagioclase, orthopyroxene, clinopyroxene, glass geobarometer, and application to Mt. Ruapehu, New Zealand. Contributions to Mineralogy and Petrology, 173(1). https://doi.org/10.1007/s00410-017-1428-z

Harrison, A., & White, R. S. (2006). Lithospheric structure of an active backarc basin: The Taupo Volcanic Zone, New Zealand. Geophysical Journal International, 167(2), 968–990. https://doi.org/10.1111/j.1365-246X.2006.03166.x

Hildreth, W. (1979). The Bishop Tuff: Evidence for the origin of compositional zonation in silicic magma chambers. Geological Society of America, Special Paper 180. https://specialpapers.gsapubs.org.proxy.library.vanderbilt.edu/content/180/43.full.pdf

Hildreth, W., & Wilson, C. J. N. (2007). Compositional zoning of the bishop tuff. Journal of Petrology, 48(5), 951–999. https://doi.org/10.1093/petrology/egm007

Houghton, B. F., Wilson, C. J. N., Mcwilliams, M. O., Lanphere, M. A., Weaver, S. D., Briggs, R. M., & Pringle, M. S. (1995). Volcanic Zone , New Zealand Chronology and dynamics of a large silicic magmatic system: Central Taupo Volcanic Zone , New Zealand. Geology, 23(1), 13–16. https://doi.org/10.1130/0091-7613(1995)023<0013

Jochum, K. P., Weis, U., Schwager, B., Stoll, B., Wilson, S. A., Haug, G. H., Andreae, M. O., & Enzweiler, J. (2016). Reference Values Following ISO Guidelines for Frequently Requested Rock Reference Materials. Geostandards and Geoanalytical Research, 40(3), 333–350. https://doi.org/10.1111/j.1751-908X.

2015.00392.x

Kaiser, J. F., de Silva, S., Schmitt, A. K., Economos, R., & Sunagua, M. (2017). Million-year melt–presence in monotonous intermediate magma for a volcanic–plutonic assemblage in the Central Andes: Contrasting histories of crystal-rich and crystal-poor super-sized silicic magmas. Earth and Planetary Science Letters, 457, 73–86. https://doi.org/10.1016/j.epsl.2016.09.048

Kodaira, S., Seton, M., Sonter, L. J., Till, C. B., & Williams, H. M. (2021). Reflections on solid Earth research. Nature Reviews Earth and Environment, 2(1), 21–25. https://doi.org/10.1038/s43017-020-00127-7

Leonard, G. S., Begg, J. G., & Wilson, C. J. N. (2010). Geology of the Rotorua area. GNS Science. https://www.researchgate.net/publication/285598682

Manning, D. A. (1995). Late Pleistocene Tephrostratigraphy of the Eastern Bay of Plenty Region, New Zealand.

Martin, R. C. (1965). Lithology and eruptive history of the Whakamaru ignimbrites in the Maraetai area of the Taupo volcanic zone, New Zealand. New Zealand Journal of Geology and Geophysics, 8(4), 680–705. https://doi.org/10.1080/00288306.1965.10423195

Matthews, N. E. (2011). Magma chamber assembly and dynamics of a supervolcano: Whakamaru, Taupo Volcanic Zone, New Zealand.

Matthews, N. E., Huber, C., Pyle, D. M., & Smith, V. C. (2012). Timescales of magma recharge and reactivation of large silicic systems from ti diffusion in quartz. Journal of Petrology, 53(7), 1385–1416. https://doi.org/10.1093/petrology/egs020

Matthews, N. E., Pyle, D. M., Smith, V. C., Wilson, C. J. N., Huber, C., & van Hinsberg, V. (2012). Quartz zoning and the pre-eruptive evolution of the 340-ka Whakamaru magma systems, New Zealand. Contributions to Mineralogy and Petrology, 163(1), 87–107. https://doi.org/10.1007/s00410-011-0660-1

Matthews, N. E., Smith, V. C., Costa, A., Durant, A. J., Pyle, D. M., & Pearce, N. J. G. (2012). Ultra-distal tephra deposits from super-eruptions: Examples from Toba, Indonesia and Taupo Volcanic Zone, New Zealand. Quaternary International, 258, 54–79. https://doi.org/10.1016/j.quaint.2011.07.010

Pamukcu, A. S., Carley, T. L., Gualda, G. A. R., Miller, C. F., & Ferguson, C. A. (2013). The evolution of the peach spring giant magma body: Evidence from accessory mineraltextures and compositions, bulk pumice and glass geochemistry, and rhyolite-MELTS modeling. Journal of Petrology, 54(6), 1109–1148. https://doi.org/10.1093/petrology/egt007

Pamukcu, A. S., Gualda, G. A. R., Bégué, F., & Gravley, D. M. (2015). Melt inclusion shapes: Timekeepers of short-lived giant magma bodies. Geology, 43(11), 947–950. https://doi.org/10.1130/G37021.1

Pamukcu, A. S., Gualda, G. A. R., Ghiorso, M. S., Miller, C. F., & McCracken, R. G. (2015). Phase-equilibrium geobarometers for silicic rocks based on rhyolite-MELTS—Part 3: Application to the Peach Spring Tuff (Arizona–California–Nevada, USA). Contributions to Mineralogy and Petrology, 169(3). https://doi.org/10.1007/s00410-015-1122-y

Pitcher, B. W., Gualda, G. A. R., & Hasegawa, T. (2021). Repetitive Duality of Rhyolite Compositions, Timescales, and Storage and Extraction Conditions for Pleistocene Caldera-forming Eruptions, Hokkaido, Japan. Journal of Petrology, 62(2). https://doi.org/10.1093/petrology/egaa106

Reid, M. R. (2008). How long does it take to supersize an eruption. Elements, 4(1), 23–28. https://doi.org/10.2113/GSELEMENTS.4.1.23

Reid, M. R., & Vazquez, J. A. (2017). Fitful and protracted magma assembly leading to a giant eruption, Youngest Toba Tuff, Indonesia. Geochemistry Geophysics Geosystems, 18, 156–177. https://doi.org/10.1002/2016GC006406

Saunders, K., Morgan, D. J., Baker, J. A., & Wysoczanski, R. J. (2010). The Magmatic Evolution of the Whakamaru Supereruption, New Zealand, Constrained by a Microanalytical Study of Plagioclase and Quartz. Journal of Petrology, 51(12), 2465–2488. https://doi.org/10.1093/petrology/egq064

Shamloo, H. I., & Till, C. B. (2019). Decadal transition from quiescence to supereruption: petrologic investigation of the Lava Creek Tuff, Yellowstone Caldera, WY. Contributions to Mineralogy and Petrology, 174(4). https://doi.org/10.1007/s00410-019-1570-x

Simon, J. I., & Reid, M. R. (2005). The pace of rhyolite differentiation and storage in an "archetypical" silicic magma system, Long Valley, California. Earth and Planetary Science Letters, 235(1–2), 123–140. https://doi.org/10.1016/j.epsl.2005.03.013

Stern, T. A., Stratford, W. R., & Salmon, M. L. (2006). Subduction evolution and mantle dynamics at a continental margin: Central North Island, New Zealand. Reviews of Geophysics, 44(4). https://doi.org/10.1029/2005RG000171

Swallow, E. J., Wilson, C. J. N., Myers, M. L., Wallace, P. J., Collins, K. S., & Smith, E. G. C. (2018). Evacuation of multiple magma bodies and the onset of caldera collapse in a supereruption, captured in glass and mineral compositions. Contributions to Mineralogy and Petrology, 173(4), 1–22. https://doi.org/10.1007/s00410-018-1459-0

van Achterbergh, E., Ryan, C. G., Jackson, S. E., & Griffen, W. L. (2001). Data reduction software for LAICPMS: appendix. In P. J. Sylvester (Ed.), Laser ablation ICPMS in the Earth Sciences: Principles and Applications (29th ed., Vol. 29, pp. 224–239). Mineralogy Association Canada Short Course Series.

Watson, E. B., & Harrison, T. M. (1983). Zircon saturation revisited: temperature and composition effects in a variety of crustal magma types. Earth and Planetary Science Letters, 64(2), 295–304. https://doi.org/10.1016/0012-821X(83)90211-X

Wilson, C. J. N., Gravley, D. M., Leonard, G. S., & Rowland, J. v. (2009a). Volcanism in the central Taupo Volcanic Zone, New Zealand: tempo styles and controls. Special Publications of IAVCEI, 2, 225–247.

Wilson, C. J. N., Gravley, D. M., Leonard, G. S., & Rowland, J. v. (2009b). Volcanism in the central Taupo Volcanic Zone, New Zealand: tempo styles and controls. In T. Thordarson, S. Self, G. Larsen, S. K. Rowland, & A. Hoskuldsson (Eds.), Studies in Volcanology: The Legacy of George Walker. Special Publications of IAVCEI (pp. 225–247).

Wilson, C. J. N., Houghton, B. F., & Lloyd, E. F. (1986). Volcanic history and evolution of the Maroa Taupo area.

Wilson, C. J. N., Houghton, B. F., Mcwilliams, M. O., Lanphere, M. A., Weaver, S. D., & Briggs, R. M. (1995). Volcanic and structural evolution of Taupo Volcanic Zone, New Zealand: a review. Journal of Volcanology and Geothermal Research, 68(68), 1–28. https://doi.org/10.1016/0377-0273(95)00006-G

Wilson, C. J. N., Rogan, A. M., Smith, I. E. M., Northey, D. J., Nairn, I. A., & Houghton, B. F. (1984). Caldera volcanoes of the Taupo volcanic zone, New Zealand. Journal of Geophysical Research, 89(B10), 8463–8484. https://doi.org/10.1029/JB089iB10p08463

CHAPTER 4

Overlooked Ultra-Shallow Magma Bodies

4.1 Introduction

Recently, there has been substantial progress towards understanding the magmatic and volcanic systems that feed silicic eruptions. Understanding where eruptible magma bodies form in the crust (Huber *et al.*, 2019; Pitcher *et al.*, 2021; Till *et al.*, 2019), their longevity (Gualda, Pamukcu, *et al.*, 2012; Pamukçu *et al.*, 2021; Pamukcu, Gualda, Bégué, *et al.*, 2015a), and timescales of eruptible magma assembly (Gualda & Sutton, 2016; Klemetti *et al.*, 2011) have been a significant goal of the wider petrologic community. Here, we shed light on previously under-reported magma bodies stored at ultra-shallow (< 4 km) depths prior to eruption.

The Krafla IDDP-1 well encountered a magma body at 2.1 km (Elders *et al.*, 2011; Mortensen *et al.*, 2014; Zierenberg *et al.*, 2013), indicating that magma bodies can be stored at shallower levels than previously recognized. While Krafla is one of the only locations where magma has been encountered at depth during geothermal drilling (magma has also been encountered at Puna Geothermal Venture wellfield, Big Island of Hawaii (Teplow *et al.*, 2009)), ultra-shallow magma storage – defined as magma stored at depths < $\sim$4 km – is not specific to Krafla (Mbia *et al.*, 2015; Teplow *et al.*, 2009). We must further explore the presence of ultra-shallow magma bodies, since coupling the magmatic information with geophysical models and volcanic hazard assessments has broad implications for both geothermal energy production and volcanic hazards. Further, if we understand the depths and conditions of these magma bodies, we could better understand the arrangement of eruptible magma bodies during ongoing eruptions. Petrologists must reimagine the possible magma body configuration in the shallow crust.

The presence of ultra-shallow magma has been potentially captured by 2D and 3D seismic exploration (Larderello geothermal field, Italy) (Cameli *et al.*, 1993; Manzella *et al.*, 2017; Rochira *et al.*, 2018) and by InSAR data (Dabbahu volcano, Afar, Ethiopia) (Ebinger *et al.*, 2008), which provides evidence for their existence. Previous rhyolite-MELTS geobarometry work in the Taupō Volcanic Zone (TVZ), Aotearoa New Zealand, has found ultra-shallow pressures (Bégué, Gualda, *et al.*, 2014; Gualda *et al.*, 2018), but they have not been the focus of those geobarometry studies due to the uncertainty on the reliability of those pressure estimates.

The Krafla IDDP-1 well magmas provide a unique opportunity to test the quality of rhyolite-MELTS pressures for ultra-shallow magma bodies, given that the storage pressure is known from drilling. Further, confirmation of rhyolite-MELTS pressures in this case would lend support to ultra-shallow pressures found

elsewhere in the world using rhyolite-MELTS. Using rhyolite-MELTS (Gualda, Ghiorso, *et al.*, 2012), we can model the pressure, temperature, f_{O_2}, and mineralogy of an eruptible magma body with an input of the composition of the erupted glass, which is a proxy for the magmatic melt in equilibrium with the observed mineral assemblage (Bégué, Gualda, *et al.*, 2014; Gualda & Ghiorso, 2014; Harmon *et al.*, 2018; Pamukcu, Gualda, Ghiorso, *et al.*, 2015). In this work, we use rhyolite compositions from the Krafla IDDP-1 well to estimate crystallization pressures using rhyolite-MELTS geobarometry. We also discuss geobarometric results from Bégué *et al.* (2014) and Gualda *et al.* (2018) in the context of the TVZ (Gravley *et al.*, 2016).

4.2 Methods

4.2.1 Krafla Glass Compositions

We use natural rhyolite glass compositions from Masotta *et al.* (2018) for Krafla IDDP-1 magmas. There are 31 individual quenched glass rhyolite (RHL) compositions, and an average composition calculated by us. The RHL samples are from mm-sized glass pieces that rapidly quenched during interaction with the drilling fluids. The observed mineral assemblage is plagioclase + augite + pigeonite + magnetite (Masotta *et al.*, 2018; Zierenberg *et al.*, 2013).

Table 4.1: Krafla RHL glass compositions and Krafla RHL average glass composition

Sample Name	SiO_2	TiO_2	Al_2O_3	FeO	MnO	MgO	CaO	Na_2O	K_2O
Massota2018_RHL-1	76.46	0.34	12.30	2.55	0.05	0.21	1.50	3.40	3.13
Massota2018_RHL-2	76.51	0.36	12.28	2.80	0.08	0.15	1.34	3.40	3.06
Massota2018_RHL-3	76.42	0.40	12.11	2.81	0.11	0.18	1.34	3.44	3.16
Massota2018_RHL-4	76.11	0.37	12.47	2.81	0.11	0.23	1.45	3.27	3.15
Massota2018_RHL-5	76.49	0.41	12.11	2.66	0.01	0.19	1.48	3.46	3.08
Massota2018_RHL-6	76.18	0.36	12.30	2.82	0.01	0.19	1.54	3.40	3.14
Massota2018_RHL-7	75.97	0.39	12.28	2.91	0.12	0.24	1.61	3.34	3.05
Massota2018_RHL-8	76.58	0.39	12.12	2.67	0.08	0.20	1.48	3.44	3.01
Massota2018_RHL-9	76.66	0.31	12.25	2.72	0.02	0.20	1.37	3.38	3.05
Massota2018_RHL-10	76.11	0.33	12.20	2.91	0.07	0.21	1.66	3.30	3.16
Massota2018_RHL-11	76.30	0.40	12.11	2.90	0.04	0.25	1.57	3.33	2.99
Massota2018_RHL-12	76.41	0.35	12.33	2.82	0.00	0.23	1.48	3.24	3.08
Massota2018_RHL-13	76.97	0.22	11.72	2.80	0.06	0.23	1.41	3.38	3.16
Massota2018_RHL-14	76.88	0.20	11.63	2.96	0.05	0.14	1.54	3.45	3.09
Massota2018_RHL-15	77.06	0.22	11.69	2.93	0.07	0.26	1.42	3.29	3.02
Massota2018_RHL-16	76.89	0.19	11.73	3.10	0.01	0.21	1.47	3.34	3.03

Massota2018_RHL-17	77.00	0.21	11.76	3.01	0.07	0.28	1.38	3.25	3.00
Massota2018_RHL-18	76.77	0.23	11.51	2.97	0.15	0.23	1.39	3.54	3.15
Massota2018_RHL-19	76.79	0.22	11.83	2.85	0.00	0.27	1.44	3.55	3.00
Massota2018_RHL-20	76.93	0.21	11.78	2.87	0.06	0.21	1.33	3.51	3.08
Massota2018_RHL-21	76.42	0.18	11.82	2.97	0.12	0.27	1.50	3.50	3.18
Massota2018_RHL-22	76.84	0.19	11.79	3.15	0.00	0.24	1.58	3.24	2.95
Massota2018_RHL-23	77.20	0.22	11.51	2.91	0.06	0.27	1.39	3.58	2.82
Massota2018_RHL-24	76.91	0.21	11.61	2.83	0.10	0.23	1.41	3.49	3.19
Massota2018_RHL-25	76.60	0.17	11.84	2.94	0.09	0.20	1.44	3.55	3.13
Massota2018_RHL-26	76.95	0.21	11.82	2.87	0.06	0.23	1.50	3.29	3.08
Massota2018_RHL-27	77.10	0.20	11.71	2.84	0.09	0.26	1.38	3.29	3.10
Massota2018_RHL-28	76.89	0.21	11.74	2.93	0.06	0.18	1.43	3.34	3.16
Massota2018_RHL-29	77.22	0.22	11.72	2.85	0.13	0.23	1.41	3.22	3.00
Massota2018_RHL-30	77.26	0.20	11.65	2.86	0.04	0.27	1.40	3.23	3.09
Massota2018_RHL-31	76.86	0.22	11.78	3.03	0.08	0.21	1.47	3.23	3.12
Massota2018_RHL-Avg	76.70	0.27	11.92	2.87	0.06	0.22	1.45	3.38	3.08

4.2.2 TVZ Glass Compositions

TVZ flare-up samples are from Gualda *et al.* (2018). The glass compositions studied are from five eruptions during an ignimbrite flare-up period (Gravley *et al.*, 2016; Gualda *et al.*, 2018). We selected a subset (36/88) of the average pumice glass compositions from Gualda *et al.* (2018), analyzing only compositions that calculated a pressure < 100 MPa (Gualda *et al.*, 2018), given our focus on the ultra-shallow pressures. In particular, we focus on compositions from the TVZ that yield coincident plagioclase and quartz saturation surfaces at low pressure – the overlap in quartz and plagioclase saturation surfaces for some melt compositions in the TVZ was originally observed by Bégué *et al.* (2014). The 36 (Gualda *et al.*, 2018) compositions used in this study are from five different ignimbrites: Ohakuri (7 samples), Mamaku (15 samples), Pokai (4 samples), Matahina (1 sample), and Whakamaru (9 samples) ignimbrites. The TVZ eruptions consistently have plagioclase + quartz + orthopyroxene + Fe-Ti oxide for all eruptions studied (Gravley *et al.*, 2016; Gualda *et al.*, 2018).

4.2.3 Projection onto the Quartz-Albite-Orthoclase Ternary Diagram

We project all Krafla and TVZ compositions onto the quartz-albite-orthoclase (Qz'-Ab'-Or') ternary diagram using the projection scheme of Blundy and Cashman (2001), which yields somewhat crude estimates of crystallization pressures for melts in equilibrium with quartz and feldspar (Gualda & Ghiorso, 2013).

4.2.4 Rhyolite-MELTS Calculations

We calculate pre-eruptive storage conditions for all samples using the Microsoft Excel interface for rhyolite-MELTS (Gualda, Ghiorso, *et al.*, 2012; Gualda & Ghiorso, 2015), following the methods detailed in Gualda and Ghiorso (2014). We explore a range of pressures (10-200 MPa in 10 MPa steps) and temperatures (1100-700 °C in 1 °C steps). Due to the potential effect of f_{O_2} on the stability of pyroxenes (Harmon *et al.*, 2018) and magnetite, we explore a range of f_{O_2} values: for Krafla, Δ NNO between -3 and 0 in 0.5 steps, with additional calculations for Δ NNO = -1.25 and -0.75; for TVZ flare-up samples, Δ NNO values we tested for are between -0.5 and +2, in 0.5 steps. The ranges of pressure, temperature, and f_{O_2} were chosen to explore very shallow storage pressures, from above the liquidus to near-solidus temperatures, and over the possible range of f_{O_2} for each system (Deering *et al.*, 2010; Gravley *et al.*, 2016; Masotta *et al.*, 2018). The mineral phases of interest for rhyolite-MELTS modeling are quartz, plagioclase, orthopyroxene, and magnetite (labeled as spinel in MELTS_Excel results). The saturation surfaces of quartz and feldspar are not sensitive to f_{O_2}, in contrast to the saturation surfaces of orthopyroxene and magnetite, due to the presence of iron in the orthopyroxene and magnetite mineral structures. Therefore, pressure calculations that include orthopyroxene and magnetite are highly dependent on f_{O_2}, which allows us to estimate f_{O_2} in addition to pressure (Harmon *et al.*, 2018; Pamukçu *et al.*, 2021).

Similarly to Foley *et al.* (2020), we extend the method of (Gualda & Ghiorso, 2014) to calculate pressures for the simultaneous saturation in quartz, plagioclase, orthopyroxene, and magnetite (which we label P_4 QFOM). We also calculate pressures based on the simultaneous saturation in quartz, plagioclase, and orthopyroxene (P_3 QFO); and based on the simultaneous saturation in quartz, plagioclase, and magnetite (P_3 QFM). All three pressures are highly dependent on f_{O_2}, allowing us to estimate f_{O_2} in addition to pressure (Harmon *et al.*, 2018). We note that all three conditions (P_4 QFOM, P_3 QFO, and P_3 QFM) imply saturation in quartz and feldspar, which is independent of f_{O_2}. Quartz is ubiquitous in TVZ magmas; we discuss below the suitability of such pressures for the Krafla case. For P_4 QFOM pressures, we calculate a pressure when the residual temperature (the difference between highest and lowest saturation temperature) is less than 10 °C (Figure 2). If no acceptable P_4 QFOM pressure is found, we calculate P_3 QFM and P_3 QFO pressures if the residual temperature is less than or equal to 5 °C, as typically done (Gualda & Ghiorso, 2014). To convert the pressure estimates to depths, we use h = ρ/P*g where h is the depth (in km), ρ is the density of the crust (estimated to be 2.75 g/cm^3), P is the calculated pressure (MPa), and g is the acceleration due to gravity (9.8 m/s^2).

4.2.5 Monte Carlo Analysis

To determine the reproducibility and quality of the rhyolite-MELTS pressure and f_{O_2} estimates, we conduct a Monte Carlo analysis using 600 synthetic glass compositions based on the average RHL composition and uncertainty around the average composition (Gualda & Ghiorso, 2014; Pamukçu *et al.*, 2021; Pitcher *et al.*, 2021). The f_{O_2} was allowed to vary in 0.5 Δ NNO steps from Δ NNO = -3 to 0. The rhyolite-MELTS calculations in the Monte Carlo simulations explore the same pressure and temperature ranges detailed above.

4.3 Results

4.3.1 Projection onto the Quartz-Albite-Orthoclase Ternary Diagram

Using the projection scheme of Blundy and Cashman (2001), the average Krafla RHL composition plots approximately on the 50 MPa (1.9 km) cotectic curve in the Qz'-Ab'-Or' ternary diagram (Figure 1). Individual RHL compositions have values just above the 50 MPa (1.9 km) cotectic (higher Qz' than the cotectic) to just below the 100 MPa (3.7 km) cotectic (lower Qz' than the cotectic). The TVZ samples have slightly deeper pressures, mostly straddling the 100 MPa (3.7 km) cotectic, but with some results close to the 50 MPa (1.9 km) cotectic (Figure 1). While the Qz'-Ab'-Or' ternary gives a somewhat crude estimate of the pressures, these results indicate that all compositions studied exhibit shallow pressures. We note that while the pressures estimated from the diagram imply saturation in quartz, these would be maximum pressures if quartz were absent. In other words, pressures could not be higher than what is predicted by using the diagram.

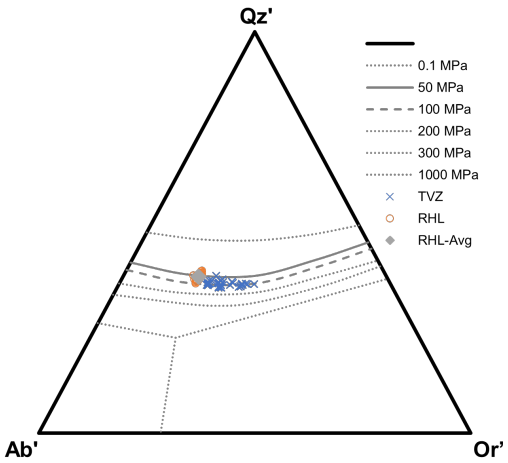

Figure 4.1: Projection of compositions of Krafla RHL glass from Massota *et al.* (2018) and TVZ ignimbrite pumice compositions from Gualda *et al.* onto the quartz-albite-orthoclase (Qz'-Ab'-Or') ternary diagram using the projection scheme of Blundy & Cashman (2001). Note that all compositions plot ∼ 50 – 100 MPa with Krafla samples plotting slightly shallower than TVZ compositions.

4.3.2 Krafla RHL

4.3.2.1 Individual Results

We performed a total of 279 rhyolite-MELTS runs for the 31 Krafla RHL individual compositions, since we modeled each composition over nine f_{O_2} values. In addition, the average Krafla RHL composition also has 9 rhyolite-MELTS runs, as it was modeled over the same f_{O_2} values. A total of 26 of the 31 individual Krafla RHL compositions (84%) calculate pressures for at least one f_{O_2} value, indicating that the residual temperature of the mineral phases is below the threshold (Figure 2).

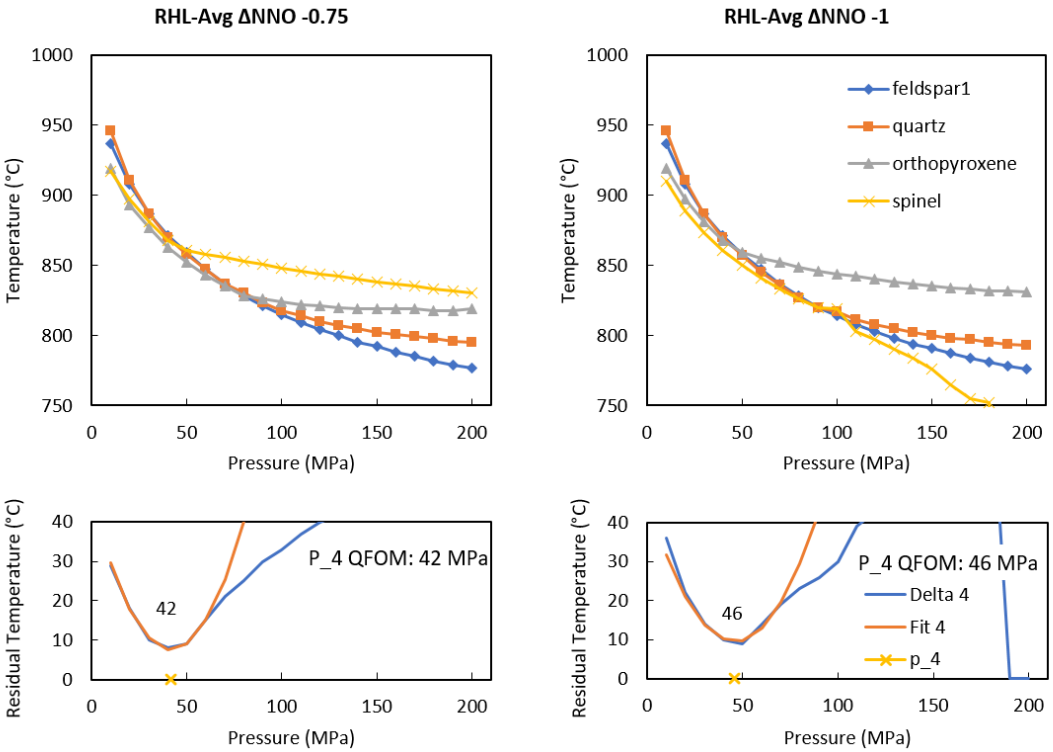

Figure 4.2: Rhyolite-MELTS storage pressures for the Krafla RHL average composition indicating the pressure and temperature estimates for which quartz, plagioclase, orthopyroxene and magnetite are saturated (P_4 QFOM). The oxygen fugacity (f_{O_2}) estimates of ΔNNO = -0.75 and -1 are the only f_{O_2} values that calculate pressures for the Krafla RHL average composition, as these are the only simulations where all four mineral phases saturate within 10 °C (the maximum residual temperature). The estimated pressures are 42 MPa and 46 MPa, respectively. Using a density of 2.75 g/cm^3, these pressures are calculated to be 1.6 km and 1.7 km. Magma was intersected by the IDDP-1 at 2.1 km.

Results from Krafla RHL individual compositions are summarized in Table 1 and Figure 3. A total of 143/279 (51%) of rhyolite-MELTS runs yield storage pressures. Individual compositions can have multiple pressures calculated due to the different f_{O_2} values.

Table 4.2: Krafla RHL individual composition results for P_4 QFOM, P_3 QFO, and P_3 QFM storage pressures

Mean pressure calculation (MPa)	-3 Δ NNO	-2.5 Δ NNO	-2 Δ NNO	-1.5 Δ NNO	-1.25 Δ NNO	-1 Δ NNO_2	-0.75 Δ NNO	-0.5 Δ NNO	0 Δ NNO
P_4 QFOM	-	-	-	-	-	57	47	35	-
P_3 QFO	40	42	45	47	48	49	46	35	-
P_3 QFM	-	-	-	-	-	55	60	32	9
Standard deviation of pressures									
P_4 QFOM	-	-	-	-	-	11	5	2	-
P_3 QFO	9	9	11	11	12	11	5	2	-
P_3 QFM	-	-	-	-	-	11	47	5	1
Number of compositions that return pressures for each f_{O_2}									
P_4 QFOM	0	0	0	0	0	9	9	2	0
P_3 QFO	14	16	17	20	20	9	1	0	0
P_3 QFM	0	0	0	0	0	2	8	14	2

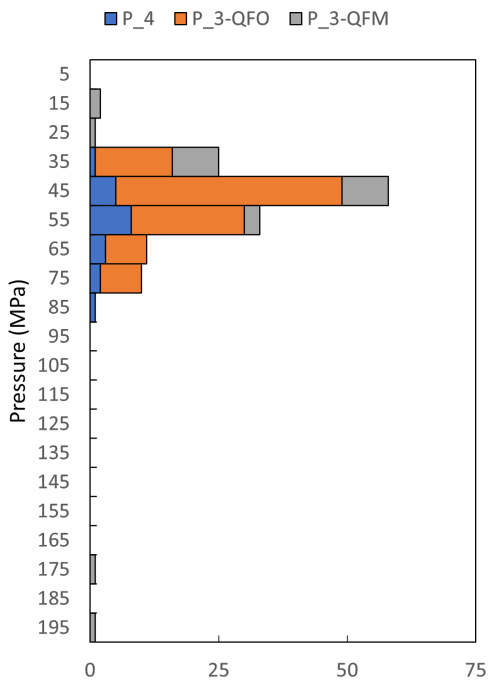

Figure 4.3: Results from rhyolite-MELTS pressure modeling for all individual Krafla RHL compositions Massota *et al.* We report the P_4 QFOM, P_3 QFO, and P_3 QFM pressures for all f_{O_2} considered.

Krafla RHL individual compositions return P_4 QFOM pressures for 20/31 (65%) of the compositions. The f_{O_2} values that produced these P_4 QFOM pressures are equal to Δ NNO = -1 (9 compositions), Δ NNO = -0.75 (9 compositions) and Δ NNO = -0.5 (2 compositions). The average pressure for all P_4 QFOM pressures (regardless of f_{O_2}) is 50 ± 11 MPa (1-sigma standard deviation), which corresponds to a depth of 1.9 ± 0.4 km.

For more reducing conditions, Krafla RHL individual compositions return predominantly P_3 QFO pressures (f_{O_2} equal to Δ NNO = -3 to -1), with only a few compositions returning P_3 QFO pressures for f_{O_2} equal to Δ NNO = -0.75 and Δ NNO = -0.5. A total of 117/279 (42%) of the Krafla RHL rhyolite-MELTS runs return P_3 QFO pressures (including cases that return P_4 QFOM, given that P_4 QFOM requires that P_3 QFO is valid). The average pressure for all P_3 QFO pressures (regardless of f_{O_2}) is 44 MPa ± 11 MPa (1.7 km ± 0.4 km).

For more oxidizing conditions, Krafla RHL individual compositions return predominantly P_3 QFM pressures (f_{O_2} equal to Δ NNO = -1 to 0). A total of 46/279 (16%) of the Krafla RHL rhyolite-MELTS runs return P_3 QFM (including P_4 QFOM given that P_4 QFOM requires that P_3 QFM is valid). The average pressure for all P_3 QFM pressures (regardless of f_{O_2}) is 47 MPa ± 32 MPa (1.7 km ± 1.2 km).

The average RHL composition returns a P_4 QFOM pressure of 42 MPa (1.5 km) for Δ NNO = -0.75 and 46 MPa (1.7 km) for Δ NNO = -1, indicating that only a narrow range of f_{O_2} can return a storage

pressure using four phases (Figure 2). The sensitivity of the compositions to f_{O_2}, temperature, and pressure are highlighted in Figure 4, where there is only a small "valley" in the Krafla RHL average composition data that produces P_4 QFOM pressures. We highlight the average Krafla RHL analyses, but the shape of the surface in Figure 4 is similar for all individual compositions (see supplementary data).

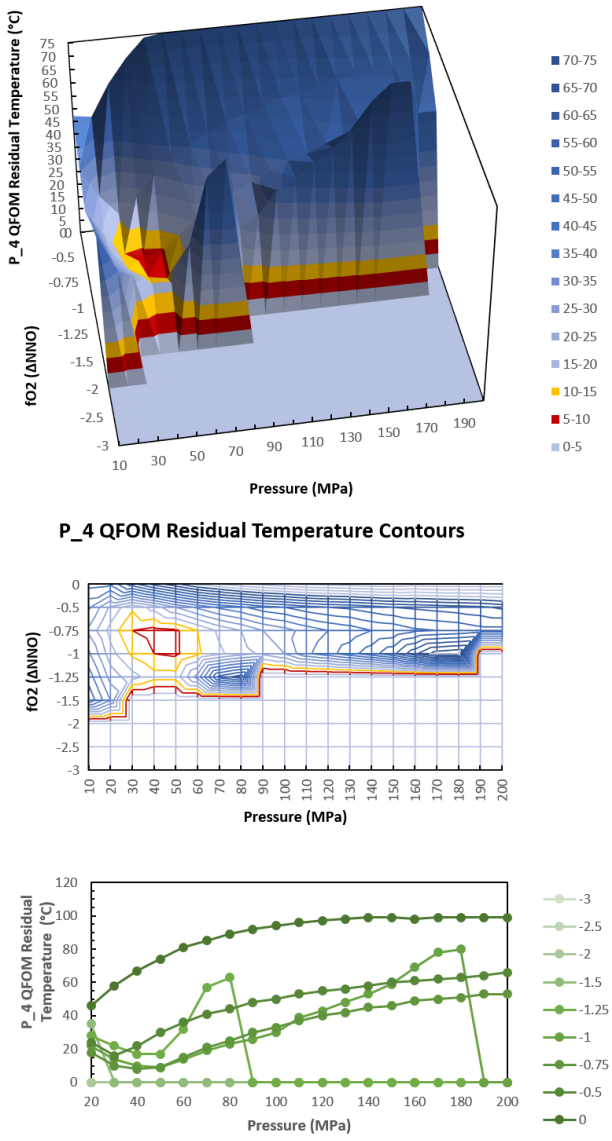

Figure 4.4: Rhyolite-MELTS storage pressures, showing the effect of f_{O_2} on pressure and temperature calculations for the Krafla RHL average composition. In the top panel, the central red divot ($\sim$40 MPa and ΔNNO $= \sim$-0.75) shows the conditions that retrieves the best pressure and f_{O_2} estimate based on the lowest P_3 residual temperature. The middle panel shows a 2D projection of the same data. The bottom panel shows the residual temperatures (the difference between the saturation curves of different phases) for individual rhyolite-MELTS calculations, which is compiled in the two upper panels.

For the Krafla RHL compositions, the P_4 QFOM pressure estimates show the best fit in both pressure and

f_{O_2} (Figures 3 and 4). As well, the P_4 QFOM pressures include the expected ferromagnesian assemblage of both orthopyroxene and magnetite.

The P_4 QFOM pressure calculation indicates that the quartz saturation surface is present in the rhyolite-MELTS calculations in addition to the plagioclase, orthopyroxene, and magnetite saturation surfaces (Figure 2). At low f_{O_2}, quartz and plagioclase saturation surfaces are very close together and near-parallel where the orthopyroxene and/or magnetite saturation surface intersects the plagioclase and quartz saturation surfaces, which indicates that both mineral phases are likely saturated (or are very close to saturation) and it is impossible to calculate a P_3 or P_4 solution that does not contain quartz. In fact, the quartz saturation surface for all RHL compositions (including the average) appears at temperatures higher than either the plagioclase or orthopyroxene saturation surfaces (Figure 2). This implies that pressures involving only plagioclase and orthopyroxene (P_2 FO) are unacceptable. Effectively, rhyolite-MELTS results suggest that quartz is present in Krafla magmas. While quartz has not been reported as part of the phenocryst assemblage, the small glass chips could make it very difficult to find any phenocrystic quartz crystals. There is evidence of resorbed quartz and alkali feldspar crystals in some quenched glass fragments, and they are interpreted to show the interaction between the host melt and the wall-rock (Zierenberg *et al.*, 2013).

4.3.2.2 Monte Carlo Simulations

Results from the Monte Carlo simulations are summarized in Figure 5. All data are included in Appendix 1. There are 600 synthetic compositions explored in the Monte Carlo analysis for the Krafla RHL rhyolite-MELTS runs. A total of 373/600 (62%) of rhyolite-MELTS runs return a valid pressure. The phase assemblages considered are the same assemblages considered for the individual Krafla RHL compositions (P_4 QFOM, P_3 QFO, and P_3 QFM). There are 27 compositions (5%) that return P_QFOM pressures. The f_{O_2} values that produced these P_4 QFOM pressures are equal to Δ NNO $=$ -1 (20 compositions) and -0.5 (7 compositions). The average pressure for all P_4 QFOM pressures (regardless of f_{O_2}) is 48 MPa ± 8 MPa (1-sigma standard deviation), which corresponds to a depth of 1.8 km ± 0.3 km. There are 317/600 compositions (53%) that return P_3 QFO pressures (where P_4 QFOM is included as P_4 QFOM requires that P_3 QFO is valid) and 83 compositions (14%) return P_3 QFM pressures (where P_4 QFOM is included as P_4 QFOM requires that P_3 QFM is valid). The average pressure for all P_3 QFO pressures (regardless of f_{O_2}) is 46 MPa ± 20 MPa (1.7 km ± 0.7 km) and the average pressure for all P_3 QFM pressures (regardless of f_{O_2}) is 37 MPa ± 13 MPa (1.4 km ± 0.5 km). A similar trend to the Krafla RHL individual compositions is observed, as P_3 QFO pressures are calculated for more reducing conditions and P_3 QFM pressures are calculated for more oxidizing conditions for the Monte Carlo results.

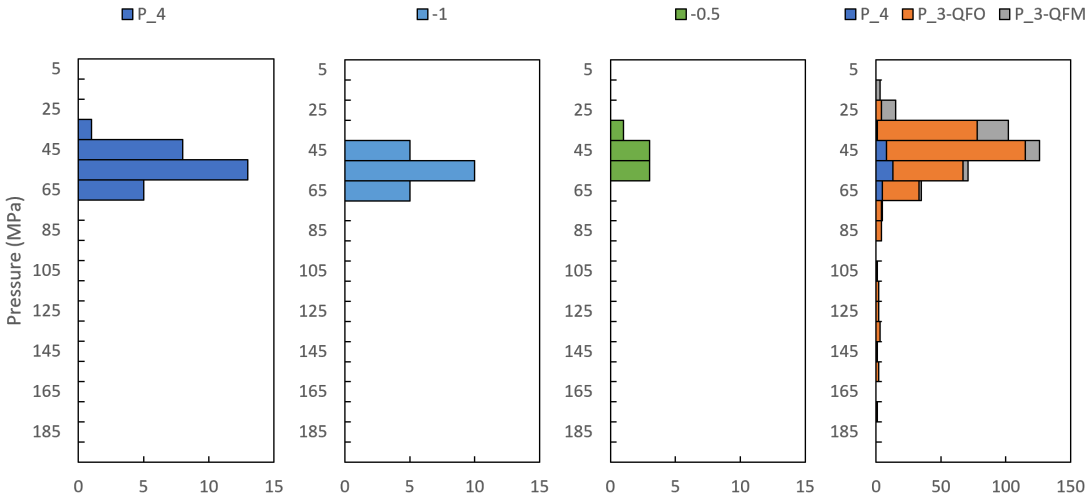

Figure 4.5: Rhyolite-MELTS results for the Monte Carlo analysis. The Monte Carlo included 600 compositions that varied about the mean of the Krafla RHL compositions, using the calculated standard deviation. f_{O_2} values from ΔNNO = -2 to 0 were distributed randomly in 0.5 f_{O_2} steps. Left panel shows rhyolite-MELTS P_4 QFOM pressure results from the Monte Carlo analysis. The only f_{O_2} values that resulted in a P_4 QFOM pressure calculation are f_{O_2} of Δ NNO = -0.5 and -1, shown in the middle two panels. The right panel shows rhyolite-MELTS P_4 QFOM, P_3 QOF and P_3 QFM pressure results from the Monte Carlo simulations for all f_{O_2} values considered.

Table 4.3: Monte Carlo results of P_4 QFOM, P_3 QFO, and P_3 QFM storage pressures for different f_{O_2}

Mean pressure calculation (MPa)	-3 Δ NNO	-2.5 Δ NNO	-2 Δ NNO	-1.5 Δ NNO	-1 Δ NNO_2	-0.5 Δ NNO	0 Δ NNO
P_4 QFOM	-	-	-	-	50	41	-
P_3 QFO	36	40	41	45	48	91	126
P_3 QFM	-	-	-	-	51	34	17
Standard deviation of pressures							
P_4 QFOM	-	-	-	-	6	8	-
P_3 QFO	9	9	9	10	11	46	25
P_3 QFM	-	-	-	-	8	8	5
Number of compositions that return pressures for each f_{O_2}							
P_4 QFOM	0	0	0	0	20	7	0
P_3-QFO	51	66	60	68	32	10	3
P_3-QFM	0	0	0	0	5	42	9
Number of compositions that had the given f_{O_2}	85	83	90	102	72	74	94

4.3.3 TVZ Results

There is a total of 208 rhyolite-MELTS runs for the 36 TVZ flare-up average pumice compositions, since we modeled each composition over six f_{O_2} values (Δ NNO = -0.5 to 2 in 0.5 steps). At high f_{O_2}, eight rhyolite-MELTS simulations failed (i.e., the rhyolite-MELTS calculations could not be completed), which implies that the f_{O_2} of these simulations is too high. A total of 33/36 (92%) TVZ flare-up average compositions returned a pressure for at least one f_{O_2} value. Two compositions from the Pokai ignimbrite (POK105A-7 and POK105A-8) and one composition from the Whakamaru ignimbrite (WHA114C-20) do not yield pressures for any f_{O_2} value. A total of 101/208 (49%) rhyolite-MELTS runs calculate pressures, where individual compositions can have multiple pressures calculated due to the different f_{O_2} values. There were no pressures calculated for Δ NNO = -0.5.

The phase assemblages considered for pressure calculations are the same as the Krafla RHL samples: P_4 QFOM, P_3 QFO, and P_3 QFM. TVZ flare-up compositions do not yield pressures for P_4 QFOM or P_3 QFO, as the orthopyroxene saturation surface does not intersect the quartz and plagioclase saturation surfaces for any composition under the f_{O_2} range we considered. Therefore, we rely on P_3 QFM pressures. Bégué *et al.* (2014) show that the quartz and plagioclase saturation surfaces often become coincident at pressures below 100 MPa, so the intersection of the magnetite saturation surface is critical to determine the best pressure estimate. Results are summarized in Figure 6, which shows the pressures calculated for previously estimated f_{O_2} values for each eruption.

Estimated P_3 QFM pressures decrease systematically from more reducing (Δ NNO = 0) to more oxidizing (Δ NNO = 2) conditions, due to the change in the magnetite saturation as a function of f_{O_2}, indicating that estimating the choice of f_{O_2} is critical for these systems (Table 2). Results from each ignimbrite are summarized below, organized from oldest to youngest eruption age.

The Whakamaru Ignimbrite is the oldest eruption, known to be compositionally distinct from later flare-up magmas. For the Whakamaru compositions, pressures are consistent and not as strongly dependent on f_{O_2}. The estimated f_{O_2} for the Whakamaru system is Δ NNO $\sim$ 1 (Deering *et al.*, 2010). Results are also stated for f_{O_2} half a log unit below and above the estimated f_{O_2} for all ignimbrites. P_3 QFM for Δ NNO = 0.5 is 88 MPa ± 13 MPa (3.3 km ± 0.5 km) (six compositions return results); Δ NNO = 1 is 88 MPa ± 13 MPa (3.3 km ± 0.5 km) (eight compositions return results); and Δ NNO = 1.5 is 76 MPa ± 21 MPa (2.8 km ± 0.8 km) (eight compositions return results).

Matahina Ignimbrite is a compositionally transitional eruption, intermediate between the Whakamaru and later flare-up eruptions (Gravley *et al.*, 2016). The f_{O_2} is estimated to be Δ NNO $\sim$ 0. P_3 QFM for Δ NNO = 0 does not return a pressure; for Δ NNO = 0.5 the result is 111 MPa (4.1 km) (1 composition gives results);

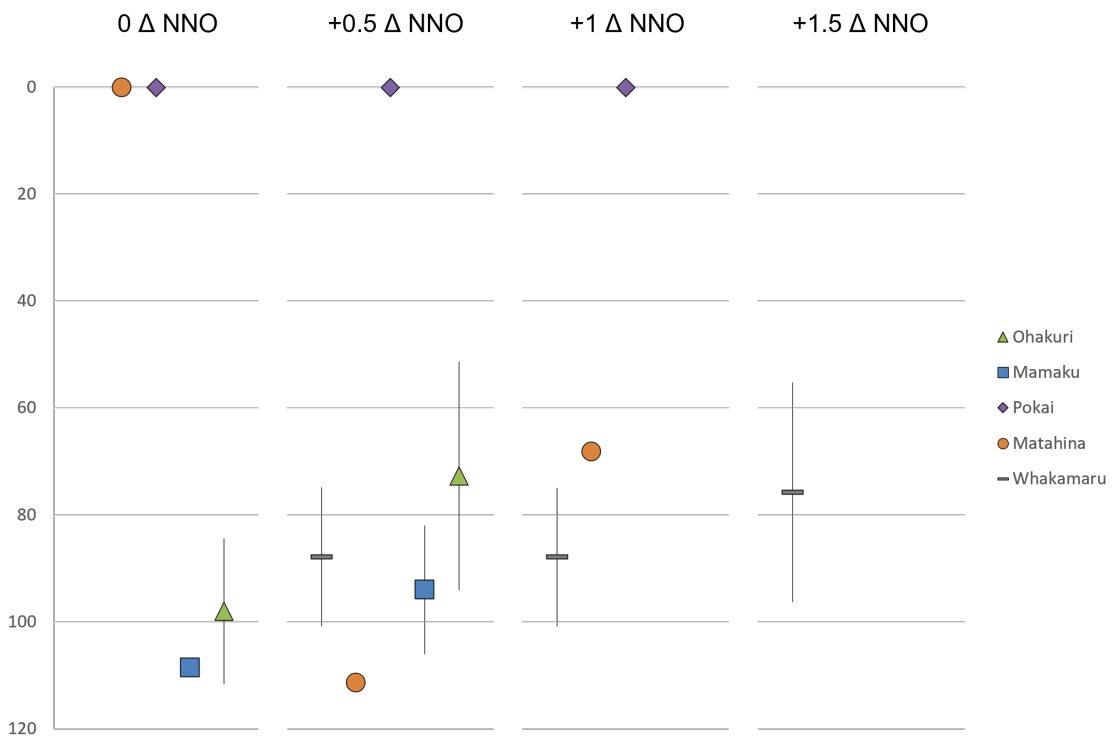

Figure 4.6: P_3 QFM storage pressure versus f_{O_2} for the different TVZ flare-up eruptions. With increasing f_{O_2} , pressures shallow (left to right). Pressures from the Whakamaru ignimbrite compositions appear to be the most consistent, regardless of f_{O_2}.

for Δ NNO $= 1$ the result is 68 MPa (2.5 km) (1 composition); and for Δ NNO $= 1.5$ the result is 43 MPa (1.6 km) (1 composition) although this f_{O_2} value is likely too high to be considered reasonable for Matahina magmas.

Pokai Ignimbrite is one of the oldest flare-up magmas that are "hot, dry, reducing" (Deering *et al.*, 2008, 2010), with Pokai Ignimbrite and all subsequent units in the flare-up having f_{O_2} of Δ NNO ~ 0 (Deering *et al.*, 2010; Gravley *et al.*, 2016). P_3 QFM for Δ NNO $= 0$, Δ NNO $= 0.5$, Δ NNO $= 1$ do not return pressures, while for Δ NNO $= 1.5$, the resulting pressures are 62 MPa ± 37 MPa (2.3 km ± 1.4 km) (2 compositions give results). An f_{O_2} of Δ NNO $= 1.5$ is likely to high to be a reasonable f_{O_2} for the Pokai eruption.

For the Mamaku Ignimbrite, which has an f_{O_2} of Δ NNO ~ 0, P_3 QFM for Δ NNO $= 0$ is 109 MPa (4.0 km) (1 composition gives results); 94 MPa ± 12 MPa (3.5 km ± 0.4 km) for Δ NNO $= 0.5$ (12 compositions give results); 67 MPa ± 17 MPa (2.5 km ± 0.6 km) for Δ NNO $= 1$ (12 compositions give results); and 44 MPa ± 14 MPa (1.6 km ± 0.5 km) for Δ NNO $= 1.5$ (10 compositions give results) although this latter f_{O_2} is likely too high to be considered reasonable for the Mamaku system.

For the Ohakuri Ignimbrite, which also has an f_{O_2} of Δ NNO ~ 0, P_3 QFM for Δ NNO $= 0$ is 98 MPa ± 14 MPa (3.6 km ± 0.5 km) (2 compositions give results); 73 MPa ± 21 MPa (2.7 km ± 0.8 km) for Δ NNO $=$

0.5 (5 compositions give results); 53 MPa ± 14 MPa (2.3 km ± 0.5 km) for Δ NNO = 1 (6 compositions give results); and 32 MPa ± 15 MPa (1.2 km ± 0.6 km) for Δ NNO = 1.5 (5 compositions give results) although the latter f_{O_2} is likely too high to be considered reasonable for Ohakuri magmas based on previous f_{O_2} estimates (Deering *et al.*, 2010; Gravley *et al.*, 2016).

Table 4.4: Results of P_3 QFM storage pressures for different TVZ flare-up magmas for different f_{O_2}

Average P_3 QFM (MPa)	-0.5 Δ NNO	0 Δ NNO	0.5 Δ NNO	1 Δ NNO	1.5 Δ NNO	2 Δ NNO
Ohakuri	-	98	73	53	32	29
Mamaku	-	109	94	67	44	29
Pokai	-	-	-	-	62	86
Matahina	-	-	111	68	43	28
Whakamaru	-	93	88	88	76	80

Standard deviation P_3 QFM (MPa)						
Ohakuri	-	14	21	14	15	15
Mamaku	-	-	12	17	14	6
Pokai	-	-	-	-	37	-
Matahina	-	-	-	-	-	-
Whakamaru	-	14	13	13	21	32

Number of compositions that return P_3 QFM for each f_{O_2}						
Ohakuri	0	2	5	6	5	3
Mamaku	0	1	12	12	10	10
Pokai	0	0	0	0	2	1
Matahina	0	0	1	1	1	1
Whakamaru	0	2	6	8	8	4

4.4 Discussion

4.4.1 Reliability of Geobarometry for Ultra-Shallow Pressures

The fact that Krafla well IDDP-1 intersected a magma at 2.1 km depth provides incontrovertible evidence that ultra-shallow magma bodies exist in the crust. The retrieved quenched glass fragments retrieved as part of the drilling allow us to test our ability to detect such magma bodies using existing geobarometry methods. We compare geobarometric estimates using glass compositions with the 2.1 km depth (57 MPa) of the Krafla IDDP-1 drilling project.

Interestingly, the SiO_2 contents of Krafla RHL major element glass compositions are relatively low for the pressure at which magma was retrieved. The average SiO_2 in RHL compositions (76.7 wt% SiO_2) is much lower than would be expected for the pressure-SiO_2 relationship given in Gualda and Ghiorso (2013). However, the Krafla RHL compositions have significantly higher FeO content (2.9 wt% FeO) when compared to all systems studied in Gualda and Ghiorso (2013). For that reason, the SiO_2 values for Krafla RHL compositions are anomalously low when presented in a normalized anhydrous basis. If the FeO value for Krafla RHL is reduced from 2.9 wt% (Masotta *et al.*, 2018) to $\sim$ 1 wt% FeO, the SiO_2 would increase to be $\sim$ 78.2 wt%, which is more in line with what would be expected for magmas crystallizing at such shallow pressures.

The projection scheme of Blundy and Cashman (2001) circumvents the issue of high FeO values in the RHL compositions, by employing normative values for Qz, Ab, Or, and An (effectively this means compositions are considered on an FeO-free, MgO-free basis). While the Qz'-Ab'-Or' ternary diagram is a somewhat crude measure of pressure, the Krafla RHL average composition sit on the 50 MPa (1.9 km) cotectic (Figure 1) which indicates that the cotectic is in good agreement with the natural samples intercepted at 2.1 km. Importantly, pressures estimated using the Qz'-Ab'-Or' ternary are maximum pressures, given that the presence of quartz cannot be unambiguously confirmed. However, the agreement between the estimated pressure and the known depth suggests that Krafla RHL compositions were in equilibrium with quartz (or very nearly so).

For the rhyolite-MELTS results, the average P_4 QFOM pressure for the individual compositions (50 MPa ± 11 MPa; 1.9 km ± 0.4 km) is in excellent agreement with the drilling depth. The average P_3 QFO pressure (44 MPa ± 11 MPa, 1.7 km ± 0.4 km) and P_3 QFM pressure (47 MPa ± 32 MPa, 1.7 km ± 1.2 km) for the individual compositions are also in excellent agreement with the observed depth. In addition to the pressure measurements, rhyolite-MELTS estimates the f_{O_2} of the Krafla system to be between Δ NNO = -0.5 and -1, which agree with the reducing f_{O_2} estimates for Krafla magmas (Jonasson, 1994). The individual and average Krafla RHL estimates are supported by the Monte Carlo results, which yield an average pressure of 48 ± 8 MPa for P_4 QFOM pressures exclusively for f_{O_2} of Δ NNO = -1 and -0.5. In addition to the pressure, the

accurate estimation of f_{O_2} and saturated fluid conditions, as calculated by Zierenberg *et al.* (2013), indicate that rhyolite-MELTS can accurately estimate the conditions from magma intersected at Krafla IDDP-1 well with a precision superior to what is possible using the Qz'-Ab'-Or' ternary diagram.

4.4.2 Application to the Taupo Volcanic Zone, New Zealand

Similarly shallow pressures have been calculated using rhyolite-MELTS for magmas from the TVZ, for equilibrium of melt with a quartz-plagioclase assemblage (Bégué, Deering, *et al.*, 2014; Bégué, Gualda, *et al.*, 2014; Gualda *et al.*, 2018). However, questions remain as to the reliability of such results. We show here that rhyolite-MELTS calculations suggest equilibration of these melt compositions with an assemblage of quartz-plagioclase-magnetite, under pressures < 120 MPa (4.5 km) – and often < 100 MPa (< 3.7 km) – for reasonable values of f_{O_2} (Figure 6), lending significant support to the existence of ultra-shallow magma bodies in the TVZ. While Bégué *et al.* (2014) could only determine a maximum pressure – because the plagioclase and quartz saturation surfaces do not have a unique intersection point – we demonstrate that we can use the magnetite saturation surface (as long as f_{O_2} can be independently constrained) to determine the most likely storage pressure. This suggests that the TVZ also contained – at various times and in various volcanic centers – bodies of eruptible magma located at very shallow crustal levels throughout the ignimbrite flare-up period (Gravley *et al.*, 2016).

Importantly, rhyolite-MELTS estimates obtained using the quartz-plagioclase-magnetite are in excellent agreement with estimates made using the Qz'-Ab'-Or' ternary diagram (Figure 1) with the projection scheme of Blundy and Cashman (2001). Yet, the results from rhyolite-MELTS allow us a more detailed perspective on the storage pressures, mineral assemblages, and f_{O_2} values.

4.4.3 Ultra-shallow magma bodies as part of transcrustal magmatic systems

There is a growing body of evidence to suggest that magmatic systems span a significant range of storage depths within the crust – leading to the idea of transcrustal magma systems (Giordano & Caricchi, 2022; Mutch *et al.*, 2019; Svoboda *et al.*, 2021). The existence of ultra-shallow magma bodies indicates that we must extend this model of storage to a shallower level. These ultra-shallow magma bodies are likely a volumetrically minor constituent of the magma systems, as the ultra-shallow pressures represent a minority of the storage pressures retrieved by geobarometry (Bégué, Gualda, *et al.*, 2014; Gualda *et al.*, 2018).

It is interesting to consider why these bodies have been largely overlooked to date, with much more attention being paid to deeper levels of magmatic systems. The lifetimes of shallow eruptible magma bodies are short (Gualda & Sutton, 2016; Pamukçu *et al.*, 2021; Pamukcu, Gualda, Bégué, *et al.*, 2015b), especially when a geothermal reservoir is present (Kelly *et al.*, 2021). It thus seems likely that these bodies are particu-

larly ephemeral features, and thus they are relatively rare at any given point in time. It is thus possible that we have overlooked this ultra-shallow magma storage level due to the short lifetimes and relatively small size of these magma bodies. Despite these ultra-shallow magma bodies likely being relatively small and short-lived, their proximity to the Earth's surface makes them economically and societally important.

4.4.4 Global existence of ultra-shallow magma bodies

The ultra-shallow storage pressures calculated here are from two different tectonic settings: Krafla in the plume-affected mid-Ocean rift of Iceland; and the rifted arc of the TVZ in New Zealand. These seems to suggest that these ultra-shallow magma bodies are not exclusive of the unique tectonic and magmatic environment of Iceland, and that they exist in different tectonic settings. It is noteworthy that both localities we studied are significantly affected by extension, which could suggest that extension and rifting may facilitate establishment of these ultra-shallow magma bodies in the crust. For both Krafla and the TVZ, the magma systems are long-established and indicate that there is a consistent high heat flux to the shallow crust (Jonasson, 1994; Kelly *et al.*, 2021; Mutch *et al.*, 2019; Wilson, 1996), consistent with involvement of greater depths of the crust in the generation and storage of eruption-forming magma bodies (Gualda *et al.*, 2018, 2019). However, the size of the TVZ flare-up eruptions and the Krafla eruptions differ by more than an order of magnitude (Gravley *et al.*, 2016; Jonasson, 1994; Rooyakkers *et al.*, 2021), indicating that these ultra-shallow magma bodies exist for magma systems of very different sizes. Be as it may, we speculate that these ultra-shallow magma bodies are likely a common phenomenon that has been largely overlooked. And even though these ultra-shallow magma bodies are likely a minority of the erupted volume, their existence revolutionizes how we conceptualize magma storage at shallow depths in the crust.

There is some evidence in the literature that ultra-shallow magma bodies may be present in the crust today. InSAR and seismic evidence from Dabbahu volcano (Afar, Ethiopia), within the East African Rift, indicates that a magma body likely exists at 2.5-6 km depth (Ebinger *et al.*, 2008; Wright *et al.*, 2006). Further, geothermal fields are highly studied regions where magma could be detected by geophysical methods. Both the Menengai geothermal field in Kenya (Mbia *et al.*, 2015) and the Larderello geothermal area in Italy (Manzella *et al.*, 2017) are locations where the presence of ultra-shallow magma has been hypothesized. Geophysical methods, including seismic data and InSAR are likely critical for determining the presence of current, ultra-shallow magma bodies.

In addition to the direct evidence at Krafla, the rhyolite-MELTS evidence from previous eruptions in the TVZ, and the indirect observations by geophysical methods, there is substantial field evidence for ultra-shallow magma bodies in the plutonic record. Shallow granites are observed in the Searchlight pluton, in which extreme tilting exposes a cross-section of the magma system (Bachl *et al.*, 2001; Faulds *et al.*, 2001).

While precise determination of storage pressures is difficult for plutonic rocks, field evidence suggests that some of felsite found within the Searchlight pluton crystallized at very shallow structural levels, within the range we consider here to represent ultra-shallow. Field evidence for shallow emplacement of magma is also evident in the Mount Scott Granite, Oklahoma, USA (Hogan *et al.*, 1998; Hogan & Gilbert, 1995). In eastern Zhejiang (China), the emplacement depth of magma is estimated to be 50-100 MPa based on the Qz'-Ab'-Or' ternary (Chen *et al.*, 2021), which is consistent with the granophyre textures observed, typically interpreted to result from rapid undercooling at shallow pressures. Similar interpretation can be made from rocks in the Alid Volcanic Center (Eritrea) (Lowenstern *et al.*, 1997). Al-in-hornblende geobarometry yields ultra-shallow emplacement depths (4-5 km) during the development of the Andean volcanic arc (Nelson *et al.*, 1999; Schaen *et al.*, 2017), as well as in several Icelandic plutons: Reyðarártindur Pluton (Rhodes *et al.*, 2021; Twomey *et al.*, 2020); Austurhorn Pluton (Blake, 1966; Furman *et al.*, 1992; Padilla *et al.*, 2016; Walker, 1960; Walker GPL, 1964); and Slaufrudalur Pluton (Burchardt *et al.*, 2012; Walker, 1974). While not intended to be exhaustive, this list of examples indicates that these ultra-shallow magma bodies may be a common occurrence within silicic magma systems in multiple tectonic settings, and they can form magma bodies of various sizes.

4.5 Conclusions, Implications, and Future Work

While the ultra-shallow magma bodies are confirmed only at Krafla IDDP-1 well, we have corroborating rhyolite-MELTS evidence from the TVZ to indicate that these ultra-shallow magma bodies are not unique to Krafla or Iceland. They may be relatively common features of transcrustal magmatic systems. We show that rhyolite-MELTS can be used to calculate not only the pressures of storage for a variety of mineral assemblages, but that it can also help constrain other intensive parameters such as temperature, f_{O_2}, and H2O saturation during pre-eruptive storage.

Methods to petrologically and geophysically monitor the existence and hazards of these ultra-shallow magma bodies should be established to mitigate volcanic hazards. The substantial petrologic evidence that these magma bodies exist should be a call for the combined use of geophysics, hazard assessment, and petrology to properly assess the presence, properties, and potential societal impacts of ultra-shallow magma bodies. As we have thus far overlooked this crustal level as a potential magma storage zone, an updated perspective on the structure of the crust is needed.

4.6 References

Bachl, C. A., Miller, C. F., Miller, J. S., & Faulds, J. E. (2001). Construction of a pluton: Evidence from an exposed cross section of the Searchlight pluton, Eldorado Mountains, Nevada. Bulletin of the Geological Society of America, 113(9), 1213–1228. https://doi.org/10.1130/0016-7606(2001)113<1213:

COAPEF>2.0.CO;2

Bégué, F., Deering, C. D., Gravley, D. M., Kennedy, B. M., Chambefort, I., Gualda, G. A. R., & Bachmann, O. (2014). Extraction, storage and eruption of multiple isolated magma batches in the paired Mamaku and Ohakuri eruption, Taupo volcanic zone, New Zealand. Journal of Petrology, 55(8), 1653–1684. https://doi.org/10.1093/petrology/egu038

Bégué, F., Gualda, G. A. R., Ghiorso, M. S., Pamukcu, A. S., Kennedy, B. M., Gravley, D. M., Deering, C. D., & Chambefort, I. (2014). Phase-equilibrium geobarometers for silicic rocks based on rhyolite-MELTS. Part 2: application to Taupo Volcanic Zone rhyolites. Contributions to Mineralogy and Petrology, 168, 1–16. https://doi.org/10.1007/s00410-014-1082-7

Blake, D. H. (1966). The Net-Veined Complex of the Austurhorn Intrusion, Southeastern Iceland. The Journal of Geology, 74(6), 891–907. https://about.jstor.org/terms

Blundy, J., & Cashman, K. (2001). Ascent-driven crystallisation of dacite magmas at Mount St Helens, 1980-1986. Contributions to Mineralogy and Petrology, 140(6), 631–650. https://doi.org/10.1007/s004100000219

Burchardt, S., Tanner, D., & Krumbholz, M. (2012). The Slaufrudalur pluton, southeast Iceland-An example of shallow magma emplacement by coupled cauldron subsidence and magmatic stoping. Bulletin of the Geological Society of America, 124(1–2), 213–227. https://doi.org/10.1130/B30430.1

Cameli, G. M., Dini, I., & Liotta ', D. (1993). Upper crustal structure of the Larderello geothermal field as a feature of post-collisional extensional tectonics (Southern Tuscany, Italy) (Vol. 224). Elsevier Science Publishers B.V.

Chen, J. Y., Yang, J. H., Zhang, J. H., & Zhu, Y. S. (2021). Construction of a highly silicic upper crust in southeastern China: Insights from the Cretaceous intermediate-to-felsic rocks in eastern Zhejiang. Lithos, 402–403. https://doi.org/10.1016/j.lithos.2021.106012

Deering, C. D., Cole, J. W., & Vogel, T. A. (2008). A rhyolite compositional continuum governed by lower crustal source conditions in the Taupo Volcanic Zone, New Zealand. Journal of Petrology, 49(12), 2245–2276. https://doi.org/10.1093/petrology/egn067

Deering, C. D., Gravley, D. M., Vogel, T. A., Cole, J. W., & Leonard, G. S. (2010). Origins of cold-wet-oxidizing to hot-dry-reducing rhyolite magma cycles and distribution in the Taupo Volcanic Zone, New Zealand. Contributions to Mineralogy and Petrology, 160(4), 609–629. https://doi.org/10.1007/s00410-010-0496-0

Ebinger, C. J., Keir, D., Ayele, A., Calais, E., Wright, T. J., Belachew, M., Hammond, J. O. S., Campbell, E., & Buck, W. R. (2008). Capturing magma intrusion and faulting processes during continental rupture: Seismicity of the Dabbahu (Afar) rift. Geophysical Journal International, 174(3), 1138–1152. https://doi.org/10.1111/j.1365-246X.2008.03877.x

Elders, W. A., Fridleifsson, G. Ó., Zierenberg, R. A., Pope, E. C., Mortensen, A. K., Gudmundsson, Á., Lowenstern, J. B., Marks, N. E., Owens, L., Bird, D. K., Reed, M., Olsen, N. J., & Schiffman, P. (2011). Origin of a rhyolite that intruded a geothermal well while drilling at the Krafla volcano, Iceland. Geology, 39(3), 231–234. https://doi.org/10.1130/G31393.1

Faulds, J. E., Feuerbach, D. L., Miller, C. F., & Smith, E. I. (2001). Cenozoic evolution of the northern Colorado River extensional corridor, southern Nevada and northwest Arizona.

Foley, M. L., Miller, C. F., & Gualda, G. A. R. (2020). Architecture of a Super-sized Magma Cham-

ber and Remobilization of its Basal Cumulate (Peach Spring Tuff, USA). Journal of Petrology, 61(1). https://doi.org/10.1093/petrology/egaa020

Furman, T., Meyer, P. S., & Frey, F. (1992). Evolution of Icelandic central volcanoes: evidence from the Austurhorn intrusion, southeastern Iceland. Bulletin of Volcanology, 55, 45–62.

Giordano, G., & Caricchi, L. (2022). Determining the State of Activity of Transcrustal Magmatic Systems and Their Volcanoes. Annual Review of Earth and Planetary Sciences, 50, 231–259.

Gravley, D. M., Deering, C. D., Leonard, G. S., & Rowland, J. v. (2016). Ignimbrite flare-ups and their drivers: A New Zealand perspective. Earth-Science Reviews, 162, 65–82. https://doi.org/10.1016/j.earscirev.2016.09.007

Gualda, G. A. R., & Ghiorso, M. S. (2013). Low-Pressure Origin of High-Silica Rhyolites and Granites. The Journal of Geology, 121, 537–545. https://doi.org/10.1086/671395

Gualda, G. A. R., & Ghiorso, M. S. (2014). Phase-equilibrium geobarometers for silicic rocks based on rhyolite-MELTS. Part 1: Principles, procedures, and evaluation of the method. Contributions to Mineralogy and Petrology, 168(1), 1–17. https://doi.org/10.1007/s00410-014-1033-3

Gualda, G. A. R., & Ghiorso, M. S. (2015). MELTS-Excel: A Microsoft Excel-based MELTS interface for research and teaching of magma properties and evolution. Geochemistry, Geophysics, Geosystems, 16(1), 315–324. https://doi.org/10.1002/2014GC005545

Gualda, G. A. R., Ghiorso, M. S., Lemons, R. v., & Carley, T. L. (2012). Rhyolite-MELTS: a Modified Calibration of MELTS Optimized for Silica-rich, Fluid-bearing Magmatic Systems. Journal of Petrology, 53(5), 875–890. https://doi.org/10.1093/petrology/egr080

Gualda, G. A. R., Gravley, D. M., Conner, M., Hollmann, B., Pamukcu, A. S., Bégué, F., Ghiorso, M. S., & Deering, C. D. (2018). Climbing the crustal ladder: Magma storage-depth evolution during a volcanic flare-up. Science Advances, 4(10). https://doi.org/10.1126/sciadv.aap7567

Gualda, G. A. R., Gravley, D. M., Deering, C. D., & Ghiorso, M. S. (2019). Magma extraction pressures and the architecture of volcanic plumbing systems. Earth and Planetary Science Letters, 522, 118–124. https://doi.org/10.1016/j.epsl.2019.06.020

Gualda, G. A. R., Pamukcu, A. S., Ghiorso, M. S., Anderson Jr, A. T., Sutton, S. R., Rivers, M. L., & Houlie, N. (2012). Timescales of Quartz Crystallization and the Longevity of the Bishop Giant Magma Body. PLoS ONE, 7(5). https://doi.org/10.1371/journal.pone.0037492

Gualda, G. A. R., & Sutton, S. R. (2016). The year leading to a supereruption. PLoS ONE, 11(7), 1–18. https://doi.org/10.1371/journal.pone.0159200

Harmon, L. J., Cowlyn, J., Gualda, G. A. R., & Ghiorso, M. S. (2018). Phase-equilibrium geobarometers for silicic rocks based on rhyolite-MELTS. Part 4: Plagioclase, orthopyroxene, clinopyroxene, glass geobarometer, and application to Mt. Ruapehu, New Zealand. Contributions to Mineralogy and Petrology, 173(1). https://doi.org/10.1007/s00410-017-1428-z

Hogan, J. P., & Gilbert, M. C. (1995). The A-type Mount Scott granite sheet: importance of crustal magma traps. Journal of Geophysical Research, 100(B8). https://doi.org/10.1029/94jb03258

Hogan, J. P., Price, J. D., & Gilbert, M. C. (1998). Magma traps and driving pressure: consequences for pluton shape and emplacement in an extensional regime. Journal of Structural Geology, 20(9/10), 1155–1168. Huber, C., Townsend, M., Degruyter, W., & Bachmann, O. (2019). Optimal depth of

subvolcanic magma chamber growth controlled by volatiles and crust rheology. Nature Geoscience. https://doi.org/10.1038/s41561-019-0415-6

Jonasson, K. (1994). Rhyolite volcanism in the Krafla central volcano, north-east Iceland. Bulletin of Volcanology, 56, 516–528.

Kelly, L. J., Gualda, G. A. R., Gravley, D. M., & Dempsey, D. E. (2021). Hydrothermal Cooling as a Requirement for Short Storage of Silicic Magmas. Geochemistry, Geophysics, Geosystems, 22(9). https://doi.org/10.1029/2021GC009794

Klemetti, E. W., Deering, C. D., Cooper, K. M., & Roeske, S. M. (2011). Magmatic perturbations in the Okataina Volcanic Complex, New Zealand at thousand-year timescales recorded in single zircon crystals. Earth and Planetary Science Letters, 305(1–2), 185–194. https://doi.org/10.1016/j.epsl.2011.02.054

Lowenstern, J. B., Clynne, M. A., & Bullen, T. D. (1997). Comagmatic A-Type Granophyre and Rhyolite from the Alid Volcanic Center, Eritrea, Northeast Africa. In JOURNAL OF PETROLOGY (Vol. 38).

Manzella, A., Gola, G., Bertini, G., Bonini, M., Botteghi, S., Brogi, A., de Franco, R., Dini, A., Donato, A., Gianelli, G., Liotta, D., Montanari, D., Montegrossi, G., Petracchini, L., Ruggieri, G., Santilano, A., Scrocca, D., & Trumpy, E. (2017). Data integration and conceptual modelling of the Larderello geothermal area, Italy. EGU General Assembly Conference Abstracts, 19034.

Masotta, M., Mollo, S., Nazzari, M., Tecchiato, V., Scarlato, P., Papale, P., & Bachmann, O. (2018). Crystallization and partial melting of rhyolite and felsite rocks at Krafla volcano: A comparative approach based on mineral and glass chemistry of natural and experimental products. Chemical Geology, 483, 603–618. https://doi.org/10.1016/j.chemgeo.2018.03.031

Mbia, P. K., Mortensen, A. K., Oskarsson, N., Bjorn, S., & Hardarson, B. S. (2015). Sub-Surface Geology, Petrology and Hydrothermal Alteration of the Menengai Geothermal Field, Kenya: Case Study of Wells MW-02, MW-04, MW-06 and MW-07. In Proceedings World Geothermal Congress.

Mortensen, A. K., Egilson, T., Gautason, B., Árnadóttir, S., & Guomundsson, A. (2014). Stratigraphy, alteration mineralogy, permeability and temperature conditions of well IDDP-1, Krafla, NE-Iceland. Geothermics, 49, 31–41. https://doi.org/10.1016/j.geothermics.2013.09.013

Mutch, E. J. F., Maclennan, J., Shorttle, O., Edmonds, M., & Rudge, J. F. (2019). Rapid transcrustal magma movement under Iceland. Nature Geoscience, 12(7), 569–574. https://doi.org/10.1038/s41561-019-0376-9

Nelson, S. T., Davidson, J. P., Heizler, M. T., & Kowallis, B. J. (1999). Tertiary tectonic history of the southern Andes: The subvolcanic sequence to the Tatara-San Pedro volcanic complex, lat 36S. GSA Bulletin, 111(9), 1387–1404.

Padilla, A. J., Miller, C. F., Carley, T. L., Economos, R. C., Schmitt, A. K., Coble, M. A., Wooden, J. L., Fisher, C. M., Vervoort, J. D., & Hanchar, J. M. (2016). Elucidating the magmatic history of the Austurhorn silicic intrusive complex (southeast Iceland) using zircon elemental and isotopic geochemistry and geochronology. Contributions to Mineralogy and Petrology, 171(8–9). https://doi.org/10.1007/s00410-016-1279-z

Pamukcu, A. S., Gualda, G. A. R., Bégué, F., & Gravley, D. M. (2015a). Melt inclusion shapes: Timekeepers of short-lived giant magma bodies. Geology, 43(11), 947–950. https://doi.org/10.1130/G37021.1

Pamukcu, A. S., Gualda, G. A. R., Bégué, F., & Gravley, D. M. (2015b). Melt inclusion shapes: Timekeepers of short-lived giant magma bodies. Geology, 43(11), 947–950. https://doi.org/10.1130/G37021.1

Pamukcu, A. S., Gualda, G. A. R., Ghiorso, M. S., Miller, C. F., & McCracken, R. G. (2015). Phase-equilibrium geobarometers for silicic rocks based on rhyolite-MELTS—Part 3: Application to the Peach Spring Tuff (Arizona–California–Nevada, USA). Contributions to Mineralogy and Petrology, 169(3). https://doi.org/10.1007/s00410-015-1122-y

Pamukçu, A. S., Gualda, G. A. R., & Gravley, D. M. (2021). Rhyolite-MELTS and the storage and extraction of large-volume crystal-poor rhyolitic melts at the Taupō Volcanic Center: a reply to Wilson *et al.* (2021). Contributions to Mineralogy and Petrology, 176(10). https://doi.org/10.1007/s00410-021-01840-2

Pitcher, B. W., Gualda, G. A. R., & Hasegawa, T. (2021). Repetitive Duality of Rhyolite Compositions, Timescales, and Storage and Extraction Conditions for Pleistocene Caldera-forming Eruptions, Hokkaido, Japan. Journal of Petrology, 62(2). https://doi.org/10.1093/petrology/egaa106

Rhodes, E. L., Barker, A. K., Burchardt, S., Hieronymus, C. F., Rousku, S. N., McGarvie, D. W., Mattsson, T., Schmiedel, T., Ronchin, E., & Witcher, T. (2021). Rapid Assembly and Eruption of a Shallow Silicic Magma Reservoir, Reyðarártindur Pluton, Southeast Iceland. Geochemistry, Geophysics, Geosystems, 22(11). https://doi.org/10.1029/2021GC009999

Rochira, F., Caggianelli, A., & de Lorenzo, S. (2018). Regional thermo-rheological field related to granite emplacement in the upper crust: implications for the Larderello area (Tuscany, Italy). Geodinamica Acta, 30(1), 225–240. https://doi.org/10.1080/09853111.2018.1488912

Rooyakkers, S. M., Stix, J., Berlo, K., Petrelli, M., Hampton, R. L., Barker, S. J., & Morgavi, D. (2021). The Origin of Rhyolitic Magmas at Krafla Central Volcano (Iceland). Journal of Petrology, 62(8). https://doi.org/10.1093/petrology/egab064

Schaen, A. J., Cottle, J. M., Singer, B. S., Brenhin Keller, C., Garibaldi, N., & Schoene, B. (2017). Complementary crystal accumulation and rhyolite melt segregation in a late Miocene Andean pluton. Geology, 45(9), 835–838. https://doi.org/10.1130/G39167.1

Svoboda, C., Rooney, T. O., Girard, G., & Deering, C. (2021). Transcrustal magmatic systems: evidence from andesites of the southern Taupo Volcanic Zone. https://doi.org/10.6084/m9.figshare.c.5494984

Teplow, W., Marsh, B., Hulen, J., Spielman, P., Kaleikini, M., Fitch, D., & Rickard, W. (2009). Dacite melt at the Puna Geothermal Venture wellfield, Big Island of Hawaii. GRC Transactions, 33.

Till, C. B., Kent, A. J. R., Abers, G. A., Janiszewski, H. A., Gaherty, J. B., & Pitcher, B. W. (2019). The causes of spatiotemporal variations in erupted fluxes and compositions along a volcanic arc. Nature Communications, 10(1). https://doi.org/10.1038/s41467-019-09113-0

Twomey, V., McCarthy, W., Magee, C., & Petronis, M. (2020). Pre-existing fault-controlled eruptions from the lateral tips of a laccolith in SE Iceland. Copernicus Meetings.

Walker, G. P. L. (1960). Zeolite Zones and Dike Distribution in Relation to the Structure of the Basalts of Eastern Iceland. The Journal of Geology, 68(5), 515–528. https://about.jstor.org/terms

Walker, G. P. L. (1974). The Structure of Eastern Iceland. In L. Kristjansson (Ed.), Geodynamics of Iceland and the North Atlantic Area (pp. 177–188). Springer Netherlands.

Walker GPL. (1964). Geological investigations in eastern Iceland. Bulletin of Volcanology, 27, 1–15.

Wilson, C. J. N. (1996). Taupo's atypical arc. Nature, 379, 27–28.

Wright, T. J., Ebinger, C., Biggs, J., Ayele, A., Yirgu, G., Keir, D., & Stork, A. (2006). Magma-maintained

rift segmentation at continental rupture in the 2005 Afar dyking episode. Nature, 442(7100), 291–294. https://doi.org/10.1038/nature04978

Zierenberg, R. A., Schiffman, P., Barfod, G. H., Lesher, C. E., Marks, N. E., Lowenstern, J. B., Mortensen, A. K., Pope, E. C., Bird, D. K., Reed, M. H., Fridleifsson, G. Ó., & Elders, W. A. (2013). Composition and origin of rhyolite melt intersected by drilling in the Krafla geothermal field, Iceland. Contributions to Mineralogy and Petrology, 165(2), 327–347. https://doi.org/10.1007/s00410-012-0811-z

CHAPTER 5

Conclusions

5.1 Final Thoughts

While substantial uncertainties remain in understanding how magma bodies form and contribute to volcanic eruptions, we use a combination of techniques to elucidate the conditions (specifically the depths, temperatures, and relative timing) of the magma bodies that contributed to the Whakamaru group eruptions. Using erupted material from both the pyroclastic fall deposits (PFDs) and the ignimbrite deposits yields new opportunities to understand these magmatic processes. I use the compositions of glass from pumice clasts to link the PFDs to the ignimbrite deposits. I take advantage of the information from the PFDs to constrain the relative timing of the magma bodies that fed the Whakamaru group eruptions. The whole-rock data from the Whakamaru group ignimbrites gives us information on the extraction conditions of eruptible magma – and thus, it informs us about the architecture of the larger magma system.

Future research could include why there is a consistent, shallow magma storage zone for the eruptible magma bodies – perhaps due to structural or tectonic controls – and why do the Whakamaru group eruptions cause a change in magma body storage for the subsequent TVZ flare-up eruptions – perhaps the evacuation of >2000 km3 of magma causes are reset of the maturity of the magma system. Putting the Whakamaru magma system in the wider context of the TVZ – and global volcanism – is imperative to understand these magma systems in general.

We also extend our understanding of where magma bodies can be stored in the upper crust. The ultra-shallow depths (< 4 km) indicate that the transcrustal magma system can extend to shallower depths than previously established. The ultra-shallow magma bodies, while likely a small proportion of all magma bodies, could pose substantial volcanic hazards and risk. It is thus imperative to study the storage conditions of magma bodies to mitigate these hazards and better understand how the Earth can generate eruptible magma.

If nothing else, I have learned that magma systems are complex, and their complexity sustains my curiosity.